

NASA
Technical
Paper
3253

November 1992

1N-02
131757
P.171

Effects of Forebody Strakes
and Mach Number on Overall
Aerodynamic Characteristics
of Configuration With
55° Cropped Delta Wing

Gary E. Erickson
and Lawrence W. Rogers

(NASA-TP-3253) EFFECTS OF FOREBODY
STRAKES AND MACH NUMBER ON OVERALL
AERODYNAMIC CHARACTERISTICS OF
CONFIGURATION WITH 55 DEG CROPPED
DELTA WING (NASA) 171 p

N93-13353

Unclass

H1/02 0131757

NASA



**NASA
Technical
Paper
3253**

1992

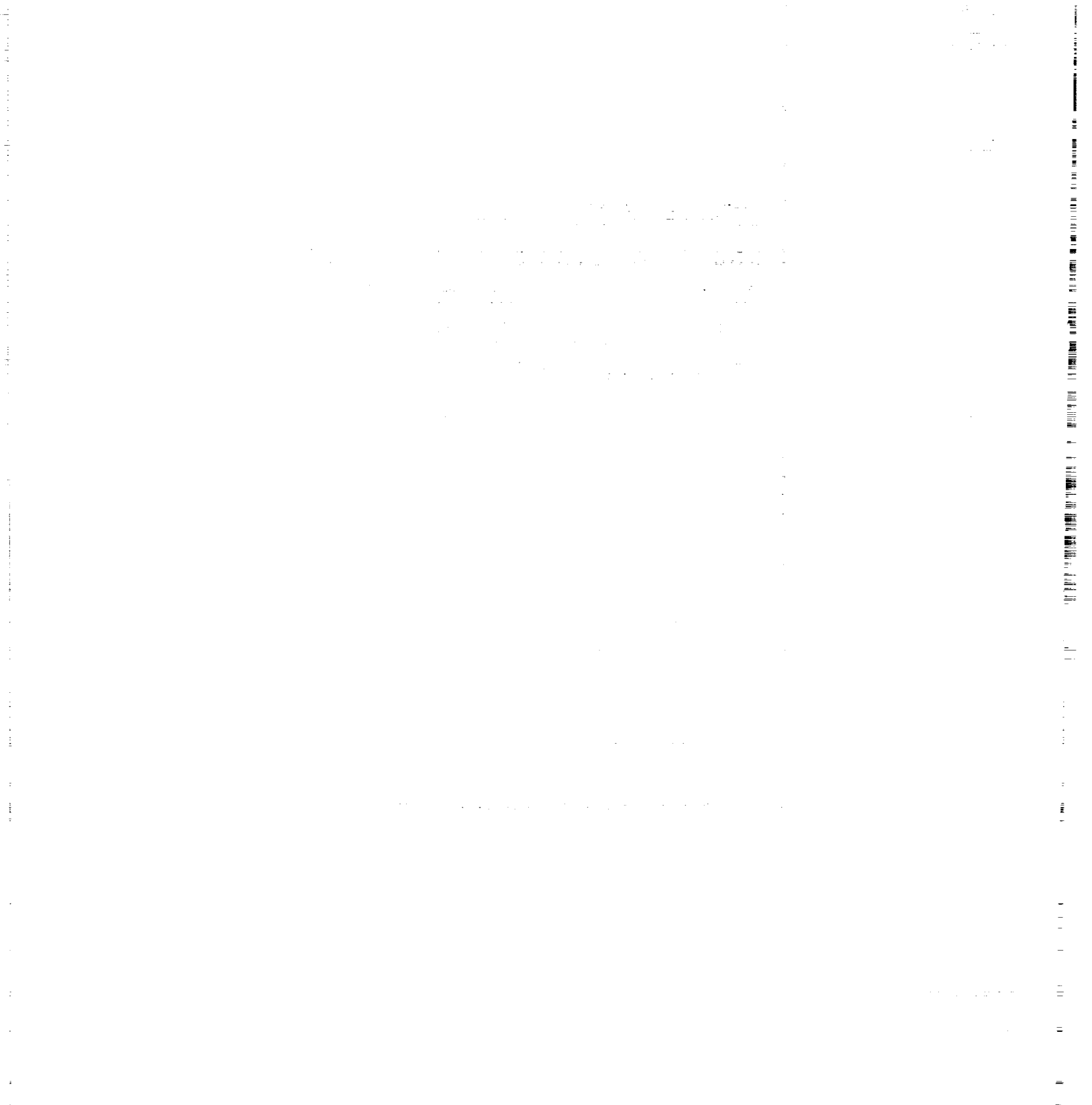
**Effects of Forebody Strakes
and Mach Number on Overall
Aerodynamic Characteristics
of Configuration With
55° Cropped Delta Wing**

Gary E. Erickson
*Langley Research Center
Hampton, Virginia*

Lawrence W. Rogers
*Wright Laboratory-FIMM
Wright-Patterson Air Force Base, Ohio*



National Aeronautics and
Space Administration
Office of Management
Scientific and Technical
Information Program



Contents

Summary	1
Introduction	1
Symbols	1
Experimental Investigation	2
Model Description and Test Apparatus	2
Flow Visualization Technique	3
Wind Tunnel Facility and Test Conditions	4
Discussion of Results	4
Effect of Forebody Strakes on Longitudinal Characteristics	4
Leading-edge flap undeflected	4
Leading-edge flap deflected 30°	7
Effect of Forebody Strakes on Lateral-Directional Characteristics	9
Leading-edge flap undeflected	9
Leading-edge flap deflected 30°	10
Effect of Mach Number on Longitudinal Characteristics	12
Leading-edge flap undeflected	12
Leading-edge flap deflected 30°	13
Effect of Mach Number on Lateral-Directional Characteristics	14
Leading-edge flap undeflected	14
Leading-edge flap deflected 30°	14
Summarization of Results	14
Concluding Remarks	16
References	16
Tables	18
Figures	19

PRECEDING PAGE BLANK NOT FILMED

Summary

A wind tunnel experiment was conducted to determine the effects of chine-like forebody strakes and the Mach number on the longitudinal and lateral-directional characteristics of a generalized fighter configuration with a 55° cropped delta wing. The testing of the model was performed in the 7- by 10-Foot Transonic Tunnel at the David Taylor Research Center (DTRC). The model six-component forces and moments, wing upper surface static pressure distributions, and off-surface flow-field patterns were obtained at free-stream Mach numbers of 0.40 to 1.10 and Reynolds numbers based on the wing mean aerodynamic chord of 1.60×10^6 to 2.59×10^6 . The test matrix included angles of attack from 0° to a maximum of 28° ; angles of sideslip of 0° , $+5^\circ$, and -5° ; and wing leading-edge flap deflection angles of 0° and 30° . The interaction of the strake vortex with the wing flow field stabilized the wing vortex, increased the lift, reduced the drag, and promoted unstable pitching-moment increments at subsonic and transonic speeds. The strake vortex flow provided a three-dimensional relief effect on the wing which prevented the development of a strong rear shock wave, delayed the onset of wing vortex breakdown, and eliminated the model buffeting associated with vortex-shock interaction at the transonic speeds. The strake effects on the longitudinal characteristics diminished when the wing leading-edge flap was deflected. The character of the separation-induced vortex flow shed from the flap hinge line, which increased the drag at the higher Mach numbers, was unaffected by the strake vortex. The direct suction effect of the strake vortex on the forebody resulted in a large increase in the directional stability at the subsonic speeds. The stable increments to the directional stability were limited at the transonic speeds because of the reduced strake vortex strength. The strake-wing flow-field interaction increased the vortex breakdown asymmetry in sideslip and promoted a decrease in the lateral stability at the subsonic speeds and higher angles of attack. This effect was eliminated within the angle-of-attack range considered in the present experiment by deflecting the wing leading-edge flaps. The effect of the strakes at the transonic speeds was to increase the vortex breakdown asymmetry in sideslip and to promote lateral instability at the higher angles of attack. The flow field at transonic speeds was characterized by rear shock development, breakdown of the strake and wing vortices on the windward wing, and stable interacting vortices without shock on the leeward wing. The burst vortices blanketed the centerline vertical tail, decreased the tail effectiveness, and

caused directional instability at the higher angles of attack. Deflecting the wing leading-edge flaps moderated the adverse effects of the strakes on the lateral-directional stability characteristics.

Introduction

The subsonic and transonic high angle-of-attack flow fields about advanced fighter aircraft configurations are characterized by flow separation-induced vortical motions, mutual interactions of multiple vortices, vortex breakdown, and interactions of the vortex flows with shock waves and stabilizing/control surfaces. Mutual vortex interactions are prominent on configurations where the corotating vortices (vortices rotating in the same direction) that develop from the forebodies and wings are in proximity to each other. The flow visualization photograph in figure 1 illustrates this situation on a small-scale model of a generalized fighter aircraft configuration having a slender "chine" forebody and highly swept diamond wing. These flow-field trends promote nonlinear aerodynamic, stability, and control characteristics.

The present wind tunnel investigation was conducted to establish a data base to improve the understanding of these flow phenomena and to enhance the design/analysis capability of high-performance military aircraft operating at subsonic and transonic speeds and at high angles of attack. The effects of chine-like forebody strakes and the Mach number on the longitudinal and lateral-directional characteristics of a generalized fighter configuration with a 55° cropped delta wing were determined. The model was tested with a centerline vertical tail, with and without the strakes, and with constant-chord wing leading-edge flap deflection angles of 0° and 30° . The testing was conducted in the 7- by 10-Foot Transonic Tunnel at the David Taylor Research Center (DTRC) at Mach numbers of 0.40 to 1.10; Reynolds numbers based on the wing mean aerodynamic chord of 1.60×10^6 to 2.59×10^6 ; angles of attack from 0° to a maximum of 28° ; and angles of sideslip of 0° , $+5^\circ$, and -5° .

Symbols

BL	butt line, in.
b	reference wing span, in.
C_D	drag coefficient, $\frac{\text{Drag}}{q_\infty S_{\text{ref}}}$
C_L	lift coefficient, $\frac{\text{Lift}}{q_\infty S_{\text{ref}}}$
C_l	body-axis rolling-moment coefficient, $\frac{\text{Rolling moment}}{q_\infty S_{\text{ref}} b}$

$C_{l\beta}$	lateral stability derivative, $\frac{\partial C_l}{\partial \beta}$, calculated by $\frac{(C_l)_{\beta=+5^\circ} - (C_l)_{\beta=-5^\circ}}{10^\circ}$, per deg	p_o	total pressure, lb/ft ²
C_m	pitching-moment coefficient refer- enced to $0.40\bar{c}$, $\frac{\text{Pitching moment}}{q_\infty S_{\text{ref}} \bar{c}}$	p_∞	free-stream static pressure, lb/ft ²
C_n	body-axis yawing-moment coefficient, $\frac{\text{Yawing moment}}{q_\infty S_{\text{ref}} b}$	q	local dynamic pressure, lb/ft ²
$C_{n\beta}$	directional stability derivative, $\frac{\partial C_n}{\partial \beta}$, calculated by $\frac{(C_n)_{\beta=+5^\circ} - (C_n)_{\beta=-5^\circ}}{10^\circ}$, per deg	q_∞	free-stream dynamic pressure, $\frac{1}{2} \gamma p_\infty M_\infty^2$, lb/ft ²
$C_{p,u}$	wing upper surface static pressure coefficient, $\frac{p - p_\infty}{q_\infty}$	$Re_{\bar{c}}$	Reynolds number based on \bar{c} , $\frac{V_\infty \bar{c} \rho}{\mu}$
$C_{p,v}$	vacuum pressure coefficient, $\frac{-2}{\gamma M_\infty^2}$	S_{ref}	reference wing area, in ²
C_p^*	pressure coefficient corresponding to sonic speed, $\left(\frac{2}{\gamma M_\infty^2} \right) \left\{ \left[\frac{(\gamma - 1) M_\infty^2}{\gamma + 1} + 2 \right]^{3.5} - 1 \right\}$	s	wing local semispan distance from fuselage centerline to wing leading edge, in.
C_Y	side-force coefficient, $\frac{\text{Side force}}{q_\infty S_{\text{ref}}}$	T_o	total temperature, °F
$C_{Y\beta}$	side force due to sideslip, $\frac{\partial C_Y}{\partial \beta}$, calculated by $\frac{(C_Y)_{\beta=+5^\circ} - (C_Y)_{\beta=-5^\circ}}{10^\circ}$, per deg	V_∞	free-stream speed, ft/sec
c	wing centerline chord, in.	WRP	wing reference plane
\bar{c}	wing mean aerodynamic chord, $\frac{2}{3} \left(c + c_t - \frac{c \times c_t}{c + c_t} \right)$, in.	x	distance along wing centerline chord measured from wing apex, in.
c_t	wing tip chord, in.	y	distance along wing local semispan measured from fuselage centerline, in.
\bar{c}_T	vertical tail mean aerodynamic chord, in.	WL	water line, in.
DTRC	David Taylor Research Center	α	angle of attack, deg
FS	fuselage station, in.	β	angle of sideslip, deg
LE	leading edge	γ	ratio of specific heat constants, 1.4
LVS	laser vapor screen	$\Lambda_{LE}, \Lambda_{TE}$	wing leading-edge and trailing-edge sweep angle, respectively, deg
M_∞	free-stream Mach number	δ_{LE}	leading-edge flap deflection angle measured normal to hinge line, positive leading edge down, deg
MHB	maximum half-breadth	μ	coefficient of viscosity, lb-sec/ft ²
MRC	moment reference center, $0.40\bar{c}$	ρ	density, lb-sec ² /ft ⁴
NSRDC	Naval Ship Research and Develop- ment Center	Experimental Investigation	
p	local upper surface static pressure, lb/ft ²	Model Description and Test Apparatus	

The testing was conducted with a model of a generalized fighter configuration with a 55° cropped delta wing, which is illustrated in figure 2. The model geometry is summarized in table I. The fuselage featured circular cross sections from FS 0.00 to FS 3.00. Farther aft, the fuselage cross sections had slab sides with circular top and bottom. The slab height increased linearly from 0.00 in. at FS 3.00 to a maximum of 0.60 in. at FS 11.50. The slab height of 0.60 in. was maintained from FS 11.50 to the model base (FS 42.00). The wings were mounted to the fuselage such that the wing reference plane (WRP)

was in the mid position (WL 0.00). The wings had a 55° leading-edge sweep and cropped delta planform with aspect ratio 1.81 and taper ratio 0.2. The attached flow supersonic wing design method described in reference 1 was used to define the camber and twist distributions to yield minimum drag at a maneuvering Mach number of 1.2 and a self-trimmed lift coefficient of 0.2. A thickness distribution according to reference 1 corresponding to an NACA 65A005 airfoil section was wrapped around the mean camber lines from the 15-percent local chord to the trailing edge. A modified thickness distribution was used from the wing leading edge to the 15-percent local chord. A cubic spline fit was employed to provide a sharp leading edge while maintaining continuity of the upper and lower surface slopes about the 15-percent-chord location. Several streamwise section profiles from the wing root to the wing tip are shown in figure 3.

The wings featured full-span leading-edge flaps having constant-chord planform as shown in figure 2. The total flap exposed area (2 flaps) was 12 percent of the wing reference area. The wings were tested with the flaps undeflected and deflected 30° measured normal to the hinge line as shown in the section cuts in figure 4. The gap at the flap knee that is depicted in the sectional cuts was filled during the testing as shown in the figure.

The sharp-edge chine-like forebody strakes had a curved, or gothic, planform and a wedge cross section as shown in figure 5. The total exposed strake area (2 strakes) was 6.7 percent of the wing reference area. For simplicity, the strakes were mounted in a mid position (WL 0.00) along the slab sides of the fuselage forebody beginning at FS 3.00 and extending to FS 16.00. The strakes were coplanar with the WRP. Because of the wing twist and camber, however, the strakes did not fair into the wing leading edges but were decoupled from the wings. At the wing root (BL 1.50), the strake trailing edge was approximately 0.50 in. above the wing leading edge. The purpose of the strakes was to generate a strong forebody vortex system that would interact with the wing flow field. This would simulate in a simple, yet effective, manner the vortex interactions on a more complex, blended chine forebody-fighter wing configuration such as that shown in figure 1. The strakes were removable to allow testing of the isolated wing-body-tail configuration.

The centerline vertical tail is illustrated in figure 2. The tail had biconvex sections and a maximum thickness of 4 percent of the local chord.

The model was tested with a canopy as shown in figure 2. The canopy served as a fairing for

pressure measurement instrumentation installed in the fuselage.

Seventy-nine surface static pressure orifices were used during the testing and were distributed in five spanwise rows on the upper surface of the right wing as illustrated in figure 6. The measurement stations were situated at $x/c = 0.30, 0.40, 0.50, 0.625,$ and 0.75 , where x is the distance along the wing centerline chord c measured from the wing apex.

A moment reference center (MRC) of $0.40\bar{c}$ was chosen as being representative of a tailless fighter aircraft with a 10-percent design instability (negative static margin) at low angles of attack (ref. 2).

The model six-component forces and moments were measured with an internally mounted strain-gauge balance. The angle of attack was measured with an accelerometer mounted inside the model nose. The sideslip angle was determined with measurement devices installed in the model support system, and the measurements were corrected for balance and sting deflection under load.

Flow Visualization Technique

The off-body flow visualization was conducted with a vapor screen technique (ref. 3). The present experiment was the first application of the vapor screen technique in the DTRC facility. Remotely controlled injection of water into the wind tunnel circuit was not available. Consequently, water was deposited into the settling chamber prior to a run. This increased the relative humidity in the test section during tunnel operation which created condensation within the vortex flows about the model. The vortex cross sections were illuminated with an intense sheet of laser light. For this reason, the flow visualization technique is referred to as laser vapor screen (LVS). The model was painted flat black to contrast with the light sheet.

Laser operational requirements prevented the laser head from being located in the low-pressure plenum around the test section. An 18-W argon-ion laser was situated inside the wind tunnel control room. The laser beam was steered by mirrors through the control room observation window, into the plenum, and to the light-sheet-generating optics mounted in a window on the right side of the test section. The light sheet optics location relative to the test section is shown in figure 7. Automated translation of the light sheet was not currently possible, hence, the light sheet was manually positioned with respect to the model. Light sheet locations at $x/c = 0.50$ and 0.75 were selected, and orthogonality of the light sheet with the model was established

at $\alpha \approx 20^\circ$. A large portion of the flow on the left side of the model was immersed in the shadow of the fuselage. A limited attempt was made during testing to illuminate the flow about the left wing through the use of a series of mirrors in the window on the opposite side of the test section from the light sheet source. The reflected laser light was marginally successful in revealing the wing vortical flow.

The off-body flow-field features were documented with video and still photography in three-quarter rear positions on the left and right sides of the test section (fig. 7). A result obtained in the present experiment with the LVS technique is shown in figure 8.

Wind Tunnel Facility and Test Conditions

The model force, moment, and surface static pressure measurements and laser vapor screen results were obtained in the 7- by 10-Foot Transonic Tunnel at DTRC (formerly NSRDC) in Bethesda, Maryland. The DTRC facility is a continuous-flow, closed-circuit facility capable of operating over a Mach number range from 0.20 to 1.17 and an equivalent pressure altitude range from sea level to 40 000 feet. A complete description of the transonic wind tunnel is provided in reference 4. The model with and without the forebody strakes is shown sting mounted in the slotted test section in figure 9.

The test results were obtained at free-stream Mach numbers from 0.40 to 1.10 and angles of attack from 0° to a maximum of 28° . Pitch polars were obtained at sideslip angles of 0° , $+5^\circ$, and -5° . The tunnel was operated in the evacuated mode (ref. 4), and the tunnel stagnation pressure varied with the Mach number. The Reynolds number based on the wing mean aerodynamic chord $Re_{\bar{c}}$ varied from approximately 1.60×10^6 to 2.59×10^6 . The range of test conditions is listed in table II.

Base pressures and balance cavity pressures were measured and used to adjust the drag data to the condition of free-stream static pressure acting over the fuselage cavity and base areas. Tunnel wall corrections were not applied since the DTRC 7- by 10-Foot Transonic Tunnel test section features slotted ceiling and floor. The strakes, wings, fuselage, and tail were tested with free transition.

Discussion of Results

Representative results obtained in the 7- by 10-Foot Transonic Tunnel at DTRC are presented in the following sections. The longitudinal forces and moments, wing upper surface static pressure distributions, and lateral-directional stability derivatives

are presented. Available laser vapor screen flow visualization results are correlated with the quantitative data trends. The model without the strakes is referred to as the "wing-body-tail configuration." All force and moment coefficients are based on the reference wing area S_{ref} .

The upper surface static pressure coefficients $C_{p,u}$ on the right wing at $x/c = 0.30, 0.40, 0.50, 0.625$, and 0.75 are plotted against the local semispan distance y measured from the fuselage centerline, normalized by the local semispan s . Consequently, y/s values of 0.0 and 1.0 correspond to the fuselage centerline and the wing leading edge, respectively.

Comparisons of the pressure data obtained on the model with the strakes off and on are typically presented at nominal angles of attack of $12^\circ, 16^\circ, 20^\circ$, and maximum α . The angles of attack are denoted as approximate in the data plots due to small variations about the scheduled, or target, α 's.

The technical discussion is divided into four major sections. The first and second sections show the effects of the forebody strakes on the longitudinal and lateral-directional characteristics, respectively, with the wing leading-edge flap deflection angles of 0° and 30° . The Mach number effects on the longitudinal and lateral-directional characteristics with $\delta_{LE} = 0^\circ$ and 30° are presented in the third and fourth sections, respectively. It is noted that a 30° deflection of the leading-edge flap is excessive at transonic speeds (ref. 5). In practice, the flap would be scheduled with the Mach number and angle of attack to yield maximum aerodynamic performance. Emphasis in the present test is on the trends associated with the addition of the strakes in the presence of a deflected wing leading-edge flap.

Effect of Forebody Strakes on Longitudinal Characteristics

Leading-edge flap undeflected. The effect of the forebody strakes on the longitudinal force and moment characteristics and the wing upper surface static pressure distributions at $M_\infty = 0.40, 0.60, 0.80, 0.95$, and 1.10 is shown in figures 10, 11, 12, 13, and 14, respectively. The wing spanwise pressure distributions are shown for selected angles of attack at each Mach number. Selected laser vapor screen flow visualization results are presented in figure 15 to augment the analysis of the force and moment data and surface pressure measurements. To highlight flow details that are not obvious in the vapor screen results, low-speed ($M_\infty = 0.05$) smoke flow visualization results obtained in reference 6 on a small-scale model of the present configuration with flat-plate strakes and

wings are shown in figure 16. In addition, fluorescent surface oil flow patterns obtained in reference 6 on the same wind tunnel model used in the present study are shown in figure 17.

The strakes promote a large increase in lift at angles of attack greater than approximately 16° , a reduction in drag at moderate and high lift, and an increase in the pitch instability at $M_\infty = 0.40$ and 0.60 (figs. 10(a) and 11(a)). The lift increase and drag reduction are due to the favorable interaction of the strake leading-edge vortex with the wing flow field. The strake vortex artificially induces spanwise flow gradients on the wing that are similar to those appearing naturally on highly swept wings (ref. 7). This effectively delays wing vortex breakdown to higher angles of attack. The increased pitch instability is due to the larger planform area and the strake vortex-induced lift ahead of the moment reference center. The planform area increase with the strakes on increases C_L , since the lift coefficient is based on the wing reference area. However, the lift increase at the higher angles of attack exceeds the effect of the strake area addition. This indicates that a synergistic effect occurs as a result of the interaction of the strake and wing flow field (ref. 8).

The wing surface pressure distributions at $M_\infty = 0.40$ and 0.60 indicate that the principal effect of the strake at $\alpha \approx 12^\circ$ (figs. 10(b) and 11(b)) is to displace the wing vortex-induced suction peak outboard. Increasing the angle of attack to approximately 16° (figs. 10(c) and 11(c)) broadens the pressure distribution and reduces the maximum suction pressure at $x/c = 0.75$ with the strakes off. These trends are consistent with the effects of wing vortex breakdown. Addition of the strakes delays the onset of vortex breakdown and reestablishes the peak suction pressure levels. The pressure distributions at $\alpha \approx 20^\circ$ with strakes off (figs. 10(d) and 11(d)) show that vortex breakdown is well advanced over the wing. Experimental results obtained in reference 9 on an isolated, flat-plate 55° delta wing and Euler code predictions in reference 10 on the wing-body configuration used in the present study also revealed the extensive nature of vortex breakdown at $\alpha \approx 20^\circ$. The strake vortex energizes the wing vortical flow at this angle of attack; this restores the vortex-induced suction peaks at all pressure measurement stations. Vortex breakdown is near the wing apex at $\alpha \approx 26^\circ$ with strakes off (figs. 10(e) and 11(e)), and the pressure distributions are flat and uniform between $x/c = 0.30$ to 0.75 . Installation of the strakes stabilizes the wing vortex and increases the suction pressure levels along the entire wing. This effect is not as pronounced at $x/c = 0.75$

because of upward displacement of the wing vortex from the surface. At $\alpha \approx 26^\circ$ and $x/c = 0.75$, there is evidence of two vortex pressure signatures. The outboard pressure peak is induced by the wing vortex, whereas the inboard pressure signature is induced by the strake vortex as it moves downward and outboard over the wing. The absence of the strake vortex "footprint" in the wing surface pressures to this point demonstrates a lack of intertwining between the strake and wing vortices. In reference 11, the observation is made that vortex cores that do not directly interact represent a more stable flow situation in comparison with a system of vortices where the vortex cores intertwine.

The laser vapor screen photographs at $M_\infty = 0.40$ and $\alpha \approx 22^\circ$ and 26° in figures 15(a) and 15(b) show stable strake and wing vortices at $x/c = 0.50$. The off-surface flow was not visible on the wing-body-tail configuration because of wing vortex breakdown. The camera position corresponds to a left three-quarter rear view. Note that the laser light sheet is projected from the right side of the test section. As a result, the vortex on the left wing is not visible, because it is in the shadow of the fuselage. At subsonic speeds, stable vortices appear as "donut-shaped" structures with the vapor screen technique and feature a bright ring of condensation surrounding a "hollow" core. The strake and wing vortices are widely spaced at $x/c = 0.50$. The low-speed smoke flow visualization photographs (ref. 6) in figure 16 corresponding to $\alpha \approx 20^\circ$ and 25° show the planview trajectories of the strake and wing vortices which are representative of those observed on the larger model. No indication of vortex breakdown is shown, and the strake and wing vortices are in mutual proximity only at $\alpha \approx 25^\circ$ (fig. 16(b)) and near the wing trailing edge.

The force and moment and pressure distribution trends are similar at $M_\infty = 0.80$ and 0.95 (figs. 12 and 13), although the data comparisons are confined to slightly lower angles of attack. Testing of the wing-body-tail configuration was limited to $\alpha \approx 22^\circ$ at $M_\infty = 0.80$ and 0.95 because of observed model dynamics or buffeting. With the strakes on, the maximum angle of attack at $M_\infty = 0.80$ was approximately 21° because of the balance pitching-moment limit.

The pressure distributions on the wing-body-tail configuration at $\alpha \approx 22^\circ$ and $M_\infty = 0.80$ and 0.95 (figs. 12(e) and 13(e)) are nearly uniform. No indication is seen of vortex-induced flow reattachment along most of the wing with strakes off. These trends are consistent with the effect of wing vortex breakdown. The Euler code predictions in reference 10

on the wing-body configuration showed that vortex breakdown effects on the wing surface pressures were extensive at $\alpha \approx 20^\circ$ and $M_\infty = 0.80$. The development of shock waves over the wing beginning at $M_\infty = 0.80$ is also plausible because most of the flow on the wing upper surface is supersonic. Locally supersonic flow can be identified by comparing the experimental surface pressure coefficients in figures 12(b)–(e) with the critical pressure coefficient C_p^* , which corresponds to the pressure coefficient where the local flow is sonic. Pressure coefficients that exceed C_p^* define regions of supersonic flow. Shock waves are identified in the surface flow pattern (ref. 6) in figure 17(a) corresponding to the wing-body configuration at $M_\infty = 0.95$ and $\alpha \approx 20^\circ$. Surface streamlines and a tentative view of the off-surface flow are sketched in figures 17(b)–(d) to highlight significant topological features. Shock waves are typically manifested in oil flow patterns by a sudden change in the surface streamline direction as the flow traverses the shock. The surface streamlines show the presence of a rear, or terminating, shock wave that is approximately perpendicular to the axis of the wing vortex. This shock extends spanwise from the wing root region and through the wing vortex footprint. The footprint of a cross-flow shock wave situated underneath the wing vortex and emanating along a ray from the apex is also apparent. The rear and cross-flow shock waves appear to intersect. The presence of the rear shock coincides with an abrupt change in the surface streamline direction along the inboard portion of the wing, the loss of the cross-flow shock footprint, a region of reversed flow near the leading edge, and a discontinuity in the secondary separation line. The reversed flow is associated with a three-dimensional separation region as sketched in figure 17(b). Downstream of the shock, the vortex-induced primary flow reattachment line is smeared, and the surface streamlines reveal an expansion of the wing vortex footprint; these effects are typical of vortex breakdown. The development of a second terminating shock wave is suggested by the marked turning of the surface streamlines near the wing trailing edge.

Reference 12 has indicated that a resulting effect of vortex breakdown coexisting with a rear shock wave is severe buffeting due to the highly unsteady flow. This effect is consistent with the model buffeting (strakes off) observed in the present experiment at $M_\infty = 0.80$ and 0.95 . Surface flow patterns showing the coexistence of vortices and shock waves at transonic speeds have also been obtained on a 50° swept wing (ref. 13), 55° delta wing-body (ref. 14), 65° cropped delta wing (refs. 15 and 16), and 65°

cropped delta wing-canard (ref. 17). The vortex-shock interaction has also been observed on a 65° cropped delta wing at $M_\infty = 0.85$ and $\alpha \approx 20^\circ$ to 25° in reference 15, where a schlieren flow visualization technique was used. The latter study also provided evidence of two terminating shock waves similar to those described in figures 17(a) and (b).

Results from the present study are insufficient to determine if the wing vortex bursts as it confronts the large pressure rise imposed by the shock wave or if the shock wave forms as a result of vortex breakdown. The wind tunnel oil flow patterns obtained at transonic speeds in reference 18 on the F-4D wing ($\Lambda_{LE} = 51.4^\circ$) indicated that the development of leading-edge vortices suppressed the formation of shock waves. In reference 18 shocks were found to exist only outside the vortex-dominated regions. These results do not support the view that vortex breakdown is shock induced. The theory that vortex breakdown initiates shock wave development is based on the analogy of the expanded burst vortex to a solid body immersed in the flow field. It is conjectured that the presence of this expanding pseudo body promotes a flow recompression and corresponding shock wave development. It is possible that the vortex-shock interaction contains elements of both views. The onset of vortex breakdown over the wing may support the initial development of the shock wave. Once the shock forms, it increases the longitudinal pressure rise which causes a more rapid forward progression of vortex breakdown with increasing angle of attack. The schlieren results in reference 15 showed an abrupt forward movement of the coexisting vortex breakdown and shock system due to a slight increase in α in contrast with a more gradual advance of the vortex breakdown position at subsonic (shock free) conditions.

Addition of the forebody strakes eliminated the model buffeting at $M_\infty = 0.80$ and 0.95 and re-established the wing vortex pressure signatures between $x/c = 0.30$ to 0.625 and at the higher angles of attack (figs. 12(d) and (e) and 13(d) and (e)). The pressure distributions at $x/c = 0.75$ in figures 12(e) and 13(e) show only a small effect due to the strakes despite the significant change in the vortex flow field. The vortex-induced pressure distributions display a different character at the higher Mach numbers. Increasing the Mach number promotes a more gradual suction pressure rise outboard of the primary flow reattachment position. In addition, a maximum suction pressure plateau typically exists underneath the wing vortical flow at the higher Mach numbers in contrast with the pronounced suction pressure peak obtained at lower Mach numbers. Similar results

were obtained on highly swept wings at transonic and supersonic speeds in references 16 and 19.

The laser vapor screen photograph in figure 15(c) shows the forebody strake vortices at $M_\infty = 0.95$, $\alpha \approx 24^\circ$, and $x/c = 0.75$. The strake vortex dominates the cross-flow pattern. The vortex is sufficiently removed from the model surface, however, that its presence cannot be detected directly from the wing pressure distributions. The induced effect of the strake vortex on the wing is significant, however, as shown in the surface flow pattern (ref. 6) in figures 17(e) and (f) for $M_\infty = 0.95$ and $\alpha \approx 20^\circ$. No indication is shown of a rear shock wave or the vortex breakdown that occurred on the wing-body configuration in figure 17(a). The spanwise flow that the strake vortex induces on the wing promotes an effective increase in the wing leading-edge sweep. This provides a three-dimensional relief effect that delays vortex breakdown and prevents the development of a strong rear shock wave. A similar shock alleviation effect has been observed in reference 18 because of the leading-edge snag, or sawtooth, vortex on the F-4D fighter wing. The surface flow pattern in figure 17(e) shows a large inboard movement of the secondary separation line with the strakes on, which is the apparent result of cross-flow shock-induced boundary layer separation (refs. 15 and 16). The corresponding flow situation is sketched in figure 17(f). The kink in the secondary separation line is due to a "tearing" of the wing vortex feeding sheet from the leading edge as sketched in figure 17(f). This phenomenon has been documented in reference 20. A region of stagnant surface flow exists outboard of the primary vortex as shown in figures 17(e) and (f).

The strake effect on the lift and drag at $M_\infty = 1.10$ (fig. 14(a)) is small in comparison with the results at $M_\infty = 0.40$ and 0.60 (figs. 10(a) and 11(a)). The strakes continue to promote a large unstable shift in the pitching-moment curve. However, the strake-wing-body-tail configuration exhibits nominal longitudinal stability over a wide range of lift coefficient due to the aft shift in the center of pressure at this Mach number. The wing-body-tail configuration was tested to $\alpha \approx 26^\circ$ without encountering the model dynamics that were observed at $M_\infty = 0.80$ and 0.95 . The lack of model dynamics is consistent with movement of the vortex breakdown and rear shock position aft toward the trailing edge at $M_\infty = 1.10$. The delay in vortex breakdown onset to a higher angle of attack at $M_\infty = 1.10$ is caused by the diminished upstream influence of the wing trailing edge and the correspondingly more moderate longitudinal pressure rise. This effect has been observed on a model with a 65° cropped delta wing

in reference 16. The strake effect on the wing surface pressures (figs. 14(b)-(e)) is accordingly small. Addition of the strakes displaced the wing vortex-induced primary flow reattachment outboard but had no effect on the character or magnitude of the suction pressure plateau underneath the wing vortical flow.

The laser vapor screen flow visualization photograph in figure 15(d) at $M_\infty = 1.10$, $\alpha \approx 24^\circ$, and $x/c = 0.75$ reveals a stable, elliptically shaped vortex about the right wing of the wing-body-tail configuration. At $M_\infty = 1.10$, condensation of the water vapor occurs in the free stream. As a result, a stable wing vortex appears as a darker region surrounded by a lighter background. The flattened wing vortex cross section is consistent with the character of the pressure distributions (fig. 14(e)), which show a maximum suction pressure plateau underneath the vortex. The brighter region above the fuselage is associated with relatively weak vortices generated by the forebody. The outboard displacement of the wing vortex-induced flow reattachment position due to the strakes is seen by comparing the vapor screen photographs in figures 15(d) and (e) corresponding to the model with strakes off and strakes on at $M_\infty = 1.10$, $\alpha \approx 24^\circ$, and $x/c = 0.75$. In both cases, the wing vortex is a dark region surrounded by a lighter background. The intersection of the inboard edge of the vortex region with the wing upper surface defines the primary flow reattachment location. With the fuselage upper surface as a reference position, the primary flow reattachment is farther outboard with the strakes on. The strake vortex flows are also visible above the fuselage on either side of the model centerline. The lateral separation of the strake and wing vortices at $M_\infty = 1.10$ is apparent in figures 15(e) and (f).

Leading-edge flap deflected 30° . The forebody strake effect on the longitudinal forces and moments and wing surface pressure distributions at $M_\infty = 0.40, 0.60, 0.80, 0.95$, and 1.10 with the constant-chord wing leading-edge flap deflected 30° is shown in figures 18, 19, 20, 21, and 22, respectively. The strake vortex-induced lift increase and drag reduction at $M_\infty = 0.40$ and 0.60 (figs. 18(a) and 19(a)) diminish when the wing flap is deflected. The deflected flap delays flow separation at the wing leading edge to a higher angle of attack. Once a vortex forms from the leading edge of the deflected flap, it is less susceptible to breakdown because the pressure rise is less severe along the wing and the vortex swirl angle is reduced (ref. 21) and, consequently, weakens the vortex at a given angle of attack. The strake effect on the wing flow diminishes since the wing efficiency is enhanced by the deflected

flap. Adding the strakes continues to promote a large unstable shift in the pitching-moment curves.

The pressure distributions on the wing-body-tail configuration at $M_\infty = 0.40$ and 0.60 and $\alpha \approx 12^\circ$ (figs. 18(b) and 19(b)) indicate that the flow along the upper surface of the flap and main wing is primarily attached. There is evidence of a small vortical flow situated close to the leading edge at $x/c = 0.40$ and 0.50 ; this is indicated by the local suction pressure rise near the leading edge. The strake effect on the attached flow-dominated pressure distributions is small. The suction pressure peak near the flap hinge line at $x/c = 0.30$ to 0.625 is associated with the acceleration of the attached flow around the flap knee. Flow separation from the flap knee has a relieving effect on the surface pressure distribution near the hinge line at $M_\infty = 0.60$ and $x/c = 0.75$ (fig. 19(b)). At higher angles of attack where flow separation occurs everywhere along the wing leading edge, the resultant primary vortex is small and weak because of the small angle between the deflected flap leading edge and the on-coming flow. As long as the vortex is confined to the flap surface, the strake effect on the wing surface pressures is small. This effect is illustrated in figures 18(c) and 19(c) for $M_\infty = 0.40$ and 0.60 and $\alpha \approx 16^\circ$. The leading-edge vortex suction peaks migrate inboard of the flap hinge line on the wing-body-tail configuration at $\alpha \approx 20^\circ$ (figs. 18(d) and 19(d)). As a result, the strake has a larger effect on the wing surface pressures. Addition of the strakes slightly delays the inboard migration of the wing vortex pressure signature from the flap to the main wing and increases the suction peak magnitude at $x/c = 0.50$ to 0.75 . At $\alpha = 24^\circ$ (figs. 18(e) and 19(e)) and $\alpha \approx 26^\circ$ (figs. 18(f) and 19(f)), where vortex breakdown dominates the flow about the wing-body-tail configuration, adding the strakes stabilizes the wing vortical flow, displaces the wing vortex outboard, and significantly increases the maximum suction pressure levels. It is interesting to note that the strake vortex pressure signature cannot be discerned in the wing pressure distributions at any angle of attack at $M_\infty = 0.40$ and 0.60 . The outboard displacement and weakening of the wing vortex due to the deflected flap decrease its induced effect on the strake vortex. As a result, the strake vortex is situated farther inboard and higher above the wing.

Deflecting the leading-edge flap reduced the buffeting of the wing-body-tail configuration at the higher Mach numbers. As a result, test data were obtained up to $\alpha \approx 26^\circ$ at $M_\infty = 0.80, 0.95$, and 1.10 (figs. 20, 21, and 22). The strake effect on the lift, drag, and pitching-moment characteristics at $M_\infty = 0.80$ and 0.95 (figs. 20(a) and 21(a))

is similar to that observed at $M_\infty = 0.40$ and 0.60 . At $M_\infty = 1.10$ (fig. 22(a)), the principal effect of the strakes is observed to be a large unstable shift in the pitching-moment curve.

The pressure distributions with and without the strakes at $M_\infty = 0.80, 0.95$, and 1.10 and $\alpha \approx 12^\circ$ (figs. 20(b), 21(b), and 22(b)) indicate attached flow along the flap. At $\alpha \approx 16^\circ$ (figs. 20(c), 21(c), and 22(c)), the pressure signature of a small leading-edge vortex confined to the flap is evident at all measurement stations, except $x/c = 0.30$ at $M_\infty = 1.10$. The dominant feature of the surface pressures is the footprint of a vortex formed by flow separation from the leading-edge flap hinge line. The oil flow patterns in figures 23(a) and (b) taken from reference 17 illustrate the sensitivity of the surface streamlines to the Mach number at a constant lift coefficient and show the hinge-line vortex footprint on the wing-body-tail configuration of the present study. The hinge-line vortex signature is characterized by flow reattachment to the inboard portion of the wing and a maximum suction pressure plateau underneath the vortex that can extend along a significant spanwise extent of the wing. Reference 22 indicated that flow separation near the flap hinge line may be shock induced at the higher Mach numbers as sketched in figure 23(c). Comparison of the wing surface pressures at $M_\infty = 0.80$ and $\alpha \approx 12^\circ$ to C_p^* in figure 20(b) suggests that the attached flow on the flap expands supersonically about the flap knee and then separates to form a vortical flow as depicted in figure 23(c). The strakes reduced the lateral extent of the hinge-line vortex. This reduction is caused by the strake vortex-induced spanwise flow on the wing and is indicated in the surface pressures by an outboard displacement of the flow reattachment induced by the hinge-line vortex. Increasing the angle of attack to 20° promotes a loss of the leading-edge vortex pressure signature on the flap at $M_\infty = 0.80$ and $x/c = 0.625$ and 0.75 , as shown in the pressure distributions on the wing-body-tail configuration in figure 20(d). This loss is attributed to a migration of the leading-edge vortex off the flap because of an interaction with the hinge-line vortex. The flow interaction coincides with vortex breakdown as indicated by the broadening of the pressure distributions and the reduced maximum suction pressure levels at $\alpha \approx 20^\circ$ to 26° in figures 20(d)-(f). This effect occurs at a higher angle of attack at $M_\infty = 0.95$ (fig. 21(e) at $\alpha \approx 24^\circ$) and does not occur up to the maximum angle of attack at $M_\infty = 1.10$. The strake vortex does not have a significant effect on the interaction of the hinge-line vortex and the leading-edge vortex at $M_\infty = 0.80$ and 0.95 but appears to slow the forward progression of vortex breakdown.

Effect of Forebody Strakes on Lateral-Directional Characteristics

Leading-edge flap undeflected. Figures 24 and 25 show the effect of the forebody strakes on the static lateral-directional stability derivatives at $M_\infty = 0.40$ and 0.90 , respectively. The stability derivatives were computed from the force and moment data obtained in angle-of-attack polars at $\beta = +5^\circ$ and -5° . Aerodynamic nonlinearities and flow-field hysteresis effects (ref. 23), which can be "masked" by computing stability derivatives in this fashion, were absent within the ranges of angle of attack and sideslip tested in the present experiment. To assist in the interpretation of the stability derivative trends, the spanwise pressure distributions on the windward and leeward wings with and without the strakes are presented at selected angles of attack in figures 24 and 25. Only the right wing was instrumented with upper surface pressure orifices. The windward and leeward wing pressure data were obtained in angle-of-attack polars at $\beta = +5^\circ$ and -5° , respectively. Sketches based on laser vapor screen flow visualizations at $M_\infty = 0.40$ and $M_\infty = 0.90$ are shown in figure 26. Testing of the wing-body-tail configuration in sideslip was limited to $\alpha \approx 22^\circ$ at $M_\infty = 0.90$ because model buffeting was observed in pitch.

Addition of the strakes increases the directional stability (more positive values of C_{n_β}) at $M_\infty = 0.40$ (fig. 24(a)). This effect is first apparent at $\alpha \approx 8^\circ$ and increases up to the maximum test angle of attack on the strake-wing-body-tail configuration of approximately 23° . The positive increments to the side force due to sideslip C_{Y_β} with the strakes on indicate that the source of the directional stability increase is the forebody. In sideslip, the windward strake vortex is in proximity to the forebody, and the high suction pressures acting on the lateral-facing surface of the forebody promote a restoring yawing moment. This effect increases with the angle of attack because of the increased strength of the strake vortex. The strakes promote a slight increase in the lateral stability at angles of attack from approximately 8° to 18° and decrease the lateral stability at higher angles of attack.

The small increase in lateral stability (more negative values of C_{l_β}) at $\alpha \approx 8^\circ$ to 18° is caused by an overall increase in the vortex-induced suction pressure levels on the windward wing relative to the leeward wing. This effect is illustrated in the surface pressure distributions at $\alpha \approx 12^\circ$ between $x/c = 0.30$ and 0.625 (figs. 24(b) and (c)) and at $\alpha \approx 16^\circ$ between $x/c = 0.30$ and 0.50 (figs. 24(d) and (e)). An

opposite effect occurs farther aft on the wing at $\alpha \approx 16^\circ$. The sketches in figure 26, which are based on flow-field observations at $M_\infty = 0.40$, clarify the pressure distribution trends. Along the forward portion of the wing, the effect of sideslip is to move the strake vortex inboard and closer to the wing surface on the windward side and outboard and upward on the leeward side. The close proximity of the windward strake vortex to the wing increases its induced effect on the wing vortical flow relative to the leeward side. In addition, more of the windward wing is immersed in the strake vortex-induced upwash field, whereas the opposite effect occurs on the leeward wing. This effect is similar to the flow-field interaction observed on closely coupled canard-wing configurations in sideslip (ref. 24). Farther aft, however, the windward strake vortex migrates inboard toward the fuselage, and its induced effect on the wing correspondingly decreases. In fact, the windward pressure distributions at $\alpha \approx 16^\circ$ and $x/c = 0.75$ (figs. 24(d) and (e)) suggest that adding the strake does not significantly delay the onset of wing vortex breakdown. The strake-wing vortex interaction increases on the leeward side as a result of the outboard migration of the strake vortex. The leeward pressure distributions at $x/c = 0.75$ in figures 24(d) and (e) indicate that adding the strakes stabilizes the leeward wing vortex and increases the wing vortex pressure signature. This effect limits the lateral stability increase with the strakes on. The ability of the windward strake vortex to affect a global change in the wing flow field diminishes at higher angles of attack (figs. 24(f)-(i)). The windward strake vortex moves farther inboard as the angle of attack increases, and the flow that it induces on the wing is insufficient to halt the forward progression of wing vortex breakdown on the windward side. Conversely, breakdown of the leeward wing vortex, which is apparent in the surface pressure distributions with strakes off (figs. 24(f) and (h)), is eliminated with the strakes on (figs. 24(g) and (i)). The wing-body-tail configuration exhibits lateral stability at the higher angles of attack since vortex breakdown asymmetry is not severe between the windward and leeward sides. Adding the strakes increases the wing vortex breakdown asymmetry at the higher values of α and, consequently, reduces the lateral stability.

Addition of the strakes slightly increases the directional stability at $M_\infty = 0.90$ (fig. 25(a)) at angles of attack between approximately 8° and 20° . The strakes promote directional instability (negative values of C_{n_β}) at higher angles of attack. The stable increments to C_{n_β} are smaller at $M_\infty = 0.90$ relative to $M_\infty = 0.40$ (fig. 24(a)) because of the reduced

forebody strake vortex strength at the higher Mach number (refs. 25 and 26). The large positive increments in $C_{Y\beta}$ at angles of attack greater than 20° suggest that the source of the directional instability is the vertical tail. The vapor screen photograph and flow-field sketch in figure 26(b) for $\alpha \approx 22^\circ$ and $\beta = +5^\circ$ reveal breakdown of the windward strake and wing vortices upstream of the centerline tail. Flow-field observations indicated that the windward strake and wing vortex bursting was more advanced at a given angle of attack at $M_\infty = 0.90$ than at $M_\infty = 0.40$. The burst vortex system blankets the centerline tail which reduces the local dynamic pressure q and promotes the unstable $C_{n\beta}$ increments. Beginning at $\alpha \approx 12^\circ$, adding the strakes decreases the lateral stability, and the unstable $C_{l\beta}$ increments increase with increasing angle of attack. At angles of attack greater than approximately 16° , the strake-wing-body-tail configuration exhibits lateral instability. The vapor screen result at $\alpha \approx 22^\circ$ and $\beta = +5^\circ$ in figure 26(b) indicates that breakdown of the windward strake and wing vortices is well advanced, whereas the leeward strake and wing vortices are stable. The severe vortex breakdown asymmetry in sideslip is consistent with the large positive (unstable) value of $C_{l\beta}$ at $\alpha \approx 22^\circ$ in figure 25(a).

Surface oil flow visualization on a 55° delta wing body configuration (ref. 14) has shown that a rear shock wave coexists with the wing vortex at $M_\infty = 0.90$ beginning at $\alpha \approx 12^\circ$. As a result, it is expected that the flow about the wing-body-tail configuration in sideslip at $M_\infty = 0.90$ will feature interacting vortices and shock waves. The surface pressure distributions on the wing-body-tail configuration at $\alpha \approx 20^\circ$ and 22° (figs. 25(f) and (h)) are uniform over most of the windward and leeward wings; this suggests that the vortex-shock interaction limits the vortex breakdown asymmetry due to sideslip. As a result, the wing-body-tail configuration exhibits lateral stability up to the maximum angle of attack of 22° despite the extensive nature of vortex breakdown.

The upper surface pressure distributions at $M_\infty = 0.90$ in figures 25(b)-(i) indicate that adding the strakes increases the overall suction pressure level on the leeward wing relative to the windward wing. This effect is first apparent along the aft wing region at $\alpha \approx 12^\circ$ ($x/c = 0.75$ in figs. 25(b) and (c)) and advances forward to encompass the entire wing at $\alpha \approx 24^\circ$ (figs. 25(h) and (i)). The vapor screen photograph in figure 26(b) suggests that the windward strake vortex has a limited effect on the wing flow field and, consequently, the vortex-rear shock

interaction. This is supported by the windward wing surface pressures in figures 25(b)-(i), which show little change due to adding the strakes. In contrast, the peak vortex suction pressure levels induced by the leeward wing vortex are maintained at $x/c = 0.30$ to 0.75 up to $\alpha \approx 24^\circ$. The interaction of the leeward strake vortex with the wing flow field stabilizes the wing vortex and moderates the effect of the shock wave in a manner similar to that shown previously in the surface oil flow pattern at $M_\infty = 0.95$ and $\beta = 0^\circ$ in figures 17(c) and (d). The extensive nature of the wing vortex breakdown on the windward side combined with the alleviation of vortex breakdown on the leeward wing results in the large unstable values of $C_{l\beta}$ at the higher angles of attack.

Leading-edge flap deflected 30° . The forebody strake effect on the lateral-directional stability derivatives and the wing surface pressure distributions with the constant-chord leading-edge flap deflected 30° is shown in figures 27 and 28 for $M_\infty = 0.40$ and 0.90 , respectively. Laser vapor screen results and the corresponding sketches for $M_\infty = 0.90$ are presented in figure 29.

The strake effect on $C_{n\beta}$ and $C_{Y\beta}$ at $M_\infty = 0.40$ (fig. 27(a)) is similar to the result obtained for $\delta_{LE} = 0^\circ$ (fig. 24(a)). The strakes promote a large increase in the directional stability due to the suction pressures induced by the windward strake vortex on the forebody side. The strakes promote larger, stable increments in $C_{l\beta}$ which extend to higher angles of attack with the flaps deflected.

The wing surface pressures at $M_\infty = 0.40$ and $\alpha \approx 12^\circ$ with the strakes off (fig. 27(b)) indicate that the flow is attached on the windward flap and along the main wing inboard of the flap knee. A small vortex is situated on the leeward flap, which induces higher suction pressures in comparison with the windward side. Flow reattachment occurs on the flap, and the reattached flow suction pressure levels along the flap knee and the main wing are comparable with those on the windward side. In sideslip, the leading-edge flap deflection angle measured in the streamwise direction increases on the windward wing and decreases on the leeward wing. As a result, leading-edge flow separation first occurs on the leeward wing. The strakes increase the attached flow suction pressure levels inboard of the flap knee on the windward wing relative to the leeward wing (fig. 27(c)). In addition, the difference between the vortex-induced suction pressures on the leeward flap and the attached flow suction pressures on the windward flap diminishes with the strakes on. These effects combine to promote a stable increment

in C_{l_β} . The strake effect on the relative suction pressure levels on the windward and leeward wings increases at $\alpha \approx 16^\circ$ (figs. 27(d) and 27(e)). Leading-edge separation occurs on both wings at this angle of attack. With the strakes off, the vortex suction pressure signature is more pronounced on the leeward flap in comparison with the windward flap. The strakes reduce the difference in the vortex-induced suction pressure levels on the forward-facing surface. The strakes promote a maximum stable increment in C_{l_β} at $\alpha \approx 20^\circ$ (fig. 27(a)). The corresponding pressure distributions (figs. 27(f) and (g)) show that the strakes significantly increase the overall suction pressure levels on the windward wing and flap relative to the leeward side. The windward and leeward wing vortex pressure signatures are prominent both with and without the strakes at this angle of attack. No vortex breakdown is indicated in the windward wing pressure distributions in contrast with the results obtained for the flap undeflected (figs. 24(f) and (g)). Both the windward and leeward wing vortices exhibit an inboard migration from the deflected flap onto the main wing as α increases. The strakes slow the migration of the leeward wing vortex but do not affect the windward wing vortex migration or the apparent discontinuity of the windward vortex feeding sheet. Evidence of feeding sheet discontinuity is provided in the surface pressures at $x/c = 0.625$ and 0.75 (figs. 27(f) and (g)). Sketches of the postulated flow mechanism are shown in figures 27(f) and (g). The pressure data reveal two suction peaks which suggest that the windward wing vortex "tears" away from the leading edge while another vortex forms from the leading edge farther outboard. Vortex sheet discontinuities have been observed in wind tunnel vapor screen flow visualizations in references 16 and 17 and in Euler code computations in reference 27. Both configurations exhibit diminished levels of lateral stability at higher angles of attack and smaller stable C_{l_β} increments due to the strakes because of the onset of wing vortex breakdown asymmetries. The surface pressures on the wing-body-tail configuration at $\alpha \approx 24^\circ$ (fig. 27(h)) indicate that the deflected flap is ineffective in containing the windward and leeward vortices, which migrate inboard onto the main wing and subsequently burst. Vortex breakdown advances farther forward on the windward wing, as indicated by the broader pressure distributions and lower maximum suction pressure levels in comparison with the leeward wing. The strakes increase the overall suction pressure levels inboard of the flap hinge line on the windward wing relative to the leeward wing (fig. 27(i)). However, vortex breakdown asymmetry increases with the strakes on. The effect of vortex

breakdown is apparent in the windward wing pressure distributions at $x/c = 0.50$ to 0.75 (fig. 27(i)). By contrast, the interaction of the leeward strake vortex with the wing flow field stabilizes the wing vortex. As a result, the suction pressure levels along the outer portion of the wing are higher on the leeward side at all stations except $x/c = 0.30$. The inability of the strakes to reduce the wing vortex breakdown asymmetry in sideslip limits the stable C_{l_β} increment at $\alpha \approx 24^\circ$. In addition, the maximum stable value of C_{n_β} with the strakes on appears limited by interaction of the burst vortex and, consequently, the lower q wake from the windward wing with the centerline tail. Reduced vertical tail effectiveness due to wing vortex breakdown effects has been documented in reference 28.

The strakes increase the directional stability at $M_\infty = 0.90$ (fig. 28(a)) beginning at an angle of attack of approximately 8° . The stable C_{n_β} increments are smaller than those obtained at $M_\infty = 0.40$ (fig. 27(a)), particularly at angles of attack of 20° and higher. A comparison of the results obtained at $M_\infty = 0.90$ and $\delta_{LE} = 0^\circ$ (fig. 25(a)) and $\delta_{LE} = 30^\circ$ (fig. 28(a)) shows that the stable increments in C_{n_β} are larger with the deflected leading-edge flaps. The stable C_{n_β} increments due to the strakes rapidly diminish, and the positive increments to C_{Y_β} abruptly increase, at angles of attack greater than 18° . These trends are associated with a decrease in the vertical tail effectiveness. Both configurations are directionally unstable at angles of attack greater than 22° . The strakes also promote unstable increments to the lateral stability derivative at $M_\infty = 0.90$ and angles of attack greater than approximately 14° . A comparison with the results obtained at $M_\infty = 0.90$ with $\delta_{LE} = 0^\circ$ (fig. 25(a)) shows that the unstable C_{l_β} increments are smaller and the lateral instability at higher α 's is less severe with the wing flaps deflected.

The wing surface pressures at $\alpha \approx 12^\circ$ (figs. 28(b) and (c)) indicate that the strakes increase the overall suction pressure levels inboard of the flap knee on the windward wing relative to the leeward wing between $x/c = 0.30$ and 0.625 . There is no net effect of the strakes on C_{l_β} at this angle of attack. The surface pressures in both cases indicate that the flow on the windward flap upper surface is attached, whereas a small vortex forms near the leading edge of the leeward flap. The character of the windward and leeward wing pressure distributions inboard of the flap knee is consistent with the development of a vortex arising from flow separation at or near the

hinge line. The hinge-line vortex pressure signature is manifested by the suction peaks and maximum suction pressure plateaus on the main wing. The surface pressure distribution trends are similar at $\alpha \approx 16^\circ$ (figs. 28(d) and (e)). A comparison of the data in figures 28(d) and (e) indicates that the strakes have essentially no effect on the windward wing pressure distributions. The primary effect of the strakes is manifested in the leeward wing surface pressures. The vapor screen flow visualization photograph at $\alpha \approx 16^\circ$ and $\beta = +5^\circ$ in figure 29(a) shows that the windward strake vortex is situated inboard near the fuselage, where its induced effect on the wing flow field is small. Conversely, the leeward strake vortex is positioned outboard over the wing, where it has a larger effect on the flow field. The downwash induced by the leeward strake vortex suppresses the hinge-line vortex pressure signature at $x/c = 0.30$. Farther aft, the leeward hinge-line vortex is smaller with the strakes on. This is indicated by the outboard displacement of the flow reattachment induced by the leeward hinge-line vortex. The induced effect of the strake vortex increases the hinge-line and leading-edge vortex pressure signatures at $x/c = 0.75$. The increased vortex pressure signatures along the rear portion of the leeward wing cause the small unstable increments to C_{l_β} at this angle of attack. The strake vortex-induced effect on the leeward wing surface pressures is more pronounced at $\alpha \approx 20^\circ$ (figs. 28(f) and (g)) which show a large increase in the hinge-line and leading-edge vortex footprints at $x/c = 0.50$ to 0.75 . The increased suction pressure levels on the leeward wing relative to the windward wing promote a larger unstable increment to C_{l_β} . The vapor screen photograph at $\alpha \approx 22^\circ$ and $\beta \approx +5^\circ$ in figure 29(b) shows a stable leeward strake vortex and the outer edge of the combined leading-edge and hinge-line vortices. The mutual proximity of the leeward vortices leads to strong induced flow-field effects. The windward strake vortex is positioned near the fuselage and bursts upstream of the centerline tail. The flow visualization is consistent with the insensitivity of the windward wing surface pressure data to the strakes and is in qualitative agreement with the directional stability decrease in figure 28(a). At $\alpha \approx 24^\circ$ (figs. 28(h) and (i)), the surface pressures with strakes off are nearly uniform on the windward and leeward wings at $x/c = 0.30$ to 0.75 . The loss of the hinge-line vortex and leading-edge vortex pressure signatures along the entire wing suggests that a strong interaction occurs between the vortical flows and a rear shock wave at the higher angles of attack. This causes a rapid forward progression of vortex

breakdown. The strakes have no effect on the windward wing pressure distributions but reestablished strong vortex pressure signatures at all measurement stations on the leeward wing. The increased loading on the leeward wing resulted in the large unstable C_{l_β} increment at $\alpha \approx 24^\circ$ in figure 28(a).

Effect of Mach Number on Longitudinal Characteristics

Leading-edge flap undeflected. The effect of the free-stream Mach number on the lift, drag, and pitching-moment characteristics and the wing upper surface static pressure distributions with strakes both off and on is presented in figures 30 and 31, respectively. Laser vapor screen flow visualization results obtained with the strakes on are presented in figure 32.

With the strakes off, the lift at a given angle of attack generally increases with increasing Mach number (fig. 30(a)). This trend is apparent up to an angle of attack of approximately 20° . At higher α 's, lift decreases with Mach number from $M_\infty = 0.40$ to 0.80 because of vortex breakdown effects. The highest lift is developed at $M_\infty = 1.10$ through the range of angle of attack because of the absence of strong rear shock wave-vortex interactions and vortex breakdown effects. The drag at a given lift is insensitive to the Mach number from $M_\infty = 0.40$ to 0.95 up to a lift coefficient of approximately 0.9 . At higher lift, the drag increases with Mach number from $M_\infty = 0.40$ to 0.80 . Supersonic wave drag at $M_\infty = 1.10$ promotes the drag increments at low and moderate lift coefficients. The drag is least for $M_\infty = 1.10$ with lift coefficients greater than 0.9 . The wing-body-tail configuration is statically unstable in pitch at $M_\infty = 0.40$. Increasing the Mach number promotes a stable shift in the pitching-moment curve at zero lift. This effect is more pronounced at $M_\infty = 0.95$ and 1.10 , where the model is neutrally stable or exhibits longitudinal stability over a wide range of lift coefficients.

The wing pressure distributions at $\alpha \approx 12^\circ$, 16° , 20° , and 22° with the strakes off (figs. 30(b)-(e)) show a large decrease in the leading-edge vortex pressure signature and a broadening of the surface pressures underneath the vortical flow as the Mach number increases. These trends are consistent with a weaker, flatter vortex at the higher Mach numbers (refs. 16, 19, 25, 26, and 29). At $\alpha \approx 20^\circ$ and 22° (figs. 30(d) and (e)), the character of the wing pressure distributions at $x/c = 0.625$ and 0.75 is similar through the range of Mach number, despite

the dominance of vortex breakdown effects at the subsonic speeds and the stabilization of the vortex flow at the transonic speeds. This indicates that the pressure signatures of the burst, expanded wing vortex and stable, elliptically shaped vortical flow are similar. The vacuum pressure limit will also affect the character of the pressure distributions, particularly at the higher Mach numbers. The vacuum pressure coefficient $C_{p,v}$ provides an upper bound for the vortex-induced suction pressure levels by assuming that the local static pressure on the wing upper surface corresponds to the vacuum pressure ($p = 0 \text{ lb/ft}^2$):

$$C_{p,v} = \frac{-p_\infty}{q_\infty} = \frac{-p_\infty}{\frac{1}{2}\gamma p_\infty M_\infty^2} = \frac{-2}{\gamma M_\infty^2} \quad (1)$$

Reference 30 applied $C_{p,v}$ as a means of estimating the attainable leading-edge thrust for wings at subsonic and supersonic speeds. The value of $C_{p,v}$ at various Mach numbers is denoted in figures 30(b)-(e). At the supersonic free-stream condition ($M_\infty = 1.10$), the experimental surface pressures may approach a limiting value of about 90 percent of vacuum pressure. Similar maximum suction pressure levels were obtained on delta wings at supersonic speeds in reference 31. The increased lift at the higher Mach numbers is caused by an increase in the positive pressures on the compression side of the wing (ref. 25) and an increase in the attached flow and vortex flow suction pressures along the inboard portion of the wing upper surface. Although the peak vortex-induced suction pressures are generally lower at the higher Mach numbers, the maximum suction pressure levels extend across a greater spanwise extent of the wing. The surface pressure signature of the burst wing vortex at $\alpha \approx 22^\circ$ and $M_\infty = 0.40$ (fig. 30(e)) is broad and encompasses a large portion of the local wing semispan. The suction pressure levels underneath the burst vortex exhibit a large decrease due to increasing Mach number from $M_\infty = 0.40$ to 0.80. The decrease in the overall suction pressure levels causes the lift decrease (fig. 30(a)) within this range of Mach number. The surface pressures show a more significant decrease in the vortex-induced loading along the front part of the wing relative to the rear wing region as the Mach number increases. This effect contributes to an aft shift in the center of pressure and, consequently, the stable shift in the pitching-moment curves.

With the strakes on, the lift is less sensitive to the Mach number from $M_\infty = 0.40$ to 0.80 and angles of attack up to approximately 20° (fig. 31(a)) compared with the results obtained with the strakes

off (fig. 30(a)). There is a marked increase in lift within this range of angle of attack at higher Mach numbers, however. At $\alpha > 20^\circ$ the highest lift occurs at $M_\infty = 0.40$. Vortex breakdown was not observed at any Mach number. The decrease in lift due to increasing Mach number is due to the weakened vortices (refs. 16, 25, 26, and 29) and a vacuum pressure limit (refs. 30 and 31). At moderate and high lift coefficients, the drag generally increases with the Mach number from $M_\infty = 0.40$ to 0.95. The drag at $M_\infty = 0.40$ is lowest through the range of lift coefficient. Increasing the Mach number beyond 0.60 promotes a stable shift in the pitching-moment curve. At $M_\infty = 1.10$, the configuration with strakes on is neutrally stable up to a lift coefficient of approximately 0.9.

Increasing the Mach number decreases the maximum suction pressure levels induced by the wing vortex and broadens the vortex pressure signature with the strakes on (figs. 31(b)-(e)). These effects are consistent with the vapor screen flow visualization photographs in figure 32 which compare the model cross-flow patterns at $M_\infty = 0.60$ and 1.10 and $\alpha \approx 20^\circ$. The wing vortex has an approximately circular cross section at $M_\infty = 0.60$ (fig. 32(a)). At $M_\infty = 1.10$ (fig. 32(b)), the wing vortex exhibits a flattened, lobe-shaped cross section and is closer to the surface. Increasing the Mach number promotes an inboard and upward displacement of the strake vortices; this is an indicator of the reduced vortex strengths and the diminished flow induced by the strake and wing vortices on each other. The Mach number effect on the maximum suction pressure levels underneath the wing vortex is observed over a smaller spanwise extent of the wing with the strakes on (figs. 31(b)-(e)). This is due to the smaller wing vortex in the presence of the strake vortex-induced flow field. As a consequence, the lift is less sensitive to increasing Mach number from $M_\infty = 0.40$ to 0.80 (fig. 31(a)). The surface pressures at $\alpha \approx 24^\circ$ (fig. 31(e)) show that the strake vortex pressure footprint apparent at subsonic speeds is absent at transonic speeds; this is attributed to the inboard and upward displacement of the strake vortex at the higher Mach numbers, which was shown previously in the flow visualization photographs in figure 32.

Leading-edge flap deflected 30° . The Mach number effect on the lift and pitching-moment characteristics with $\delta_{LE} = 30^\circ$ is similar to the effect discussed in the previous section with the undeflected flap. This effect is shown in figures 33 and 34 for configurations with strakes off and on, respectively. The onset of wing vortex breakdown (strakes off) is delayed to a higher angle of attack because of the

deflected flap. As a result, the lift decrease due to increasing Mach number that was noted previously in figure 30(a) with $\delta_{LE} = 0^\circ$ does not occur until angles of attack greater than 22° (fig. 33(a)). In contrast with the results obtained with $\delta_{LE} = 0^\circ$ (figs. 30(a) and 31(a)), the drag increases with increasing Mach number through most of the range of lift coefficient. This effect is apparent with the strakes off (fig. 33(a)) and strakes on (fig. 34(a)). The surface pressure distributions in figures 33(b)–(e) and 34(b) (e) show that increasing the Mach number decreases the suction pressure levels on the forward-facing surface of the deflected flap and, consequently, the aerodynamic thrust component produced by the flap. In addition, the development of a strong hinge-line vortex situated over the main wing at the higher Mach numbers increases the suction pressure levels inboard of the flap knee and contributes to the drag increase.

Effect of Mach Number on Lateral-Directional Characteristics

Leading-edge flap undeflected. The lateral-directional stability derivatives obtained at $M_\infty = 0.40$ and 0.90 with the strakes both off and on are presented in figures 35 and 36, respectively. The overall effect of increasing Mach number is small with the strakes off (fig. 35). This effect is because of the relatively mild vortex breakdown asymmetries in sideslip and the absence of strong, adverse flow-field interactions between the burst vortices and the centerline tail. Increasing the Mach number from 0.40 to 0.90 promotes small positive C_{n_β} increments at angles of attack from 0° to 16° . The corresponding negative increments to C_{Y_β} indicate that the directional stability increase is due to increased loading on the centerline vertical tail. The higher tail load contributes to the stable C_{l_β} increments within the same range of angle of attack. The unstable C_{n_β} increments and positive C_{Y_β} increments at $\alpha \approx 18^\circ$ and 20° coincide with reduced levels of lateral stability; this suggests that the forward progression of the windward wing vortex breakdown reduces the dynamic pressure at the tail.

The lateral-directional stability characteristics with the strakes on are sensitive to the Mach number (fig. 36). At angles of attack greater than 12° , increasing the Mach number from 0.40 to 0.90 promotes large unstable increments to C_{n_β} and C_{l_β} . The strake vortices are weaker at the higher Mach number. As a result, the strake vortex-induced effect on the forebody and the corresponding stable increments to the directional stability diminish at $M_\infty = 0.90$. The vortex breakdown asymmetry in sideslip is more severe

at the transonic speeds. The progression of strake and wing vortex breakdown on the windward side is more rapid at $M_\infty = 0.90$ due to the interaction of the vortices with a rear shock wave. The effective increase in the leading-edge sweep on the leeward side provides a three-dimensional relief which stabilizes the vortical flows and moderates the shock effect. The lower q wake associated with the burst windward strake and wing vortices blankets the centerline tail which leads to the directional instability at the higher angles of attack.

Leading-edge flap deflected 30° . The Mach number effect on the lateral-directional stability characteristics with $\delta_{LE} = 30^\circ$ is shown in figures 37 and 38. The directional stability trends with the strakes off (fig. 37) and strakes on (fig. 38) are similar to the results obtained with the undeflected flap (figs. 35 and 36). With the strakes off (fig. 37), increasing the Mach number from 0.40 to 0.90 promotes unstable increments to the lateral stability at angles of attack from approximately 10° to 20° . With the strakes on (fig. 38), the unstable C_{l_β} increments due to increasing Mach number are larger with the deflected flap. These results are due to the development of the flap hinge-line vortex which increases the asymmetries in the strake-wing flow-field interactions in sideslip.

Summarization of Results

A wind tunnel experiment was conducted in the 7- by 10-Foot Transonic Tunnel at DTRC to determine the effects of chine-like forebody strakes and the Mach number on the longitudinal and lateral-directional characteristics of a generalized fighter configuration with a 55° cropped delta wing. The model six-component forces and moments, wing upper surface static pressure distributions, and laser vapor screen flow visualizations were obtained at free-stream Mach numbers from 0.40 to 1.10 ; Reynolds numbers based on the wing mean aerodynamic chord of 1.60×10^6 to 2.59×10^6 ; angles of attack from 0° to a maximum of 28° ; and angles of sideslip of 0° , $+5^\circ$, and -5° . The model was tested with and without the forebody strakes, with a centerline vertical tail, and with a constant-chord wing leading-edge flap undeflected and deflected 30° .

A favorable interaction occurred between the strake and wing flow fields that stabilized the wing vortex at subsonic and transonic speeds and at zero angle of sideslip, increased the lift at moderate and high angles of attack, and reduced the drag at moderate and high lift levels. The favorable effects on the lift and drag diminished with increasing Mach number due to the weaker strake and wing vortices and a

corresponding decrease in the flow that the vortices induced on each other. Adding the strakes resulted in a large unstable shift in the pitching-moment curve due to the increased planform area and the strake lift acting ahead of the moment reference center. The strake effect on the character of the pitching-moment curve was insensitive to increasing Mach number.

The strake vortex induced favorable spanwise flow gradients on the wing that were similar to those occurring naturally on more highly swept wings. This three-dimensional relief effect prevented the development of a strong rear shock wave, delayed wing vortex breakdown, and eliminated the model buffet-ing due to the vortex-shock interaction that was observed with strakes off at $M_\infty = 0.80$ and 0.95 . Wing vortex breakdown did not occur with the strakes off at $M_\infty = 1.10$, and the strake effect on the lift and drag was correspondingly small.

Deflecting the wing leading-edge flaps delayed the onset of vortex breakdown to a higher angle of attack. The strake effect on the lift and drag was accordingly reduced because of the improved efficiency of the isolated wing.

Flow separation occurred near the knee of the deflected flap at the higher subsonic and transonic speeds. The resulting hinge-line vortex was a dominant feature of the wing flow field and contributed to the increased drag at the higher Mach numbers. The character of the hinge-line vortex was unaffected by the strakes.

The direct suction effect induced by the windward strake vortex on the forebody resulted in a large increase in the directional stability at subsonic speeds. This effect diminished at the transonic speeds because of the weaker strake vortex.

With the wing leading-edge flaps undeflected, the strakes increased the vortex breakdown asymmetry in sideslip and decreased the lateral stability at the subsonic speeds and higher angles of attack. In combination with the deflected flaps, however, the strakes increased the lateral stability through the test range of angle of attack. The test results indicated that the strakes promoted stable increments to the lateral stability when the wing vortex was confined to the leading edge, and its size and strength were reduced by deflecting the leading-edge flaps. The onset of windward vortex breakdown and the increased interaction of the leeward strake and wing vortices at the higher angles of attack limited the magnitude of the stable C_{l_β} increments.

The strakes increased the vortex breakdown asymmetry in sideslip and promoted lateral instability at the transonic speeds. The induced effect of the

windward strake vortex on the wing flow was small. The flow about the windward wing was dominated by vortex breakdown and vortex-shock interactions. In contrast, the leeward wing was characterized by stable strake and wing vortices and the absence of vortex-rear shock interaction. The burst windward vortices blanketed the centerline vertical tail which promoted directional instability at the higher angles of attack. The adverse effects of the strakes on the lateral-directional characteristics at the transonic speeds were reduced by wing flap deflection.

The Mach number effect on the longitudinal characteristics was similar both with and without the forebody strakes. The lift at a given angle of attack increased with increasing Mach number provided that the effects of wing vortex breakdown were small. At higher angles of attack where vortex breakdown dominated the flow field about the wing-body-tail configuration, the lift decreased with increasing Mach number. A similar trend occurred with the strakes on due to the diminished vortex strengths and a vacuum pressure limit at the higher Mach numbers. The drag was sensitive to increasing Mach number when the wing leading-edge flaps were deflected. The drag increased with Mach number due to a reduction in the aerodynamic thrust component generated by the flap and the development of a large-scale vortex on the main wing arising from hinge-line flow separation. The center of pressure moved aft with increasing Mach number which promoted a stable shift in the pitching-moment curve.

The effect of increasing Mach number on the lateral-directional stability characteristics of the wing-body-tail configuration was small. At the subsonic speeds, the difference in the effective leading-edge sweep angle of the windward and leeward wings was insufficient to promote a large asymmetry in the vortex breakdown positions. The vortex breakdown asymmetry was also limited at the transonic speeds by the development of a rear shock wave on the windward and leeward wings.

The lateral-directional stability characteristics were more sensitive to the Mach number with the forebody strakes on. The difference in the effective sweep angles of the windward and leeward wings was greater because of the limited "communication" between the strake and wing vortices on the windward side and the stronger mutual induced effects of the strake and wing vortices on the leeward side. This effect increased the vortex breakdown asymmetry at the subsonic speeds. The resultant vortex breakdown asymmetry in sideslip was more severe at the transonic speed due to vortex-shock interaction.

Concluding Remarks

The present wind tunnel experiment established a data base on the overall longitudinal and lateral-directional aerodynamic characteristics of a generalized fighter configuration with a 55° cropped delta wing at subsonic and transonic speeds. Emphasis was placed on determining the effects of chine-like forebody strakes and the Mach number on the model six-component forces and moments, wing upper surface static pressures, and off-body flow-field behavior. Key fluid mechanics phenomena at subsonic and transonic maneuvering conditions were identified. These phenomena included coexisting and interacting vortex flows and shock waves, vortex breakdown, vortex flow interactions with a centerline vertical tail, and separation-induced vortical flows from the hinge line of a deflected wing leading-edge flap. The flow mechanisms were correlated with the longitudinal and lateral-directional aerodynamic data trends.

The observed benefits of the forebody strakes at the subsonic speeds included stabilization of the wing vortices at zero sideslip, increased lift at the moderate and high angles of attack, reduced drag at moderate-to-high lift, increased directional stability up to the maximum test angle of attack, and increased lateral stability through a more limited range of angle of attack. The disadvantages included increased longitudinal instability and reduced lateral stability at the higher angles of attack because of an increase in the wing vortex breakdown asymmetry in sideslip. The strakes increased the lateral stability through the test range of angle of attack when the wing leading-edge flaps were deflected.

The strake benefits at the transonic speeds were increased lift, reduced drag, reduced wing vortex-shock wave interactions, elimination of model buffeting in pitch, and increased directional stability up to moderate angles of attack. The disadvantages consisted of increased vortex breakdown asymmetry in sideslip, adverse vortex flow interaction with the centerline vertical tail, and lateral-directional instabilities at the higher angles of attack. The adverse effects of the strakes on the lateral-directional stability were reduced when the wing flaps were deflected.

The principal effects on the model flow field due to increasing the Mach number were reduced strake-wing vortex interactions, development of shock waves coexisting with vortex flows, flow separation from the hinge line of the deflected wing flap, and increased vortex breakdown asymmetry in sideslip (strakes on). Increasing the Mach number reduced the vortex pressure signatures; promoted model buffeting (strakes

off); reduced the longitudinal instability; reduced the favorable strake effects on lift, drag, and directional stability; and promoted lateral-directional instabilities at the higher angles of attack (strakes on).

NASA Langley Research Center
Hampton, VA 23681-0001
September 29, 1992

References

1. Stevens, J. R.: A New Lifting Surface Approach to the Design of Supersonic Wings. *Design Conference Proceedings—Technology for Supersonic Cruise Military Aircraft*, Volume I, AFFDL-TR-77-85-VOL I, U.S. Air Force, 1976. (Available from DTIC as AD B025 253L.)
2. Mangold, P.: Some Aerodynamic/Flightmechanic Aspects for the Design of Future Combat Aircraft. *ICAS Proceedings 1982—13th Congress of the International Council of the Aeronautical Sciences/AIAA Aircraft Systems and Technology Conference*, B. Laschka and R. Staufenbiel, eds., 1982, pp. 34-43. (Available as ICAS-82-1.1.3.)
3. McGregor, I.: The Vapor-Screen Method of Flow Visualization. *J. Fluid Mech.*, vol. 11, pt. 4, Dec. 1961, pp. 481-511.
4. ASED Staff: *Transonic Wind-Tunnel Facility at the Naval Ship Research and Development Center*. ASED Rep. 332, David W. Taylor Naval Ship Research and Development Center, June 1975. (Available from DTIC as AD A014 927.)
5. Erickson, Gary, E.: *Vortex/Linear Lift Augmentation*. U.S. Air Force, Sept. 1986.
Volume I—Program Summary. AFWAL-TR-86-3068, Vol. I. (Available from DTIC as AD B109 978L.)
Volume II, Part A—Analysis of Subsonic and Transonic Surface Pressure Data—Constant Chord (Untwisted) Leading-Edge Flap. AFWAL-TR-86-3068, Vol. II, Pt. A. (Available from DTIC as AD 8109 796L.)
Volume II, Part B—Analysis of Subsonic and Transonic Surface Pressure Data—Constant Chord (Untwisted) Leading-Edge Flap. AFWAL-TR-86-3068, Vol. II, Pt. B. (Available from DTIC as AD B109 797L.)
Volume III—Analysis of Subsonic and Transonic Surface Pressure Data—Twisted Constant Chord Leading-Edge Flap. AFWAL-TR-86-3068, Vol. III. (Available from DTIC as AD B109 979L.)
Volume IV—Analysis of Subsonic and Transonic Surface Pressure Data—Reverse Taper Leading-Edge Flap. AFWAL-TR-86-3068, Vol. IV. (Available from DTIC as AD B109 980L.)
Volume V—Analysis of Force and Moment Data at Subsonic and Transonic Speeds—All Flap Configurations. AFWAL-TR-86-3068, Vol. V. (Available from DTIC as AD B109 900L.)
6. Erickson, Gary E.; Rogers, Lawrence W.; Schreiner, John A.; and Lee, David G.: Subsonic and Transonic

- Vortex Aerodynamics of a Generic Forebody Strake-Cropped Delta Wing Fighter. AIAA-88-2596, June 1988.
7. Polhamus, Edward C.: *Charts for Predicting the Subsonic Vortex-Lift Characteristics of Arrow, Delta, and Diamond Wings*. NASA TN D-6243, 1971.
 8. Campbell, James F.; and Erickson, Gary E.: *Effects of Spanwise Blowing on the Surface Pressure Distributions and Vortex-Lift Characteristics of a Trapezoidal Wing-Strake Configuration*. NASA TP-1290, 1979.
 9. Wentz, William H., Jr.; and Kohlman, David L.: *Wind Tunnel Investigations of Vortex Breakdown on Slender Sharp-Edged Wings*. NASA CR-98737, 1969.
 10. Goodsell, Aga M.; Madson, Michael D.; and Melton, John E.: Tranair and Euler Computations of a Generic Fighter Including Comparisons With Experimental Data. AIAA-89-0263, Jan. 1989.
 11. Rao, Dhanvada M.; and Bhat, M. K.: *A Low-Speed Wind Tunnel Study of Vortex Interaction Control Techniques on a Chine-Forebody/Delta-Wing Configuration*. NASA CR-189616, 1992.
 12. Cunningham, Atlee M., Jr.: Practical Problems: Airplanes. *Unsteady Transonic Aerodynamics*, David Nixon, ed., American Inst. of Aeronautics and Astronautics, Inc., c.1989, pp. 75-132.
 13. Rogers, E. W. E.; and Hall, I. M.: An Introduction to the Flow About Plane Swept-Back Wings at Transonic Speeds. *J. Royal Aeronaut. Soc.*, vol. 64, no. 596, Aug. 1960, pp. 449-464.
 14. Sutton, E. P.: *Some Observations of the Flow Over a Delta-Winged Model With 55-Deg Leading-Edge Sweep, at Mach Numbers Between 0.4 and 1.8*. R. & M. No. 3190, British Aeronautical Research Council, 1960.
 15. Elsenaar, A.; Hjelmberg, L.; Bütetisch, K.; and Bannink, W. J.: The International Vortex Flow Experiment. *Validation of Computational Fluid Dynamics, Volume 1—Symposium Papers and Round Table Discussion*, AGARD-CP-437, Vol. 1, Dec. 1988, pp. 9-1-9-23.
 16. Erickson, Gary E.: *Wind Tunnel Investigation of the Interaction and Breakdown Characteristics of Slender-Wing Vortices at Subsonic, Transonic, and Supersonic Speeds*. NASA TP-3114, 1991.
 17. Erickson, Gary E.; Schreiner, John A.; and Rogers, Lawrence W.: Canard-Wing Vortex Interactions at Subsonic Through Supersonic Speeds. AIAA-90-2814, Aug. 1990.
 18. Grose, G. G.; Brady, C. C.; and Bristow, D. R.: *Investigation of Scaling Effects in Transonic Wind Tunnel Testing*. AFFDL-TR-72-60, U.S. Air Force, June 1972.
 19. Squire, L. C.: Leading-Edge Separations and Cross-Flow Shocks on Delta Wings. *AIAA J.*, vol. 23, no. 3, Mar. 1985, pp. 321-325.
 20. Erickson, Gary E.; Schreiner, John A.; and Rogers, Lawrence W.: Multiple Vortex and Shock Interactions at Subsonic, Transonic, and Supersonic Speeds. AIAA-90-3023, Aug. 1990.
 21. Hall, M. G.: Vortex Breakdown. *Annual Review of Fluid Mechanics*, Volume 4, Milton Van Dyke, Walter G. Vincenti, and J. V. Wehausen, eds., Annual Reviews Inc., 1972, pp. 195-218.
 22. Erickson, Gary E.; and Rogers, Lawrence W.: *Experimental Study of the Vortex Flow Behavior on a Generic Fighter Wing at Subsonic and Transonic Speeds*. NASA TM-89446, 1987.
 23. Hall, R. M.; Erickson, G. E.; Banks, D. W.; and Fisher, D. F.: Advances in High-Alpha Experimental Aerodynamics: Ground Test and Flight. *High-Angle-of-Attack Technology*, Volume I, Joseph R. Chambers, William P. Gilbert, and Luat T. Nguyen, eds., NASA CP-3149, Part 1, 1992, pp. 69-115.
 24. Karling, Krister: *Aerodynamics of Aircraft 37. Part 1: General—Characteristics at Low Speed*. NASA TM-88403, 1986.
 25. Vorropoulos, G.; and Wendt, J. F.: Laser Velocimetry Study of Compressibility Effects on the Flow Field of a Delta Wing. *Aerodynamics of Vortical Type Flows in Three Dimensions*, AGARD-CP-342, July 1983, pp. 9-1-9-13.
 26. Küchemann, D.: *The Aerodynamic Design of Aircraft*. Pergamon Press Inc., c.1978.
 27. Kern, Steven B.: A Numerical Investigation of Vortex Flow Control Through Small Geometry Modifications at the Strake/Wing Junction of a Cropped Double-Delta Wing. AIAA-92-0411, Jan. 1992.
 28. Lorincz, Dale J.: *A Water Tunnel Flow Visualization Study of the F-15*. NASA CR-144878, 1978.
 29. Squire, L. C.; Jones, J. G.; and Stanbrook, A.: *An Experimental Investigation of the Characteristics of Some Plane and Cambered 65° Delta Wings at Mach Numbers From 0.7 to 2.0*. R. & M. No. 3305, British Aeronautical Research Council, 1963.
 30. Carlson, Harry W.; Mack, Robert J.; and Barger, Raymond L.: *Estimation of Attainable Leading-Edge Thrust for Wings at Subsonic and Supersonic Speeds*. NASA TP-1500, 1979.
 31. Miller, David S.; and Wood, Richard M.: *Lee-Side Flow Over Delta Wings at Supersonic Speeds*. NASA TP-2430, 1985.

Table I. Model Geometry

Wing aspect ratio, $AR, b^2/S_{ref}$	1.81
Reference wing span, b , in.	24.94
Wing centerline chord, c , in.	22.95
Wing tip chord, c_t , in.	4.68
Wing mean aerodynamic chord, \bar{c} , in.	15.83
Vertical tail mean aerodynamic chord, \bar{c}_T , in.	5.61
Model length, l , in.	42.00
Leading-edge flap exposed area (2 flaps), S_{flap} , in ²	41.07
Reference wing area, S_{ref} , in ²	344.55
Forebody strake exposed area (2 strakes), S_{strake} , in ²	22.94
Vertical tail exposed area, S_{tail} , in ²	30.34
Wing leading-edge sweep angle, Λ_{LE} , deg	55.0
Wing trailing-edge sweep angle, Λ_{TE} , deg	-2.1
Wing taper ratio, $\lambda, c_t/c$	0.2

Table II. Wind Tunnel Test Conditions

M_∞	p_∞ , lb/ft ²	T_∞ , °F	q_∞ , lb/ft ²	$Re_{\bar{c}}$
0.40	982	69	100	1.60×10^6
0.60	900	71	178	1.99×10^6
0.80	890	80	264	2.31×10^6
0.90	800	79	268	2.18×10^6
0.95	775	73	275	2.19×10^6
1.10	895	77	355	2.59×10^6

ORIGINAL PAGE
BLACK AND WHITE PHOTOGRAPH

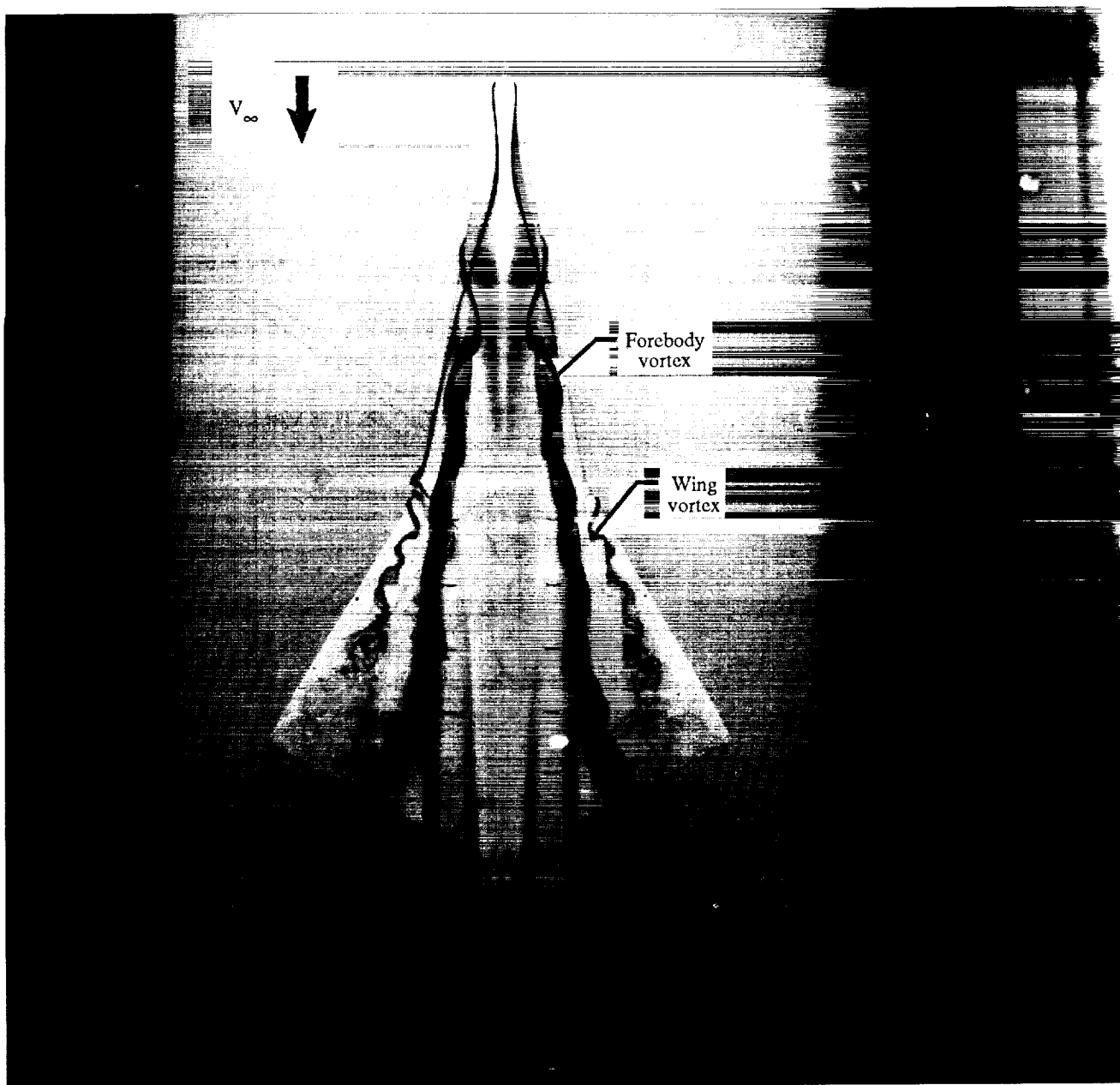


Figure 1. Flow visualization of forebody and wing vortex interaction (Langley 16- by 24-Inch Water Tunnel).

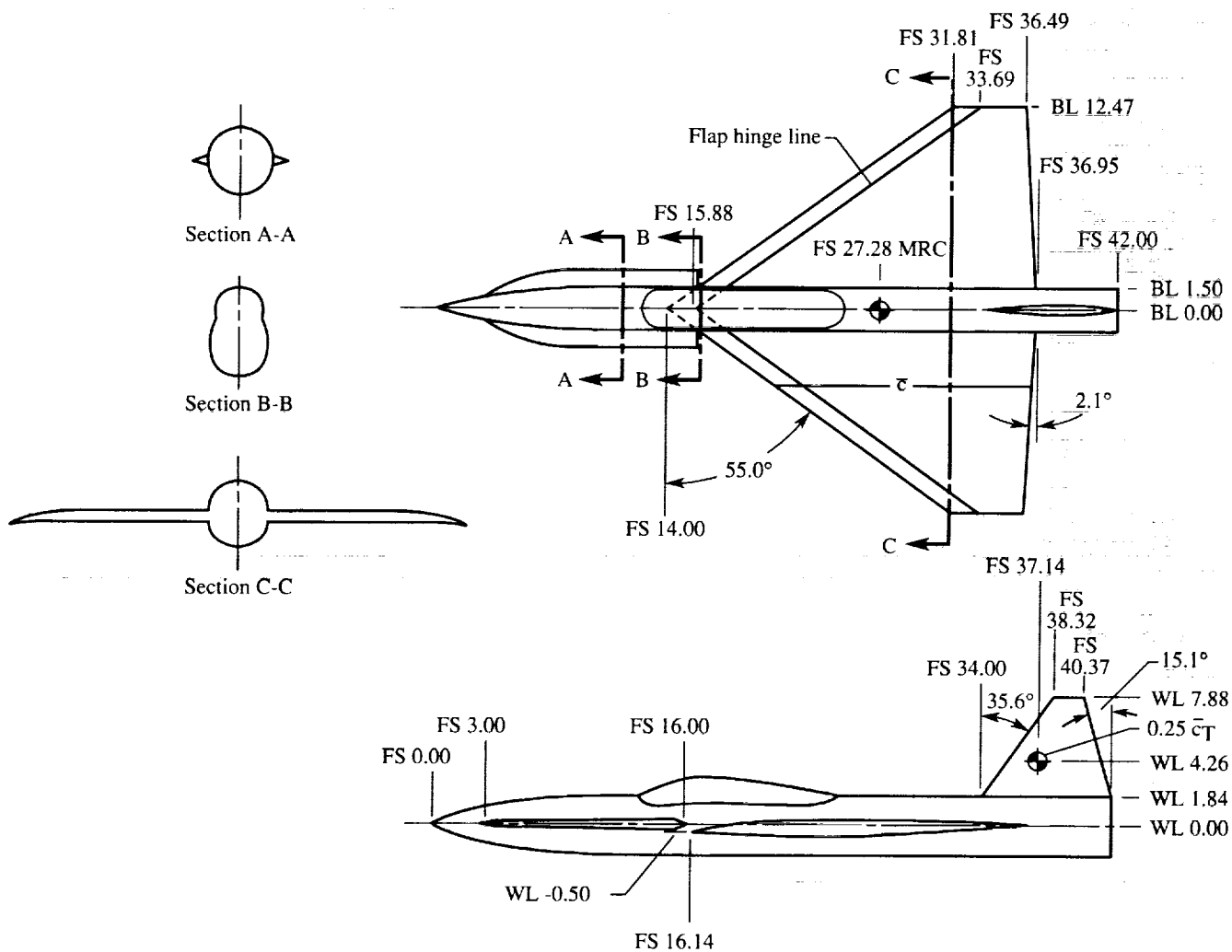


Figure 2. Geometry details of wind tunnel model. Linear dimensions are in inches.

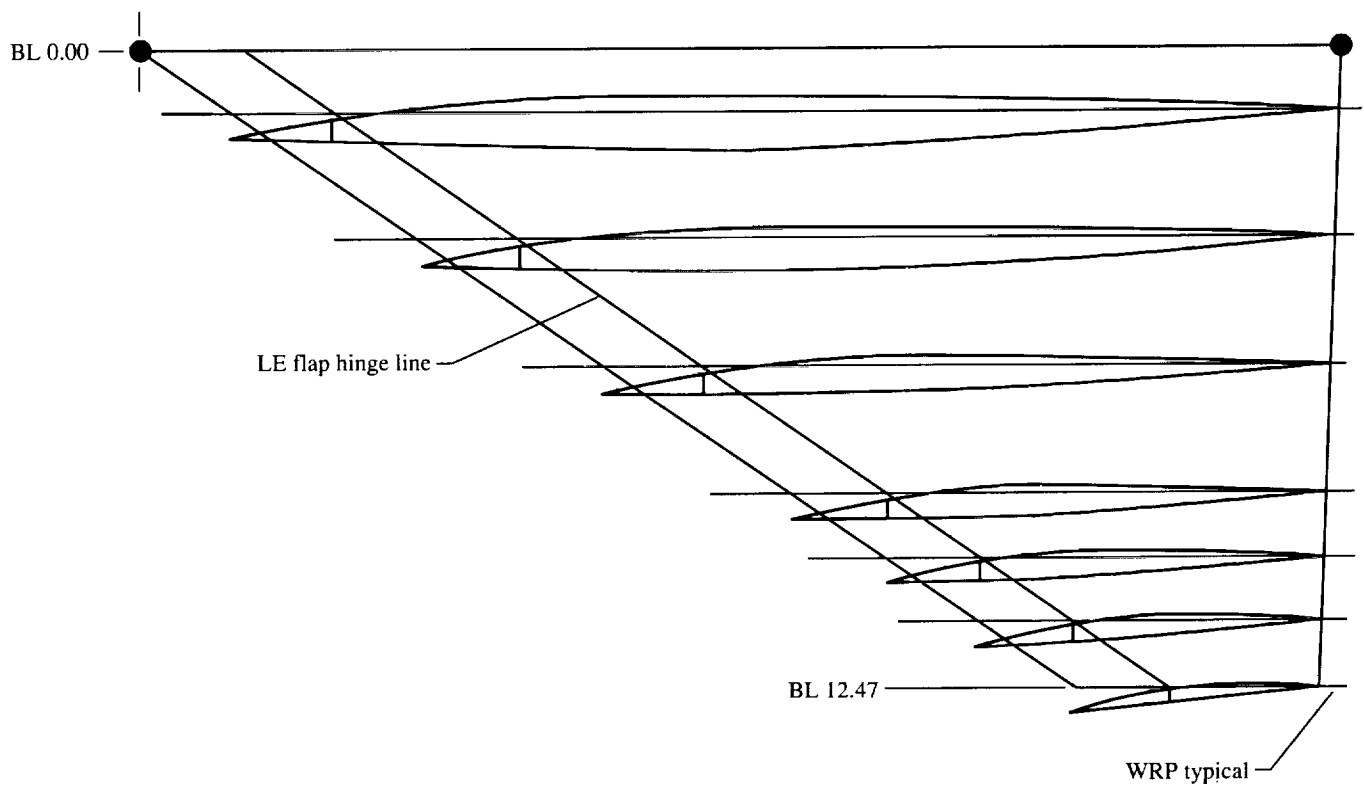


Figure 3. Streamwise section cuts of 55° cropped delta wing.



Figure 4. Section cuts normal to leading-edge flap hinge line with flap deflected 30° .

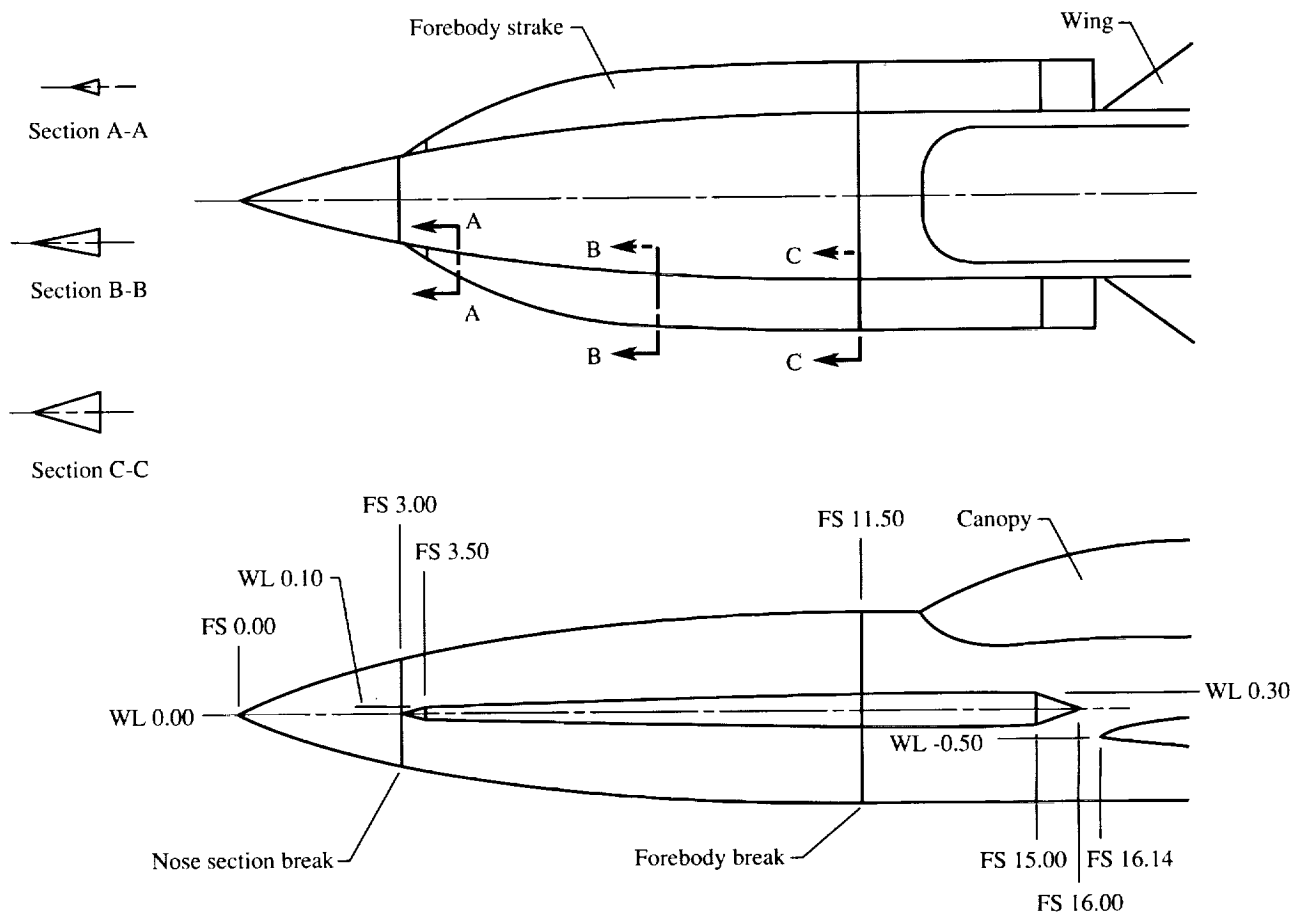


Figure 5. Geometry details of chine-like forebody strakes. Linear dimensions are in inches.

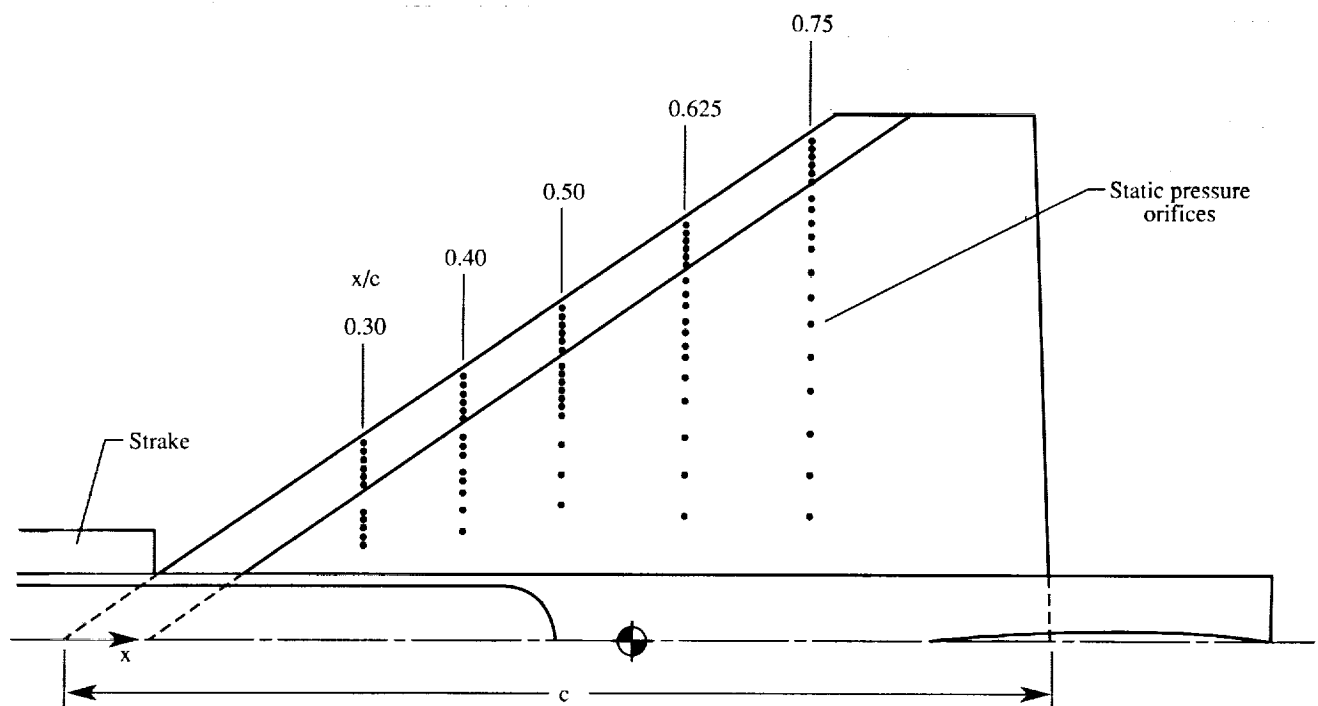
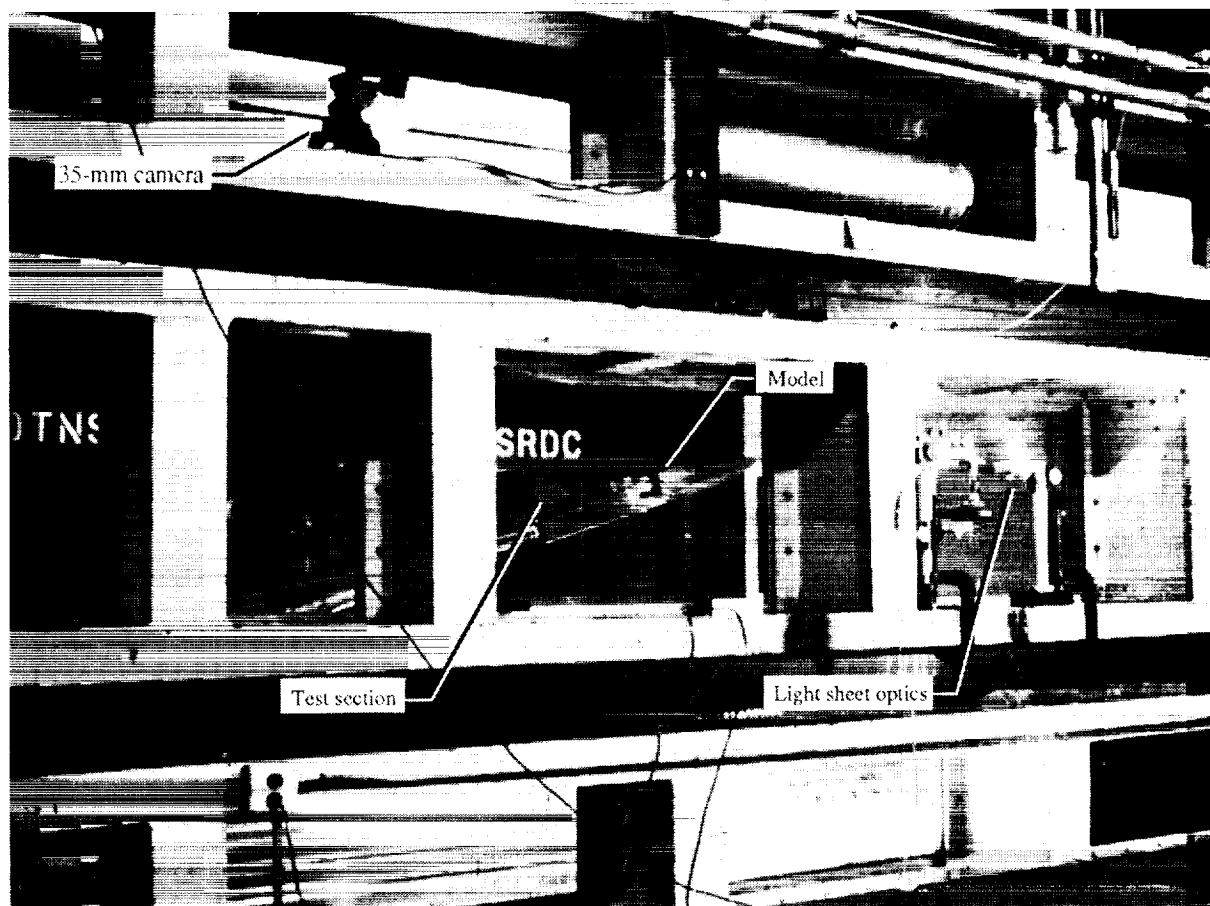


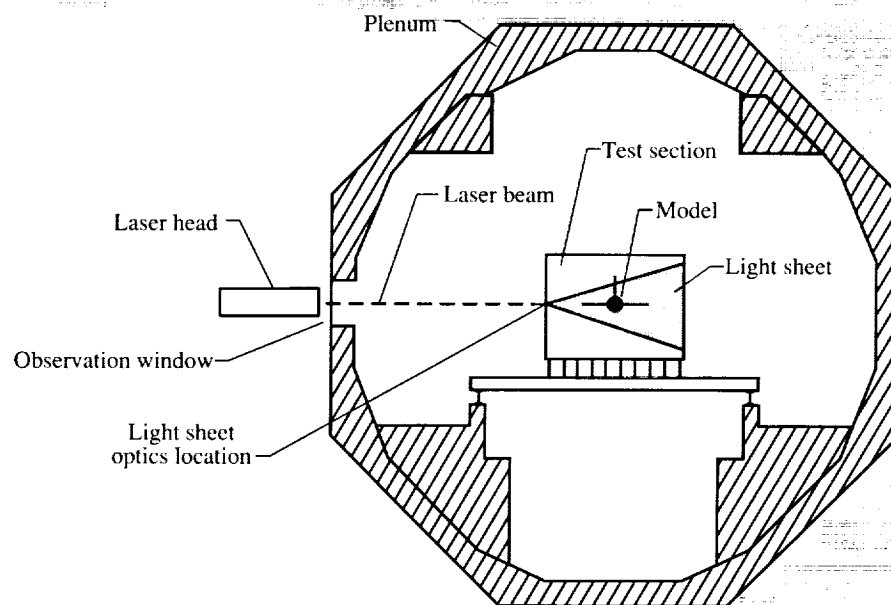
Figure 6. Static pressure orifice locations on upper surface of right wing.

ORIGINAL PAGE
BLACK AND WHITE PHOTOGRAPH



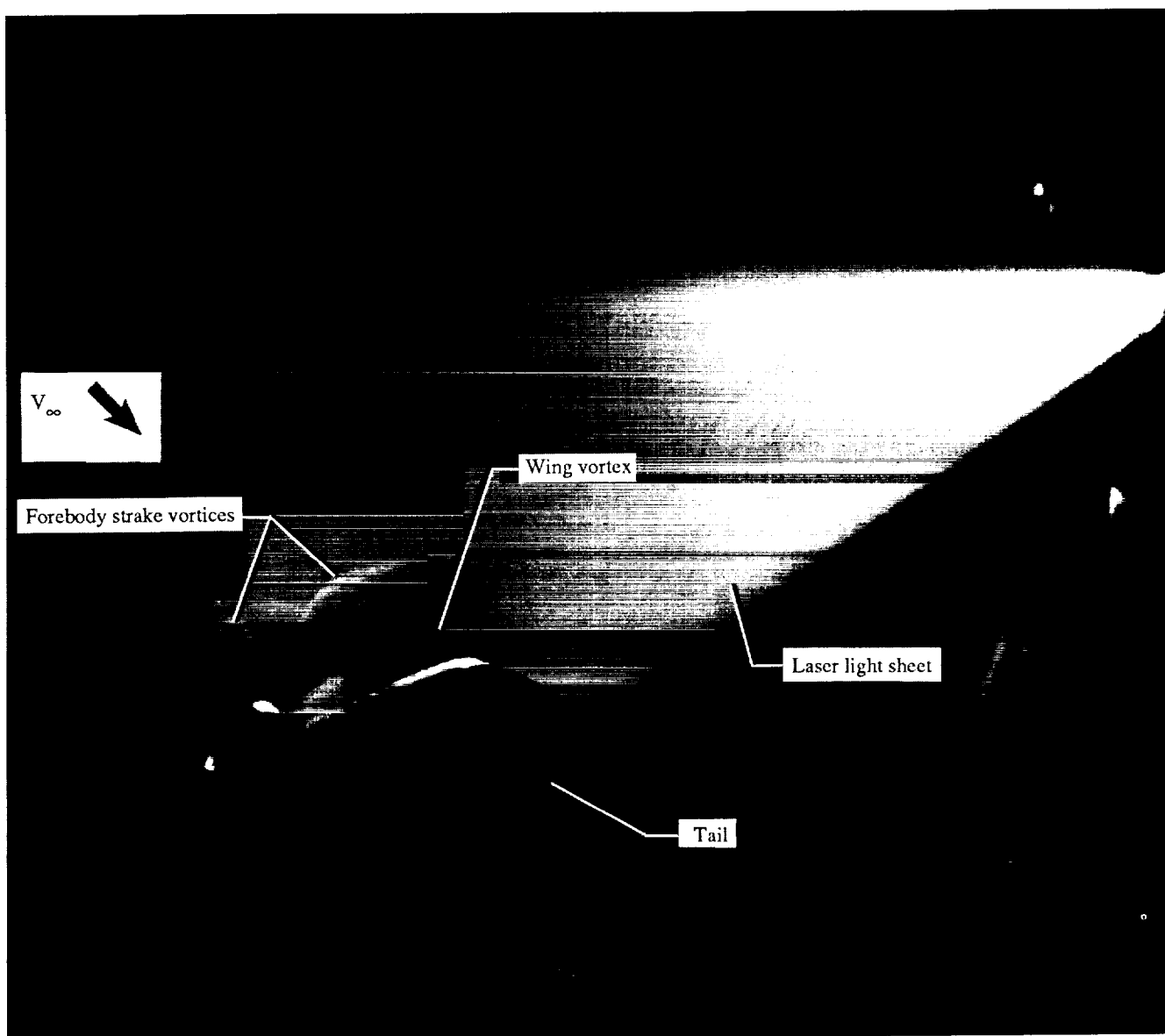
(a) Light sheet optics in test section window.

Figure 7. Setup of laser light sheet optics in 7- by 10-Foot Transonic Tunnel at DTRC.



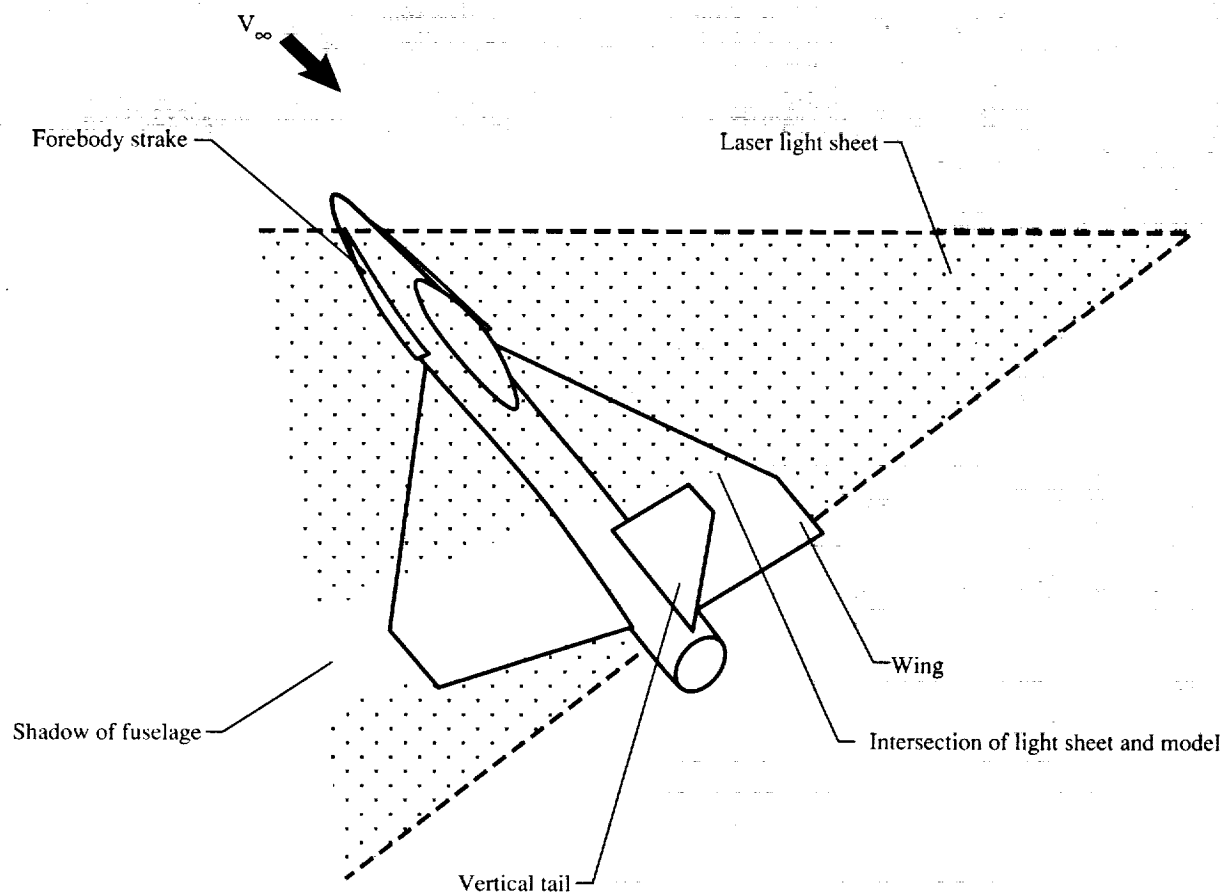
(b) Cross section of wind tunnel with laser light sheet setup shown.

Figure 7. Concluded.



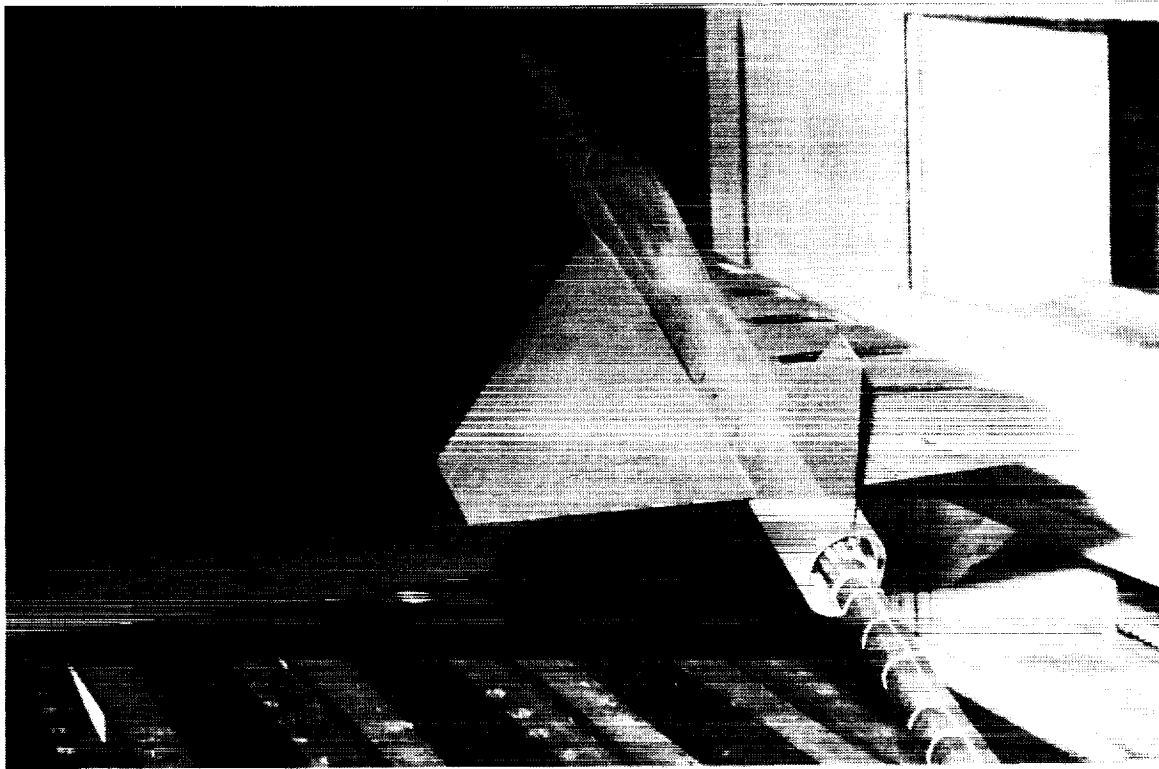
(a) Laser vapor screen pattern.

Figure 8. Laser vapor screen flow visualization at $M_\infty = 1.10$, $\alpha \approx 20^\circ$, and $x/c = 0.75$. Left three-quarter rear view.

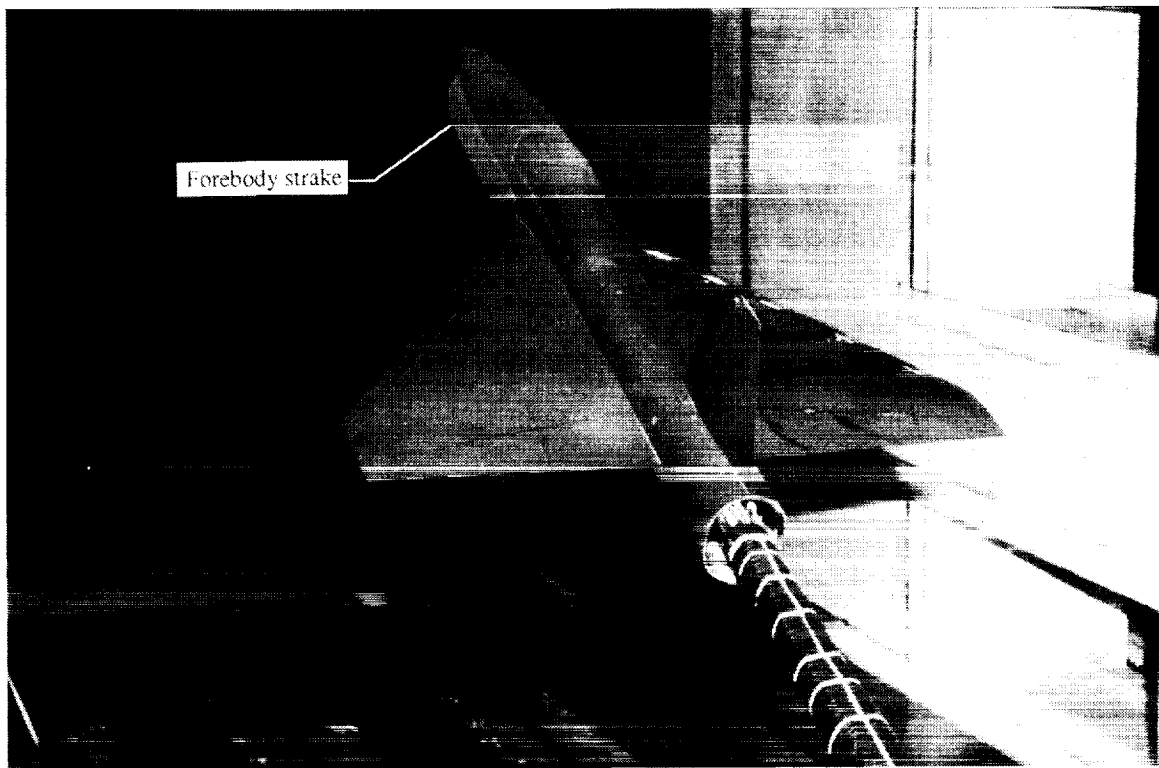


(b) Sketch of laser light sheet position with respect to model.

Figure 8. Concluded.

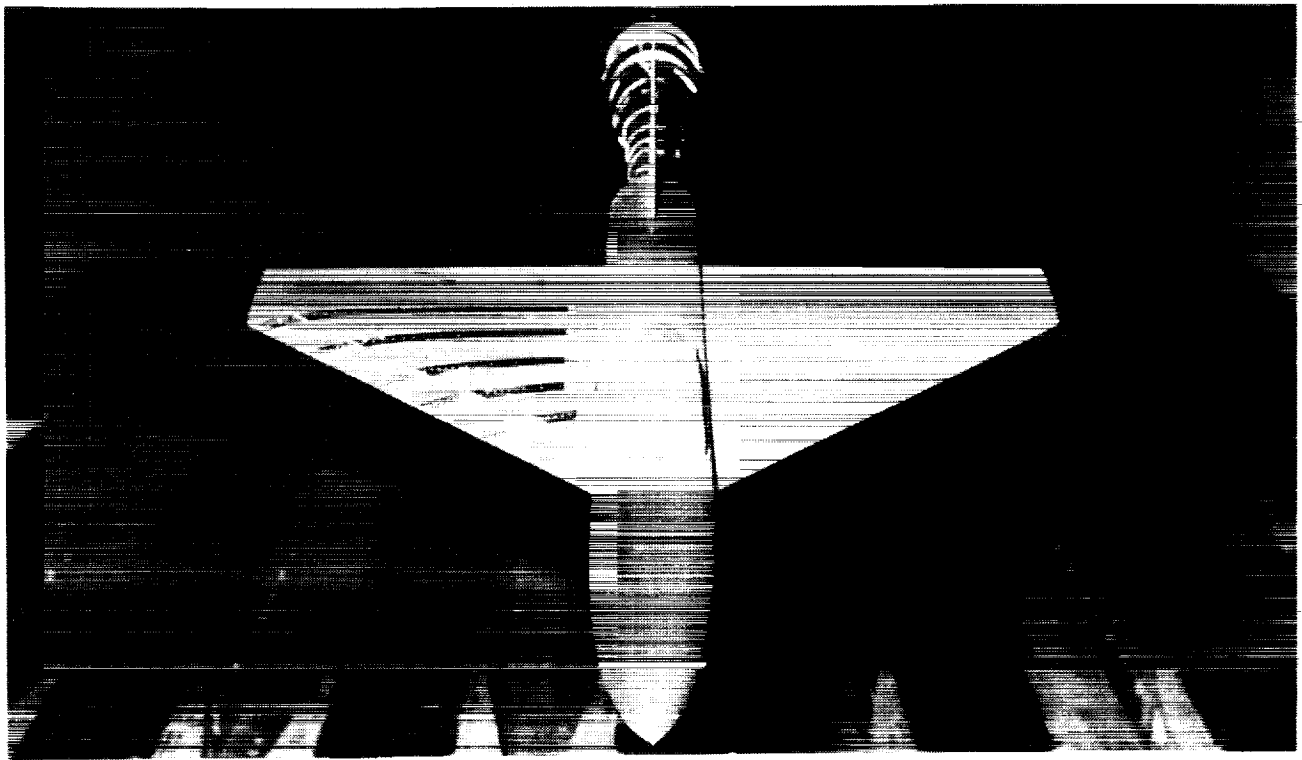


(a) Forebody strakes off; rear view.

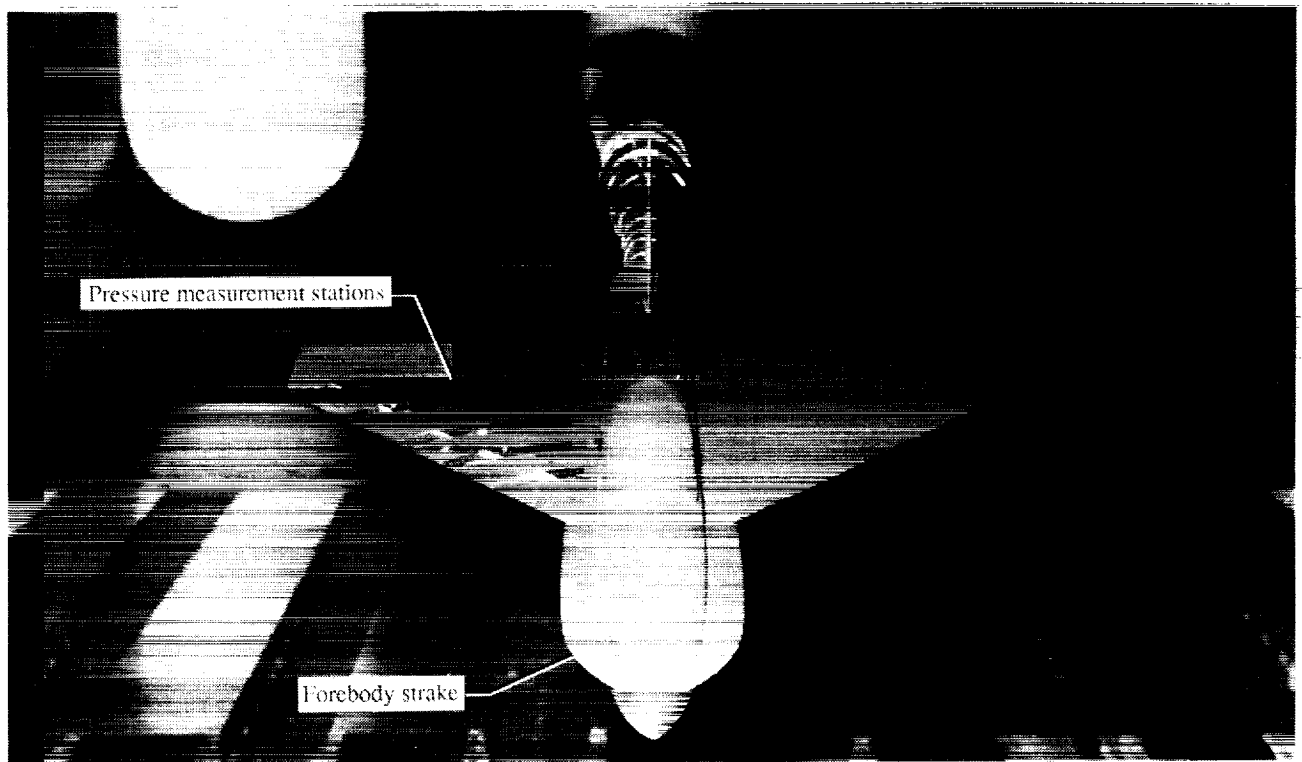


(b) Forebody strakes on; rear view.

Figure 9. Model installed in test section of 7- by 10-Foot Transonic Tunnel at DTRC.

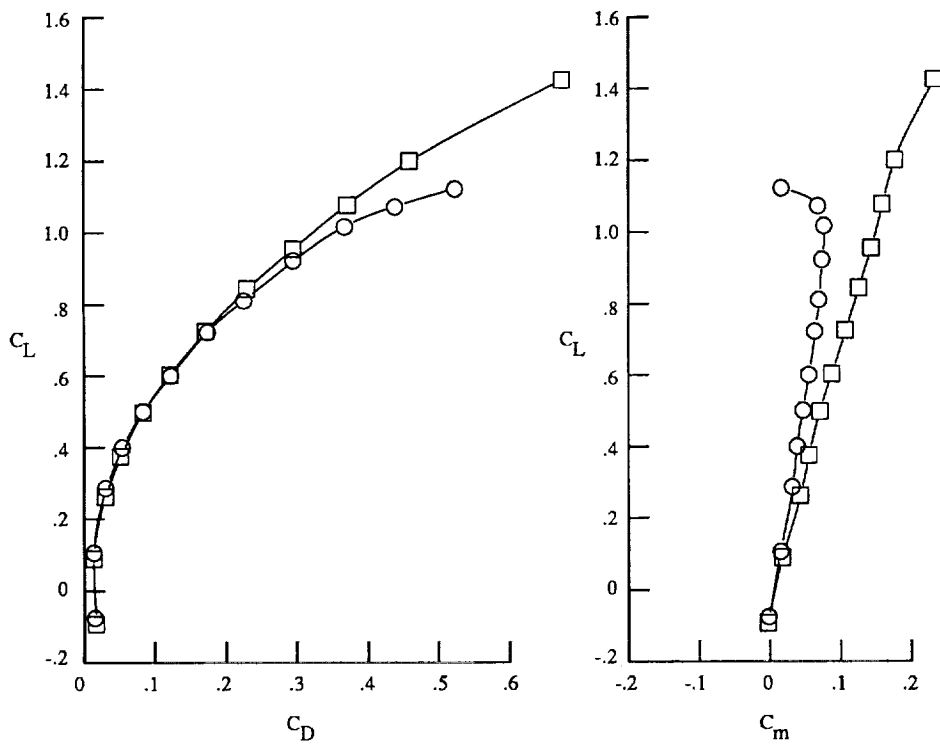
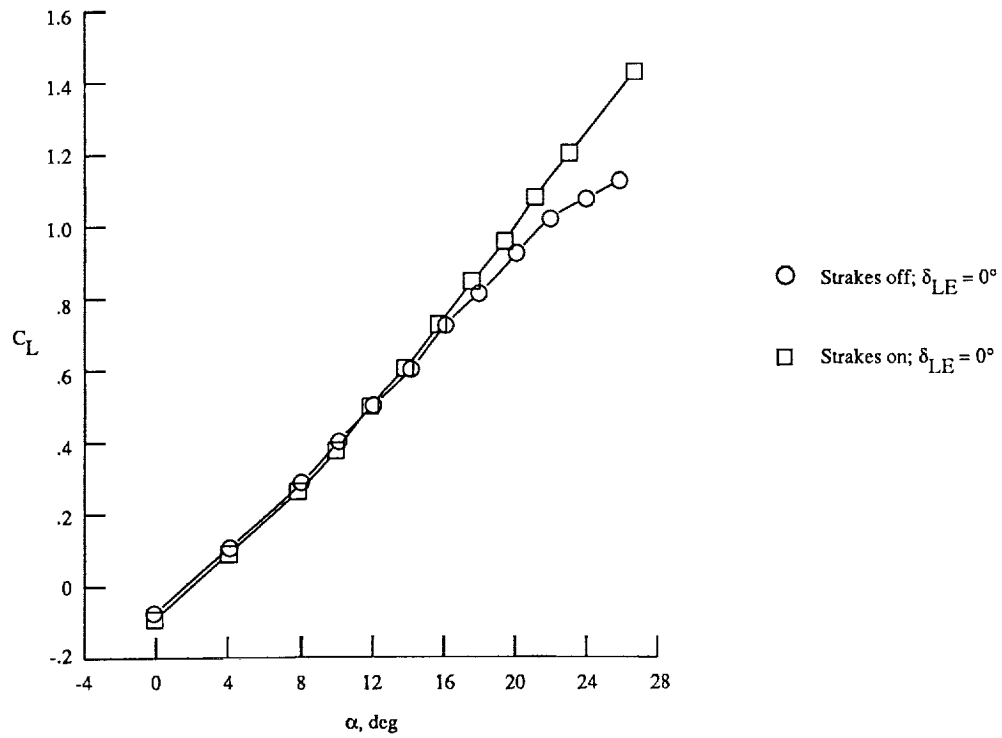


(c) Forebody strakes off; top view.



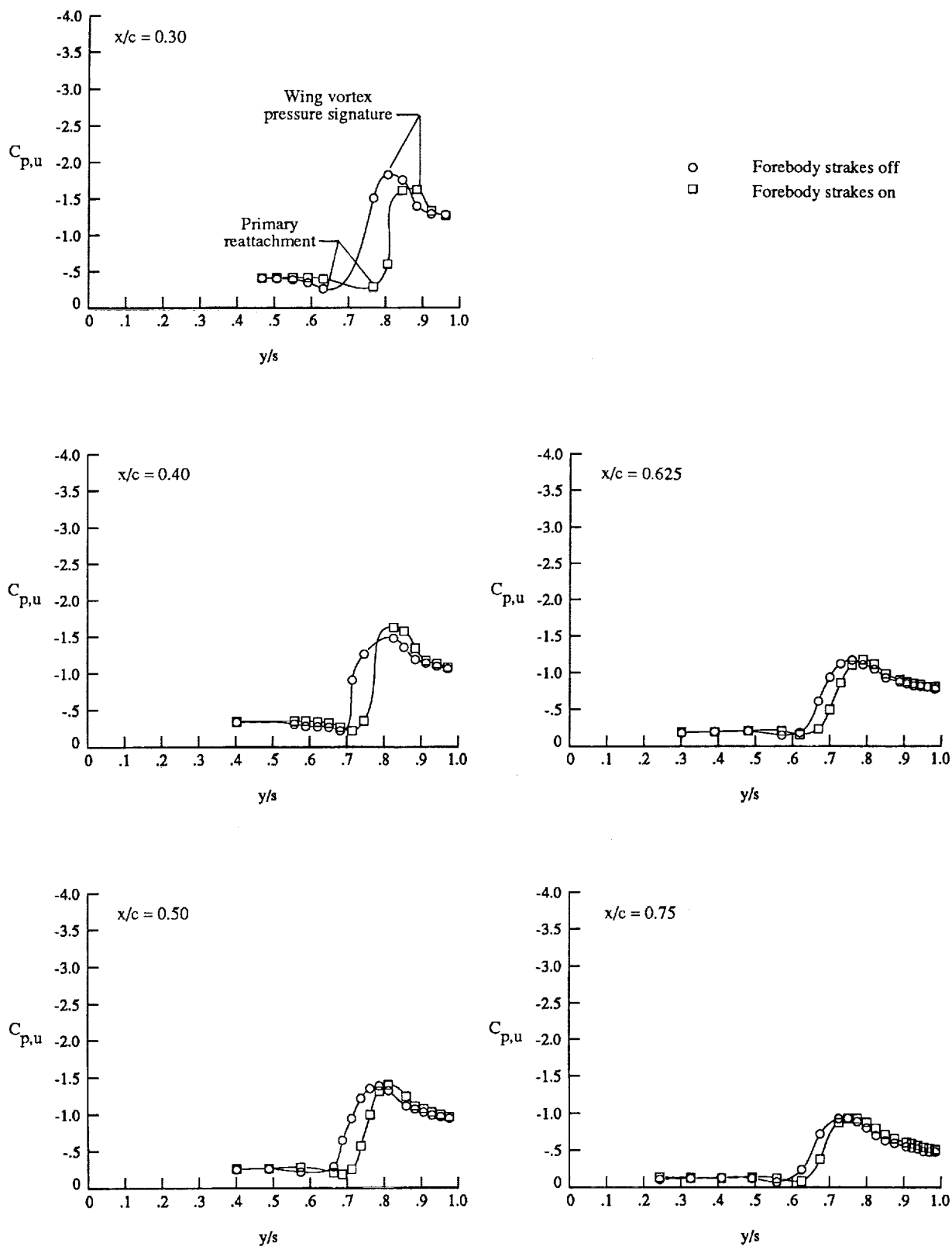
(d) Forebody strakes on; top view.

Figure 9. Concluded.



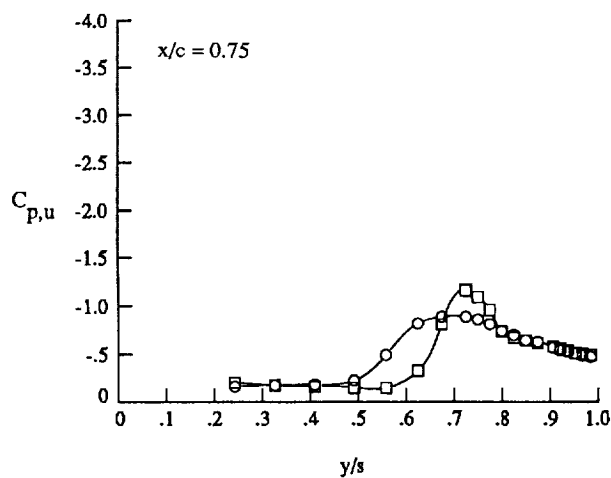
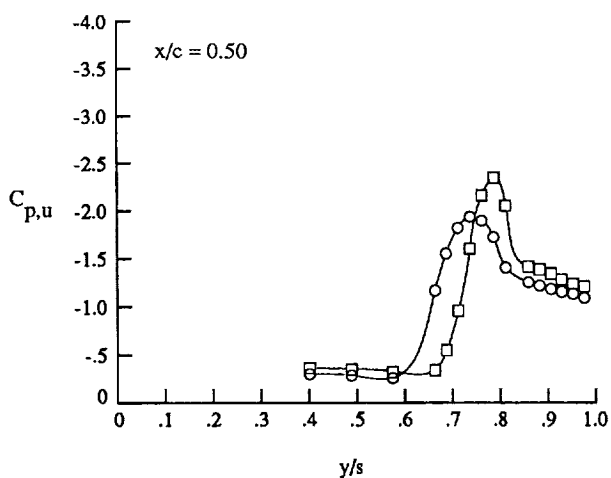
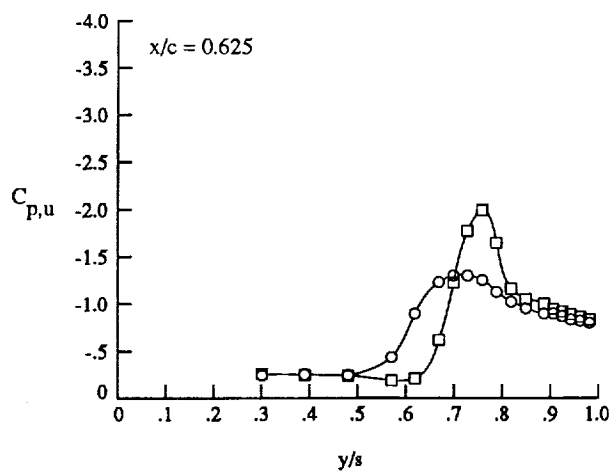
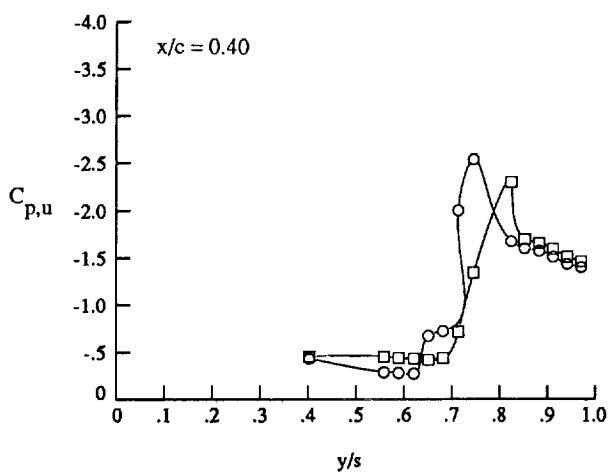
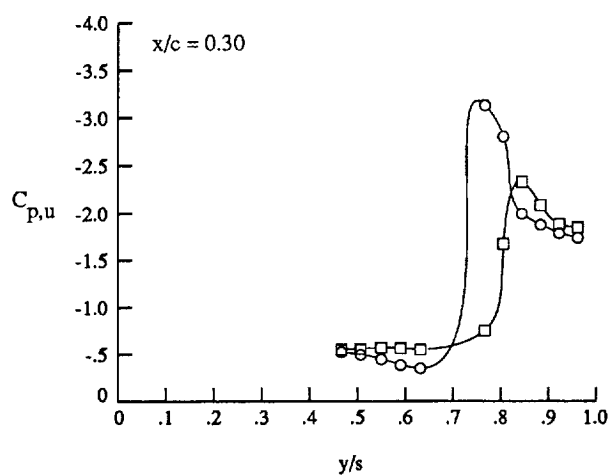
(a) Lift, drag, and pitching moment.

Figure 10. Effect of forebody strakes on longitudinal characteristics at $M_\infty = 0.40$ with $\delta_{LE} = 0^\circ$.



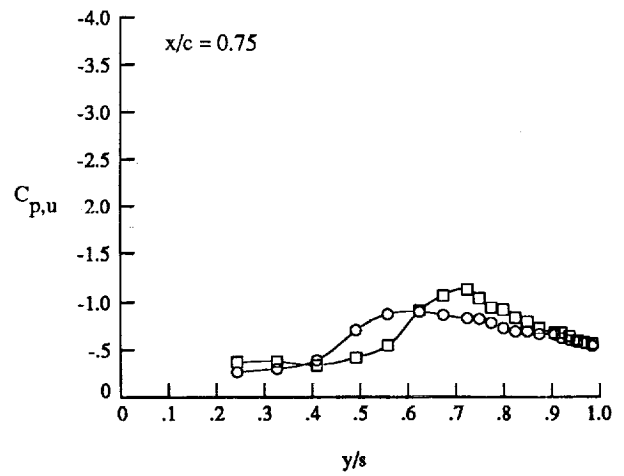
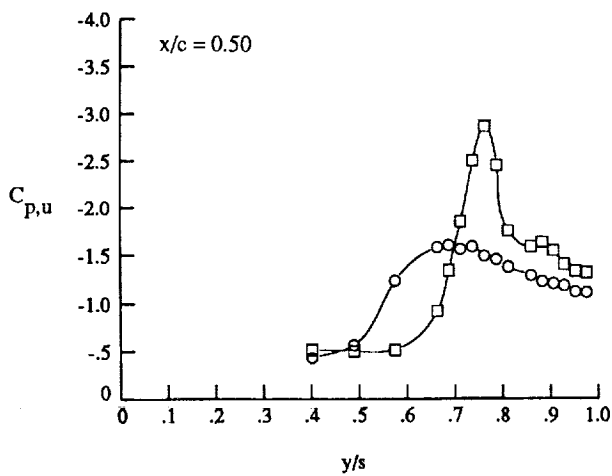
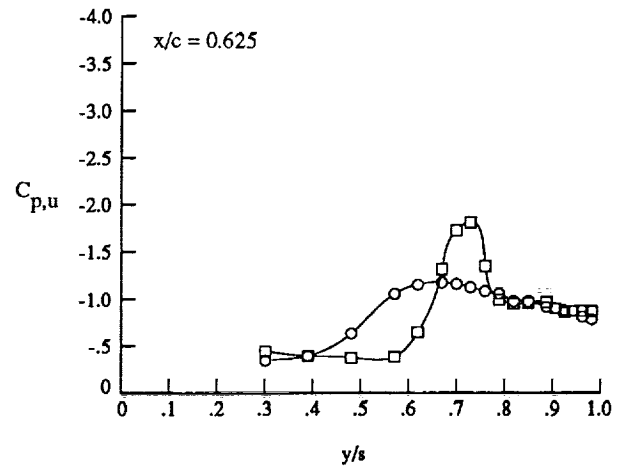
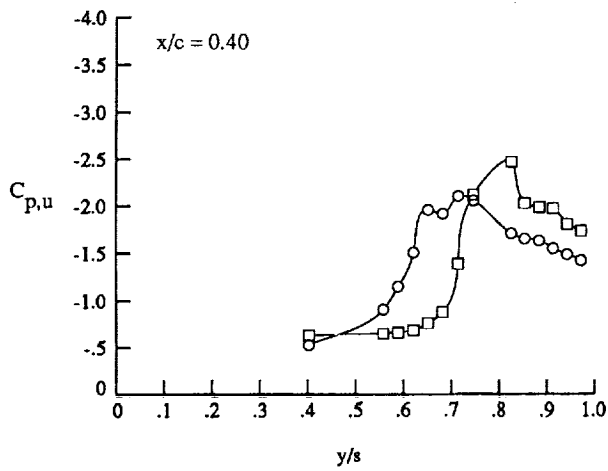
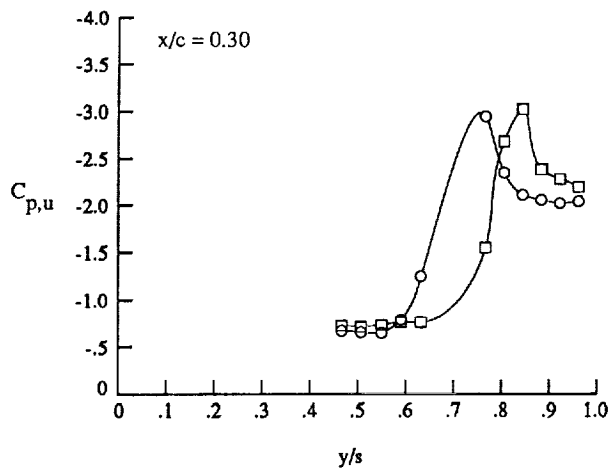
(b) Wing upper surface static pressure distributions at $\alpha \approx 12^\circ$.

Figure 10. Continued.



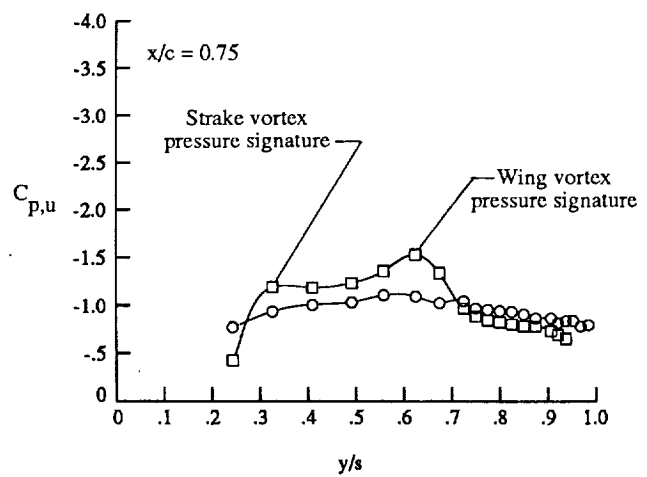
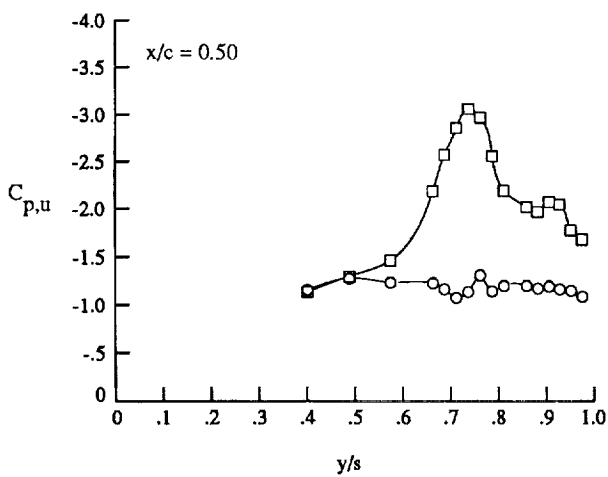
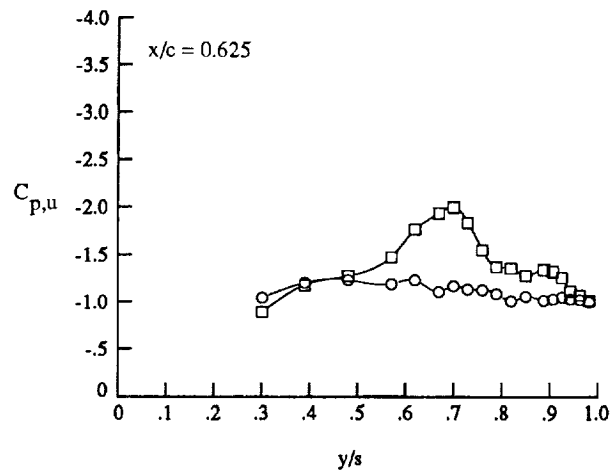
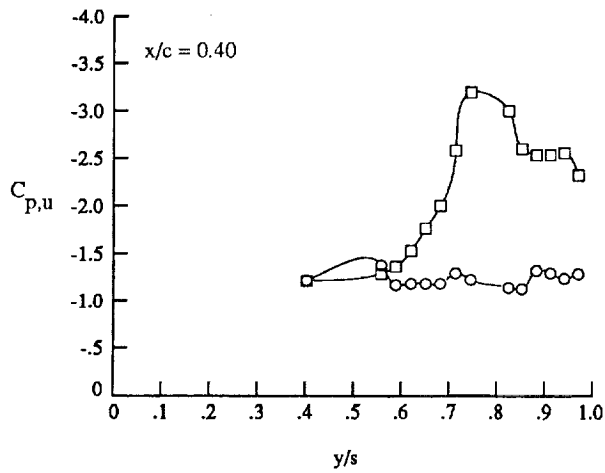
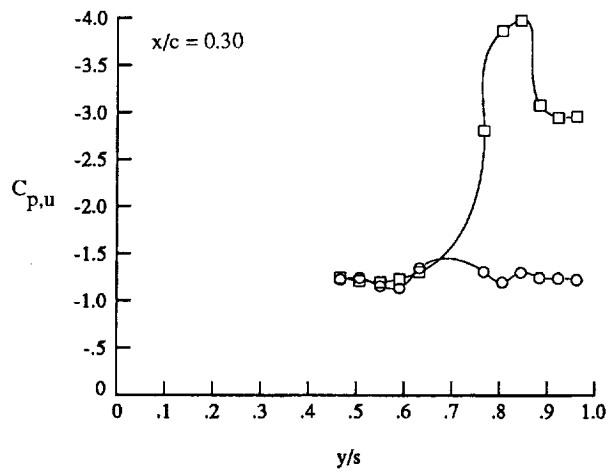
(c) Wing upper surface static pressure distributions at $\alpha \approx 16^\circ$.

Figure 10. Continued.



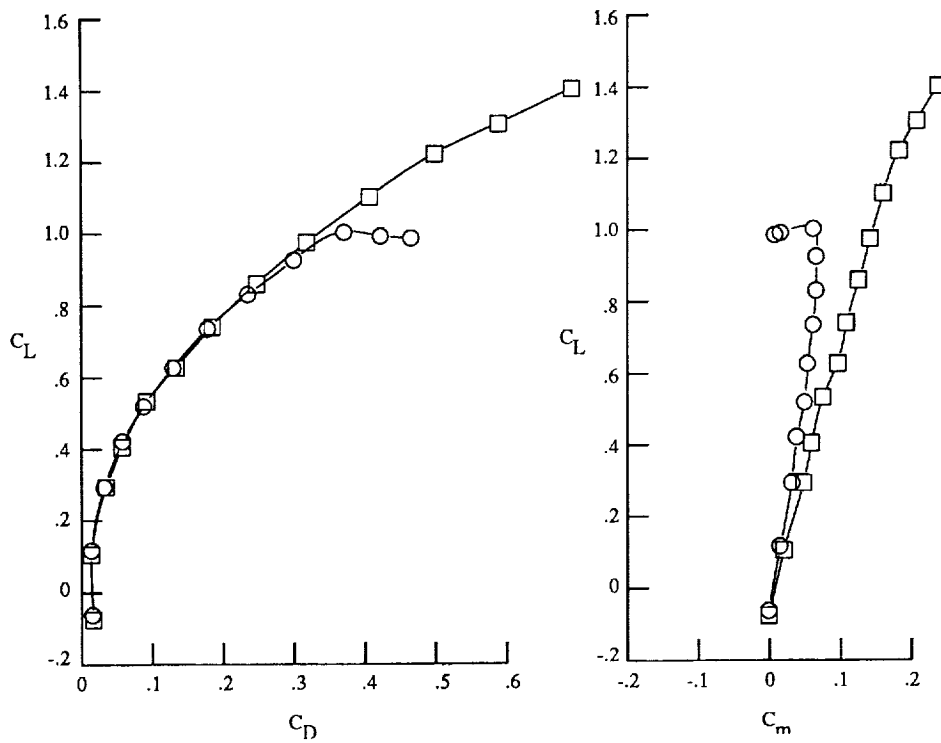
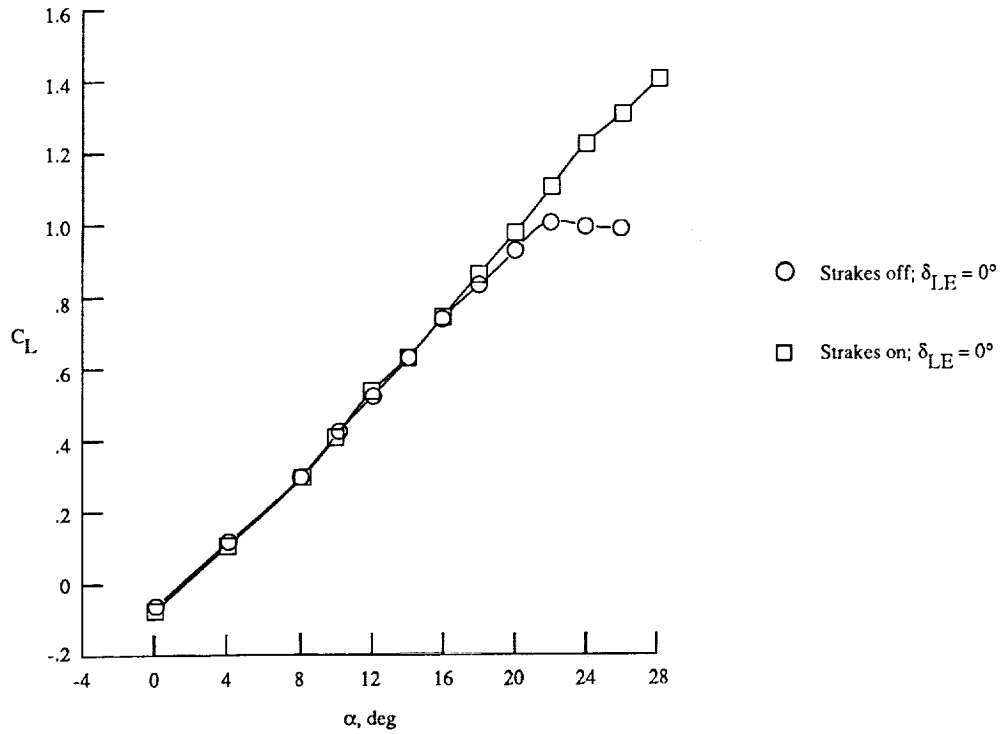
(d) Wing upper surface static pressure distributions at $\alpha \approx 20^\circ$.

Figure 10. Continued.



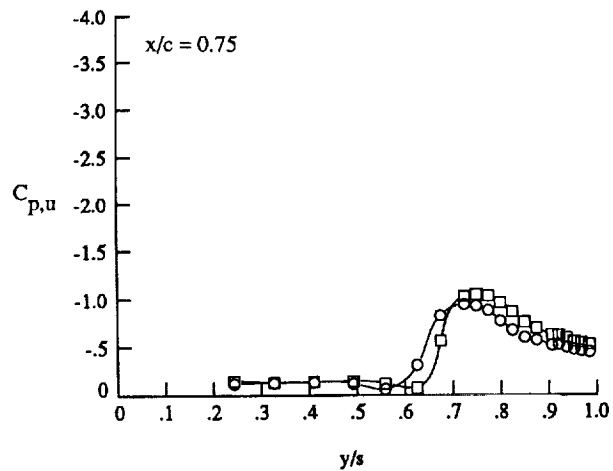
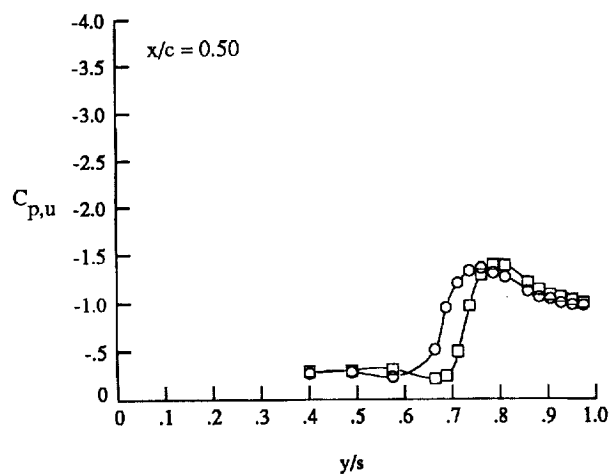
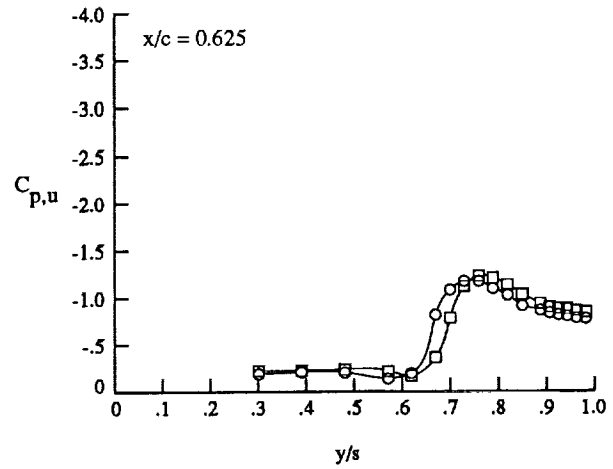
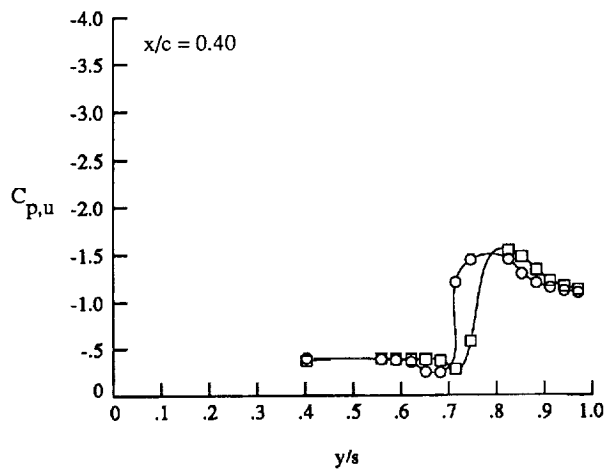
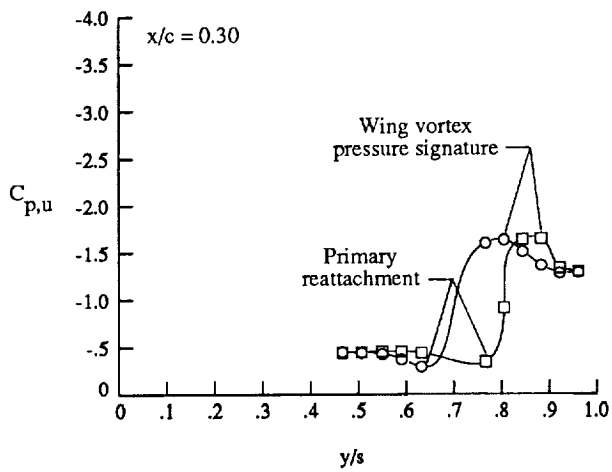
(e) Wing upper surface static pressure distributions at $\alpha \approx 26^\circ$.

Figure 10. Concluded.



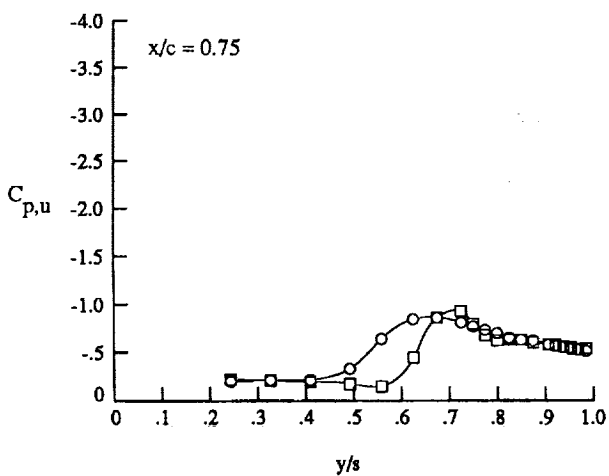
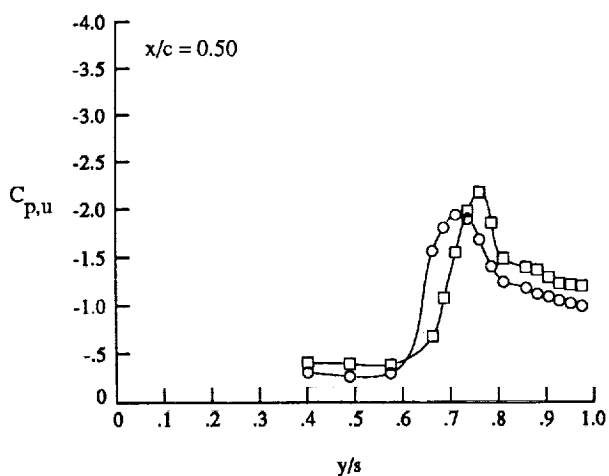
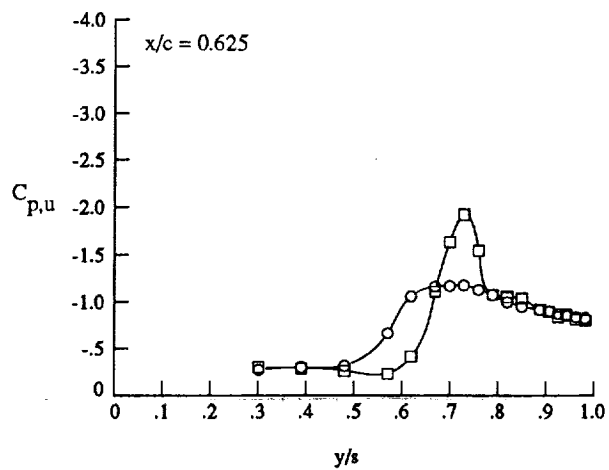
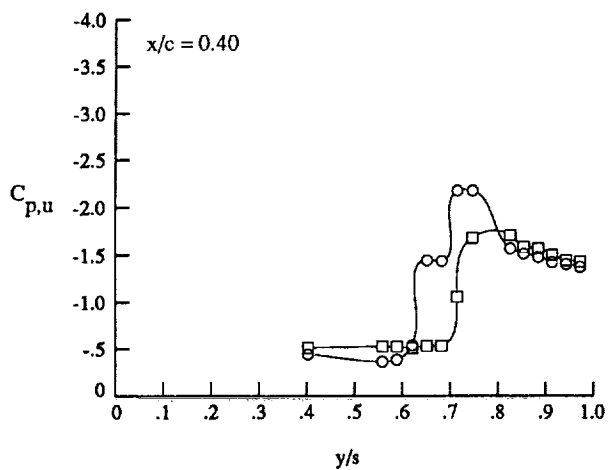
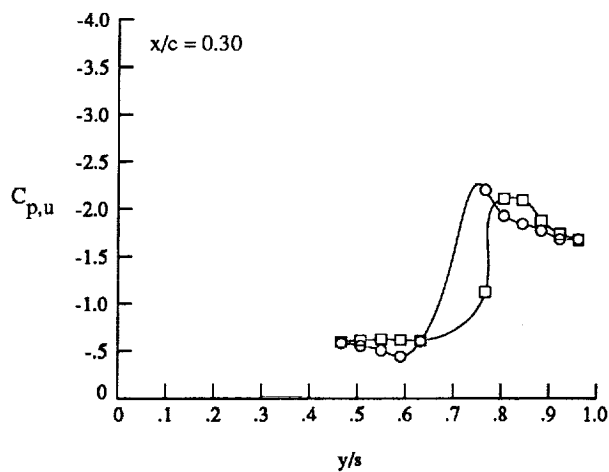
(a) Lift, drag, and pitching moment.

Figure 11. Effect of forebody strakes on longitudinal characteristics at $M_\infty = 0.60$ with $\delta_{LE} = 0^\circ$.



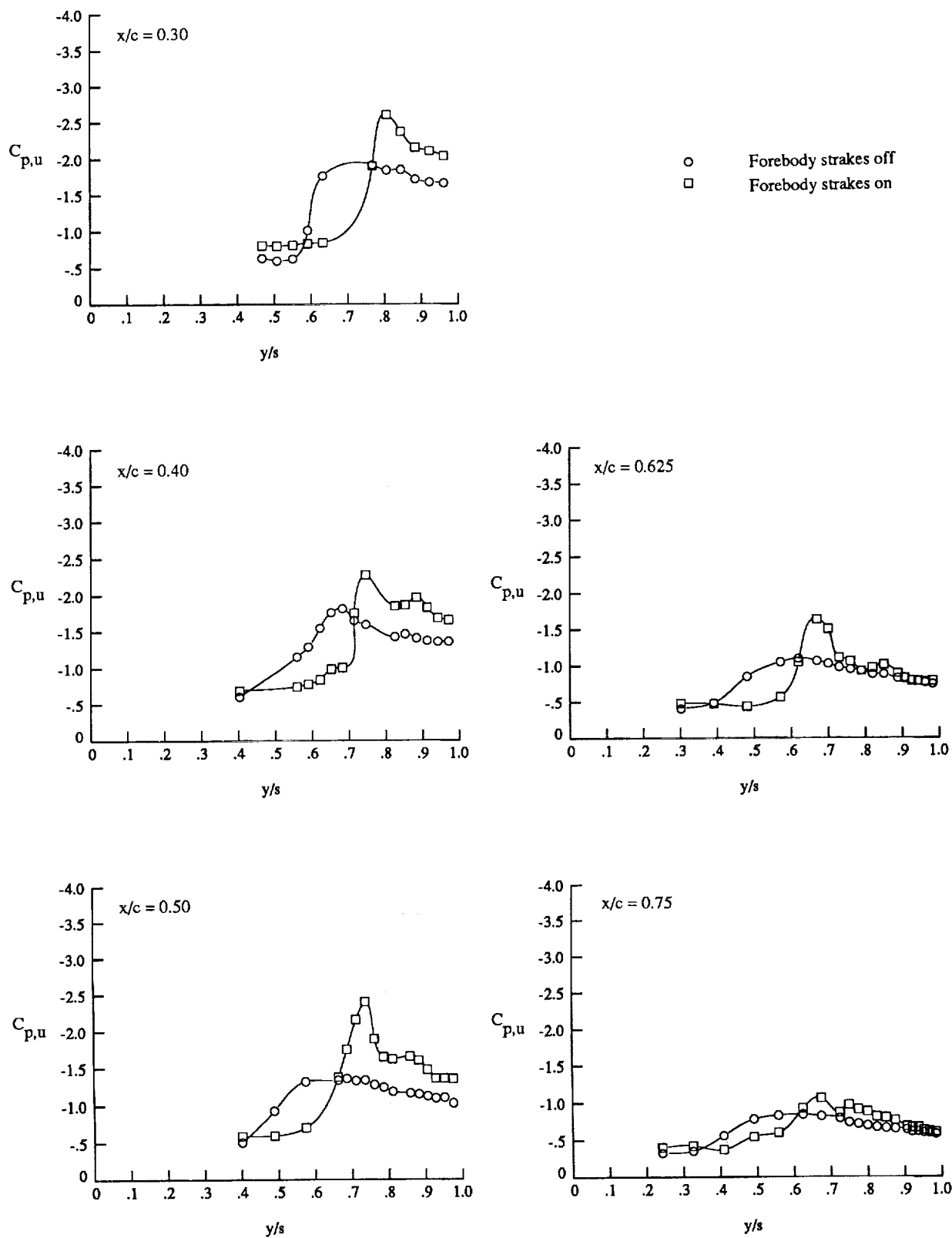
(b) Wing upper surface static pressure distributions at $\alpha \approx 12^\circ$.

Figure 11. Continued.



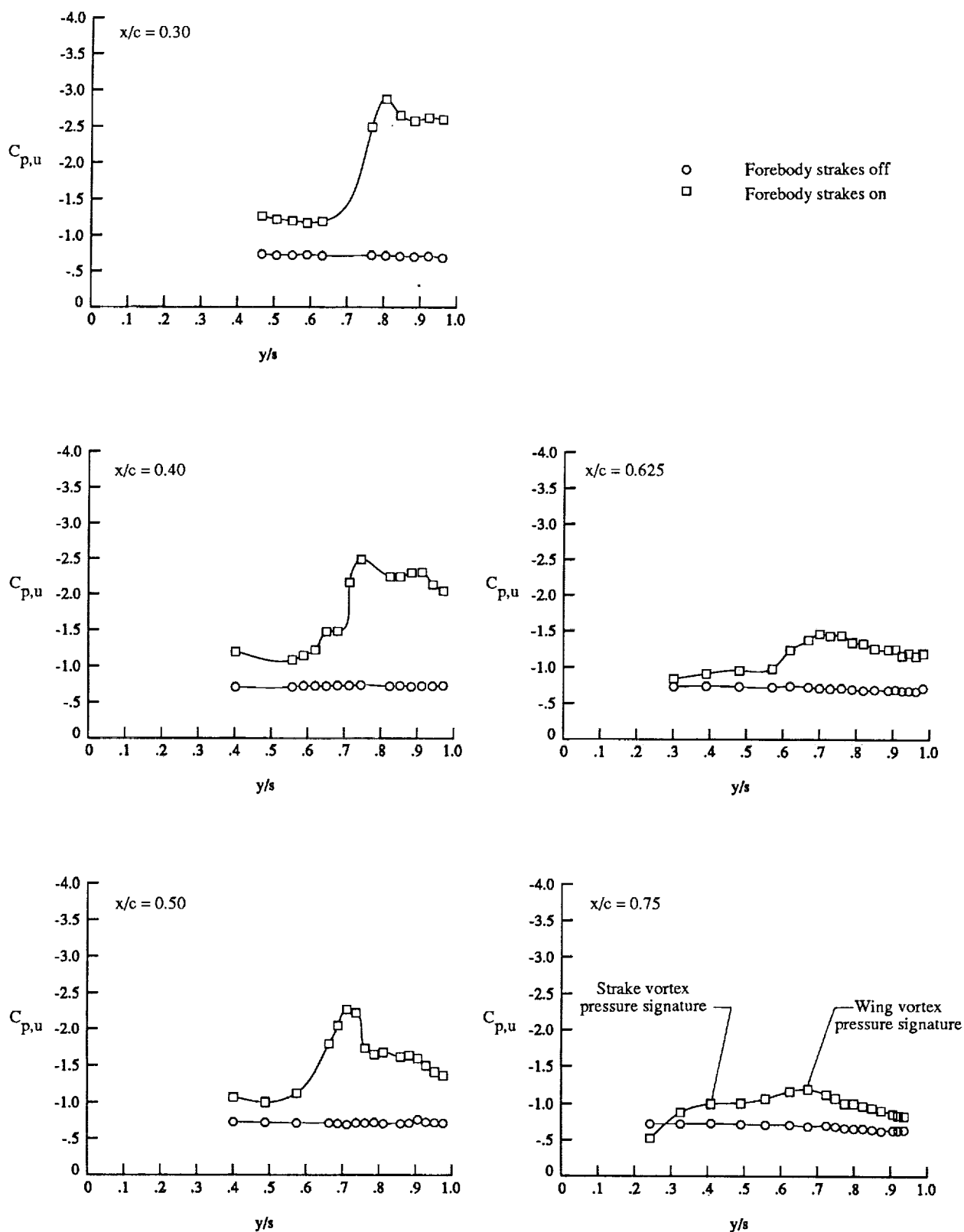
(c) Wing upper surface static pressure distributions at $\alpha \approx 16^\circ$.

Figure 11. Continued.



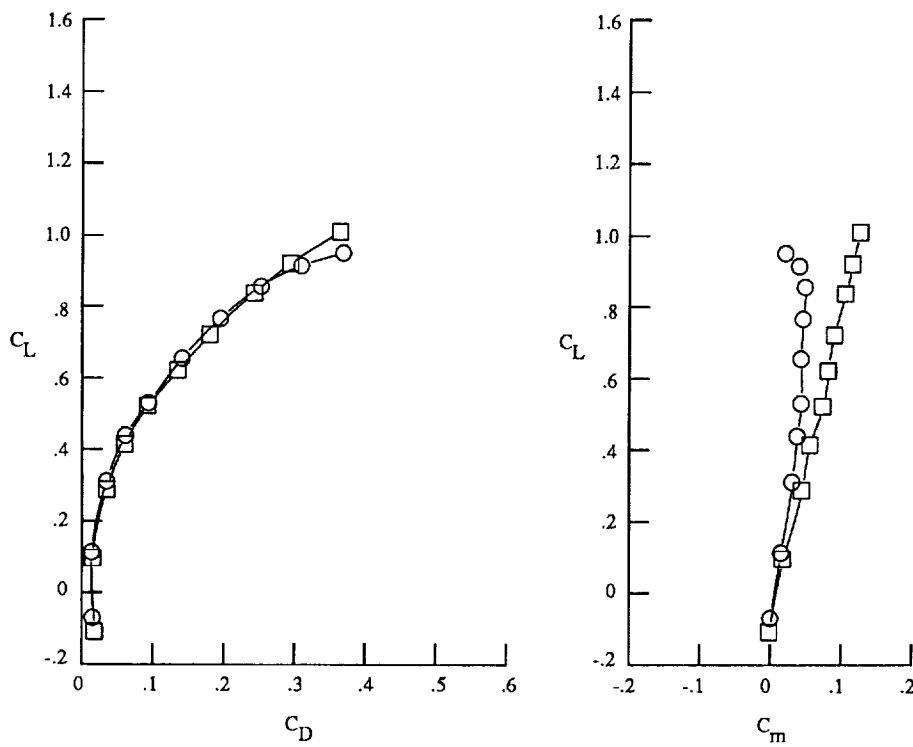
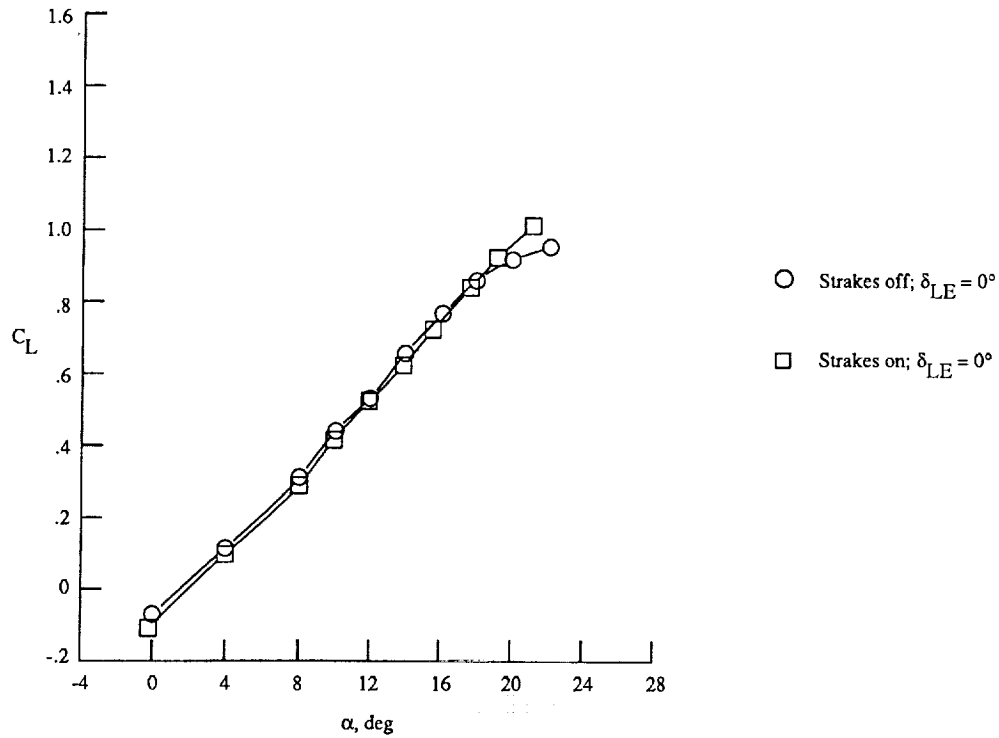
(d) Wing upper surface static pressure distributions at $\alpha \approx 20^\circ$.

Figure 11. Continued.



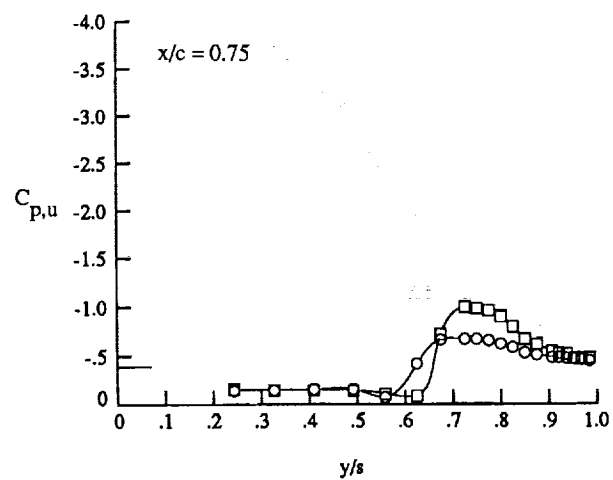
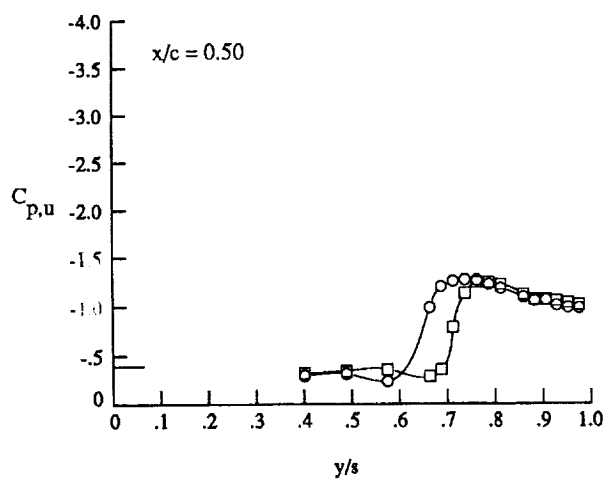
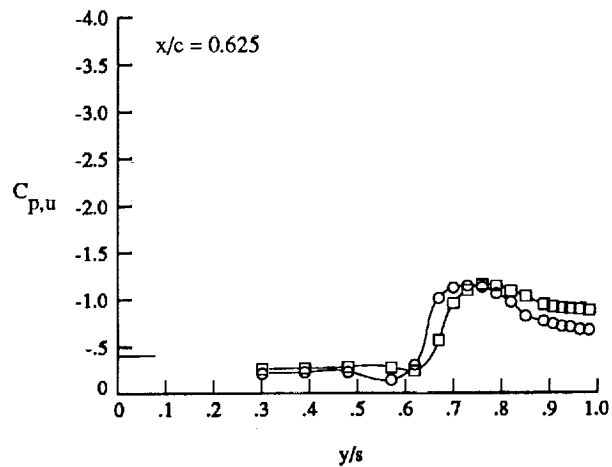
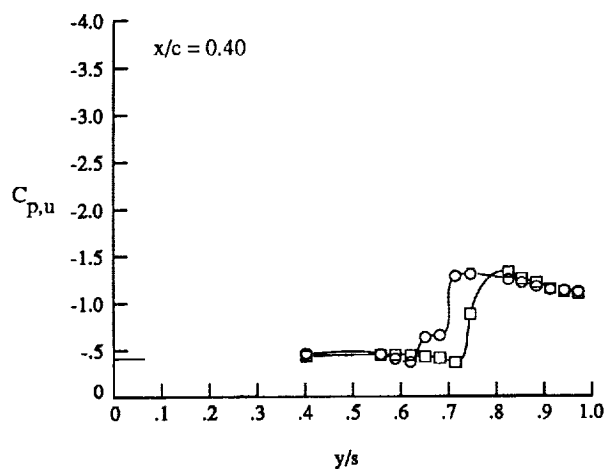
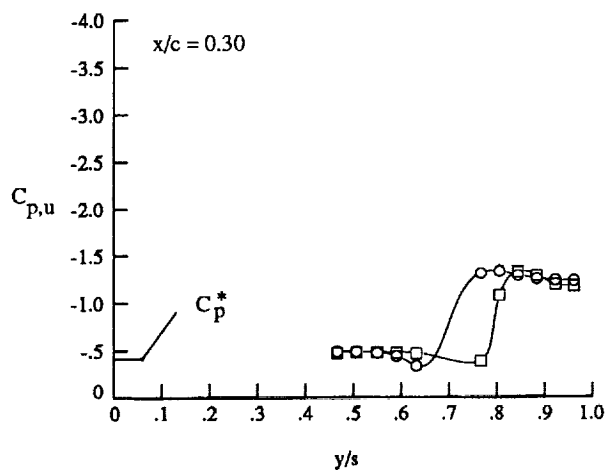
(e) Wing upper surface static pressure distributions at $\alpha \approx 26^\circ$.

Figure 11. Concluded.



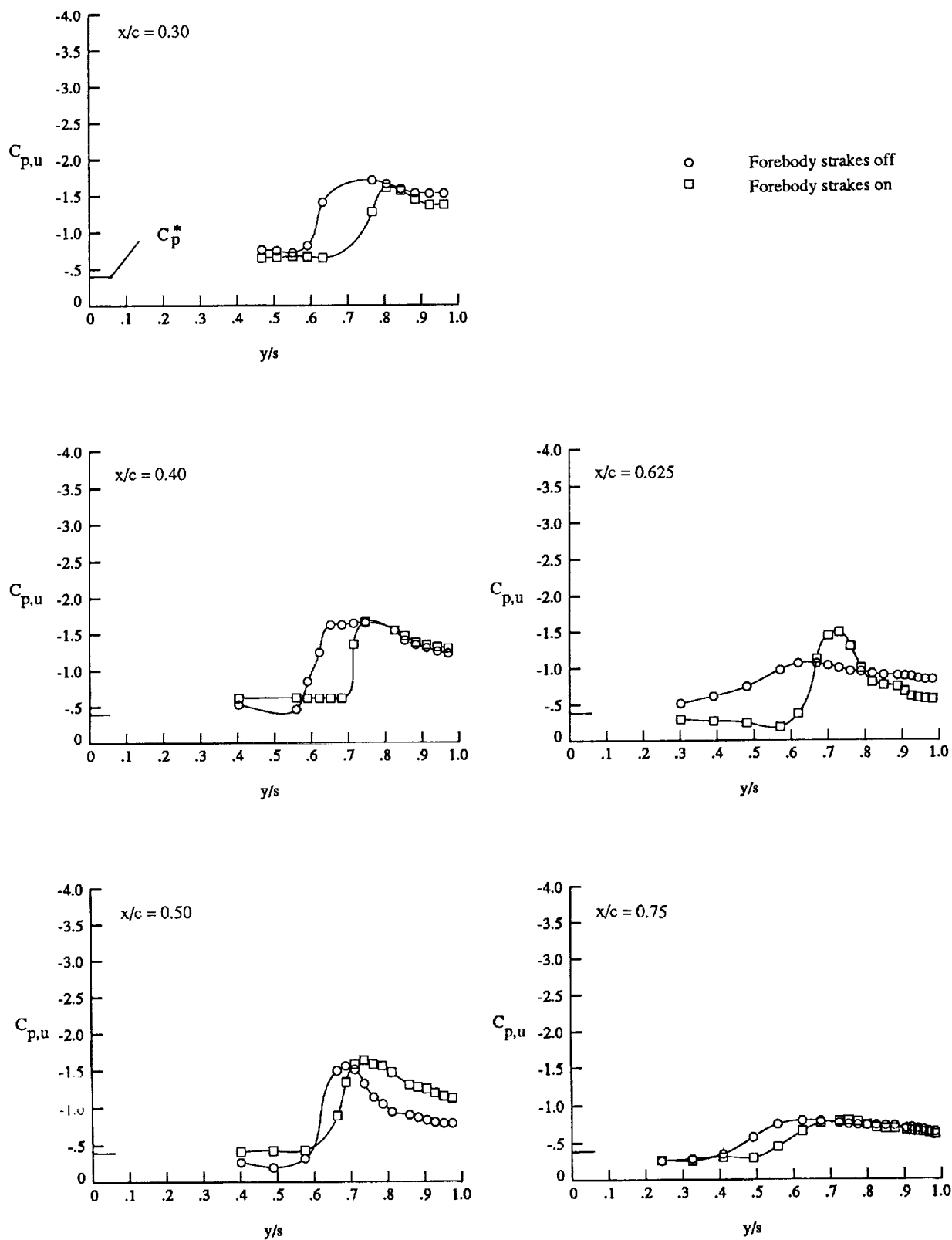
(a) Lift, drag, and pitching moment.

Figure 12. Effect of forebody strakes on longitudinal characteristics at $M_\infty = 0.80$ with $\delta_{LE} = 0^\circ$.



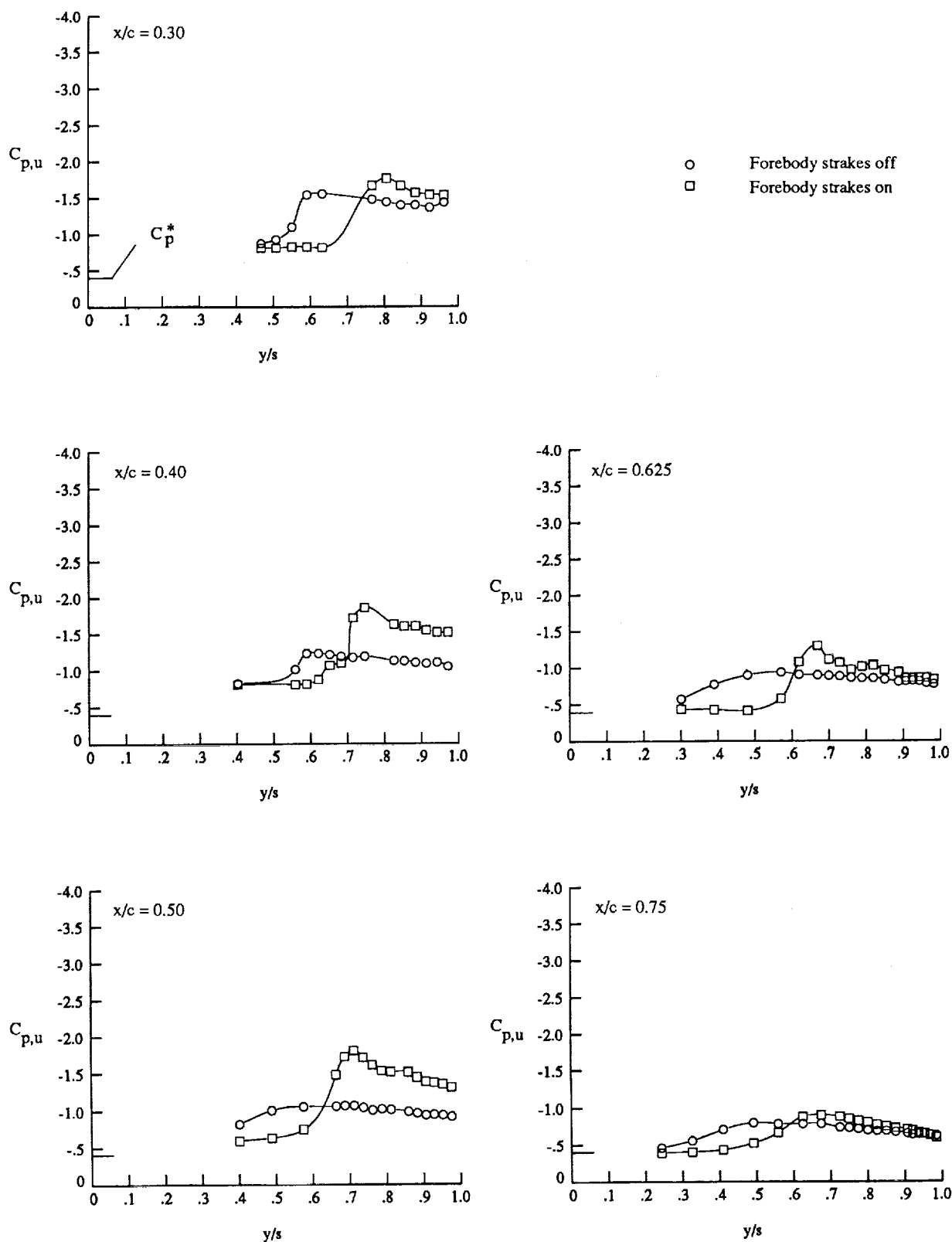
(b) Wing upper surface static pressure distributions at $\alpha \approx 12^\circ$.

Figure 12. Continued.



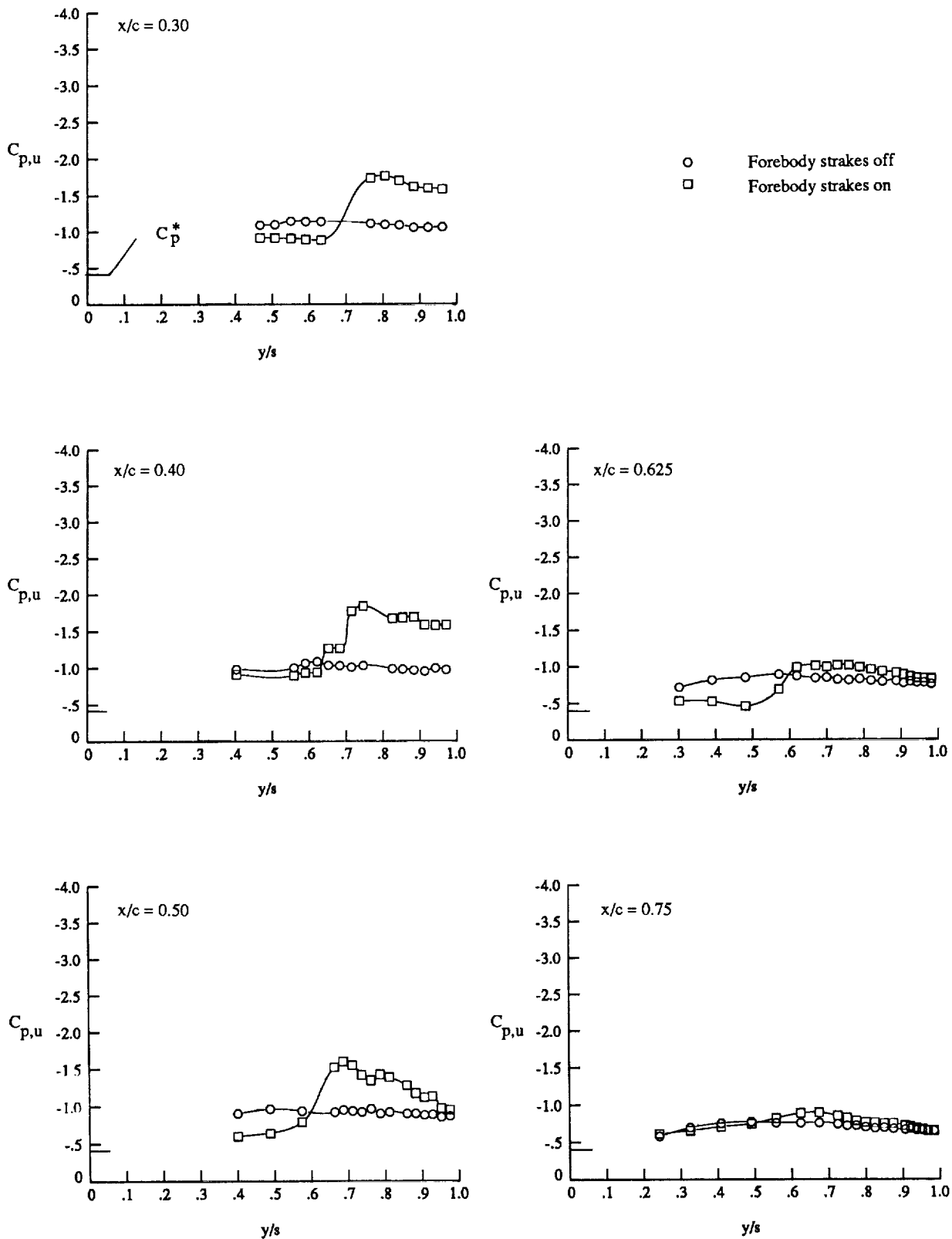
(c) Wing upper surface static pressure distributions at $\alpha \approx 16^\circ$.

Figure 12. Continued.



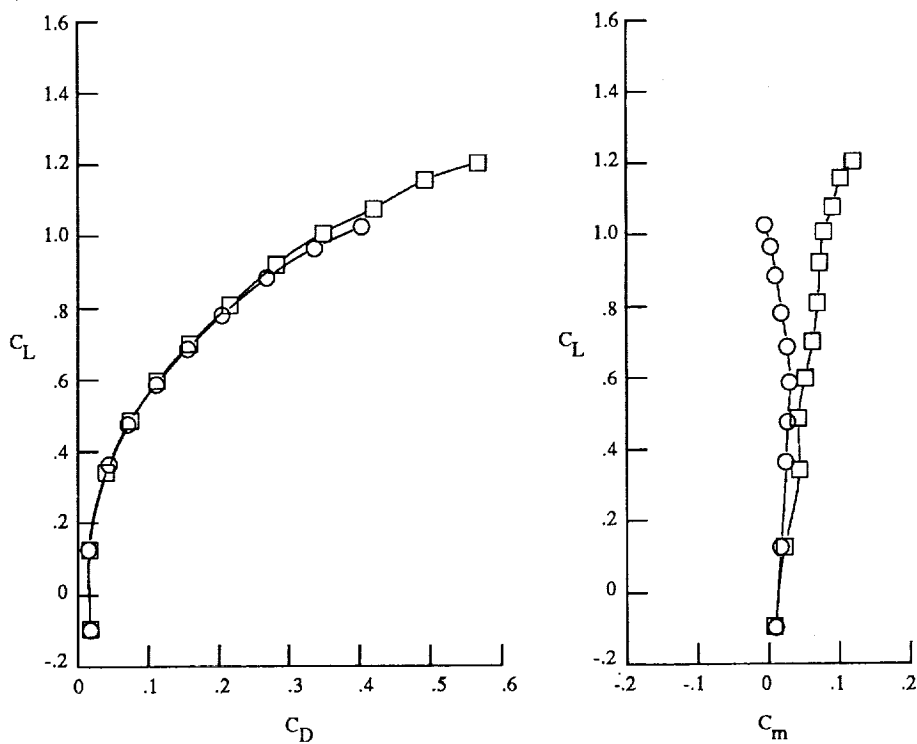
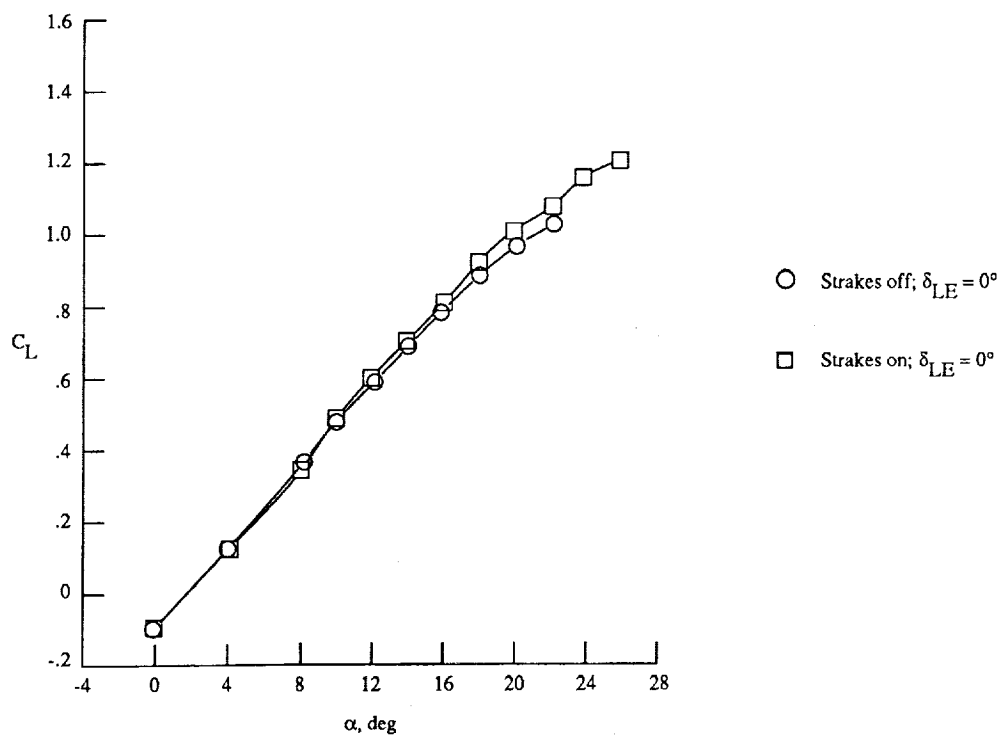
(d) Wing upper surface static pressure distributions at $\alpha \approx 20^\circ$.

Figure 12. Continued.



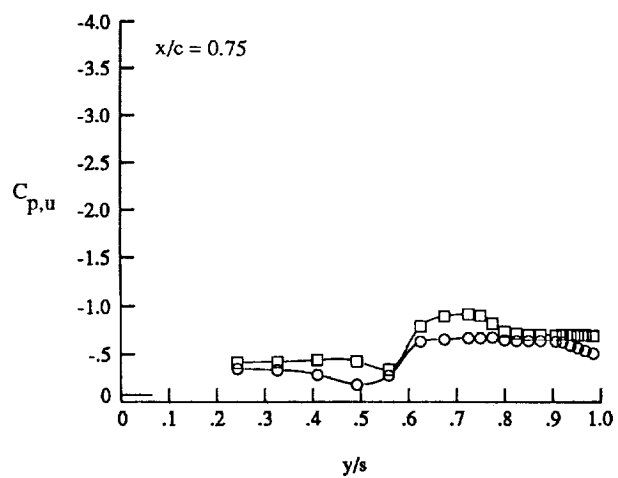
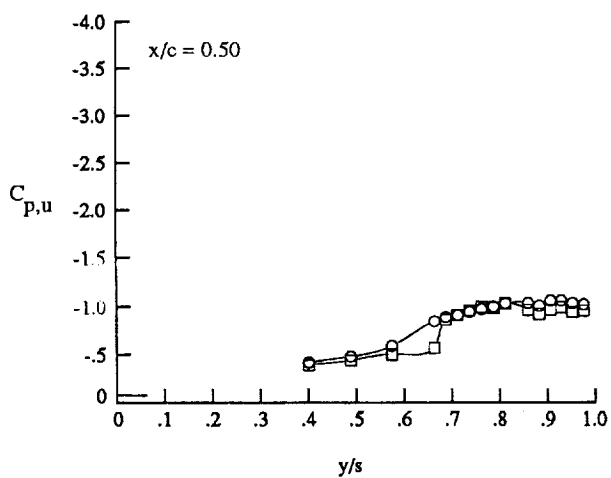
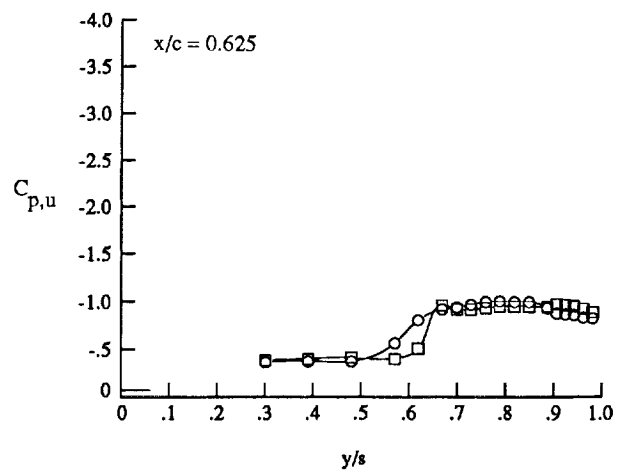
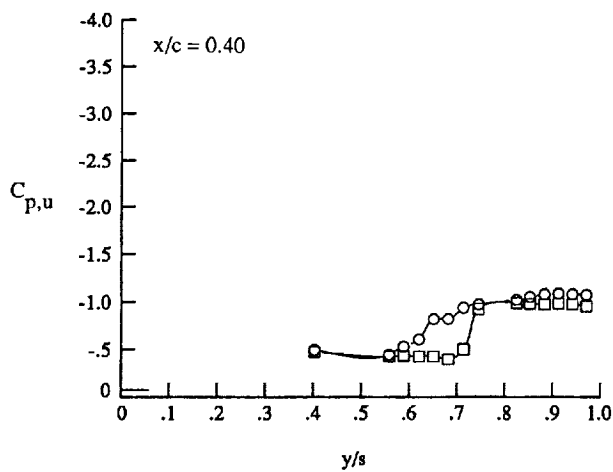
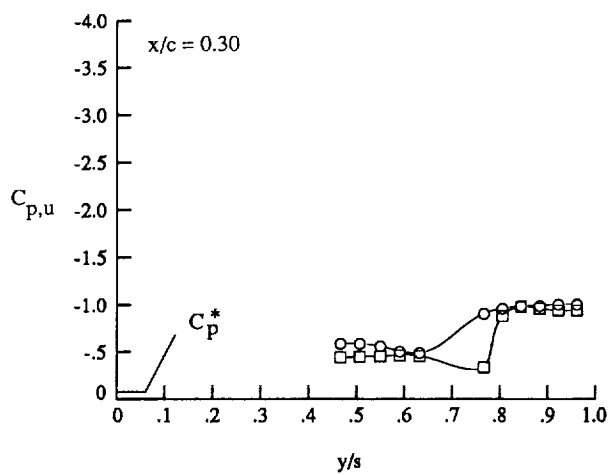
(e) Wing upper surface static pressure distributions at $\alpha \approx 22^\circ$ (strakes off) and $\alpha \approx 21^\circ$ (strakes on).

Figure 12. Concluded.



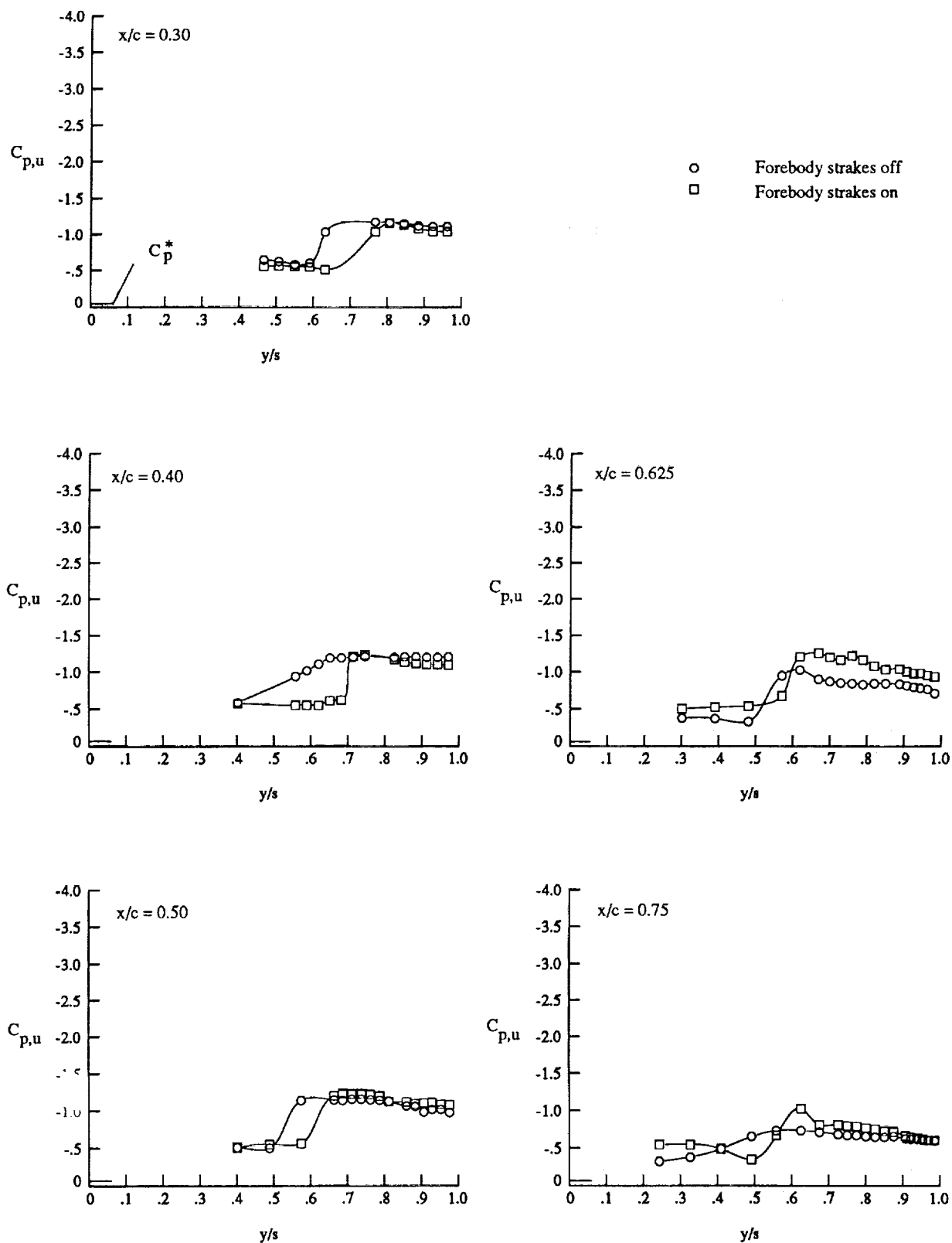
(a) Lift, drag, and pitching moment.

Figure 13. Effect of forebody strakes on longitudinal characteristics at $M_\infty = 0.95$ with $\delta_{LE} = 0^\circ$.



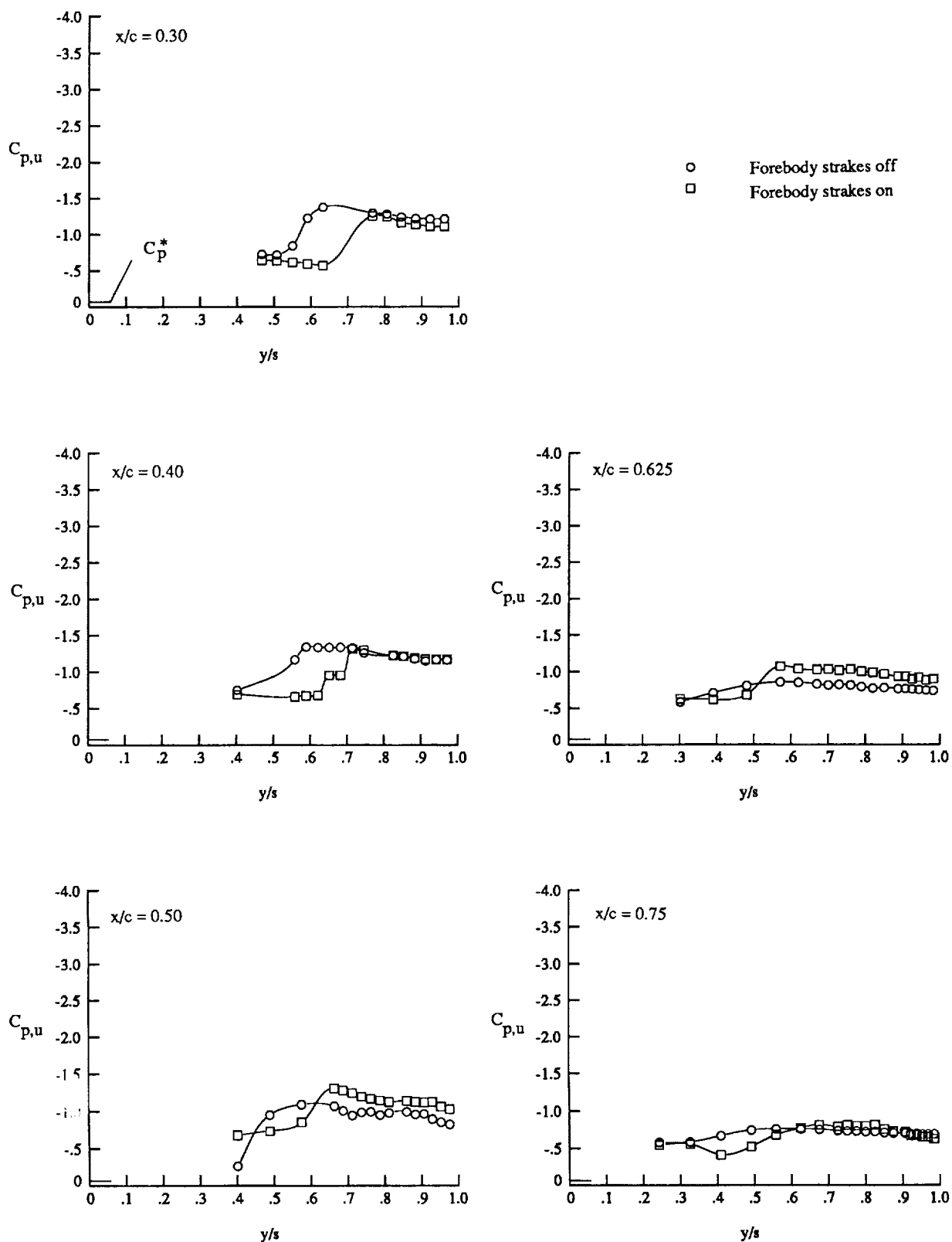
(b) Wing upper surface static pressure distributions at $\alpha \approx 12^\circ$.

Figure 13. Continued.



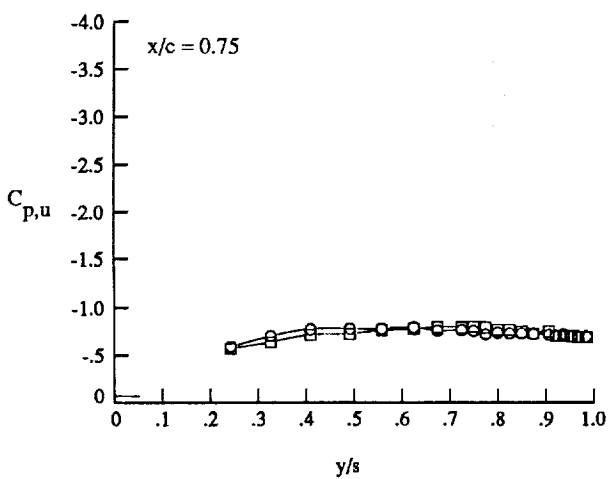
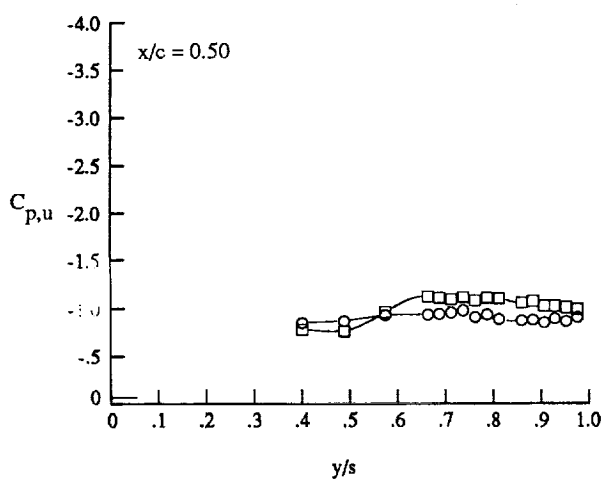
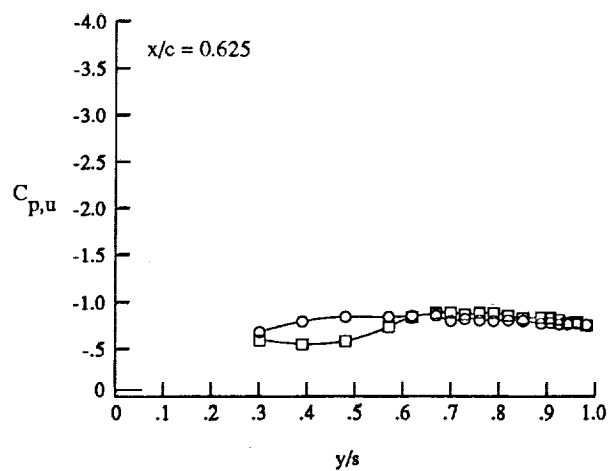
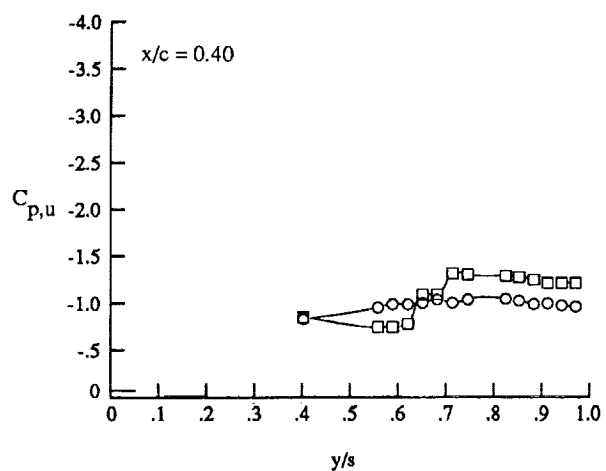
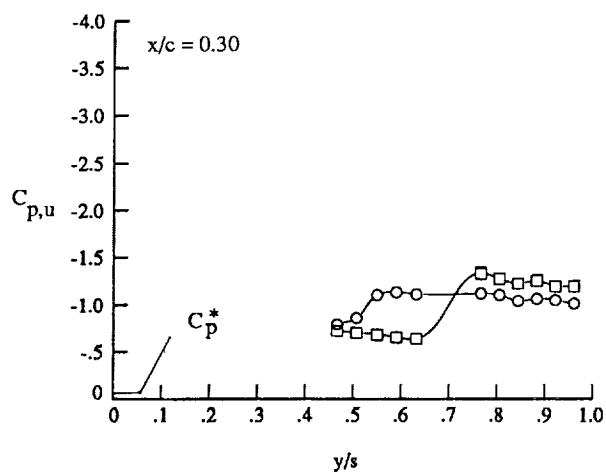
(c) Wing upper surface static pressure distributions at $\alpha \approx 16^\circ$.

Figure 13. Continued.



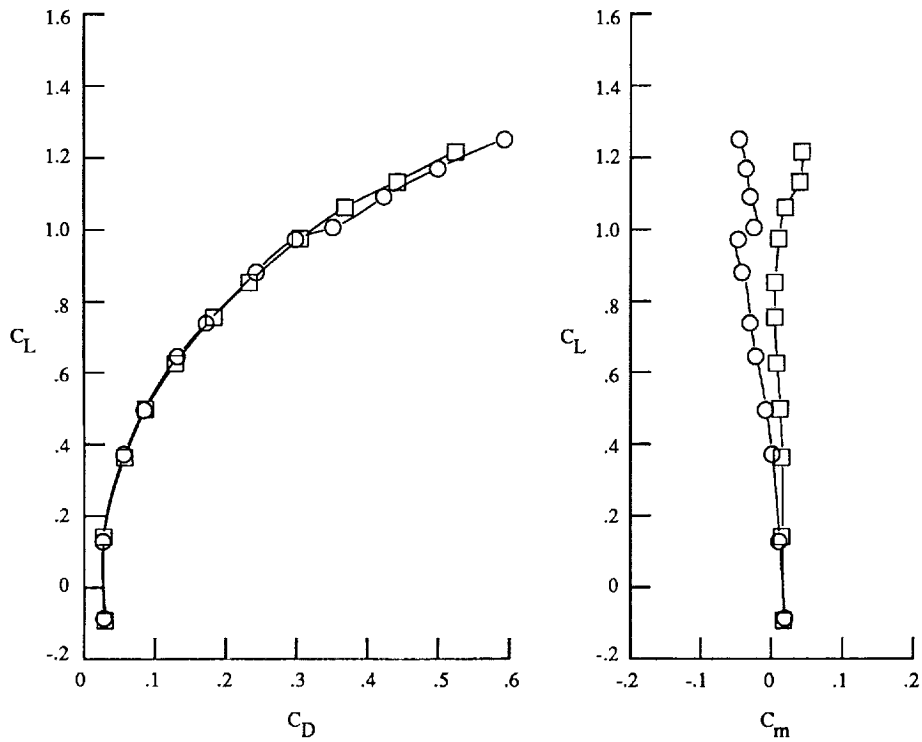
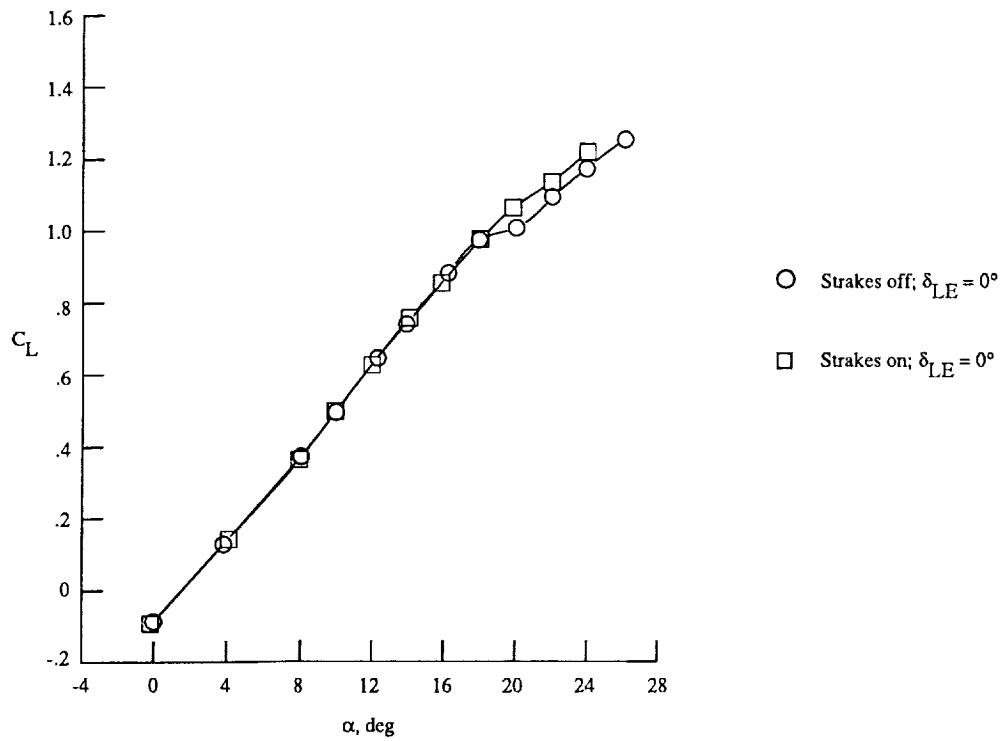
(d) Wing upper surface static pressure distributions at $\alpha \approx 20^\circ$.

Figure 13. Continued.



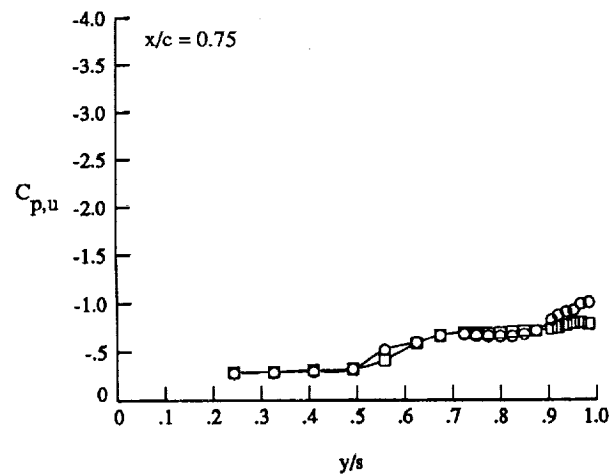
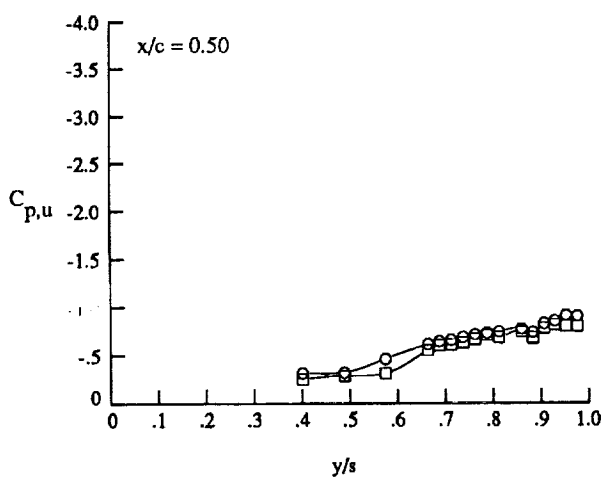
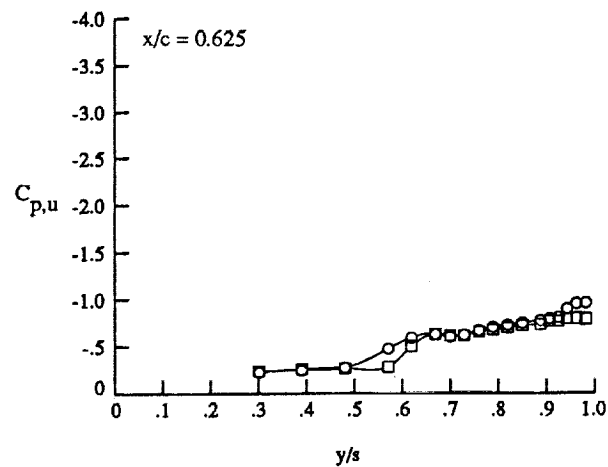
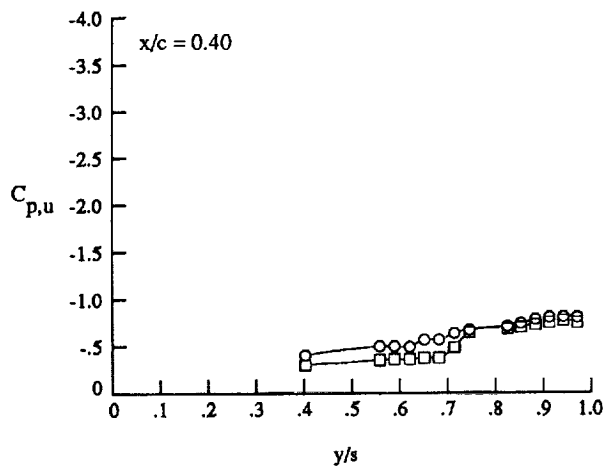
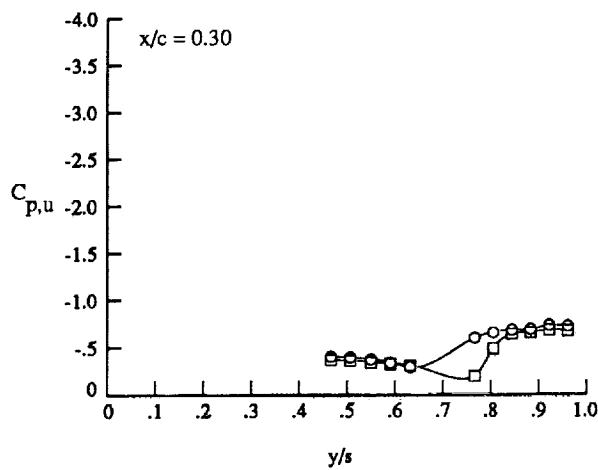
(c) Wing upper surface static pressure distributions at $\alpha \approx 22^\circ$.

Figure 13. Concluded.



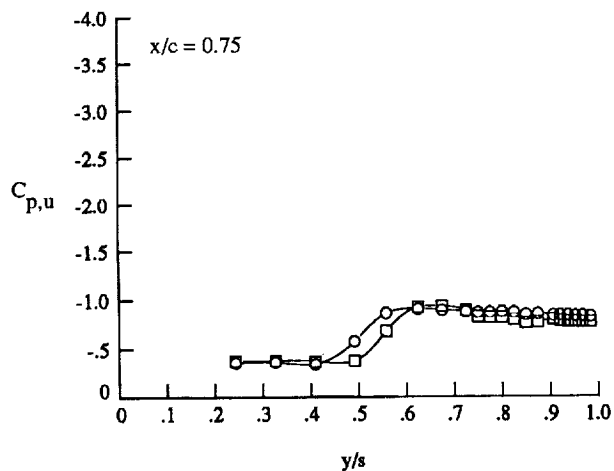
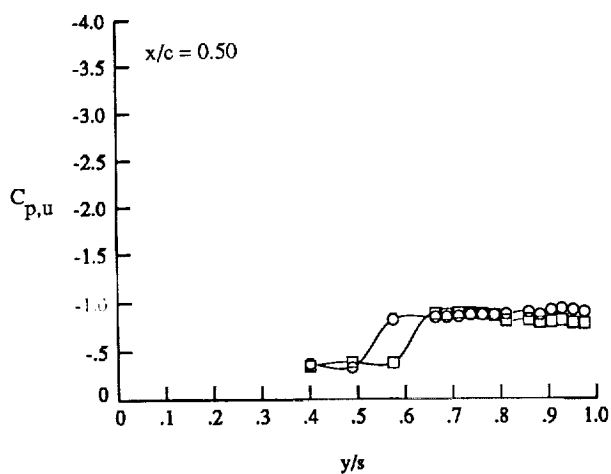
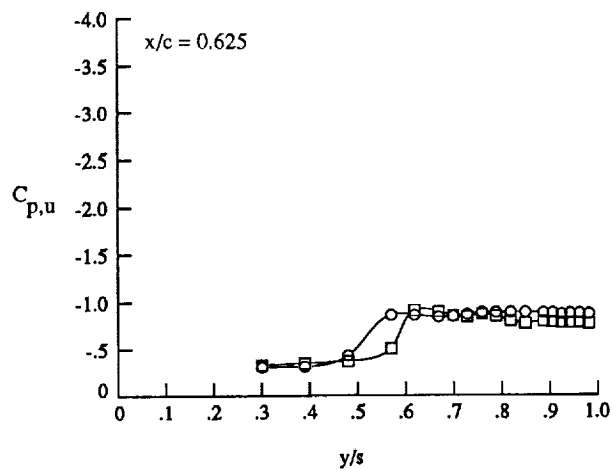
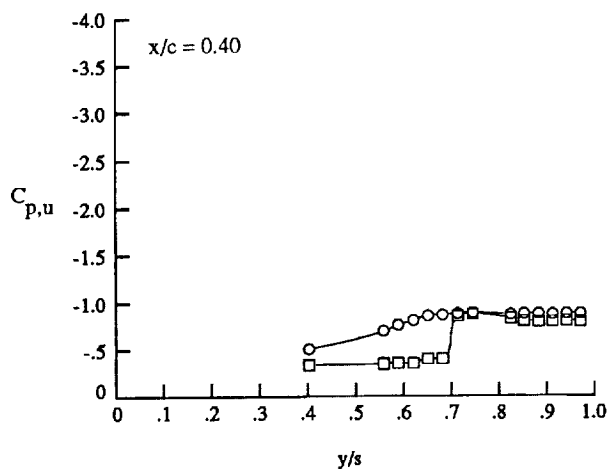
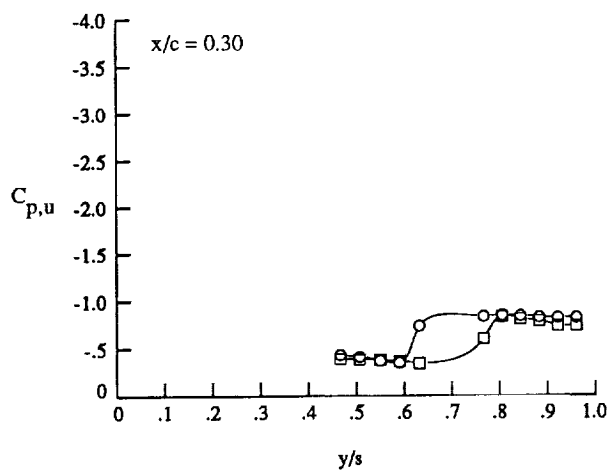
(a) Lift, drag, and pitching moment.

Figure 14. Effect of forebody strakes on longitudinal characteristics at $M_\infty = 1.10$ with $\delta_{LE} = 0^\circ$.



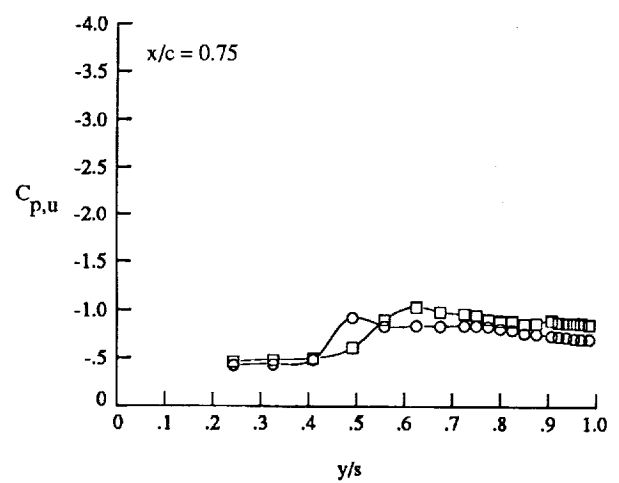
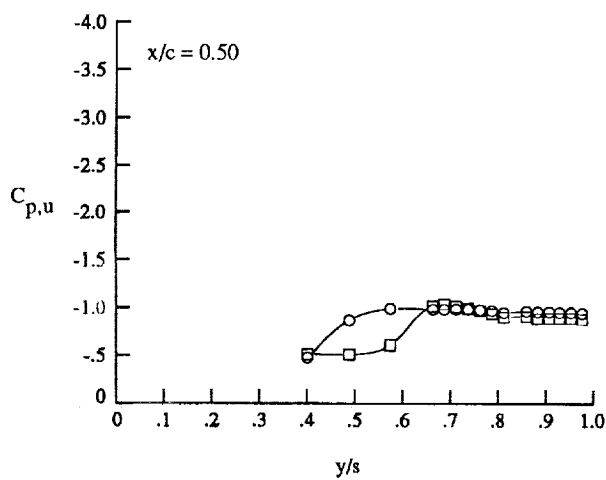
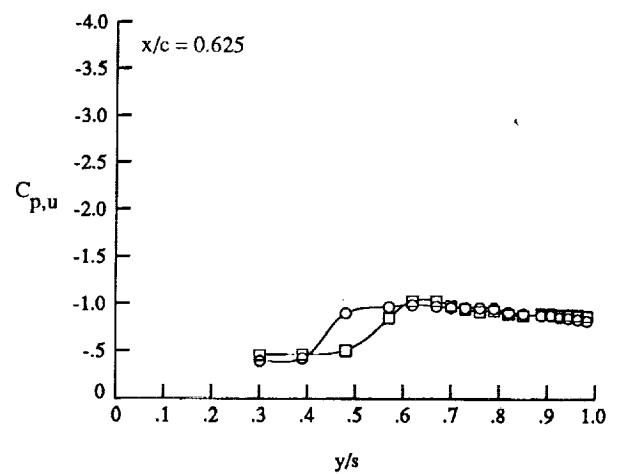
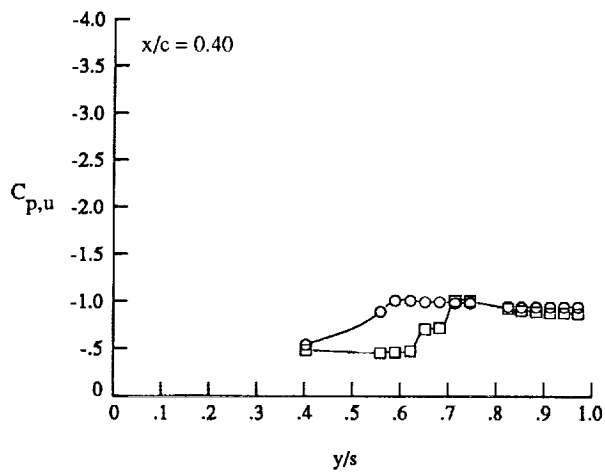
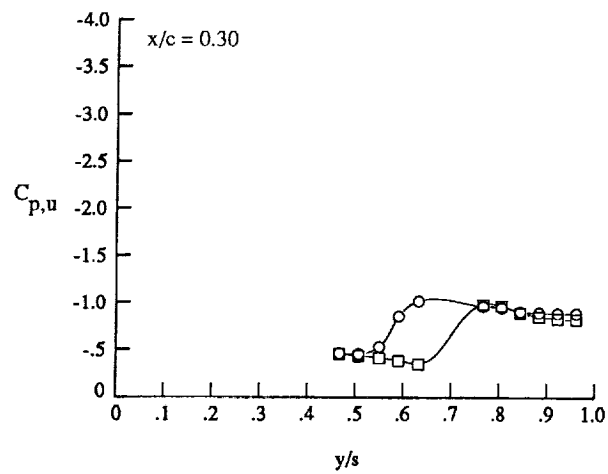
(b) Wing upper surface static pressure distributions at $\alpha \approx 12^\circ$.

Figure 14. Continued.



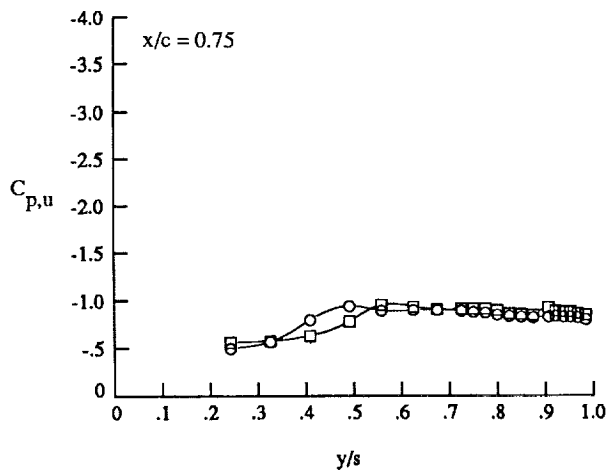
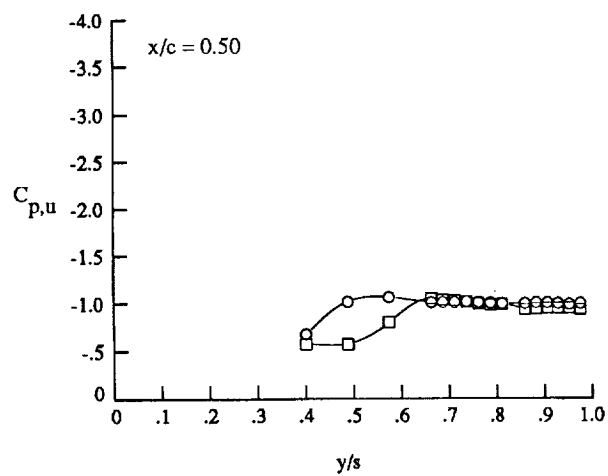
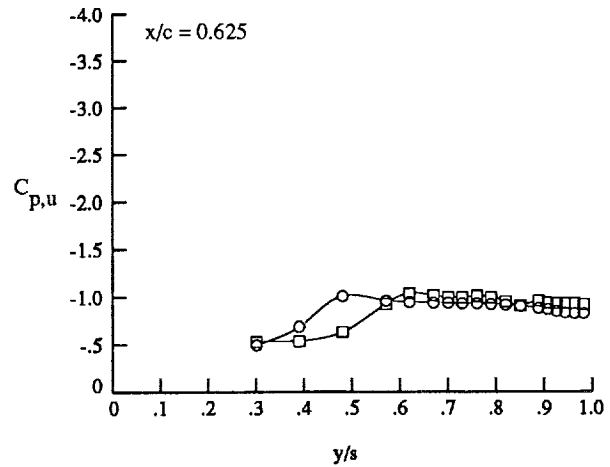
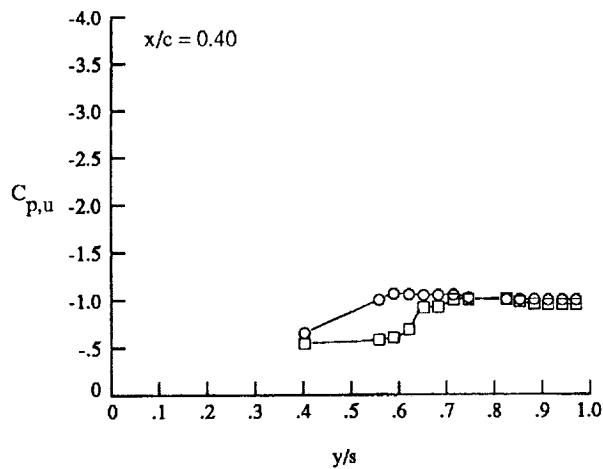
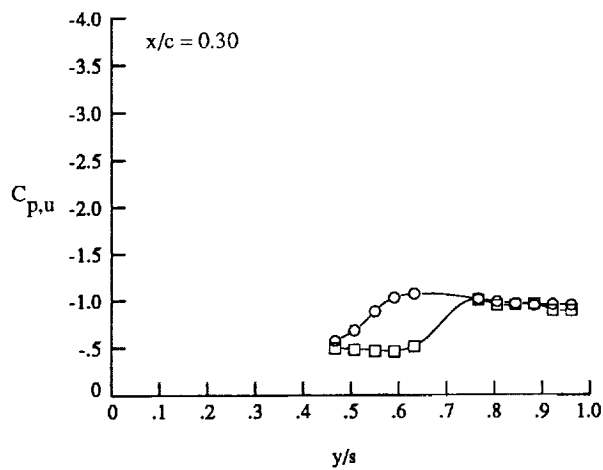
(c) Wing upper surface static pressure distributions at $\alpha \approx 16^\circ$.

Figure 14. Continued.



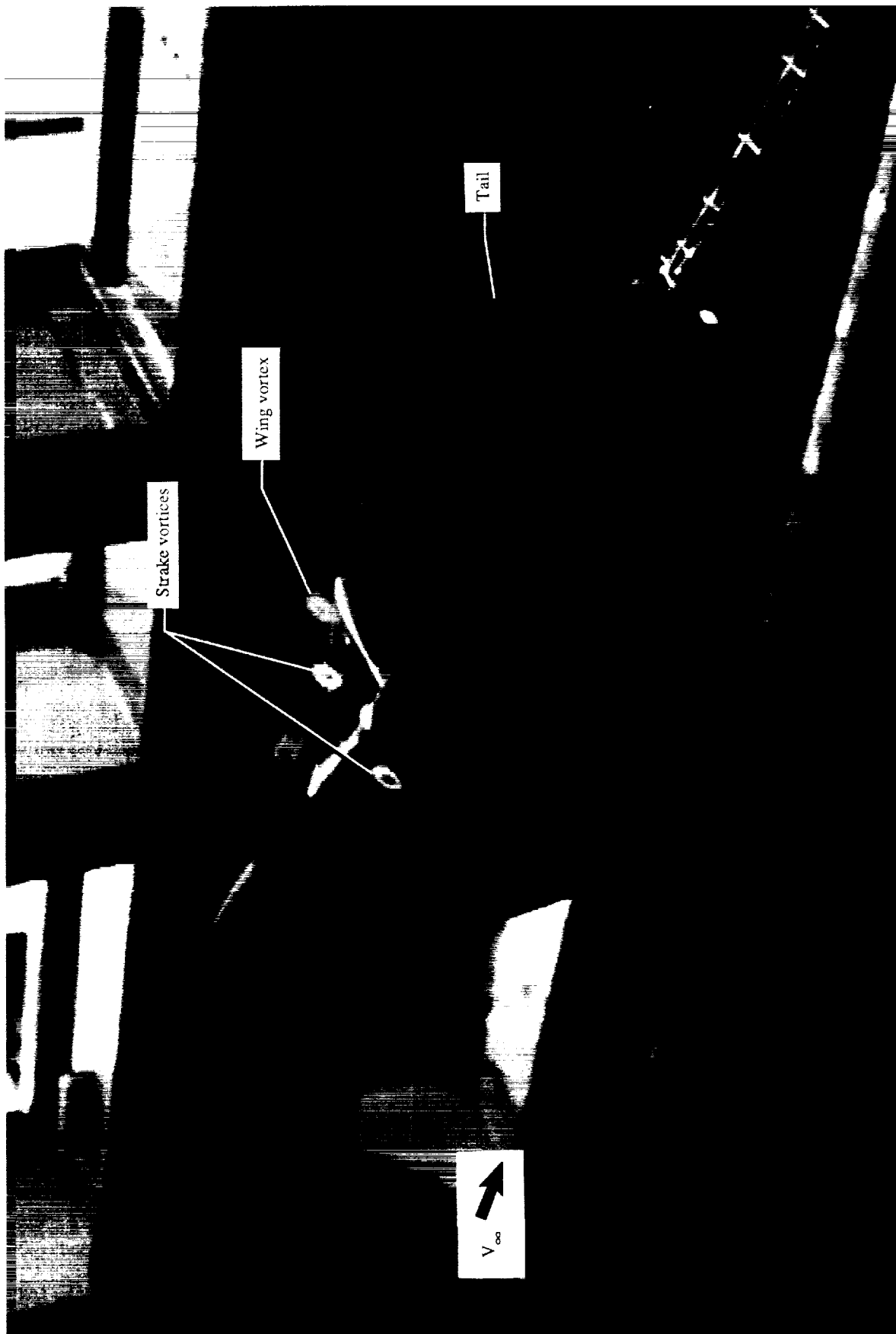
(d) Wing upper surface static pressure distributions at $\alpha \approx 20^\circ$.

Figure 14. Continued.



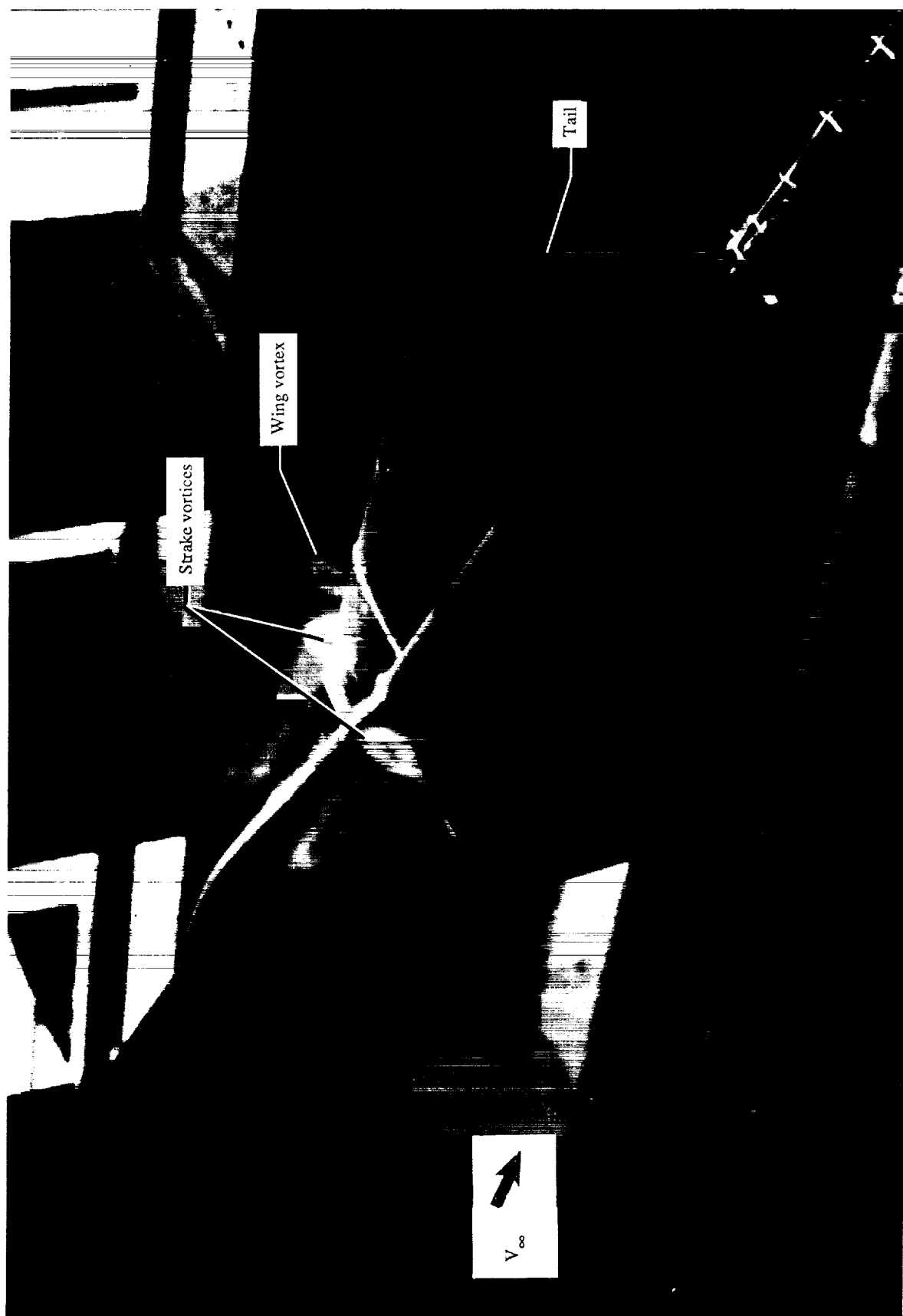
(c) Wing upper surface static pressure distributions at $\alpha \approx 24^\circ$.

Figure 14. Concluded.



(a) $M_\infty = 0.40$; $\alpha \approx 22^\circ$; $x/c = 0.50$; strakes on; left three-quarter rear view.

Figure 15. Laser vapor screen flow visualization results for $\delta_{LE} = 0^\circ$.



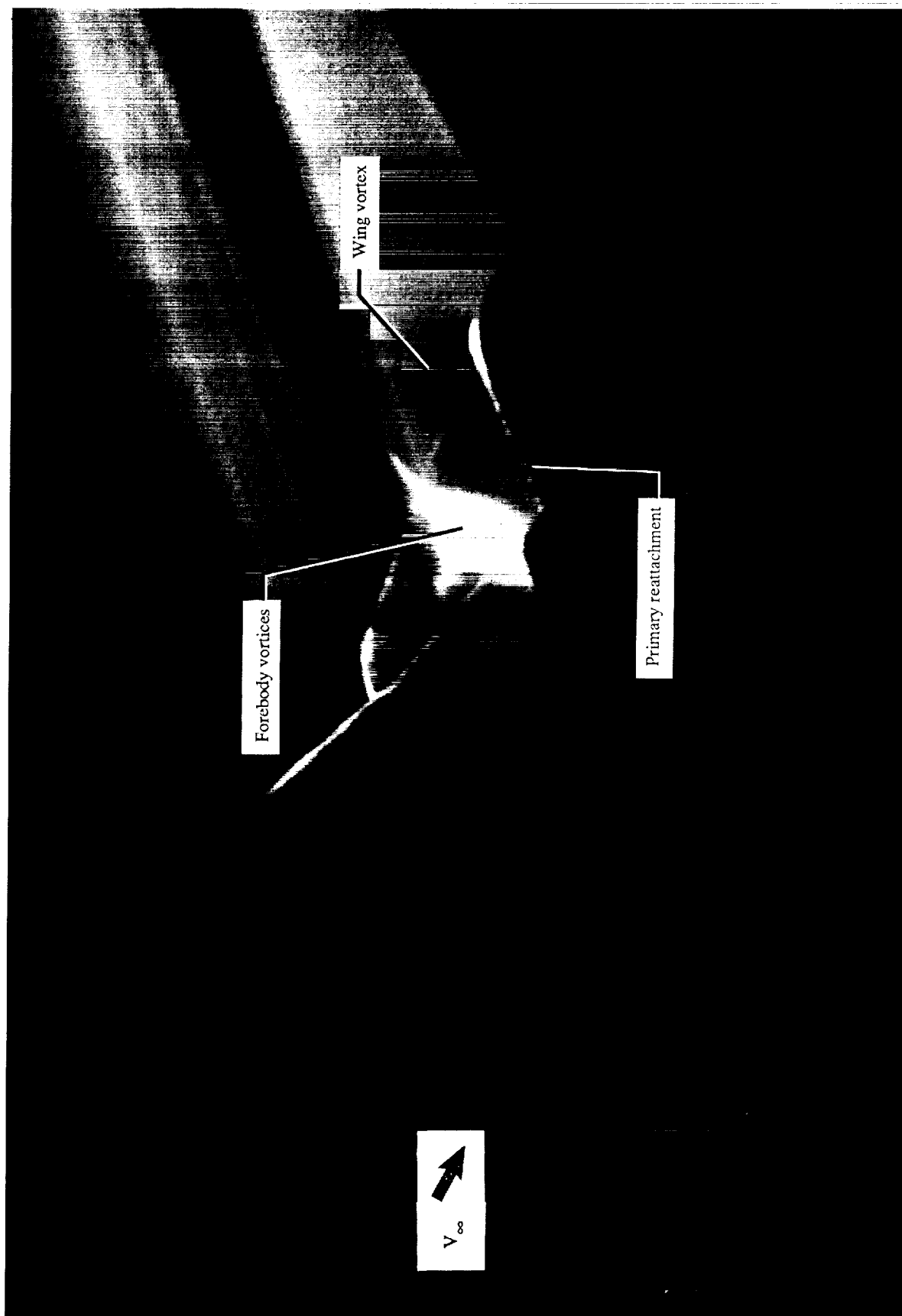
(b) $M_\infty = 0.40$; $\alpha \approx 26^\circ$; $x/c = 0.50$; strakes on; left three-quarter rear view.

Figure 15. Continued.



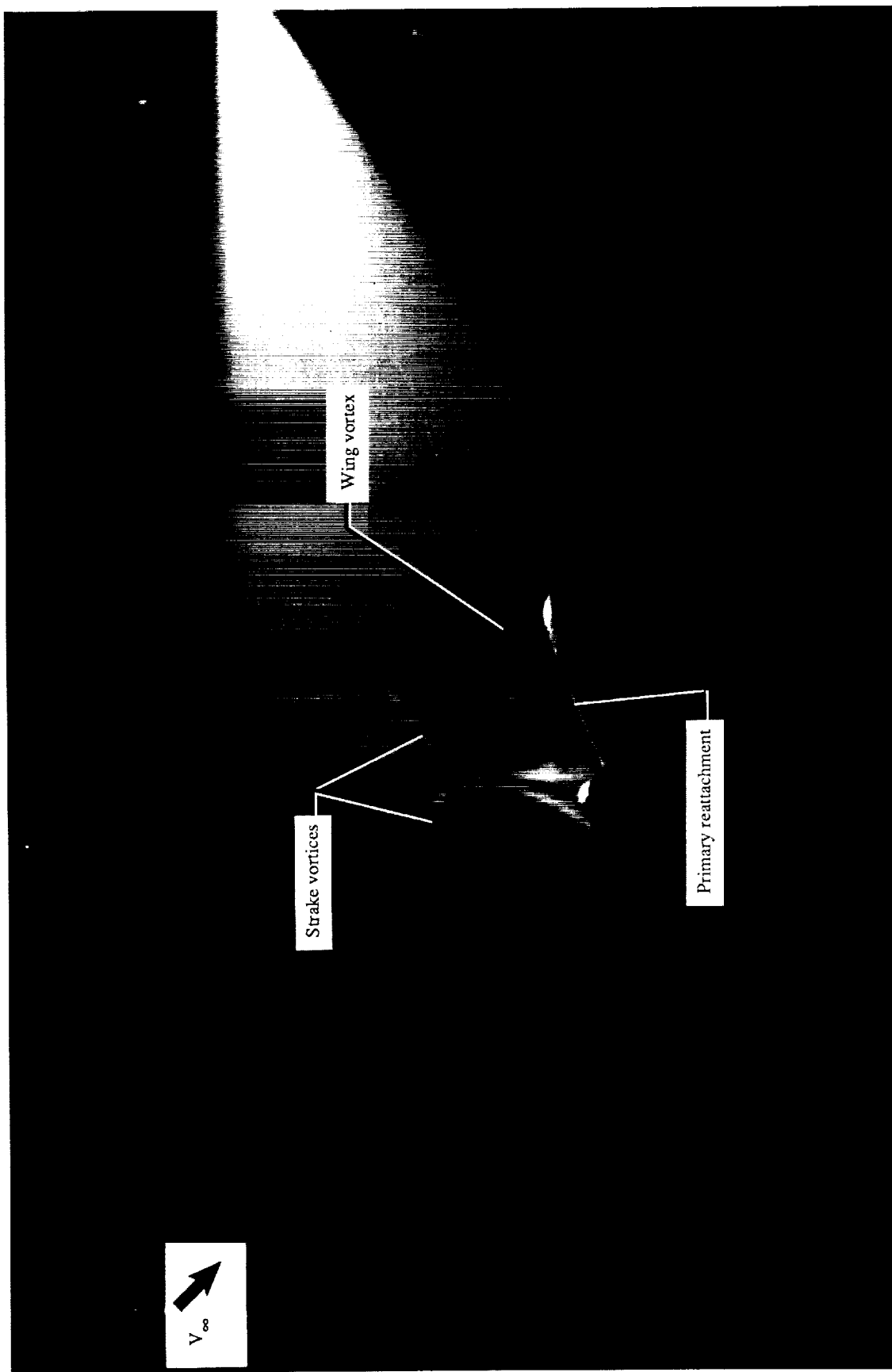
(c) $M_\infty = 0.95$; $\alpha \approx 24^\circ$; $x/c = 0.75$; strakes on; right three-quarter rear view.

Figure 15. Continued.



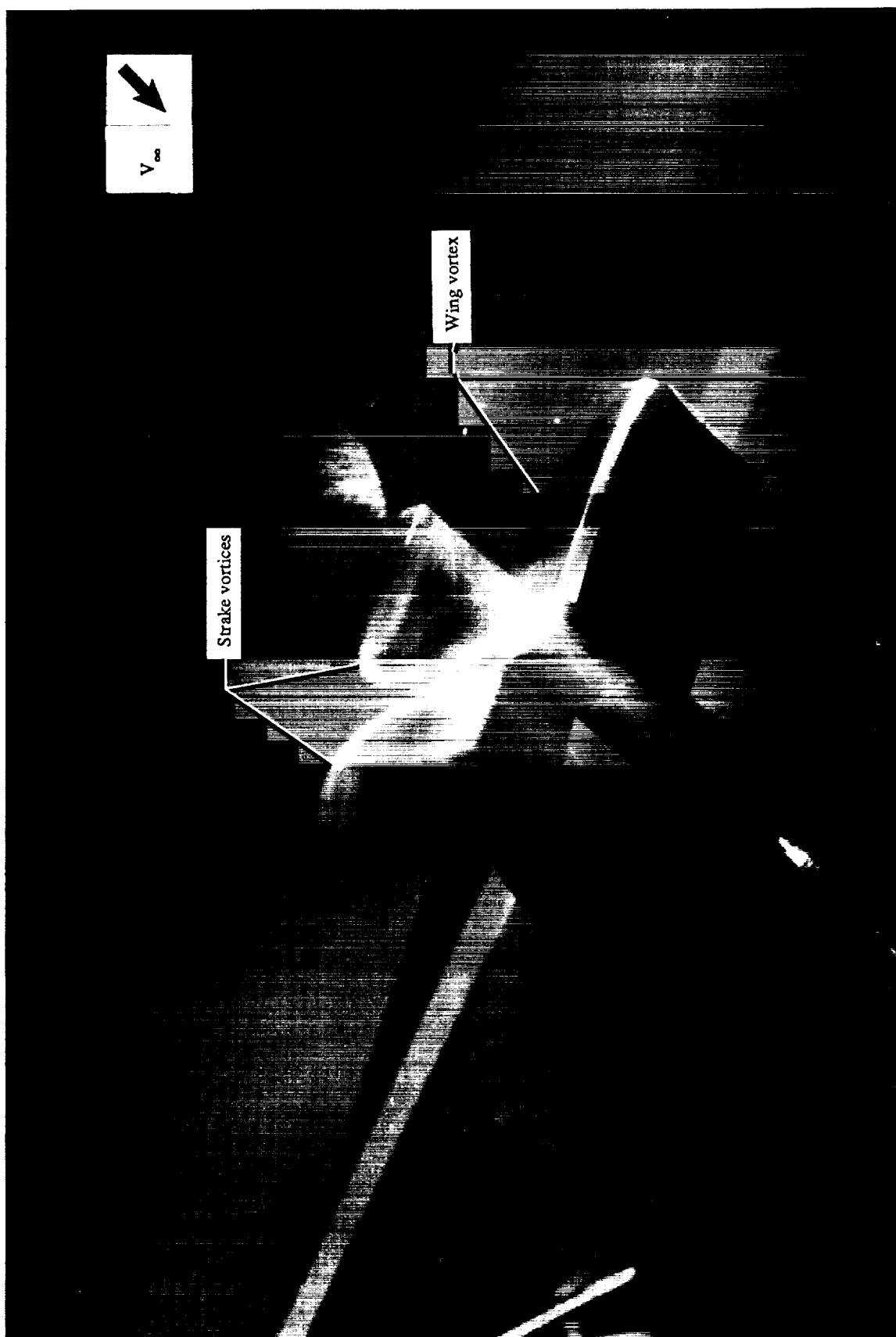
(d) $M_\infty = 1.10$; $\alpha \approx 24^\circ$; $x/c = 0.75$; strakes off; left three-quarter rear view.

Figure 15. Continued.



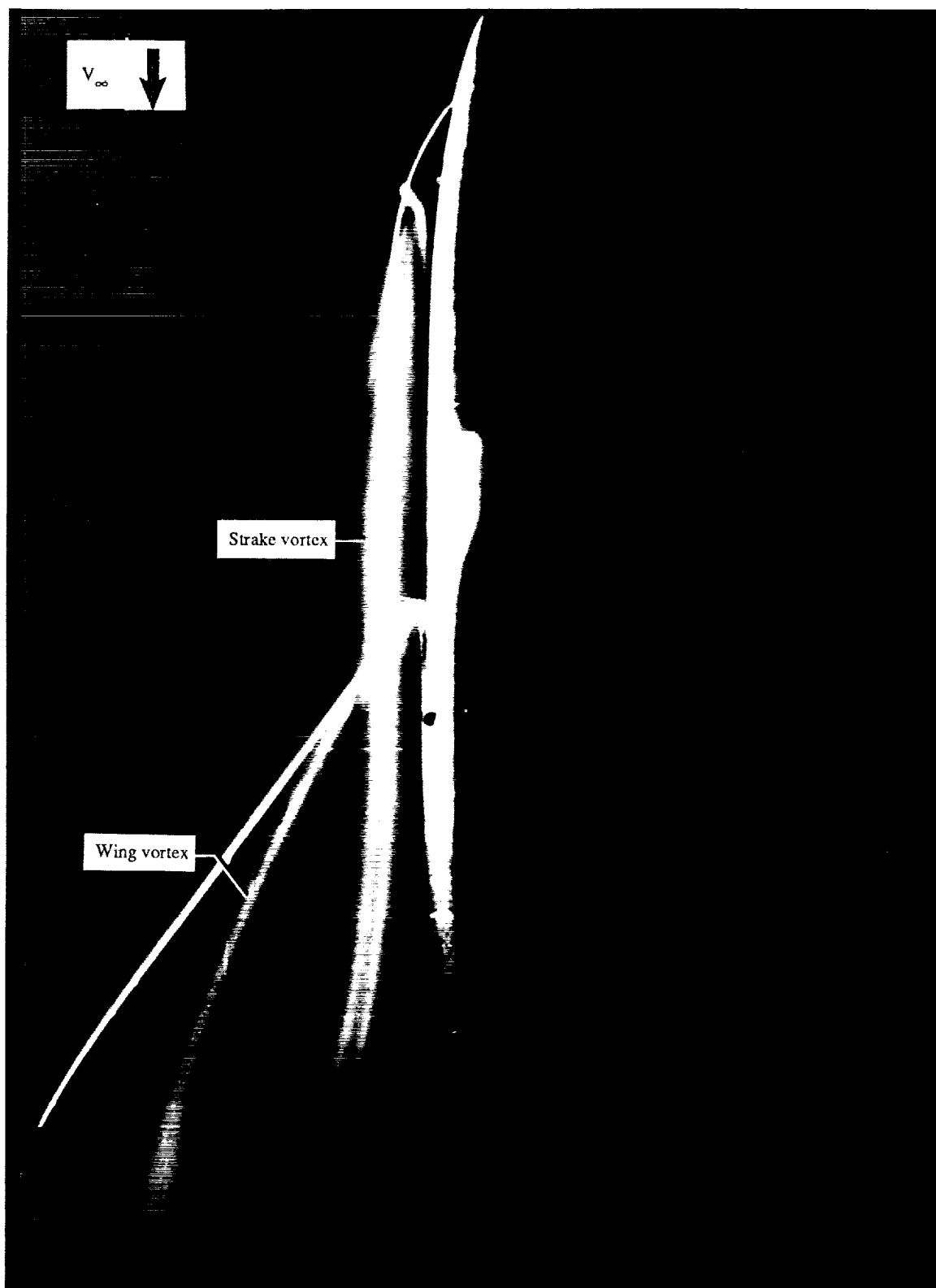
(e) $M_\infty = 1.10$; $\alpha \approx 24^\circ$; $x/c = 0.75$; strakes on, left three-quarter rear view.

Figure 15. Continued.



(f) $M_\infty = 1.10$; $\alpha \approx 24^\circ$; $x/c = 0.75$; strakes on; right three-quarter rear view.

Figure 15. Concluded.



(a) $\alpha \approx 20^\circ$.

Figure 16. Small-scale model smoke flow visualization at $M_\infty = 0.05$ with $\delta_{LE} = 0^\circ$. (From ref. 6.)

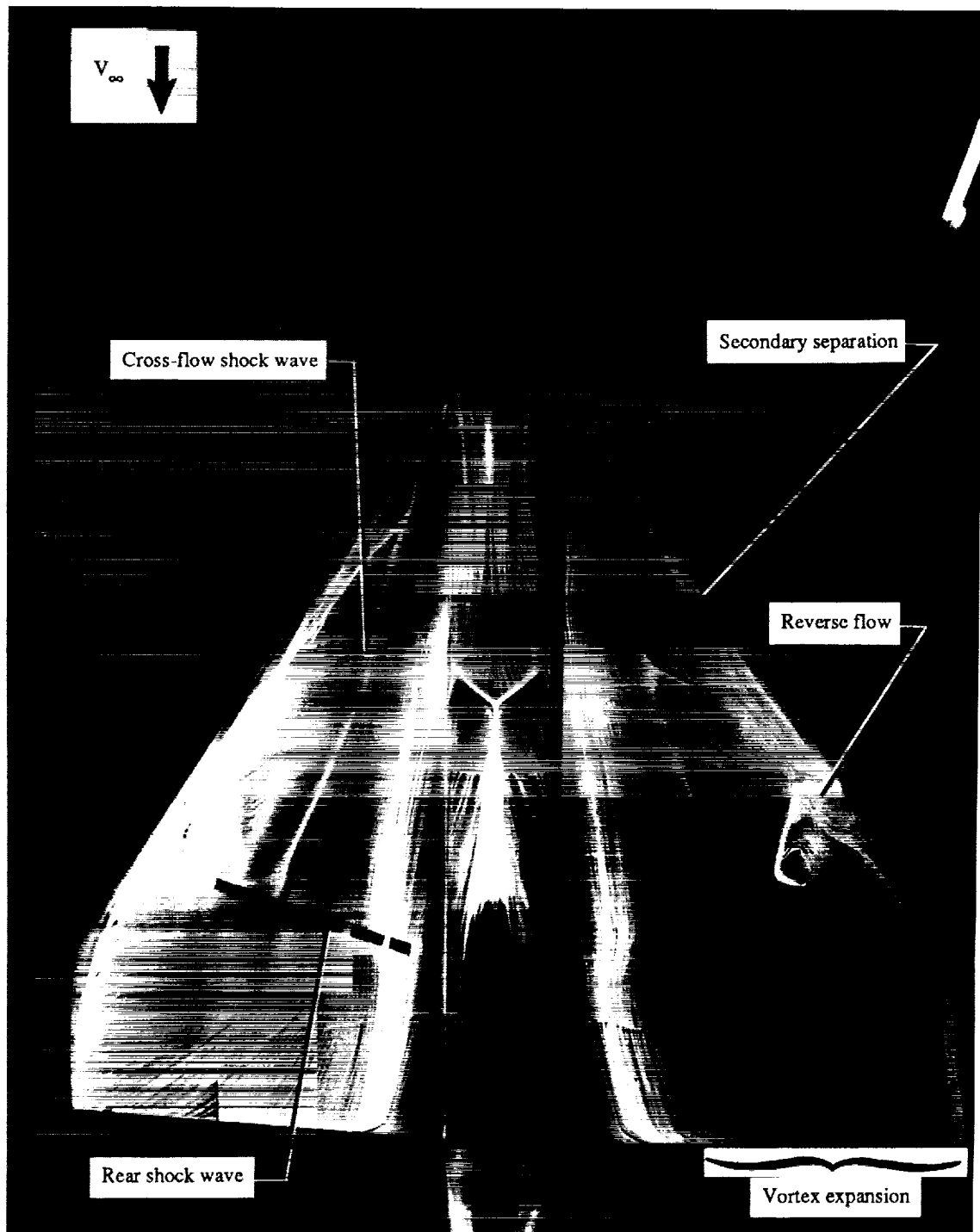


(b) $\alpha \approx 25^\circ$.

Figure 16. Concluded.

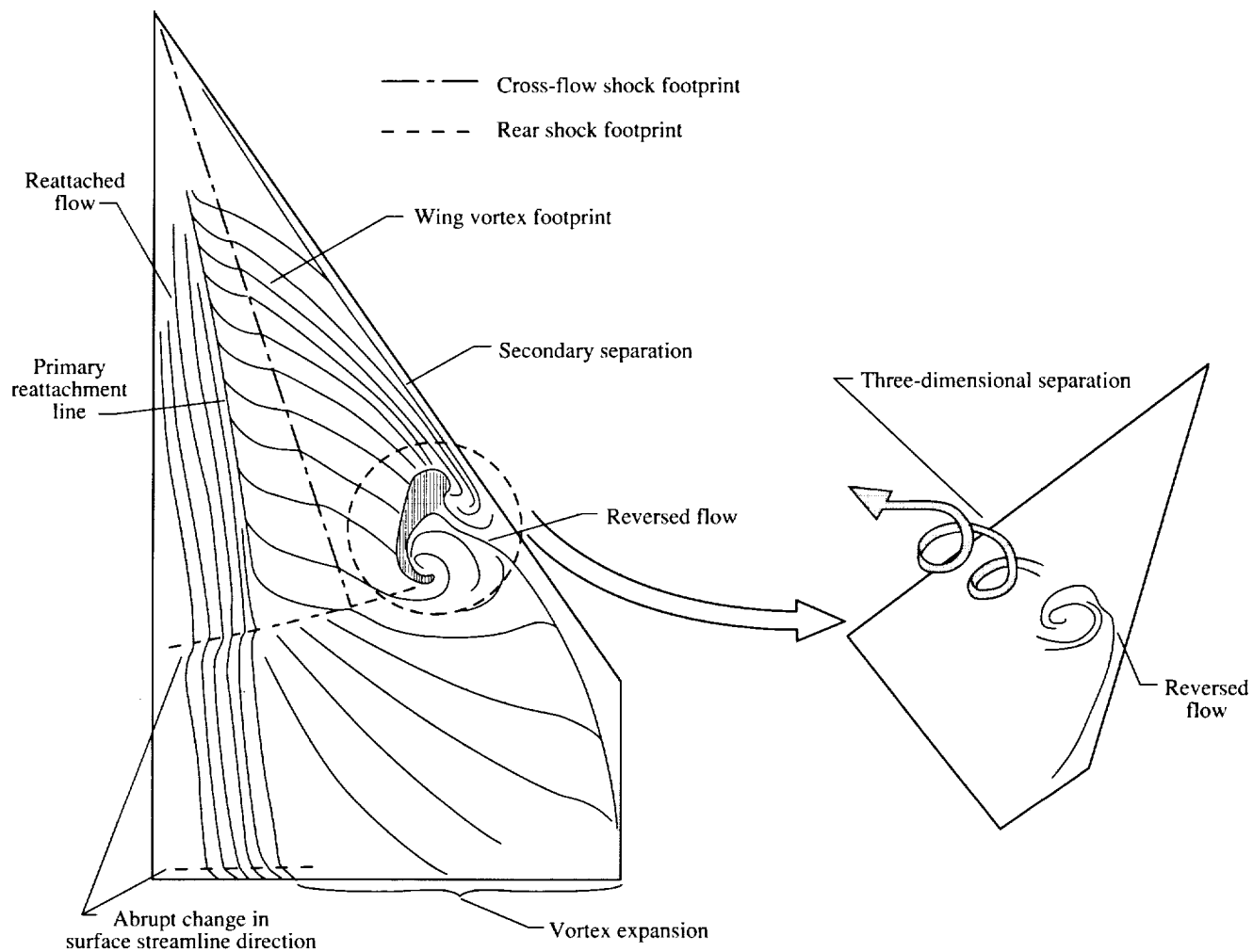
ORIGINAL PAGE

ORIGINAL PAGE
BLACK AND WHITE PHOTOGRAPH



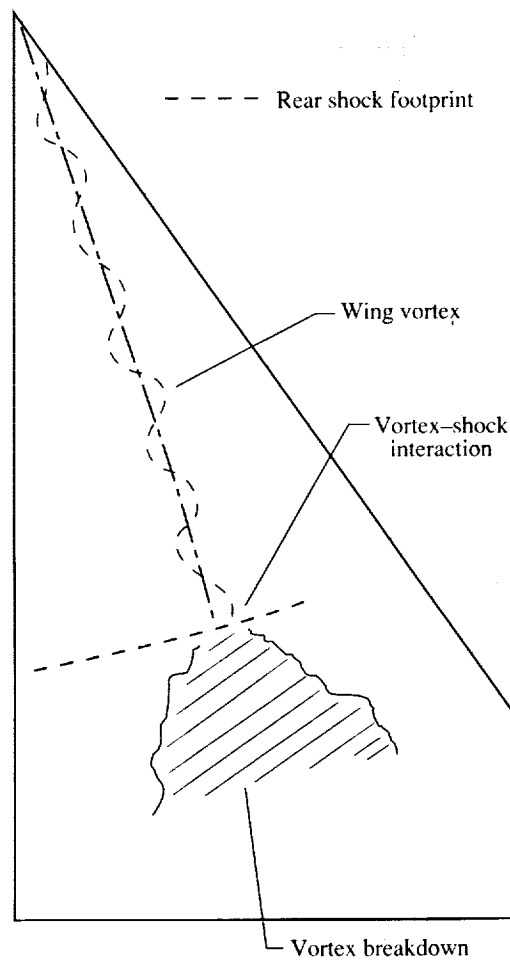
(a) Forebody strikes off.

Figure 17. Wing surface flow and off-surface flow behavior at $M_\infty = 0.95$ and $\alpha \approx 20^\circ$ with $\delta_{LE} = 0^\circ$ and vertical tail off. (Oil flow photographs from ref. 6.)



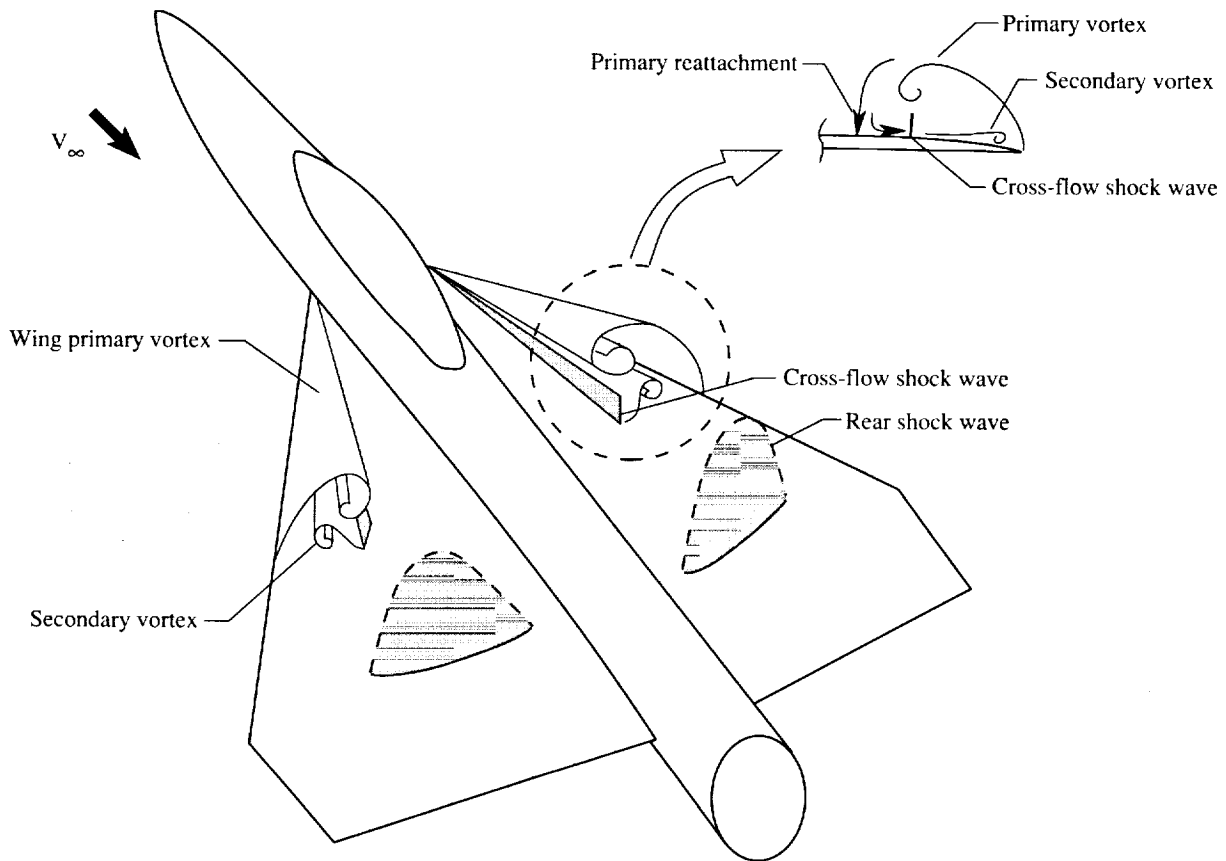
(b) On-surface and off-surface flows with strakes off.

Figure 17. Continued.



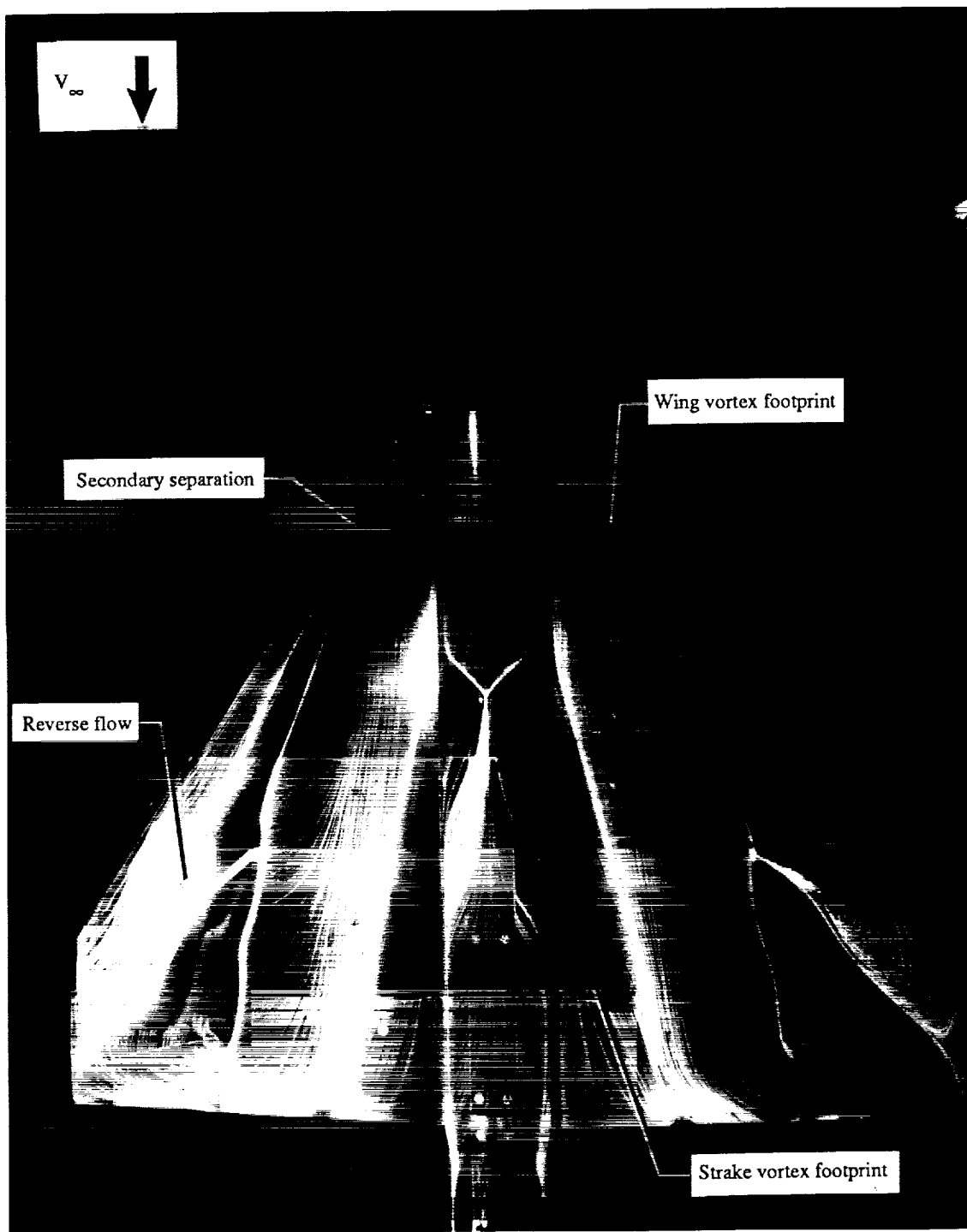
(c) Vortex-shock interaction with strakes off.

Figure 17. Continued.



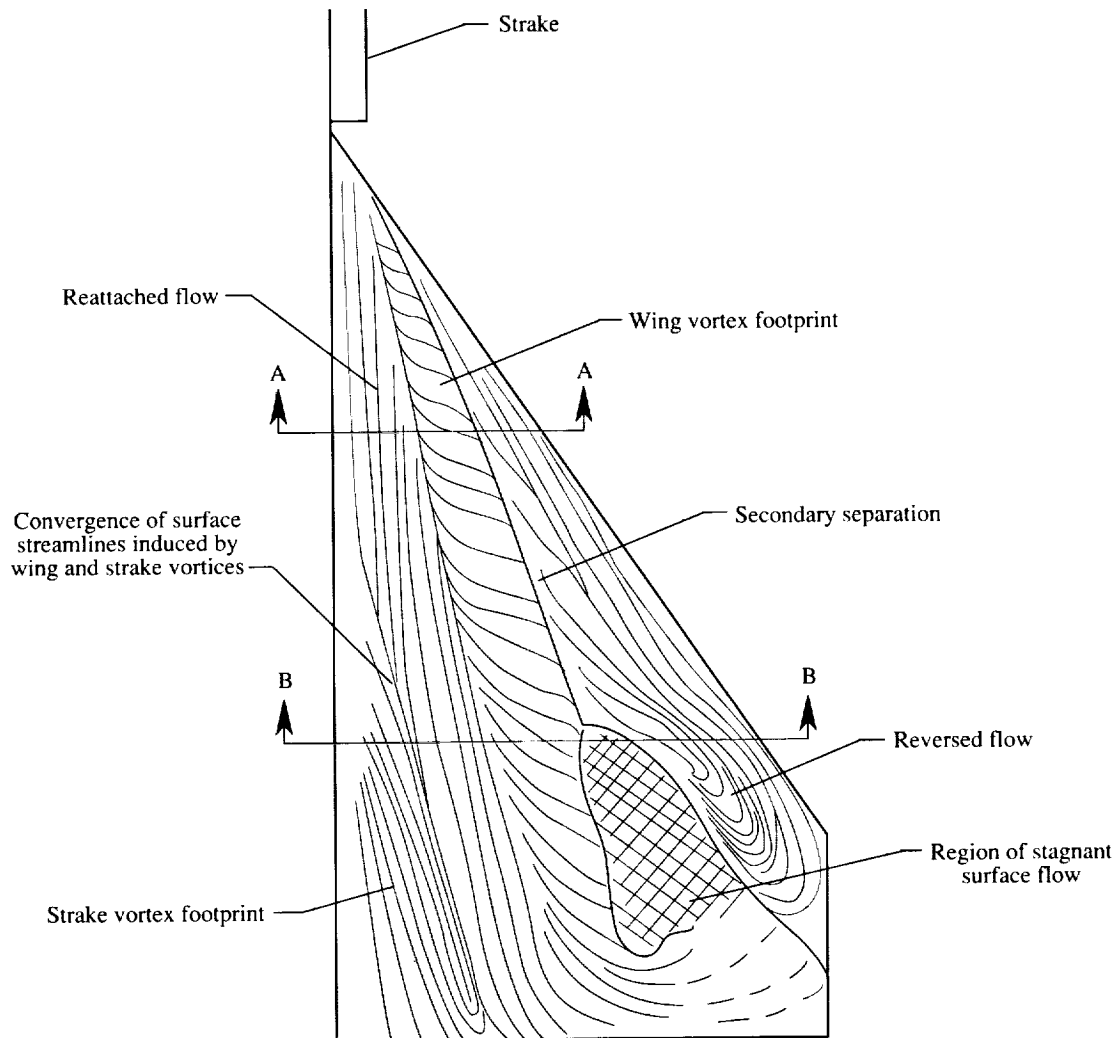
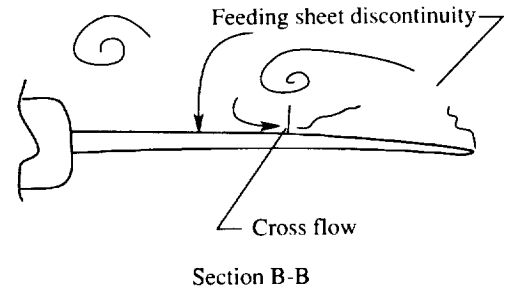
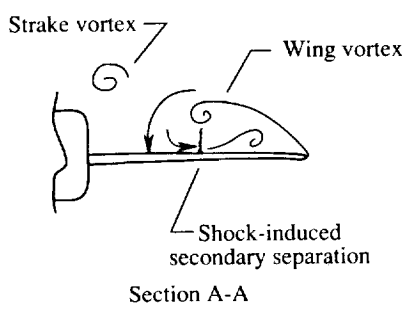
(d) Coexisting vortices and shock waves with strakes off.

Figure 17. Continued.



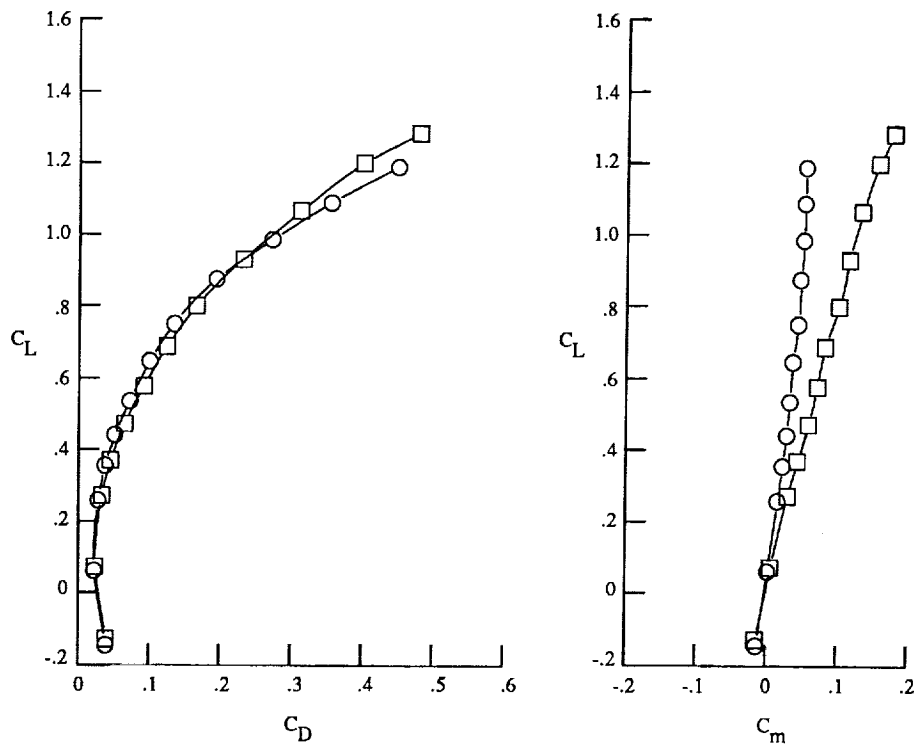
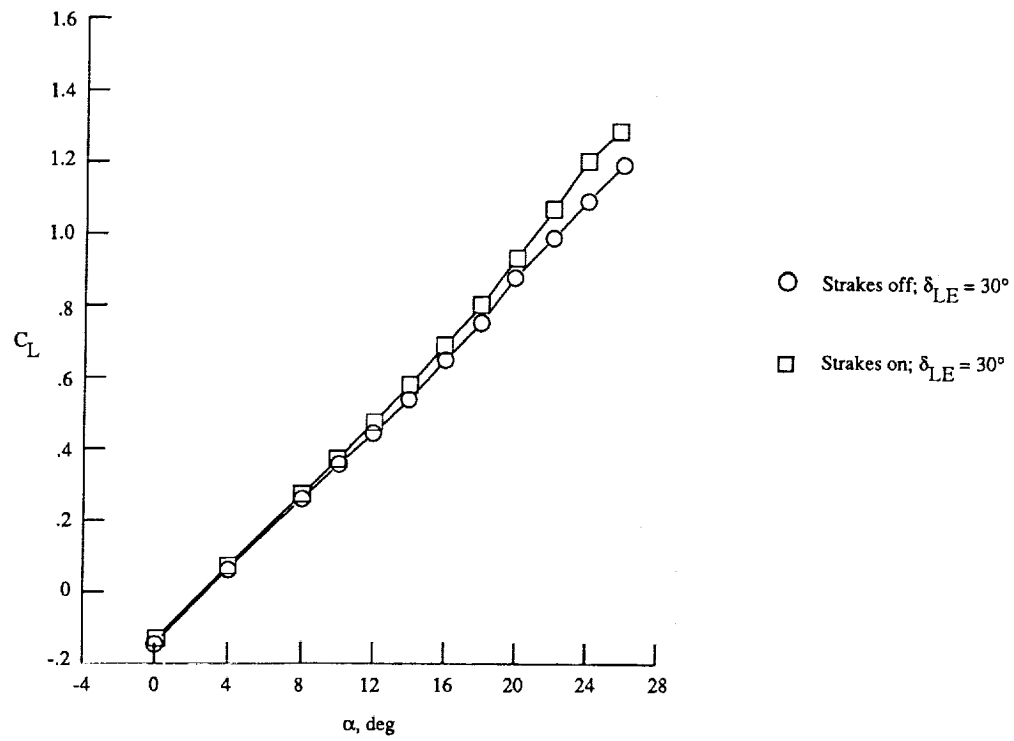
(e) Forebody strakes on.

Figure 17. Continued.



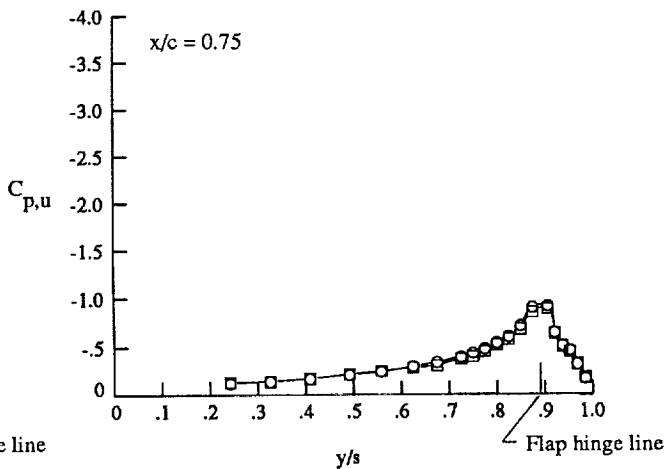
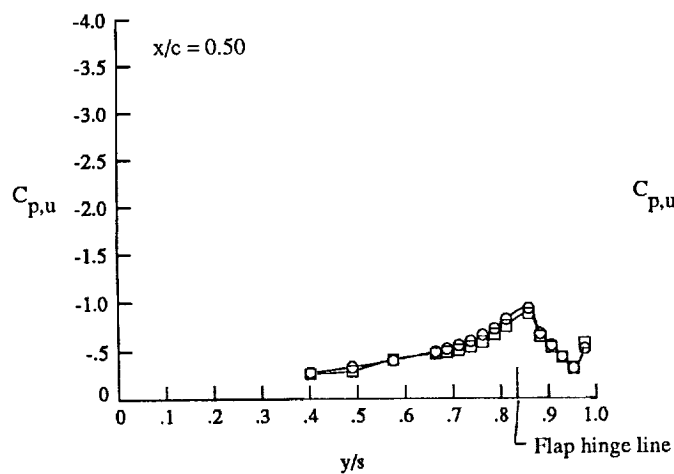
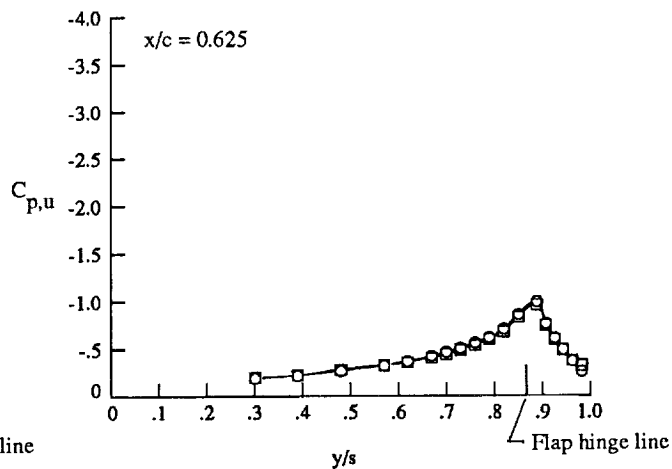
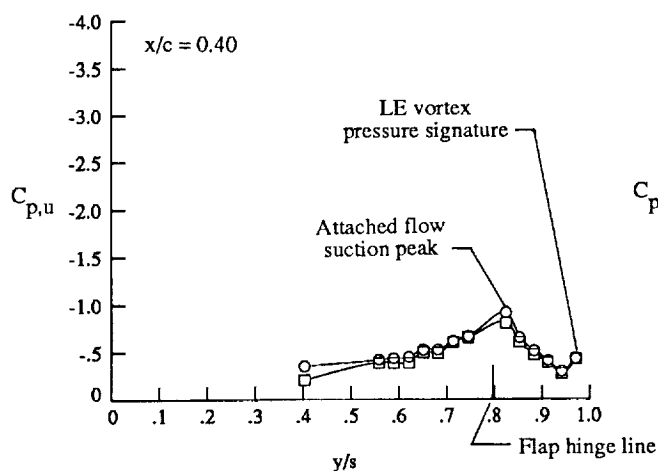
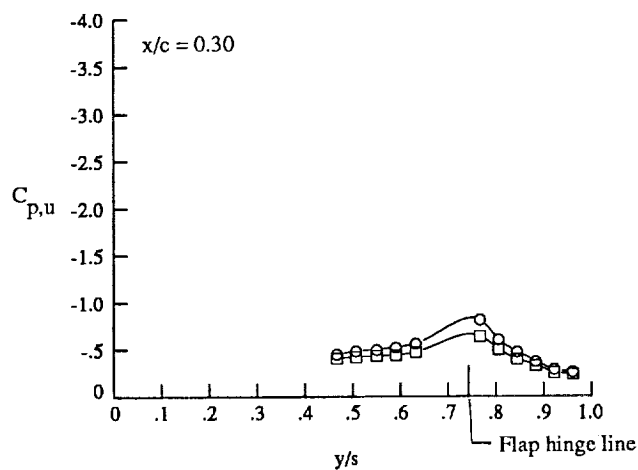
(f) Sketches of on-surface and off-surface flows with strakes on.

Figure 17. Concluded.



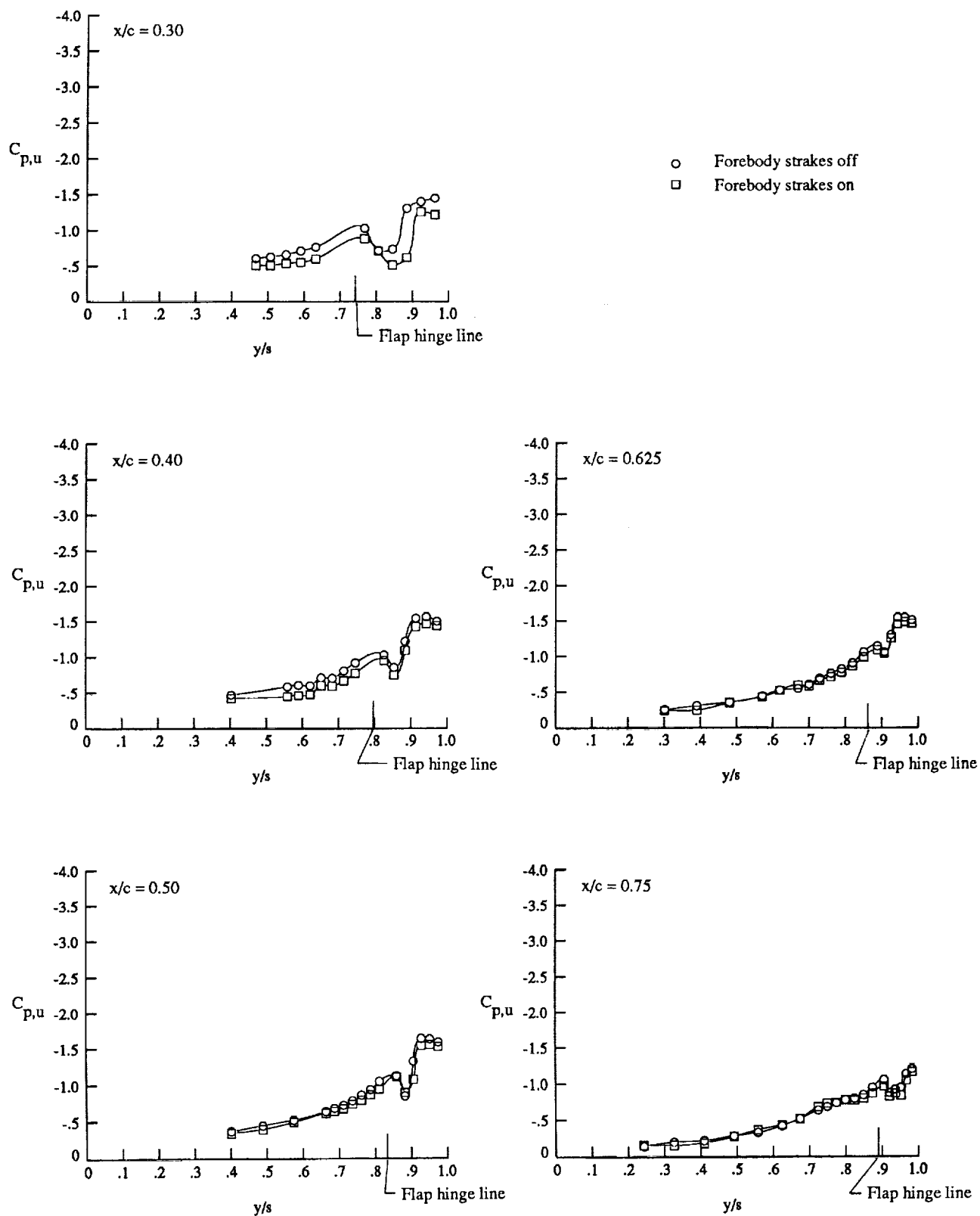
(a) Lift, drag, and pitching moment.

Figure 18. Effect of forebody strakes on longitudinal characteristics at $M_\infty = 0.40$ with $\delta_{LE} = 30^\circ$.



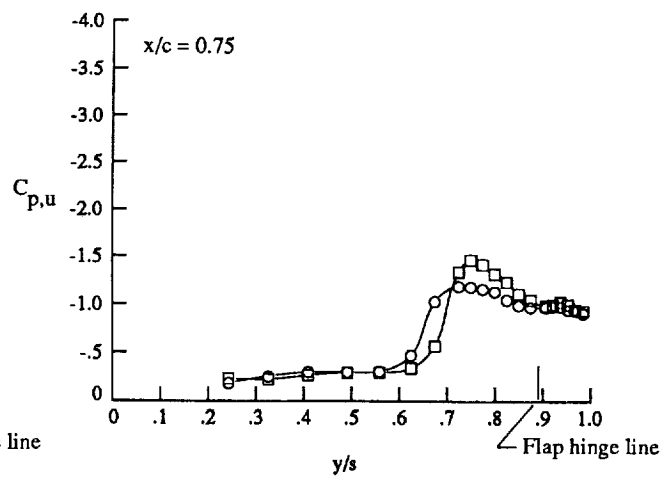
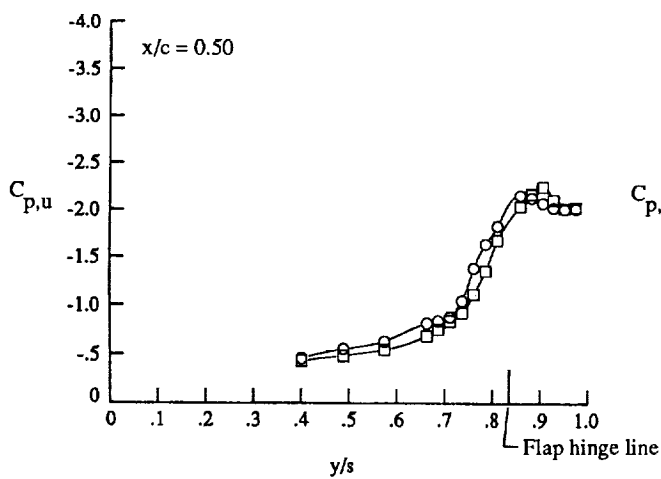
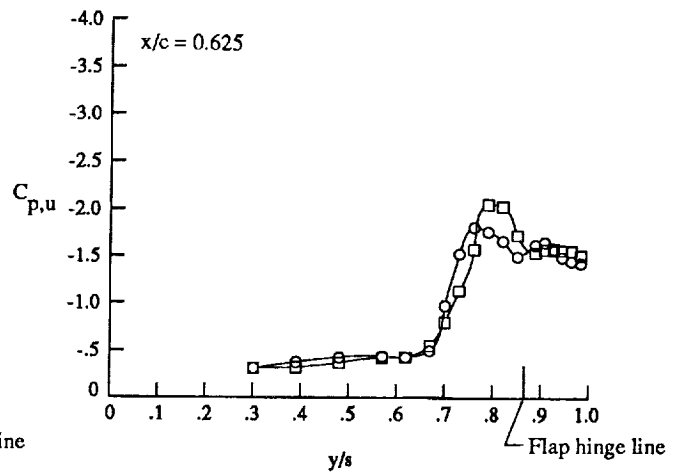
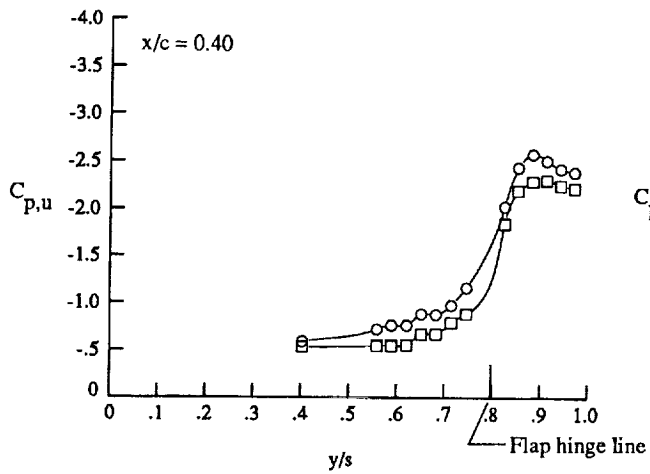
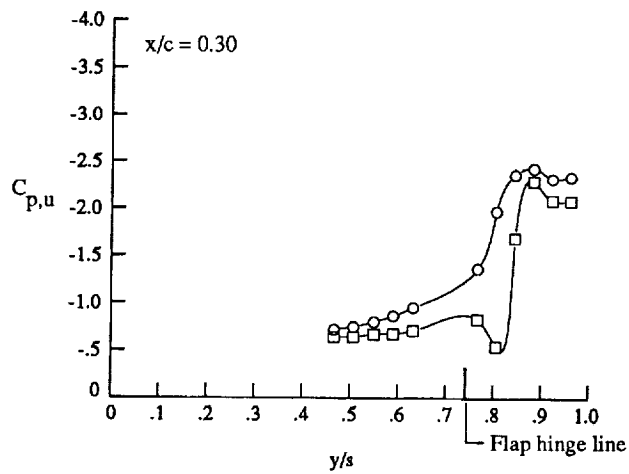
(b) Wing upper surface static pressure distributions at $\alpha \approx 12^\circ$.

Figure 18. Continued.



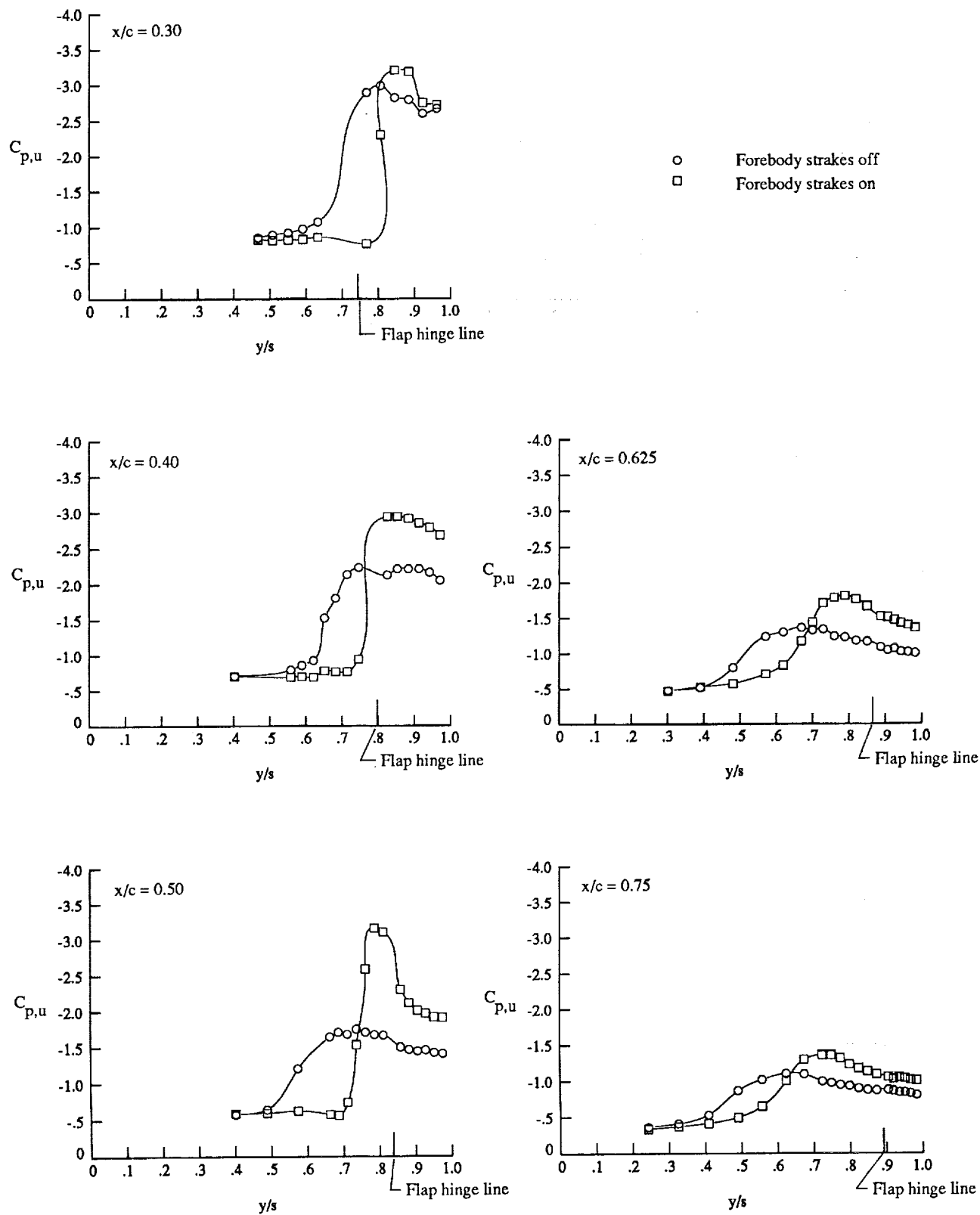
(c) Wing upper surface static pressure distributions at $\alpha \approx 16^\circ$.

Figure 18. Continued.



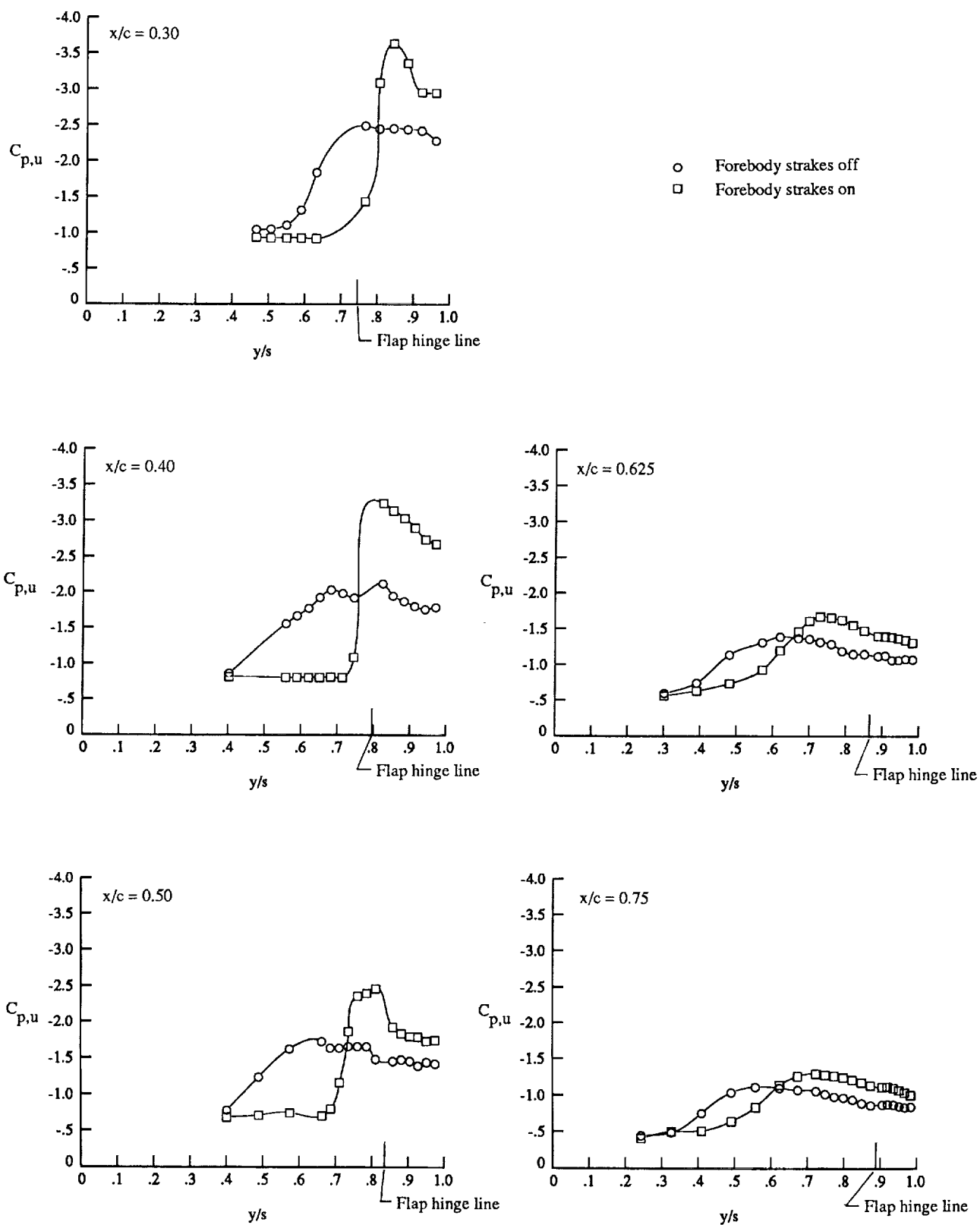
(d) Wing upper surface static pressure distributions at $\alpha \approx 20^\circ$.

Figure 18. Continued.



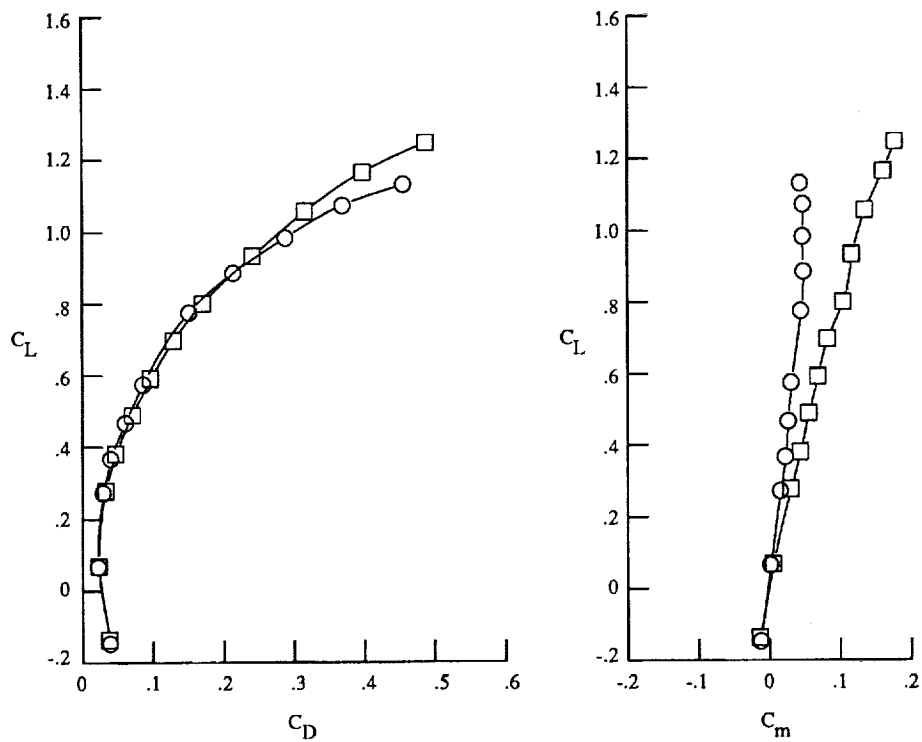
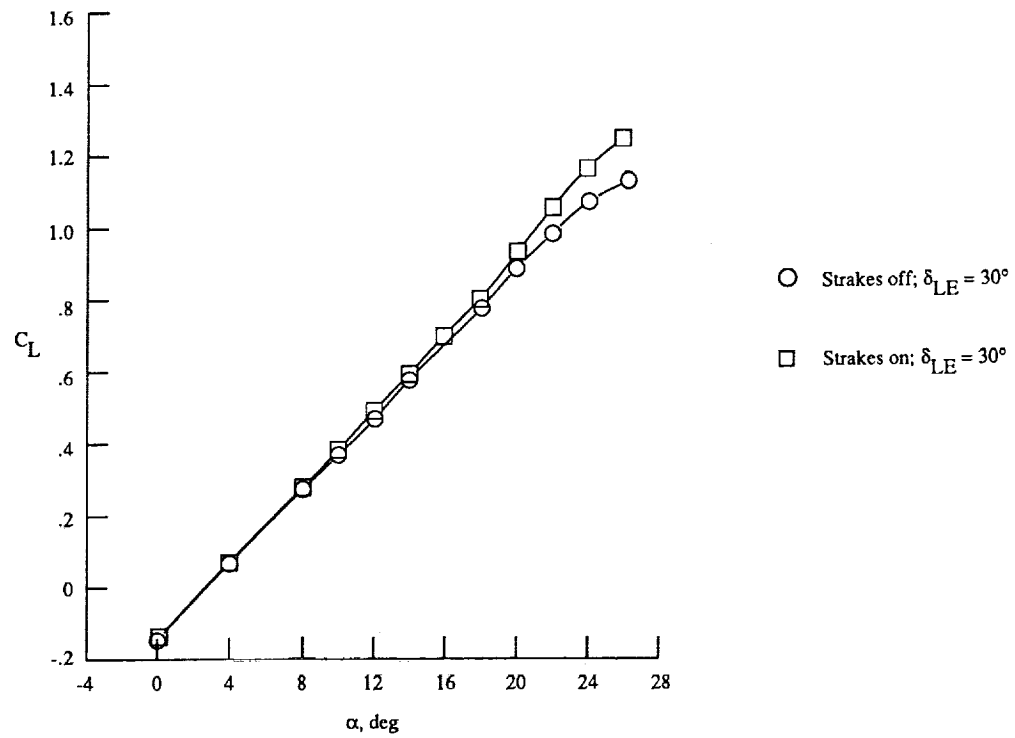
(e) Wing upper surface static pressure distributions at $\alpha \approx 24^\circ$.

Figure 18. Continued.



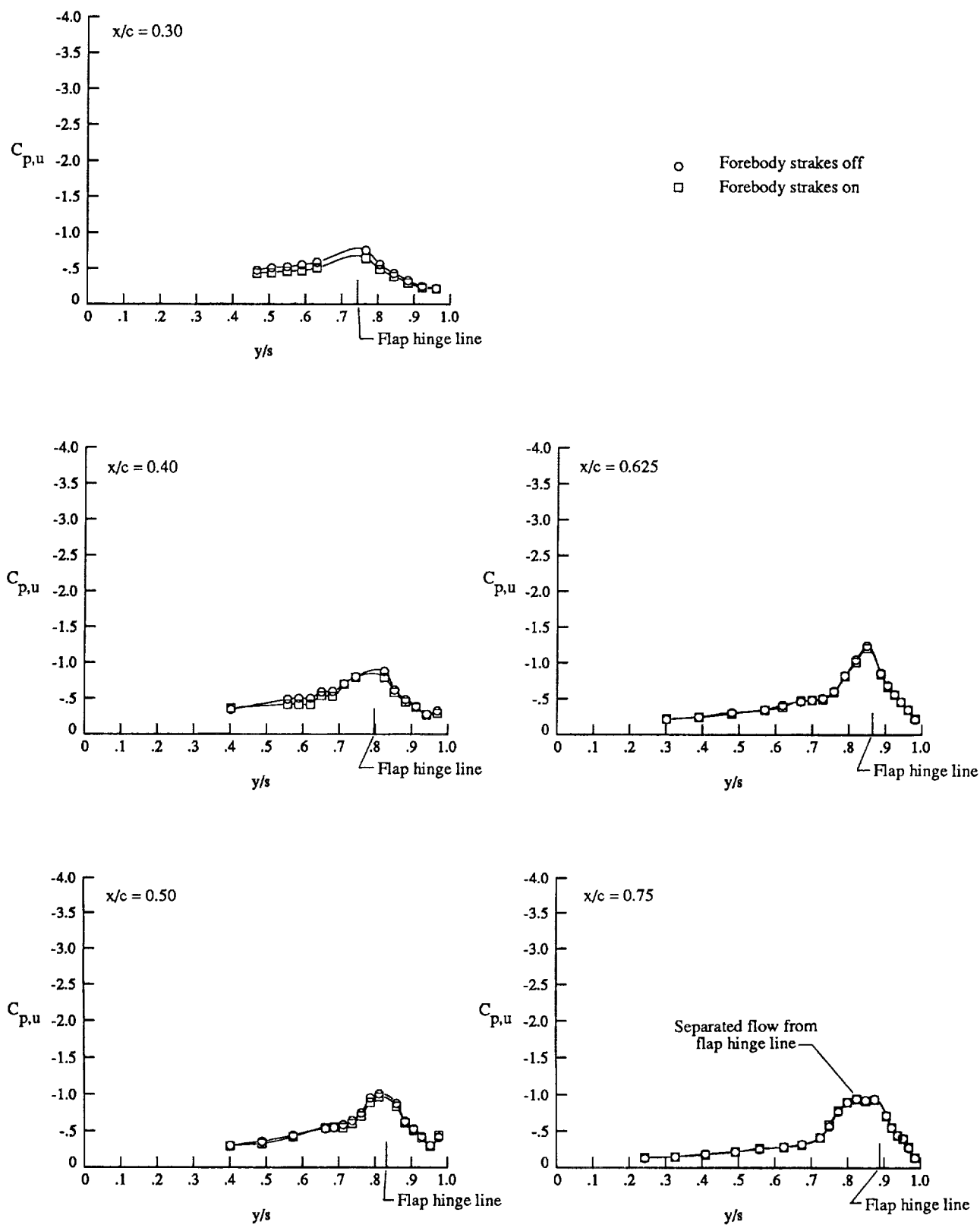
(f) Wing upper surface static pressure distributions at $\alpha \approx 26^\circ$.

Figure 18. Concluded.



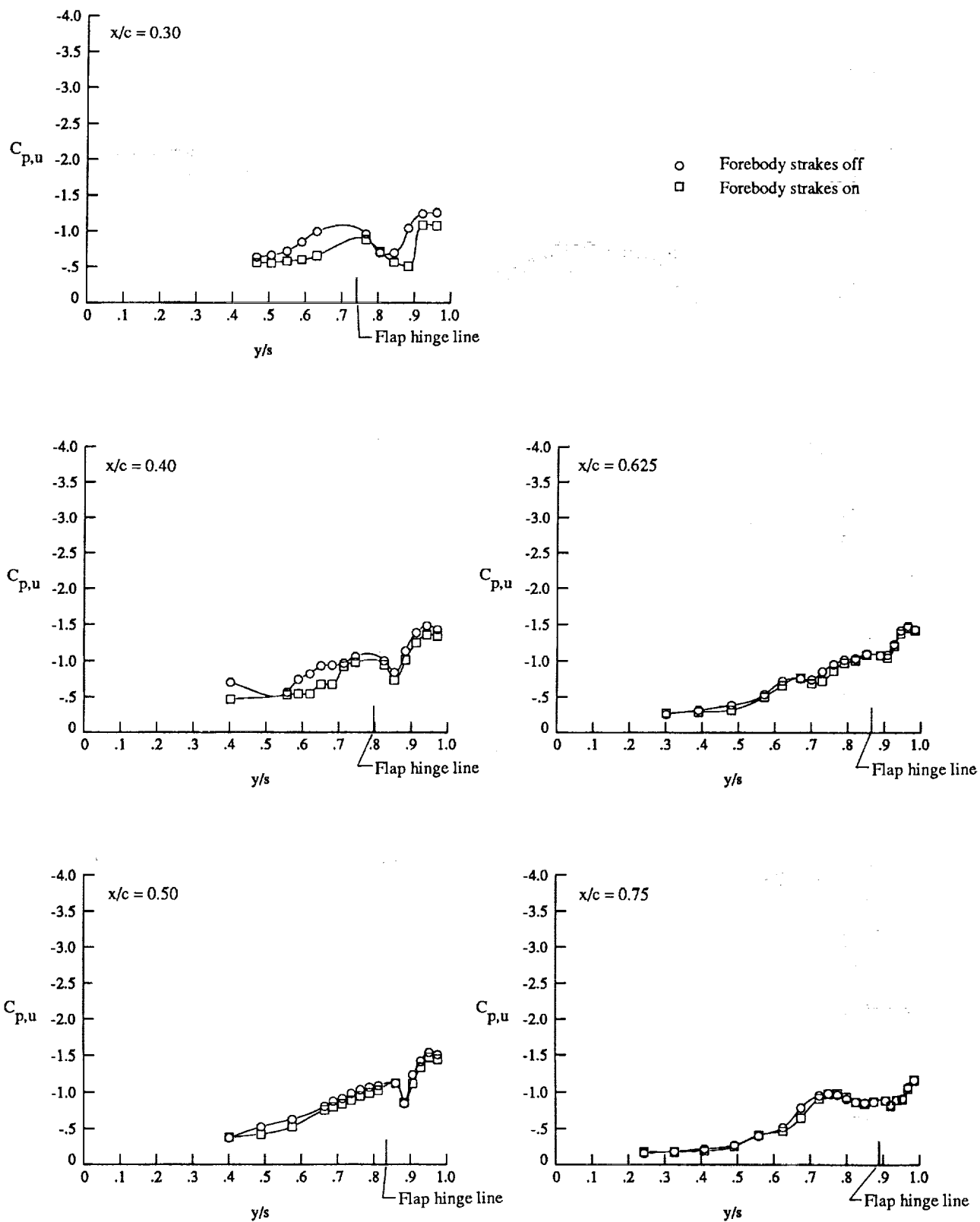
(a) Lift, drag, and pitching moment.

Figure 19. Effect of forebody strakes on longitudinal characteristics at $M_\infty = 0.60$ with $\delta_{LE} = 30^\circ$.



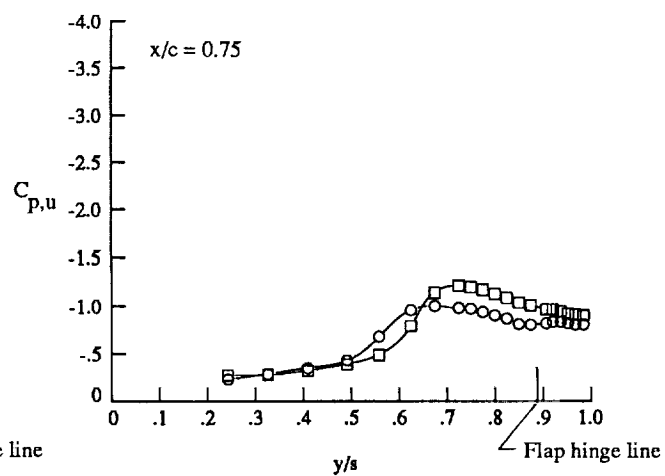
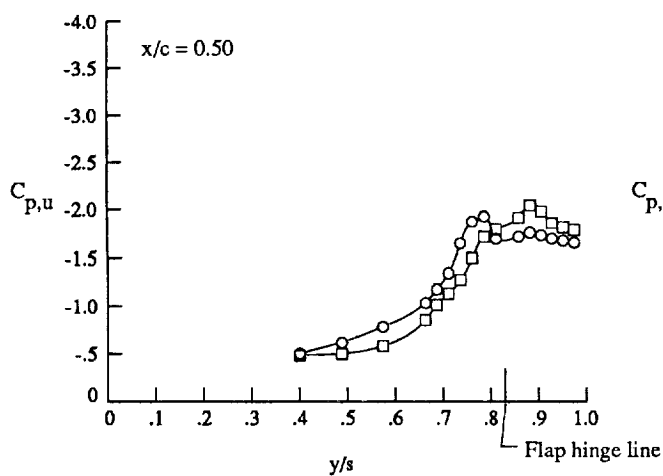
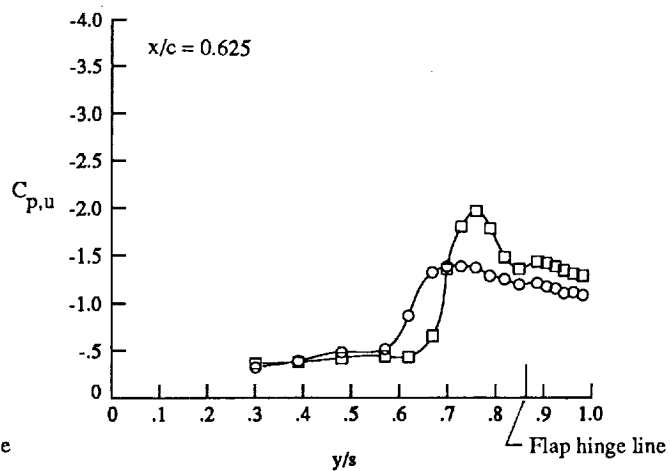
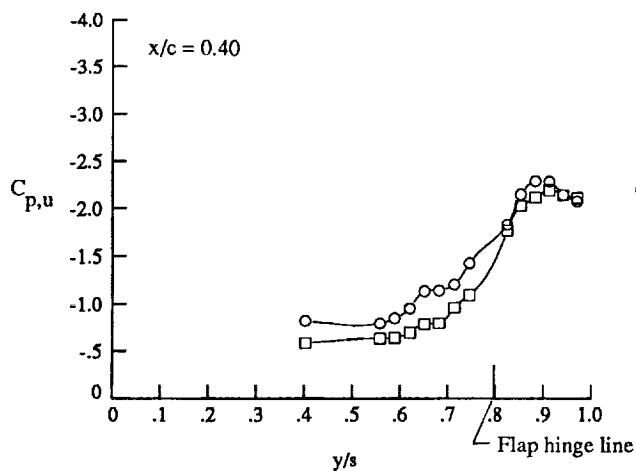
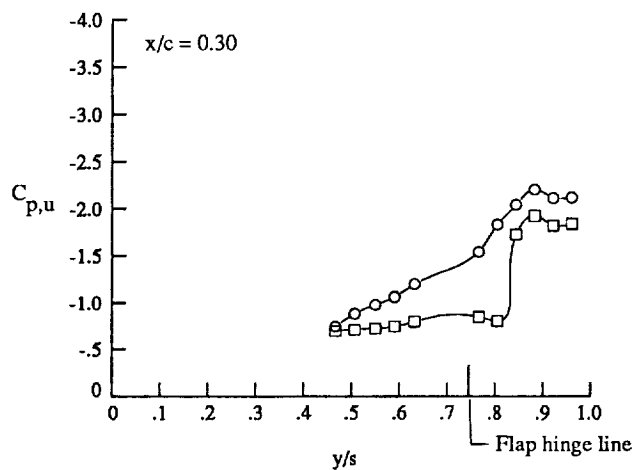
(b) Wing upper surface static pressure distributions at $\alpha \approx 12^\circ$.

Figure 19. Continued.



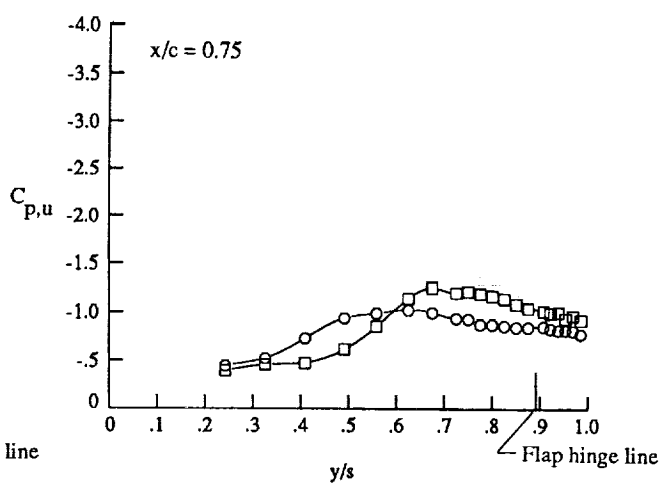
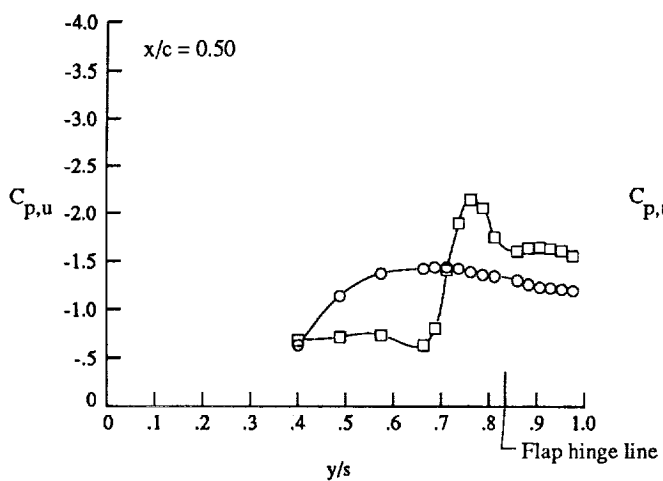
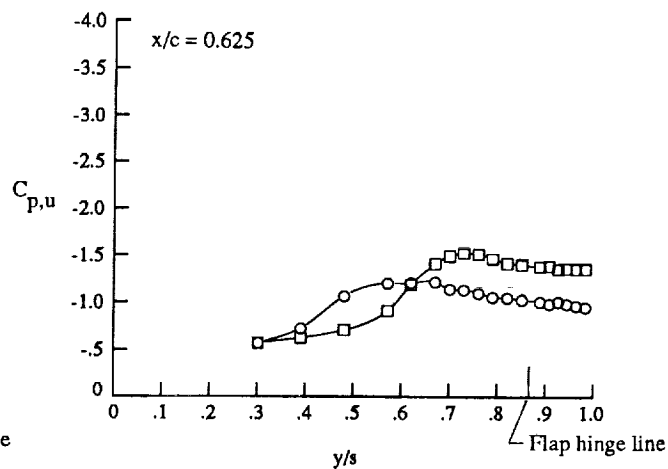
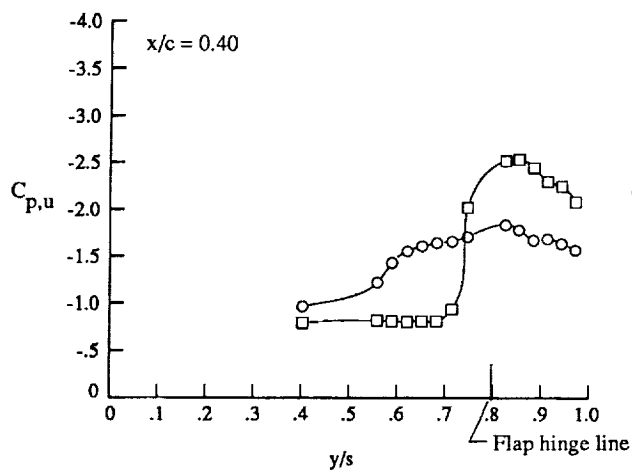
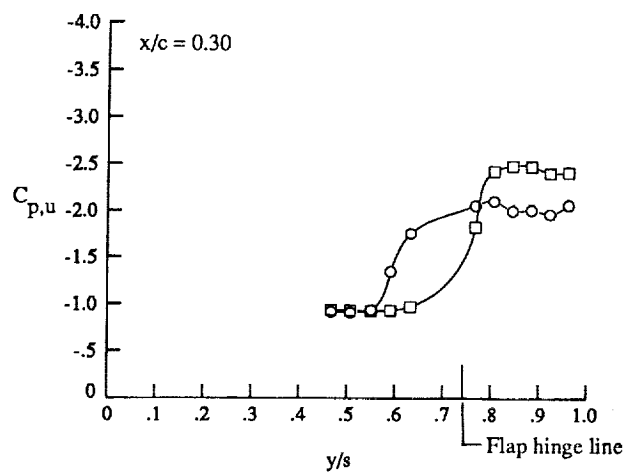
(c) Wing upper surface static pressure distributions at $\alpha \approx 16^\circ$.

Figure 19. Continued.



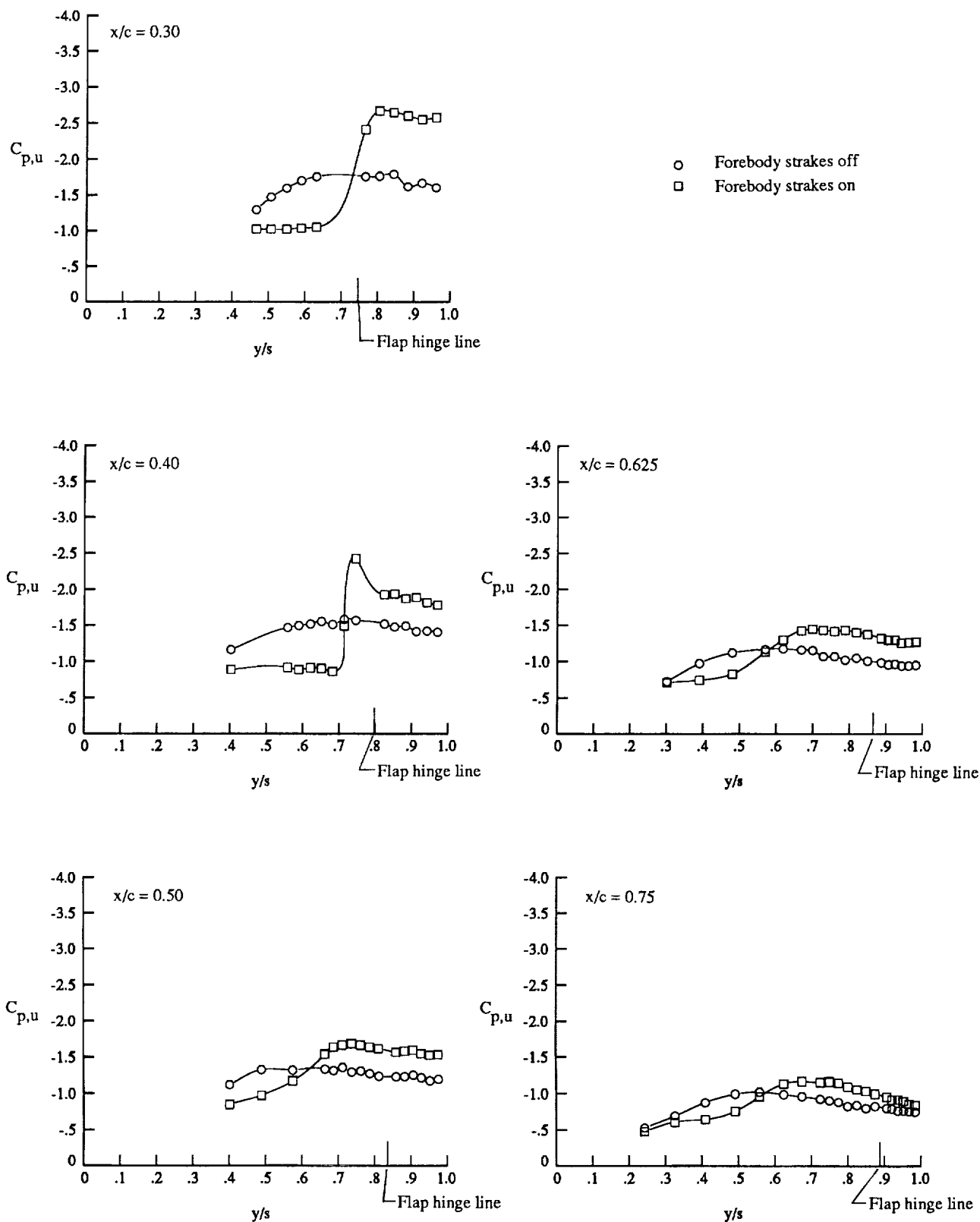
(d) Wing upper surface static pressure distributions at $\alpha \approx 20^\circ$.

Figure 19. Continued.



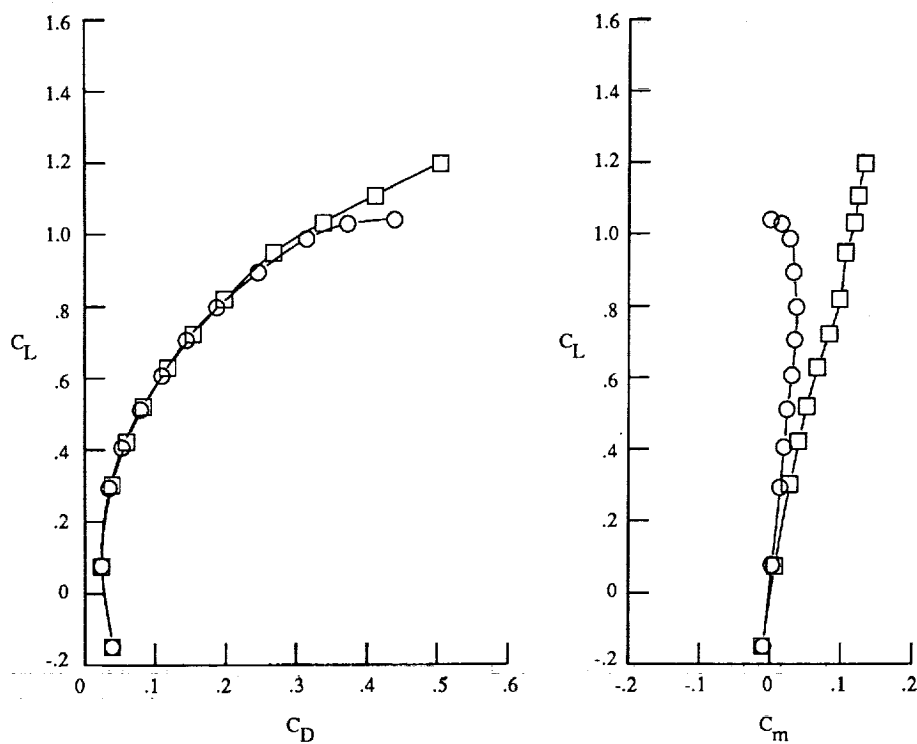
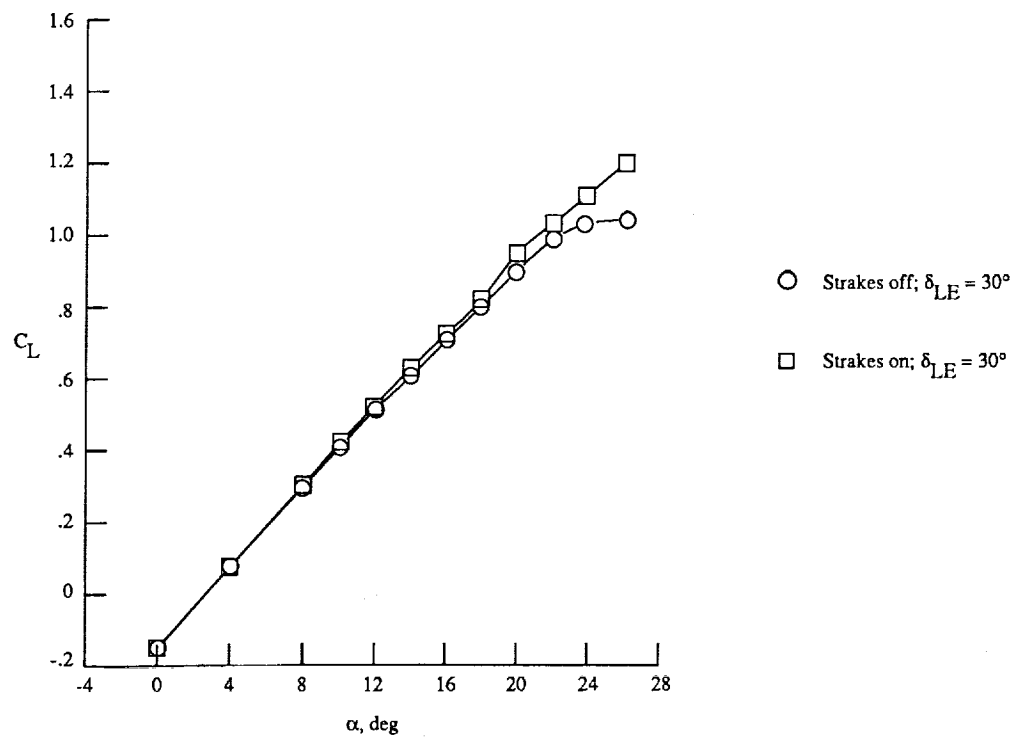
(e) Wing upper surface static pressure distributions at $\alpha \approx 24^\circ$.

Figure 19. Continued.



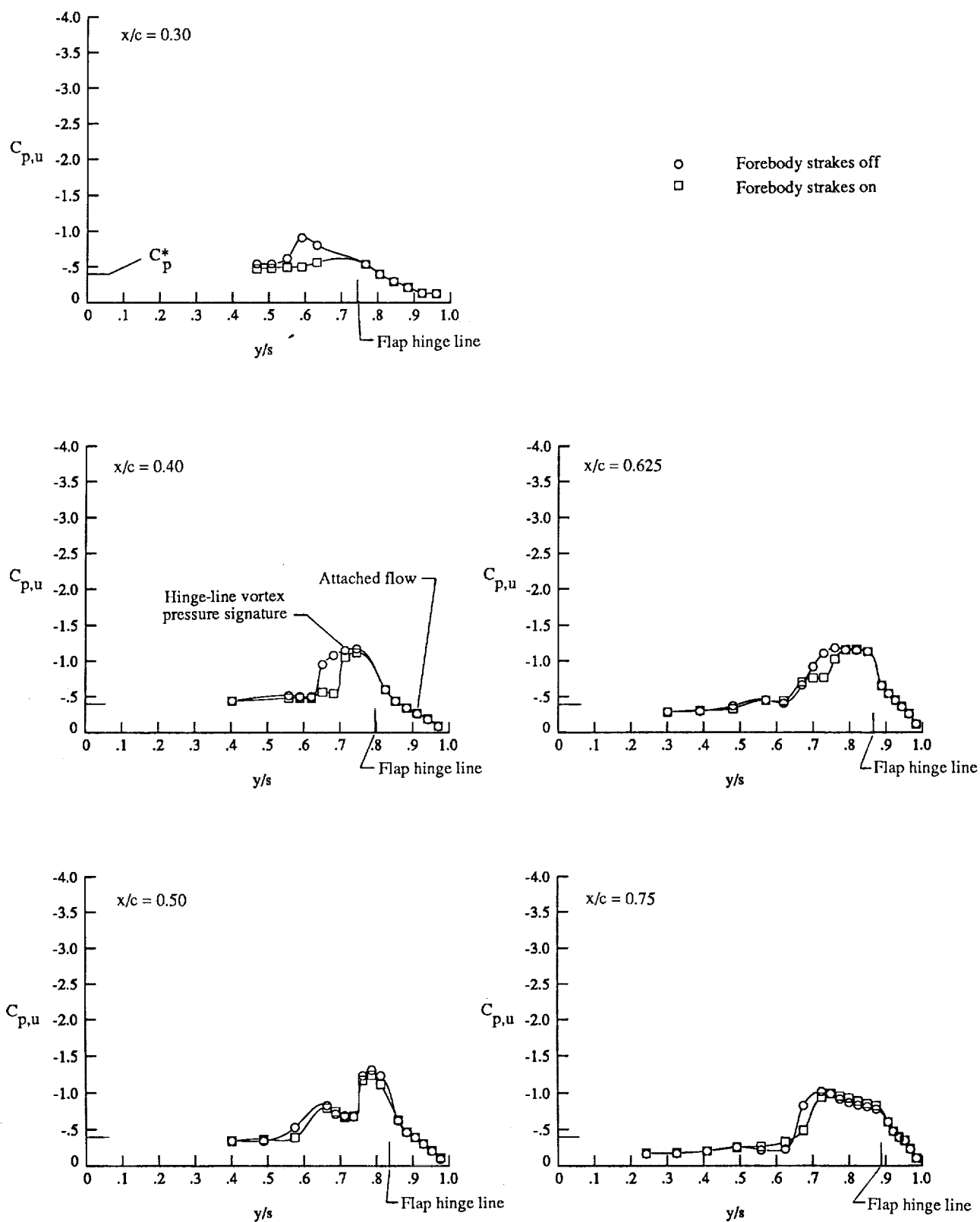
(f) Wing upper surface static pressure distributions at $\alpha \approx 26^\circ$.

Figure 19. Concluded.



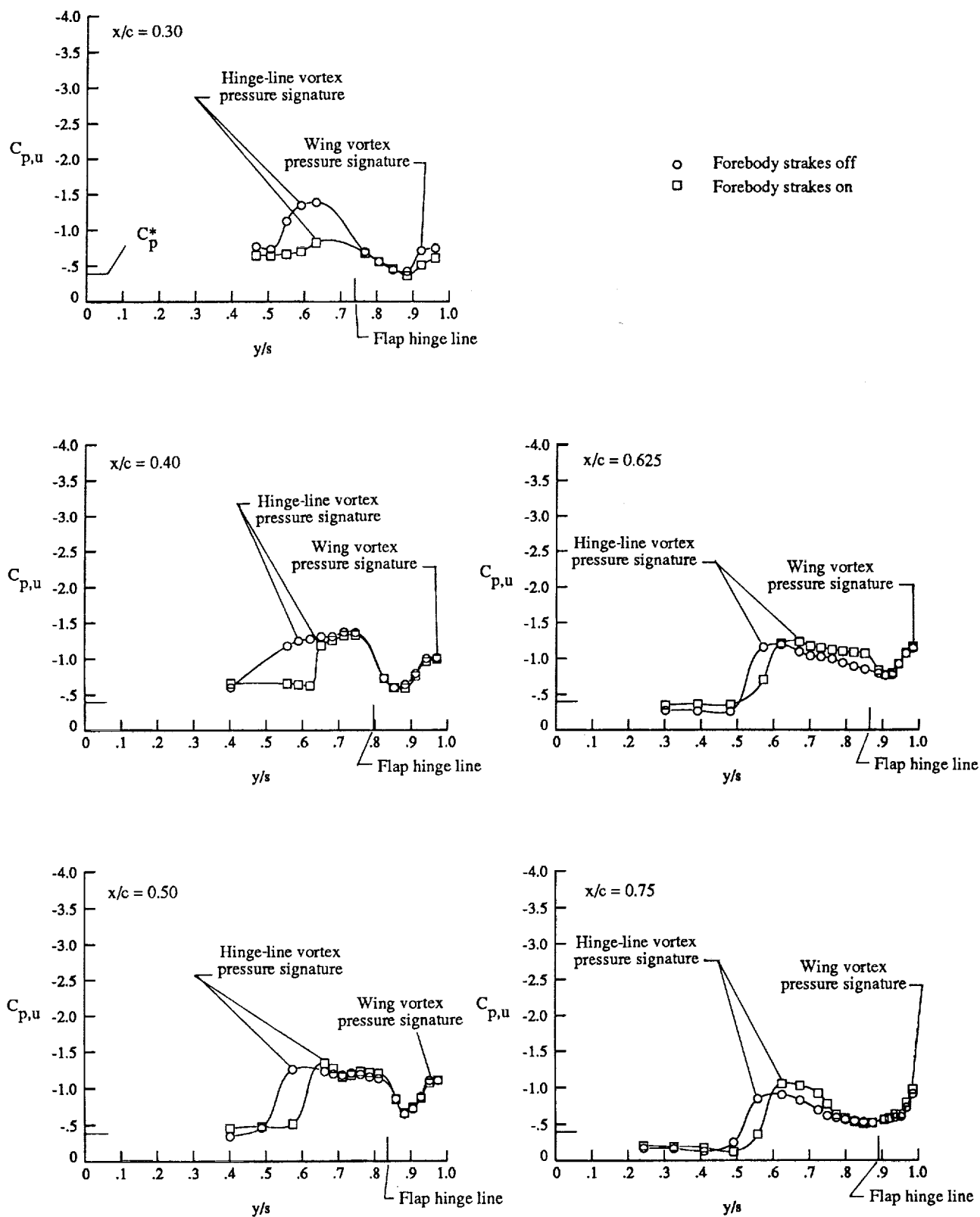
(a) Lift, drag, and pitching moment.

Figure 20. Effect of forebody strakes on longitudinal characteristics at $M_\infty = 0.80$ with $\delta_{LE} = 30^\circ$.



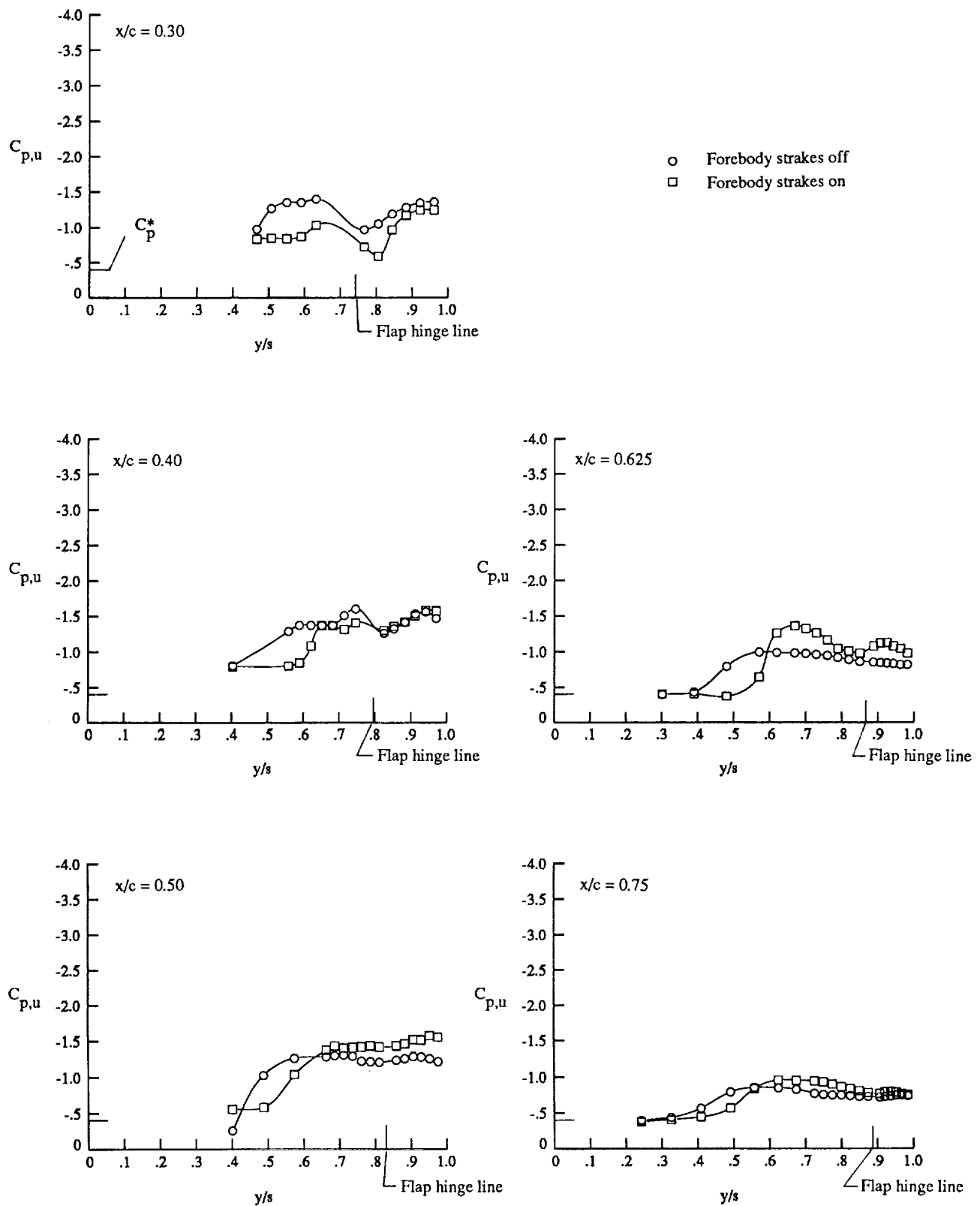
(b) Wing upper surface static pressure distributions at $\alpha \approx 12^\circ$.

Figure 20. Continued.



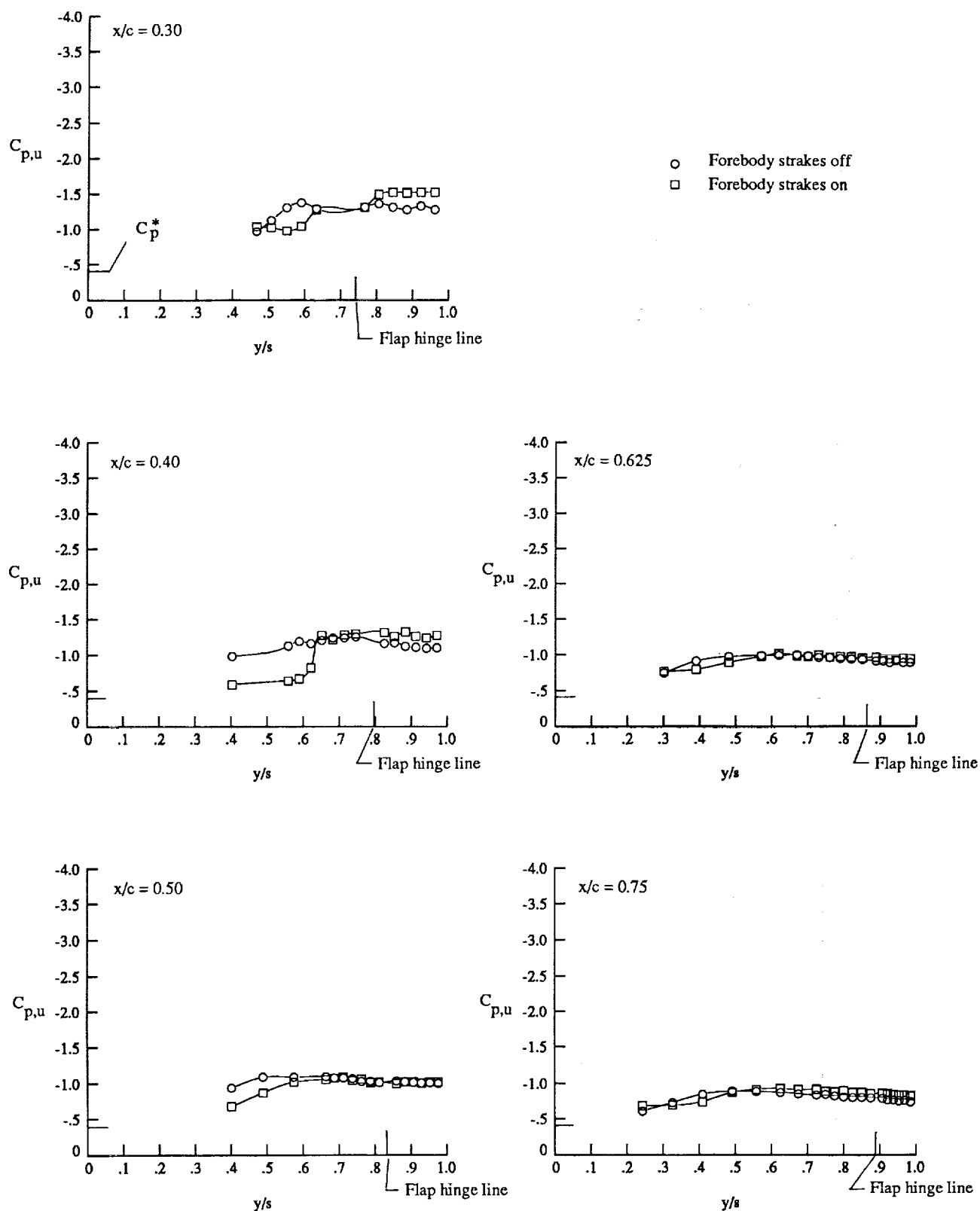
(c) Wing upper surface static pressure distributions at $\alpha \approx 16^\circ$.

Figure 20. Continued.



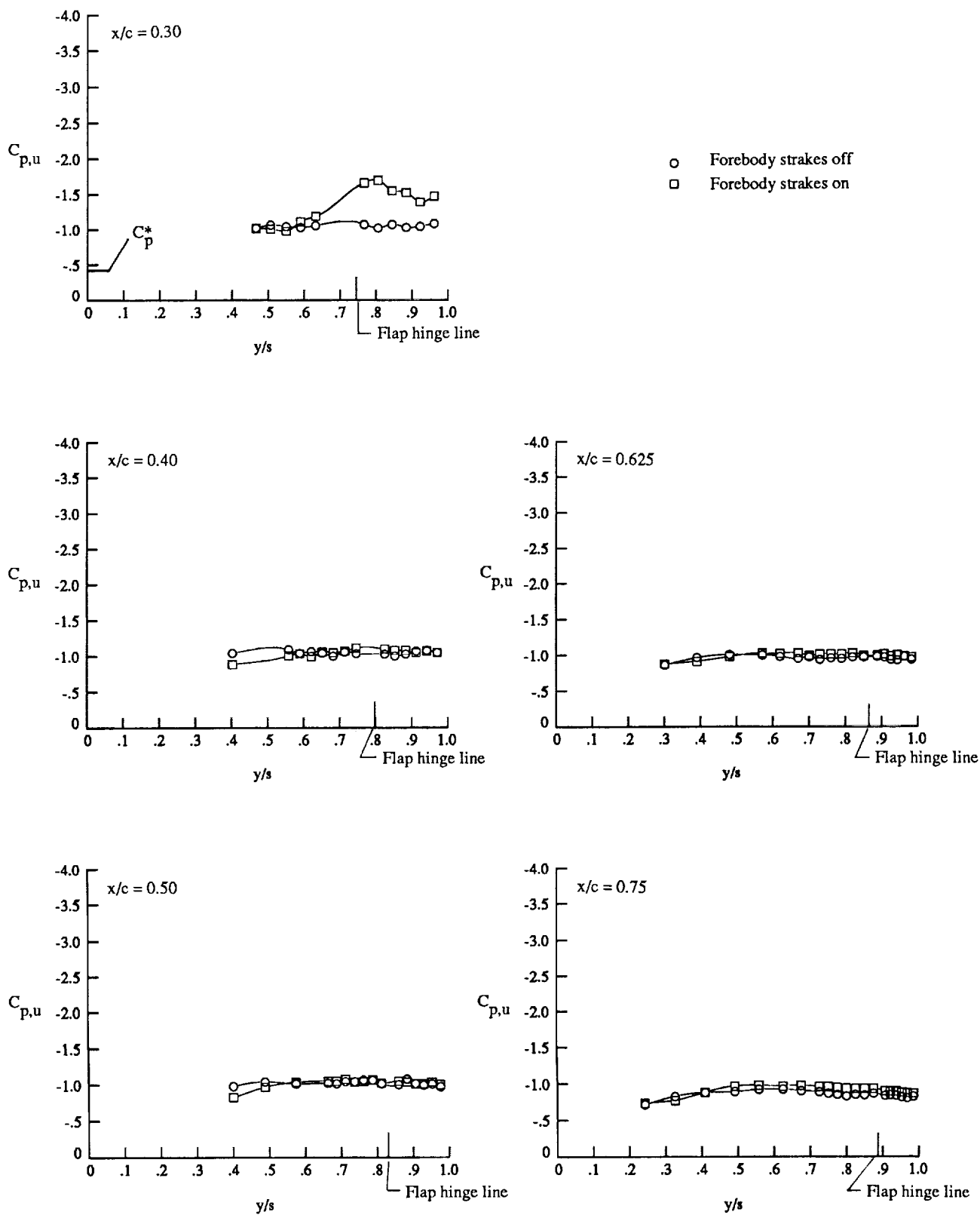
(d) Wing upper surface static pressure distributions at $\alpha \approx 20^\circ$.

Figure 20. Continued.



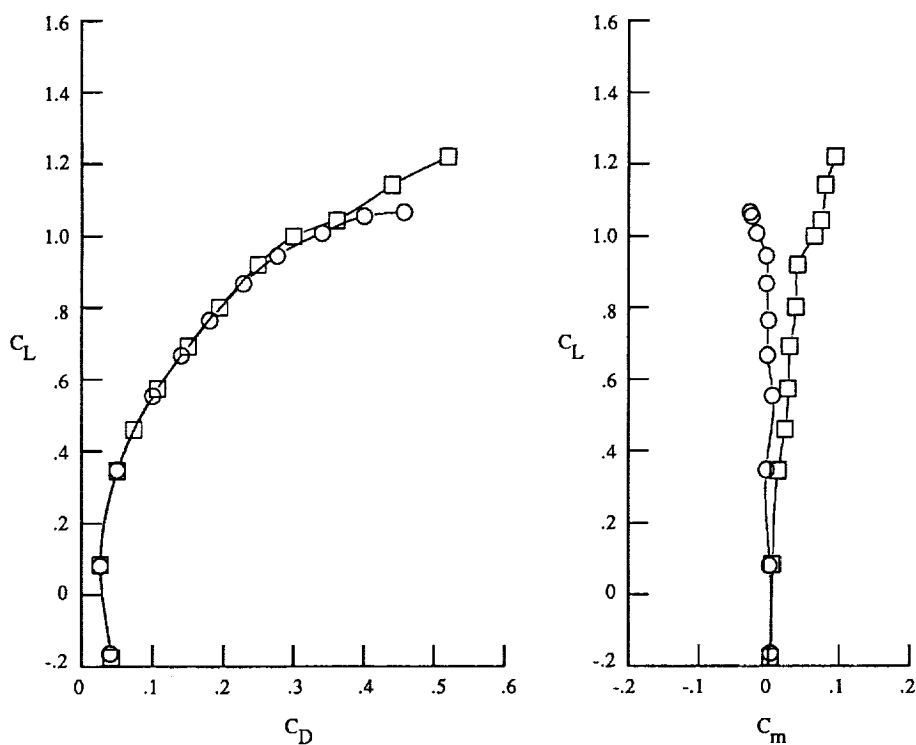
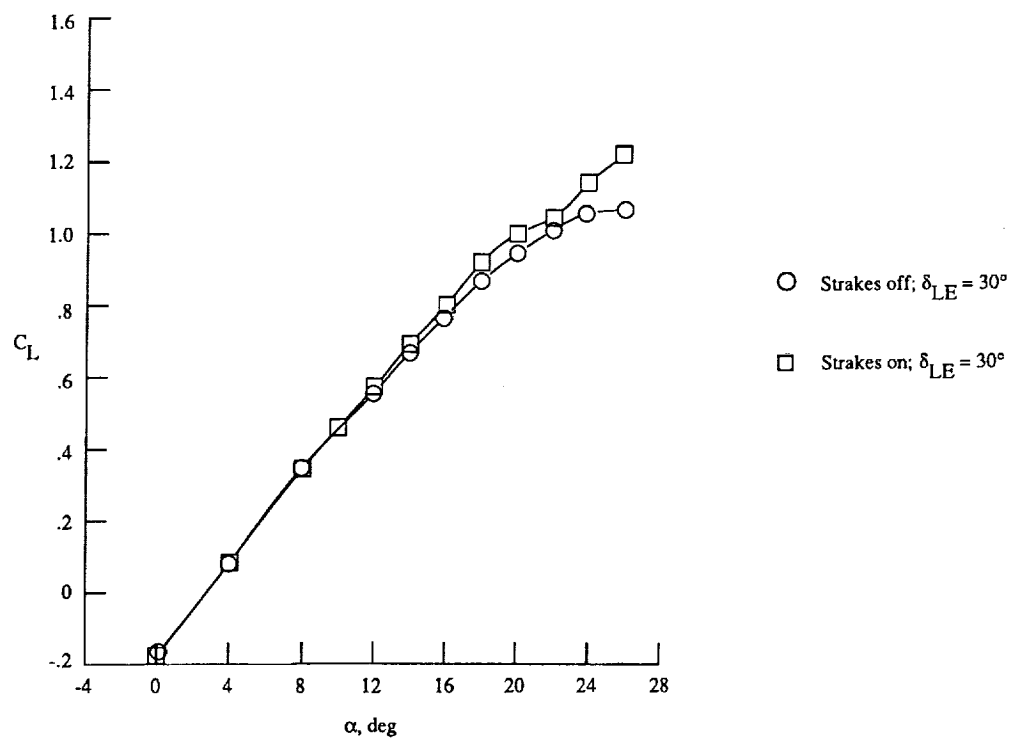
(e) Wing upper surface static pressure distributions at $\alpha \approx 24^\circ$.

Figure 20. Continued.



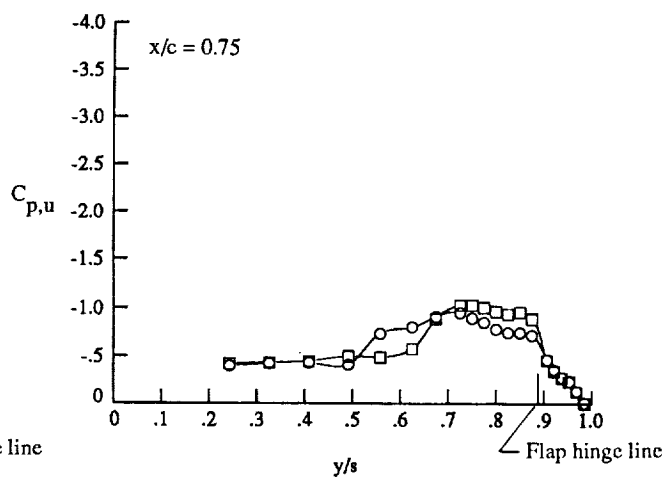
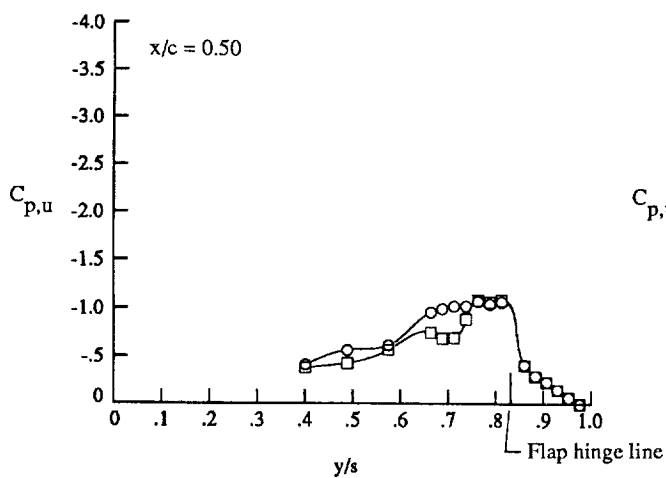
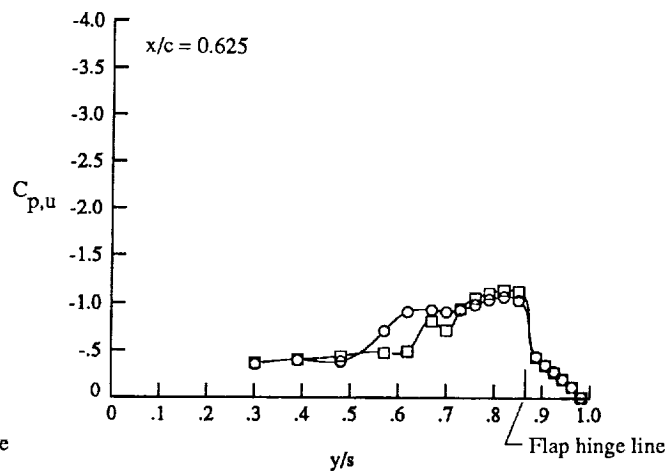
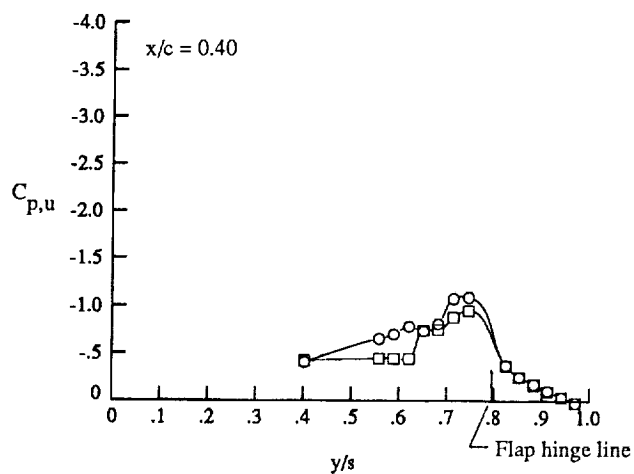
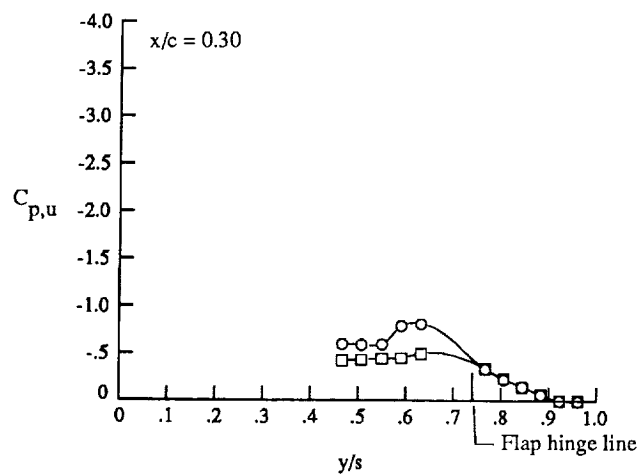
(f) Wing upper surface static pressure distributions at $\alpha \approx 26^\circ$.

Figure 20. Concluded.



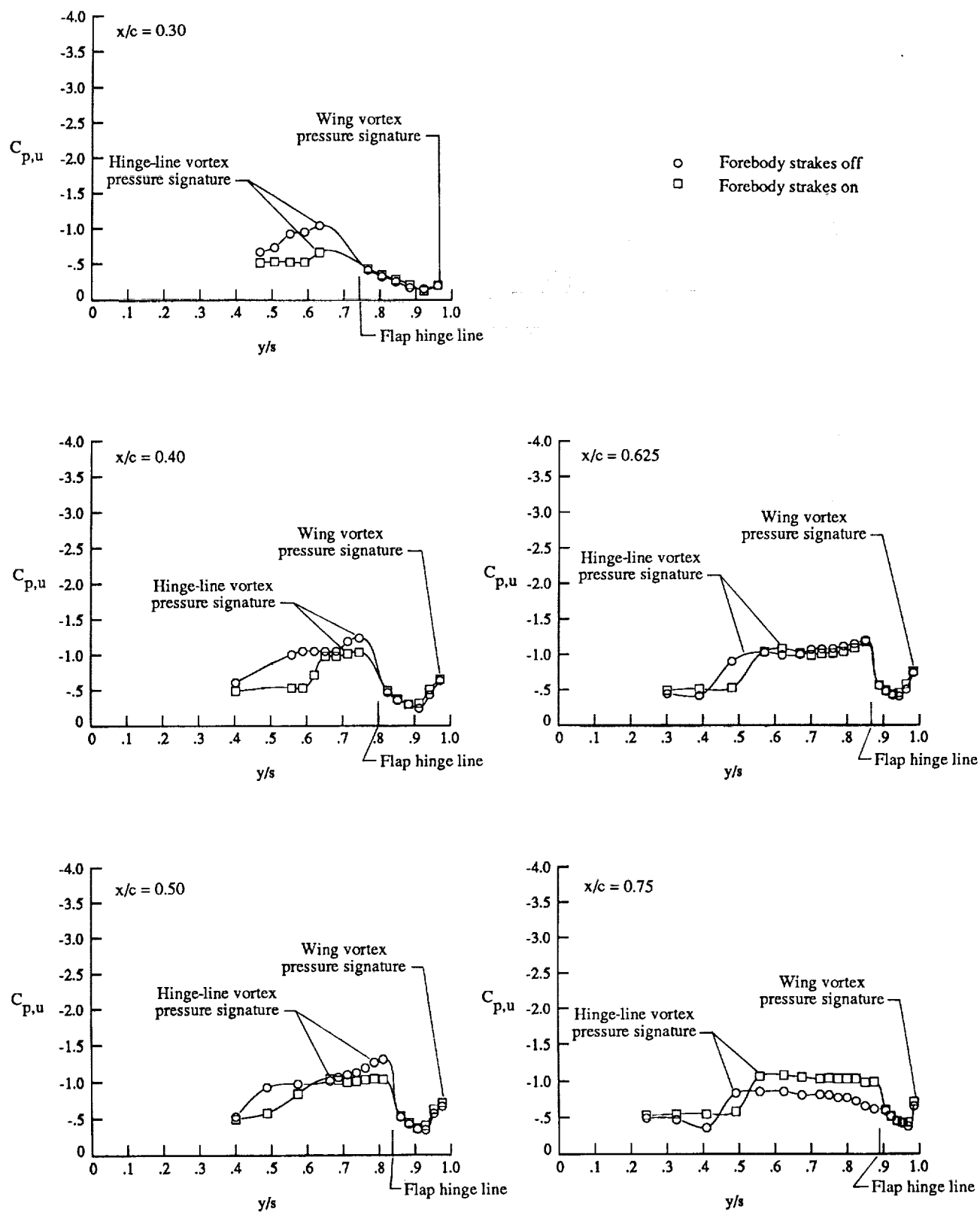
(a) Lift, drag, and pitching moment.

Figure 21. Effect of forebody strakes on longitudinal characteristics at $M_\infty = 0.95$ with $\delta_{LE} = 30^\circ$.



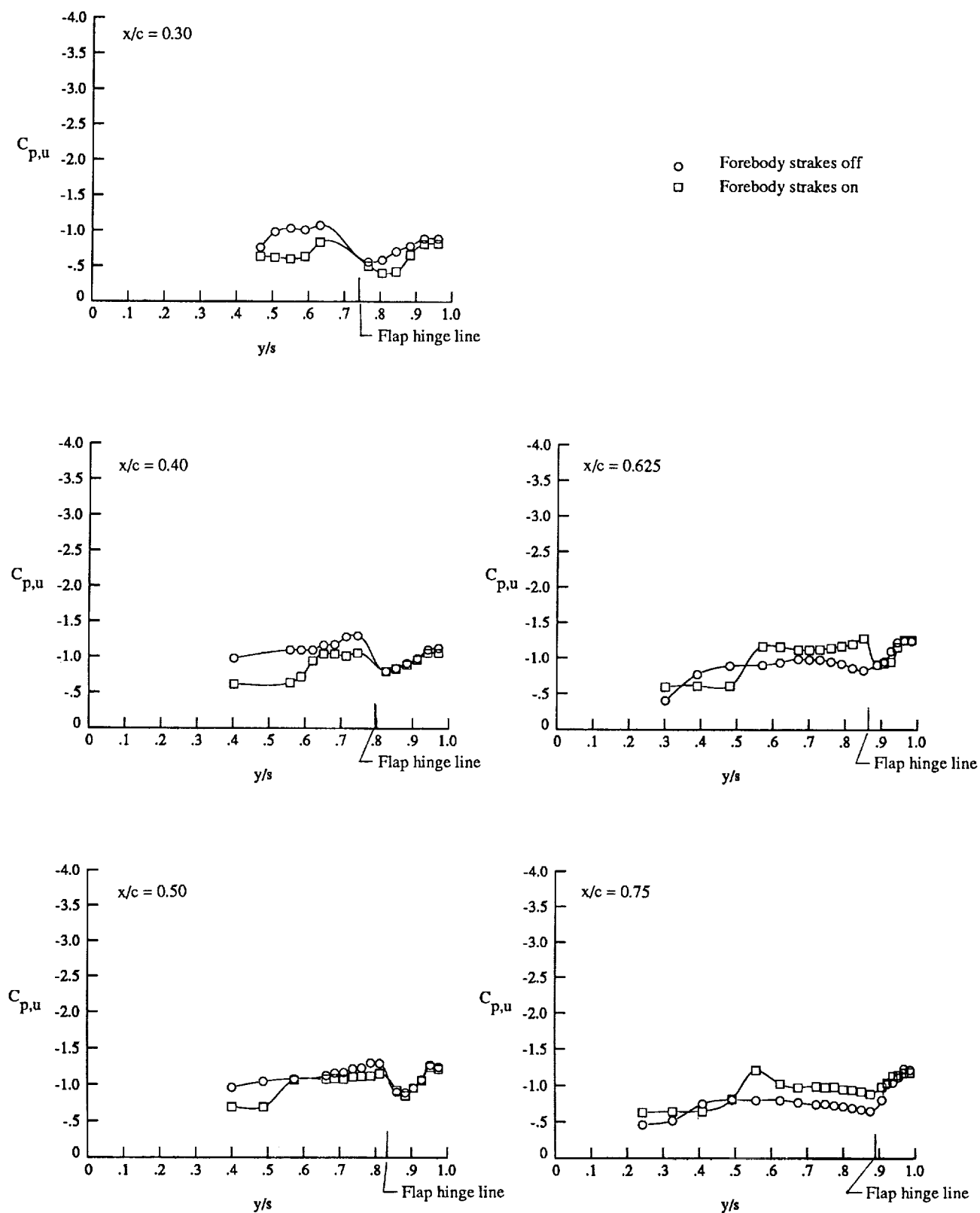
(b) Wing upper surface static pressure distributions at $\alpha \approx 12^\circ$.

Figure 21. Continued.



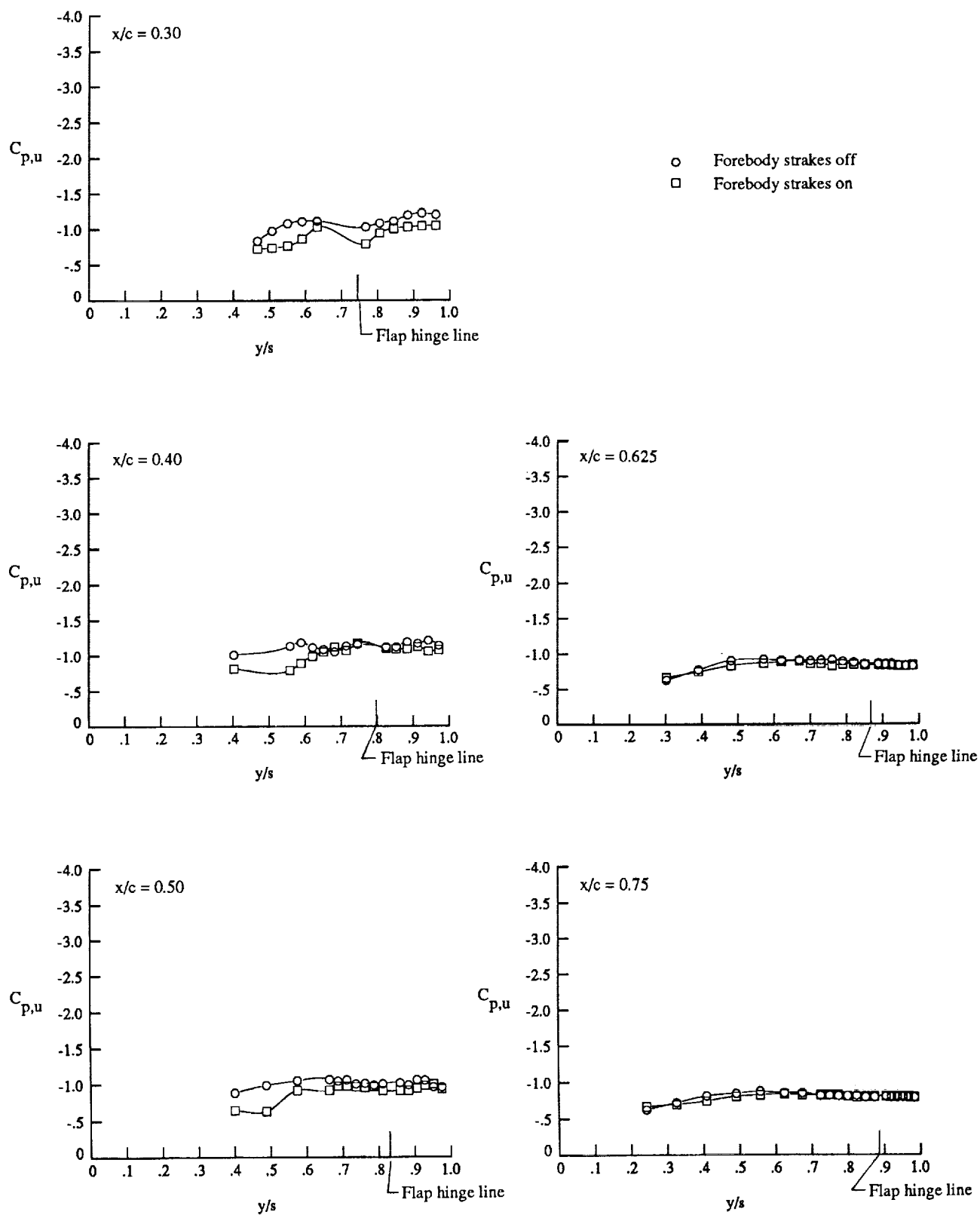
(c) Wing upper surface static pressure distributions at $\alpha \approx 16^\circ$.

Figure 21. Continued.



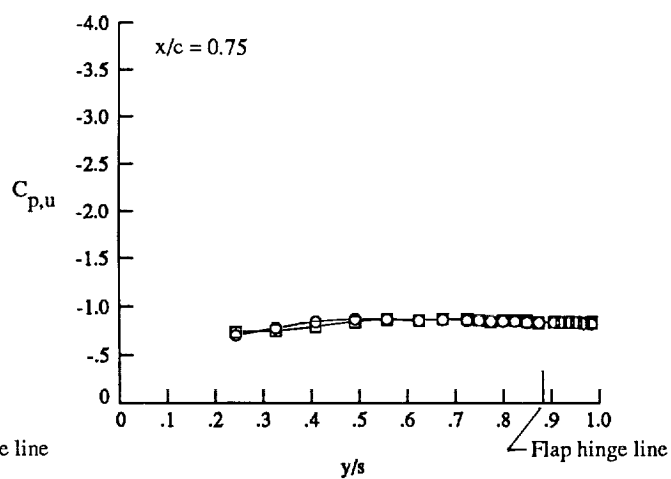
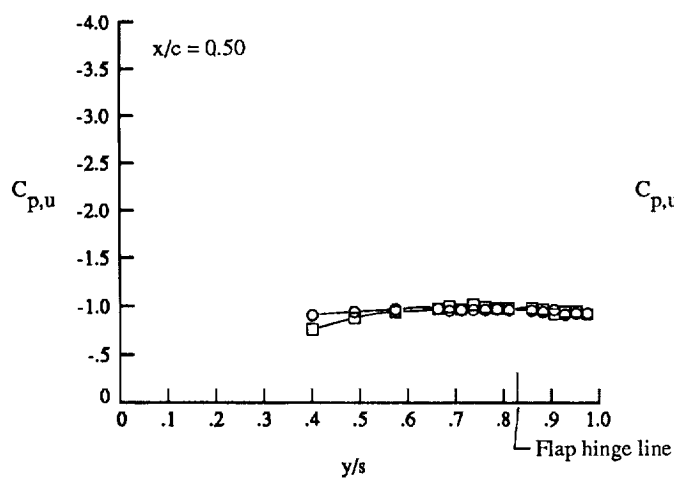
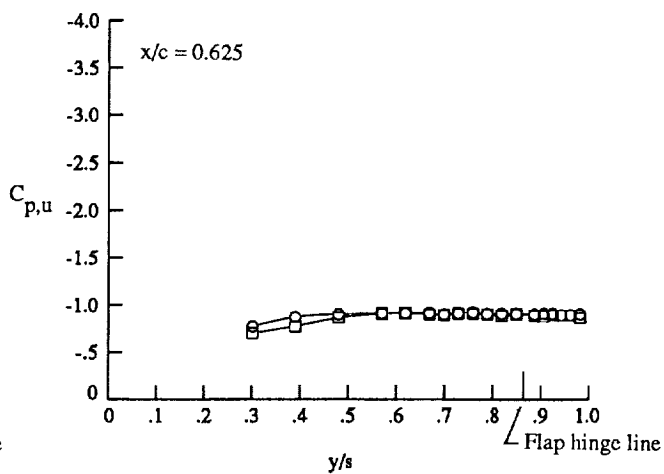
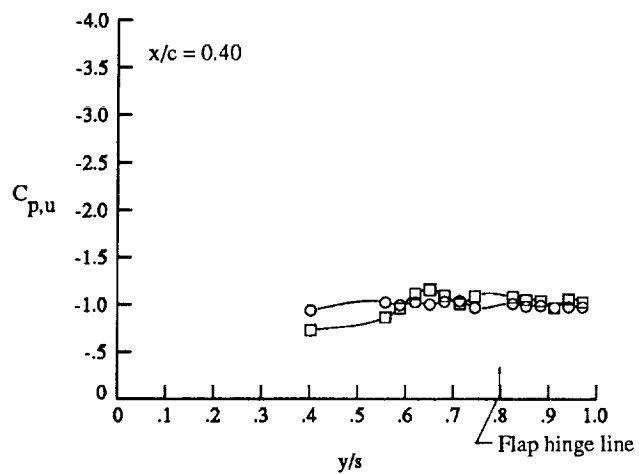
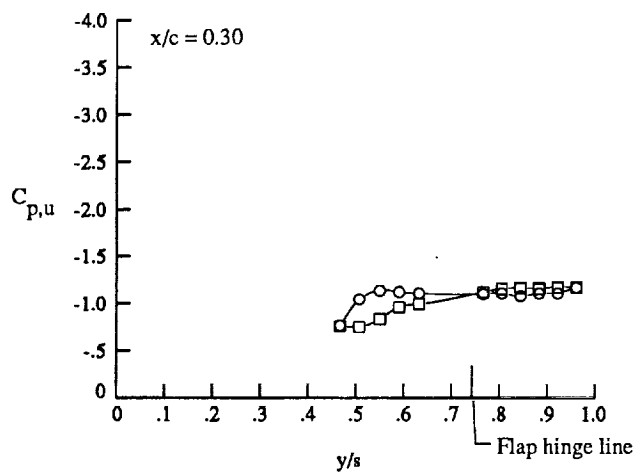
(d) Wing upper surface static pressure distributions at $\alpha \approx 20^\circ$.

Figure 21. Continued.



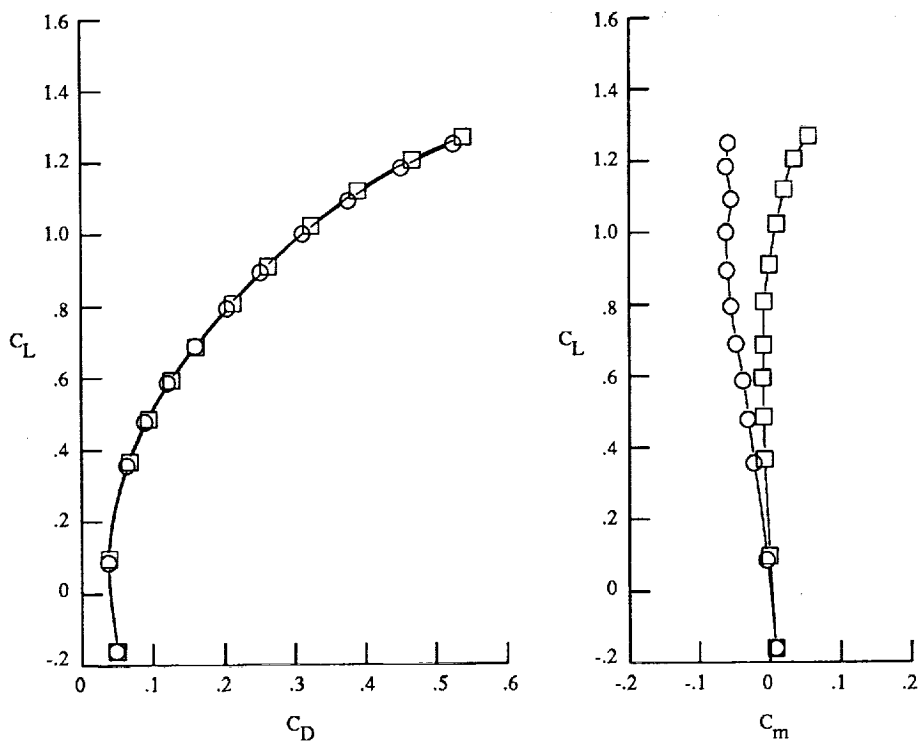
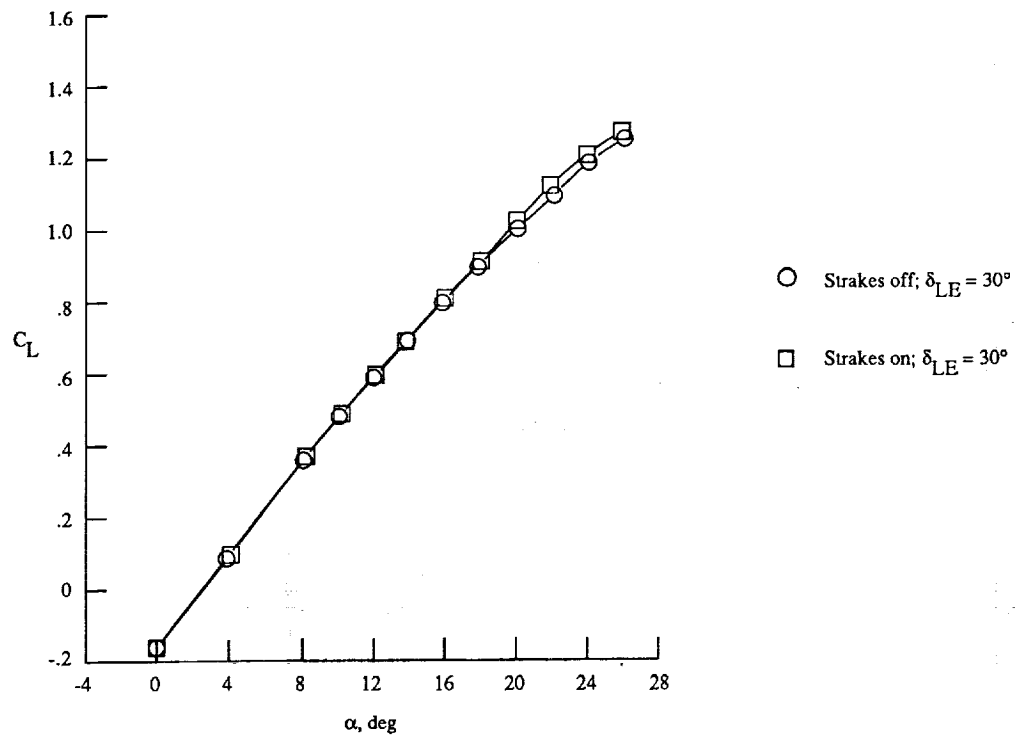
(e) Wing upper surface static pressure distributions at $\alpha \approx 24^\circ$.

Figure 21. Continued.



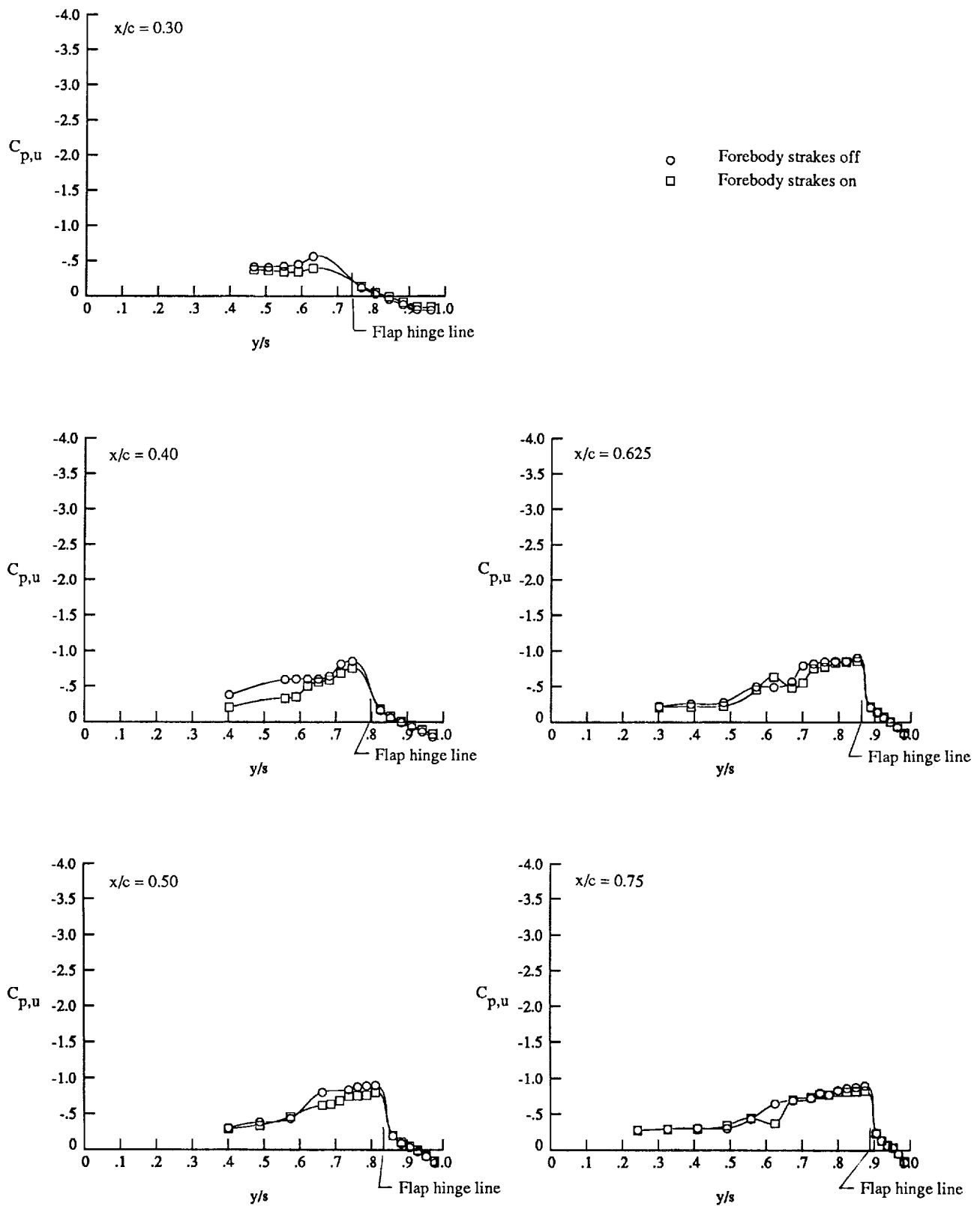
(f) Wing upper surface static pressure distributions at $\alpha \approx 26^\circ$.

Figure 21. Concluded.



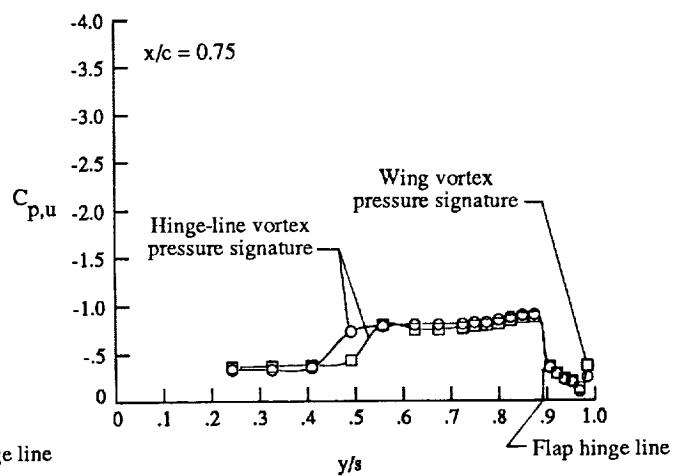
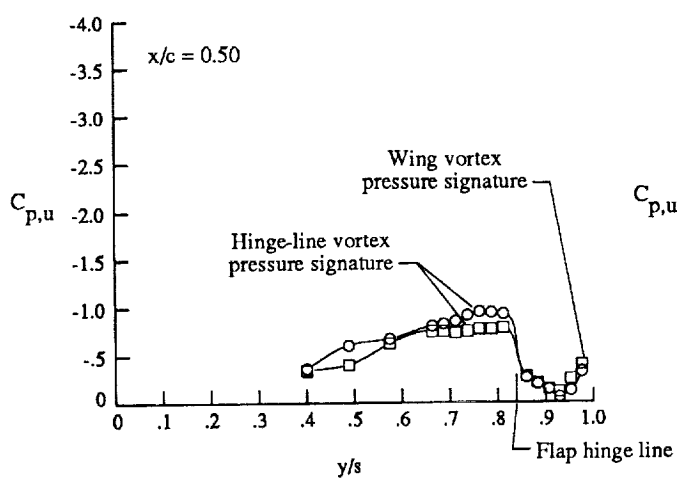
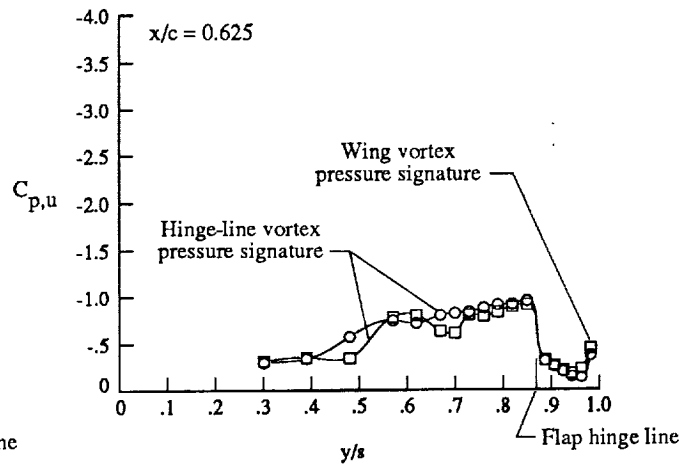
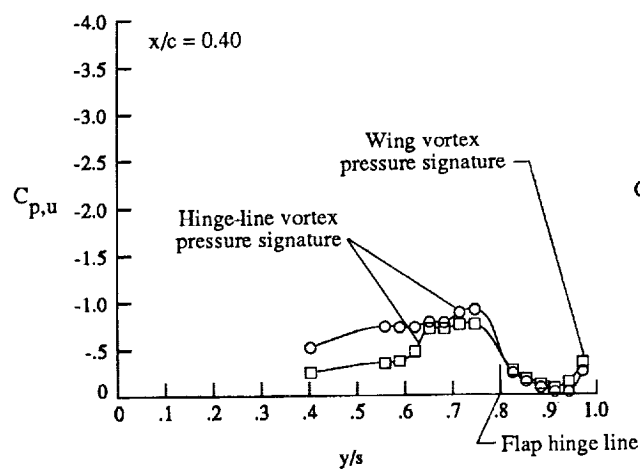
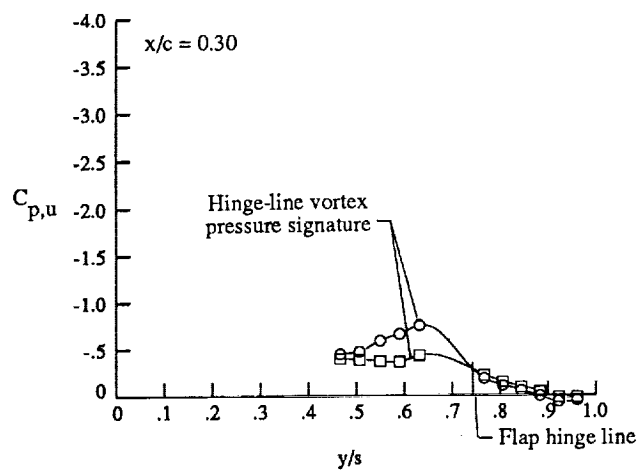
(a) Lift, drag, and pitching moment.

Figure 22. Effect of forebody strakes on longitudinal characteristics at $M_\infty = 1.10$ with $\delta_{LE} = 30^\circ$.



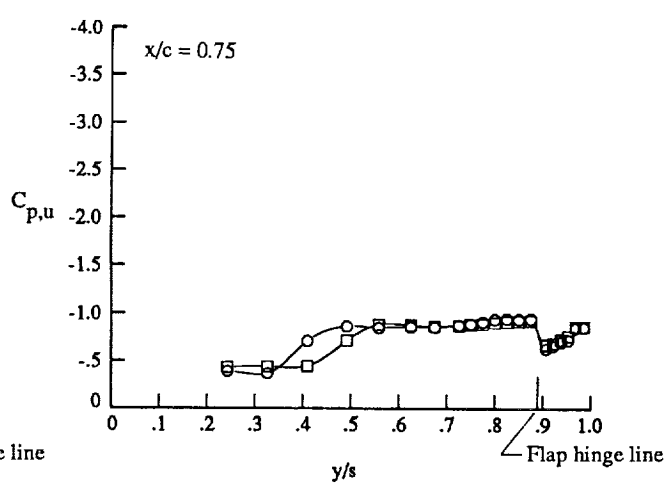
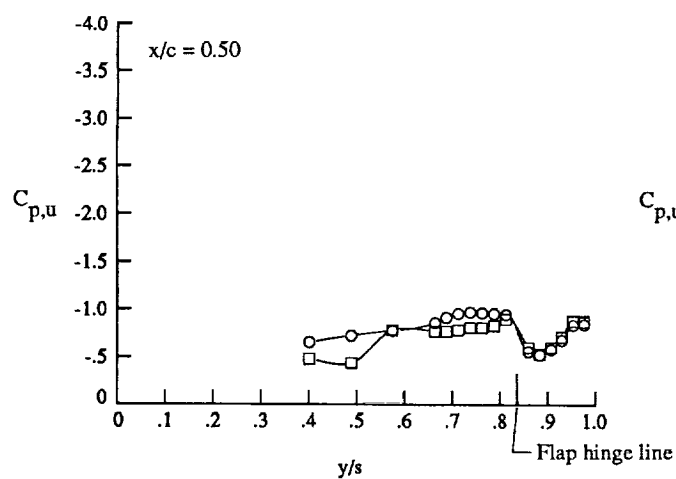
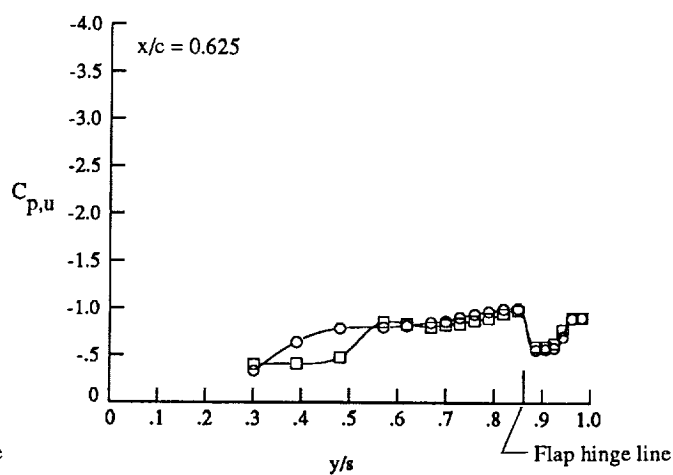
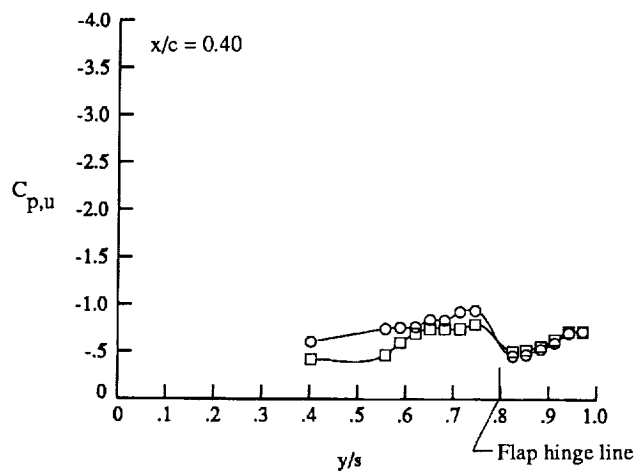
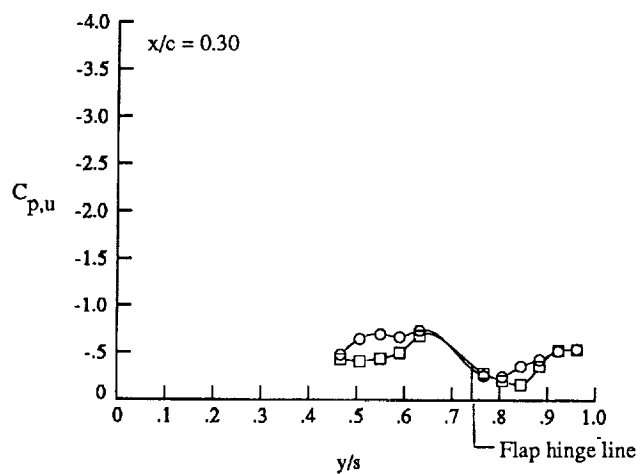
(b) Wing upper surface static pressure distributions at $\alpha \approx 12^\circ$.

Figure 22. Continued.



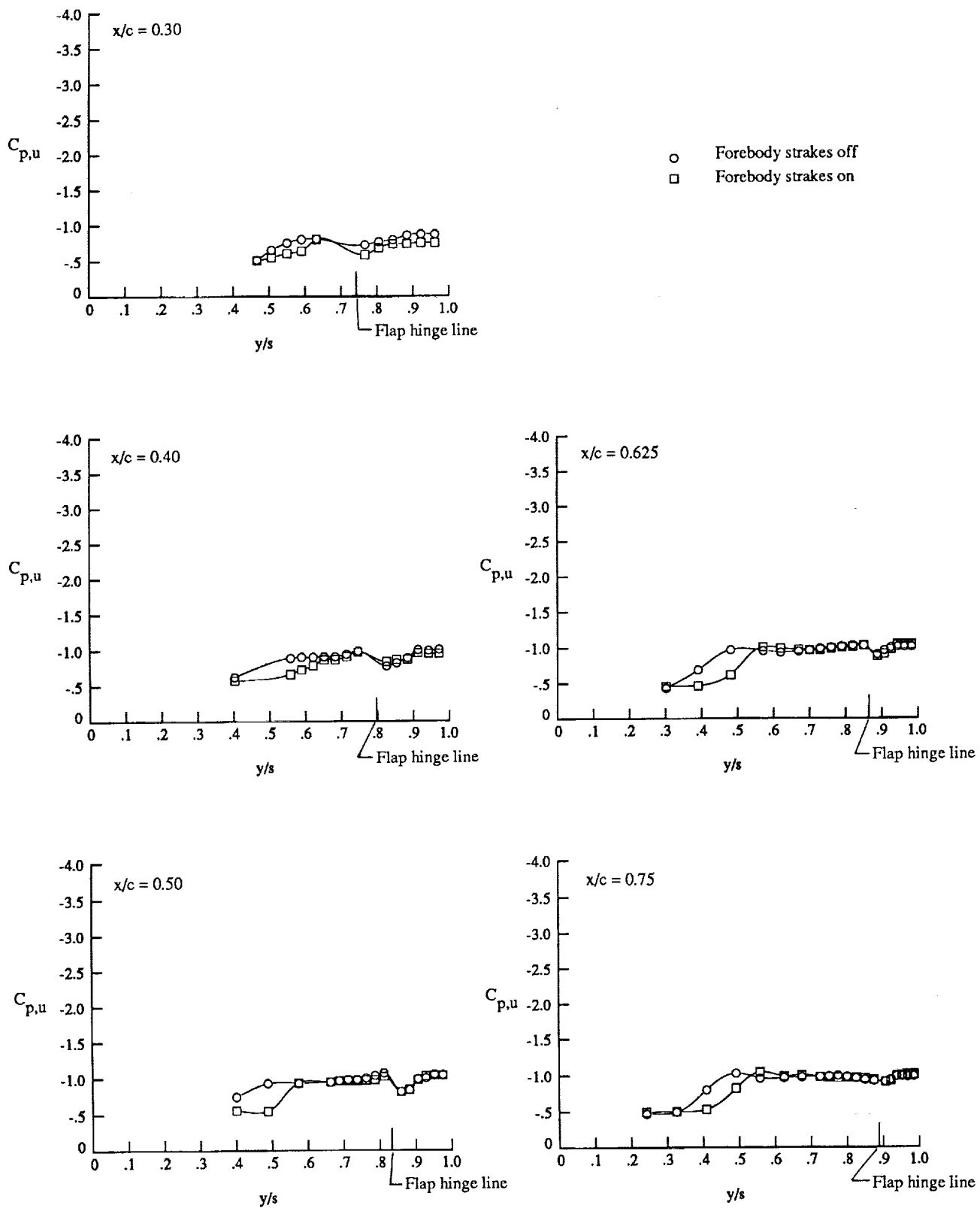
(c) Wing upper surface static pressure distributions at $\alpha \approx 16^\circ$.

Figure 22. Continued.



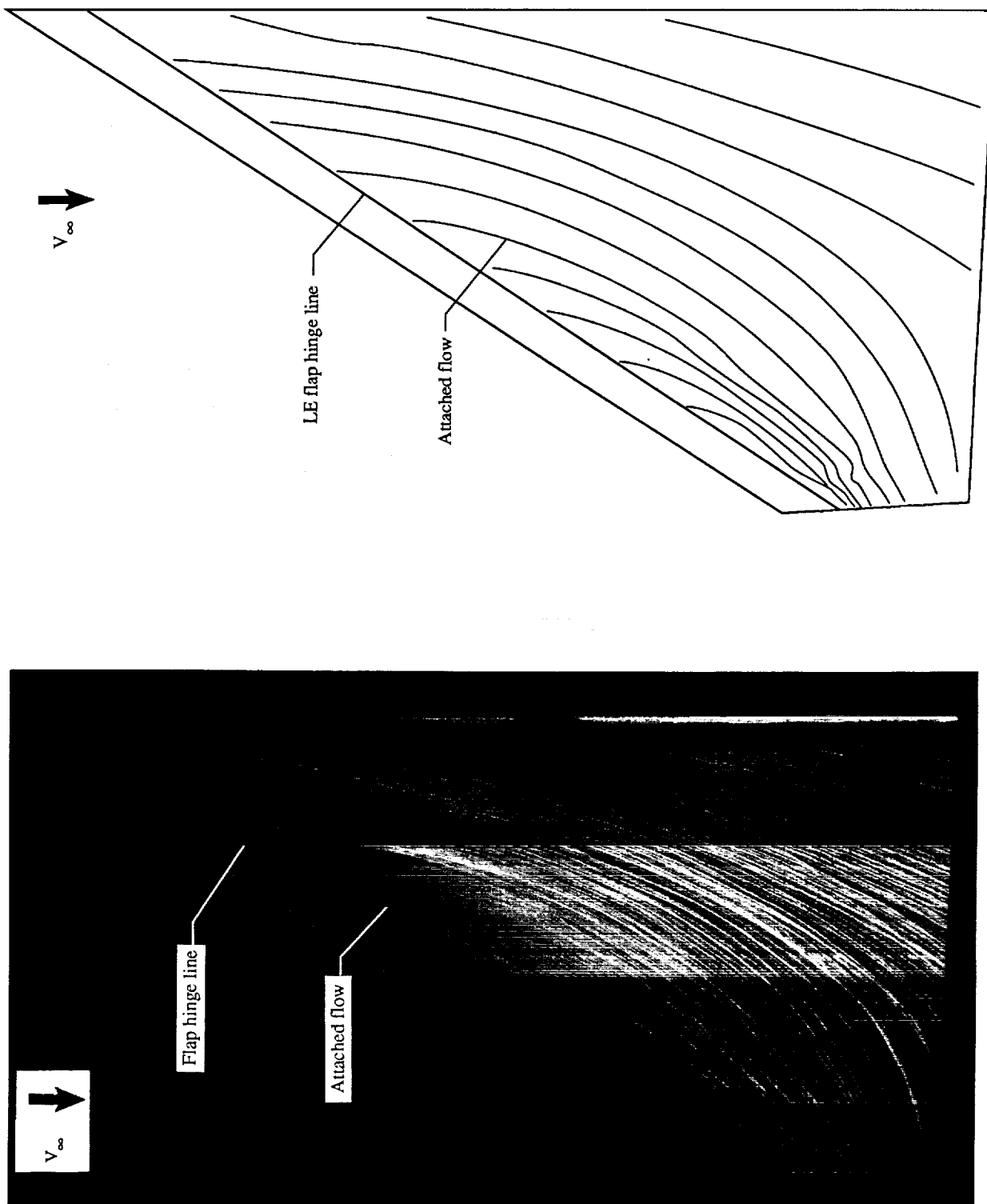
(d) Wing upper surface static pressure distributions at $\alpha \approx 20^\circ$.

Figure 22. Continued.



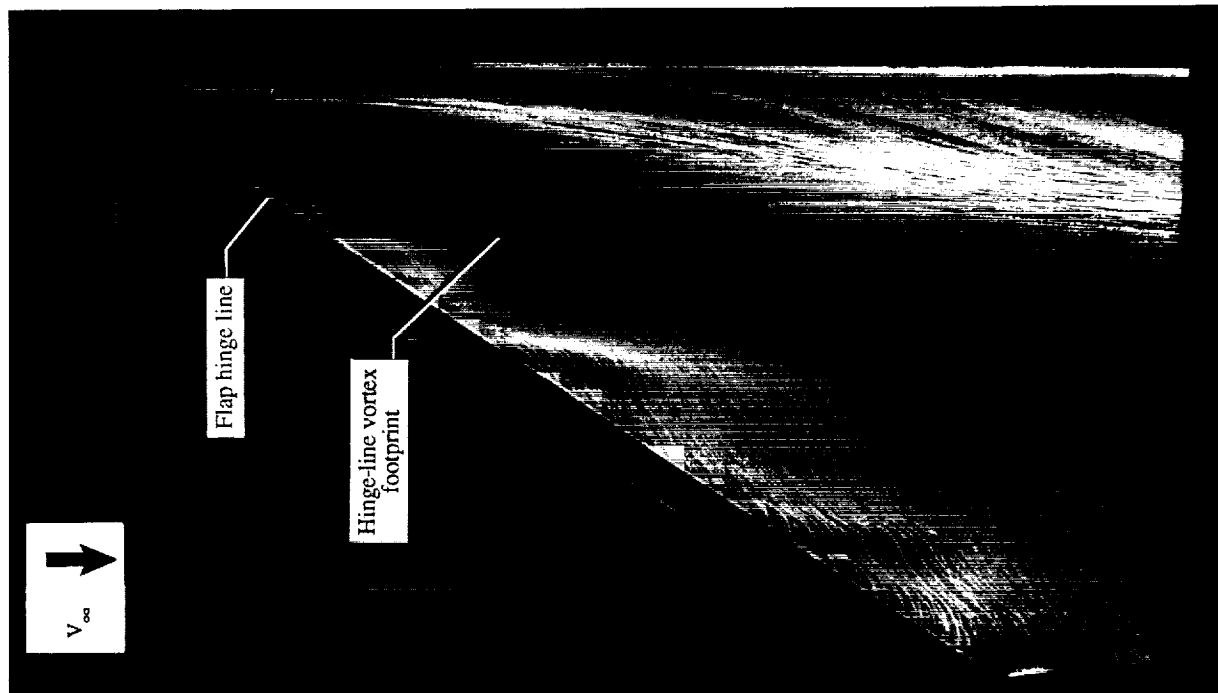
(e) Wing upper surface static pressure distributions at $\alpha \approx 24^\circ$.

Figure 22. Concluded.



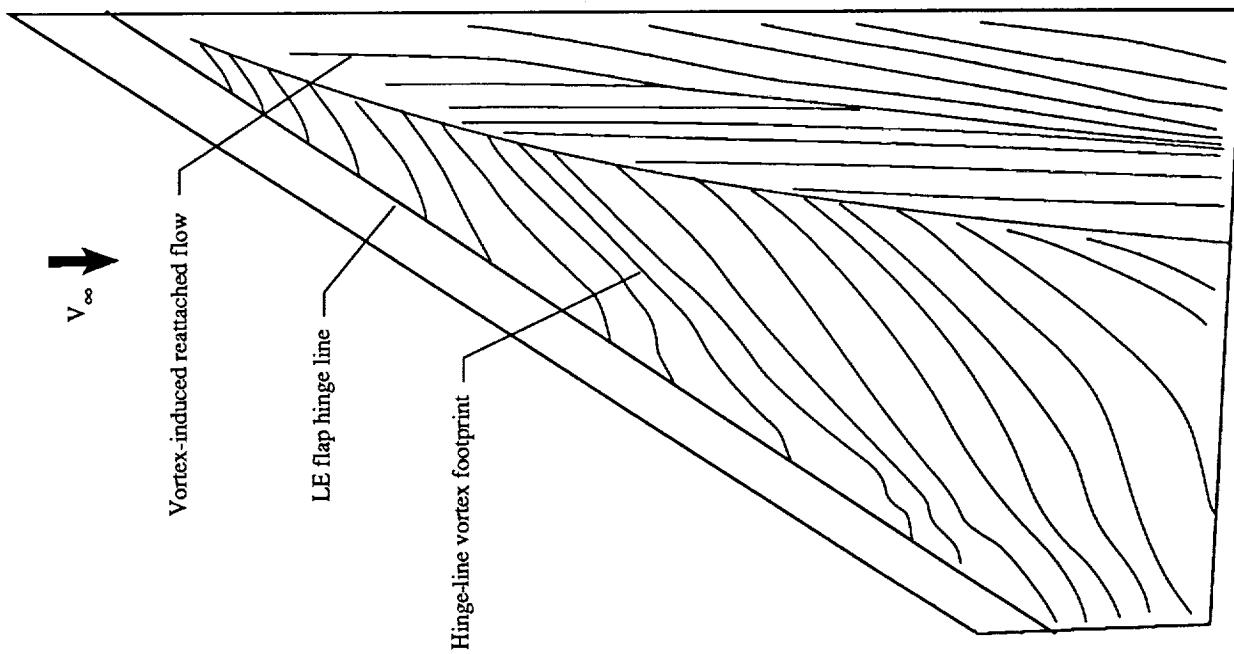
(a) $M_\infty = 0.40$; $\alpha \approx 17^\circ$; $C_L \approx 0.67$.

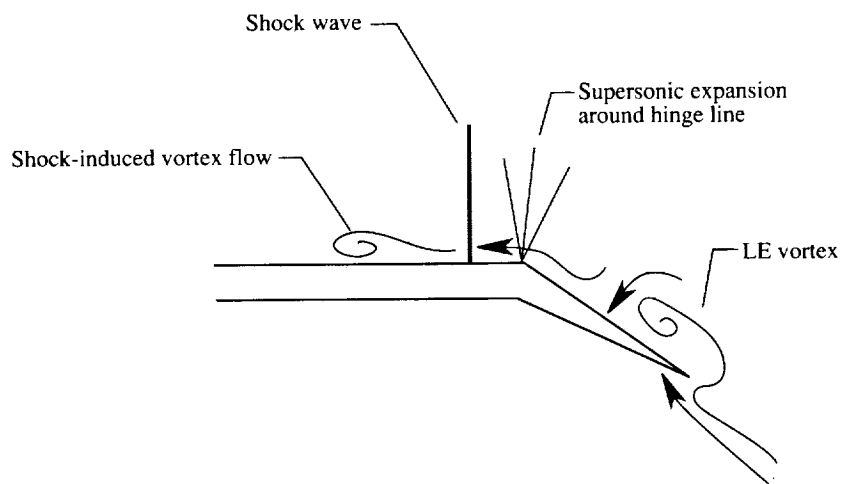
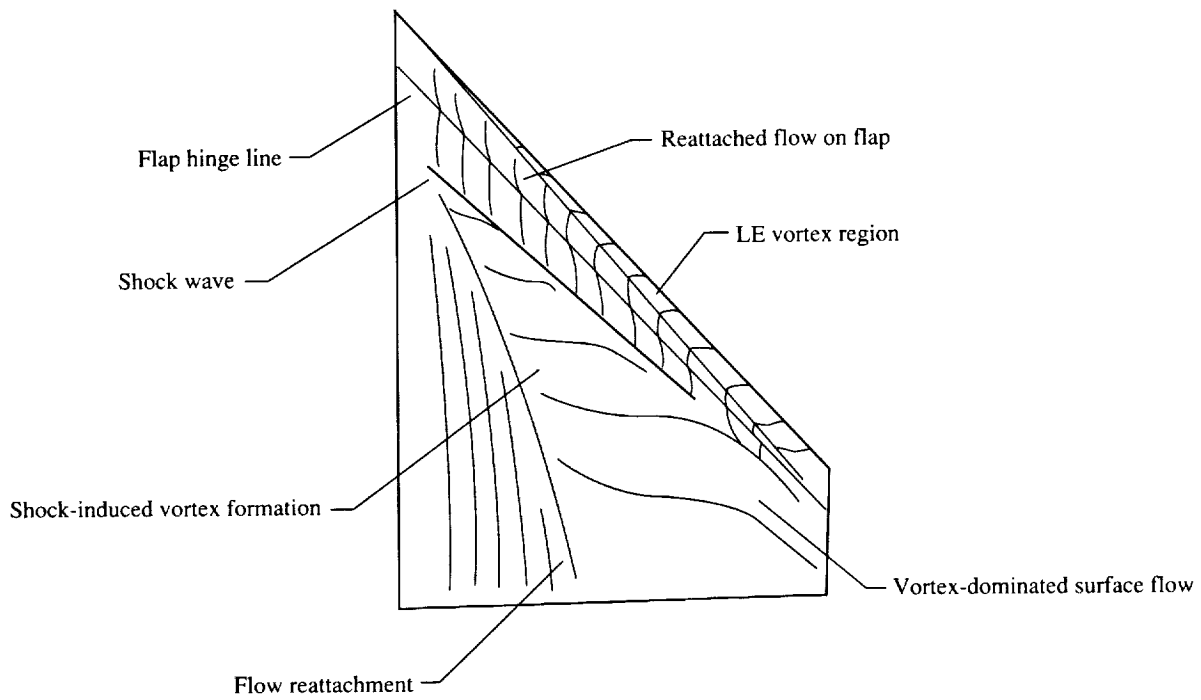
Figure 23. Wing upper surface flow patterns illustrating leading-edge flap hinge-line vortex for $\delta_{LE} = 30^\circ$.
(Oil flow photographs taken from ref. 17.)



(b) $M_\infty = 0.70$; $\alpha \approx 16^\circ$; $C_L \approx 0.67$.

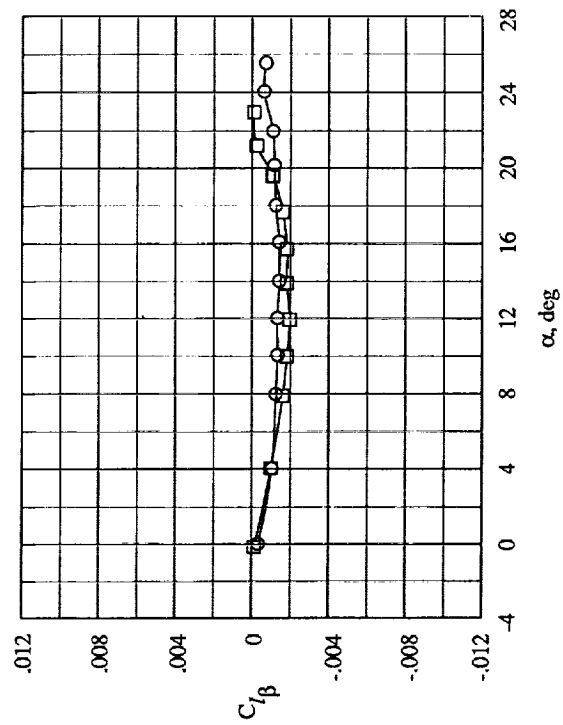
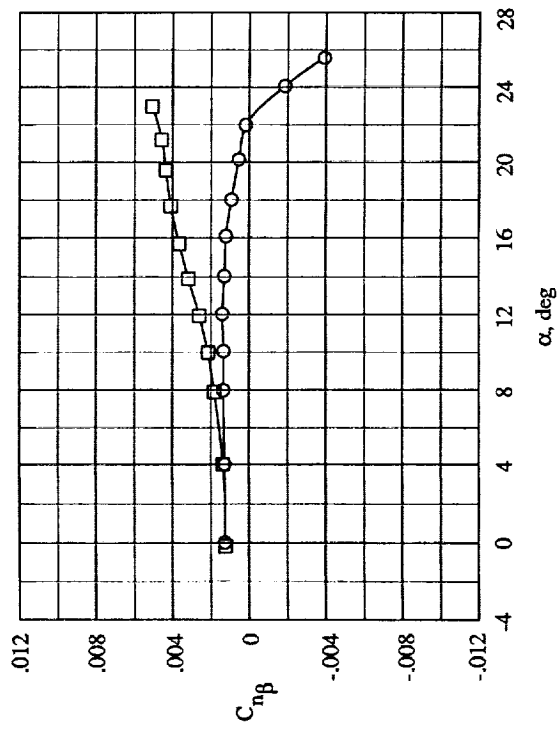
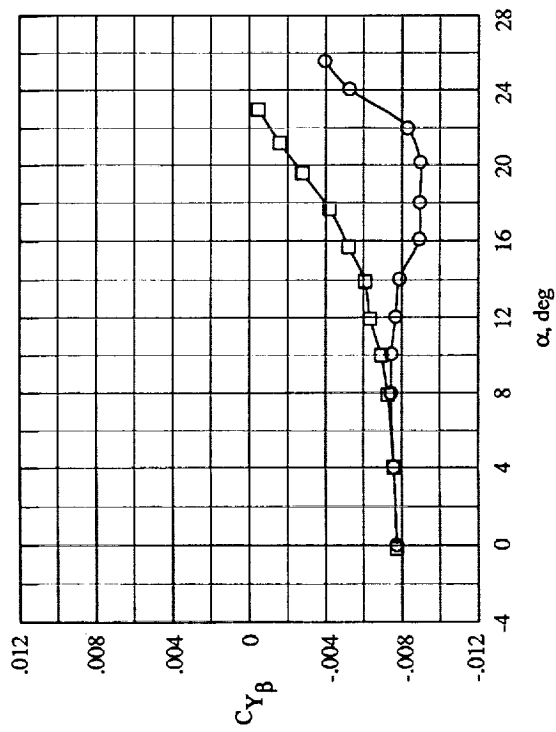
Figure 23. Continued.





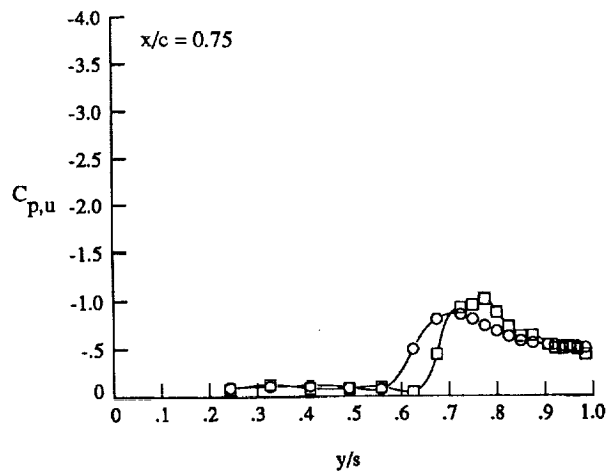
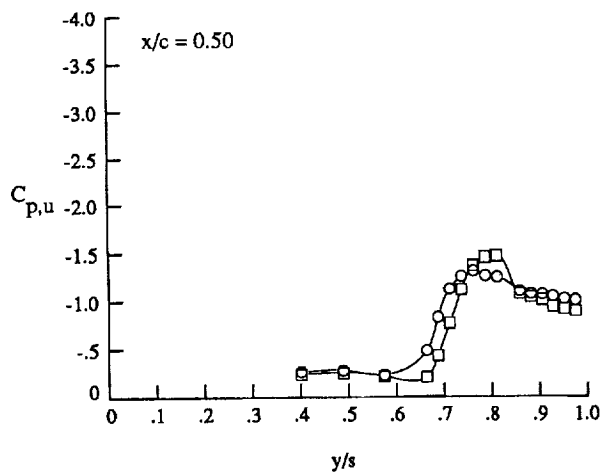
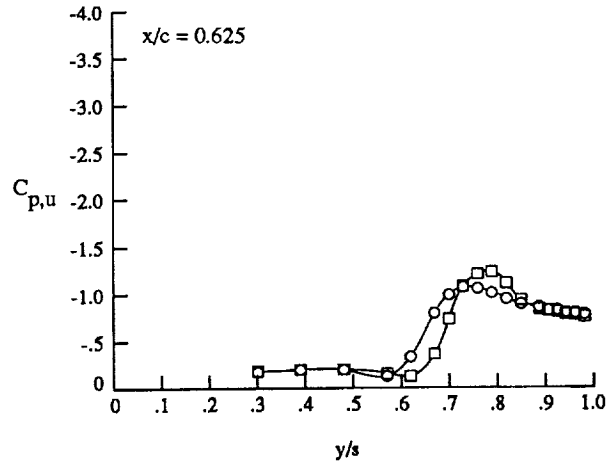
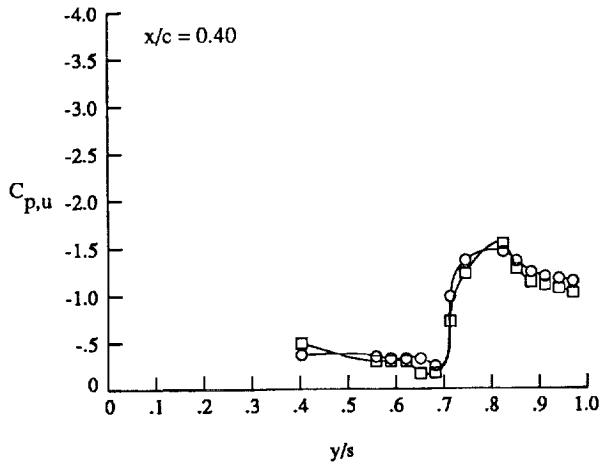
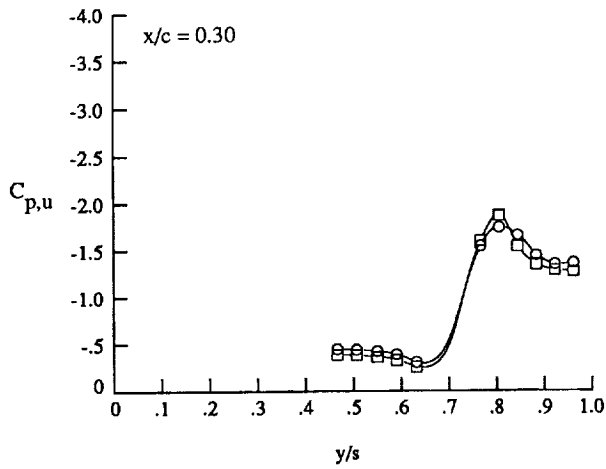
(c) Shock-induced hinge-line vortex formation.

Figure 23. Concluded.



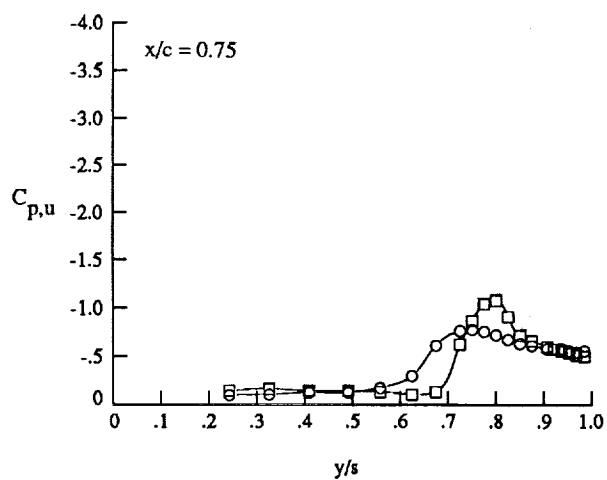
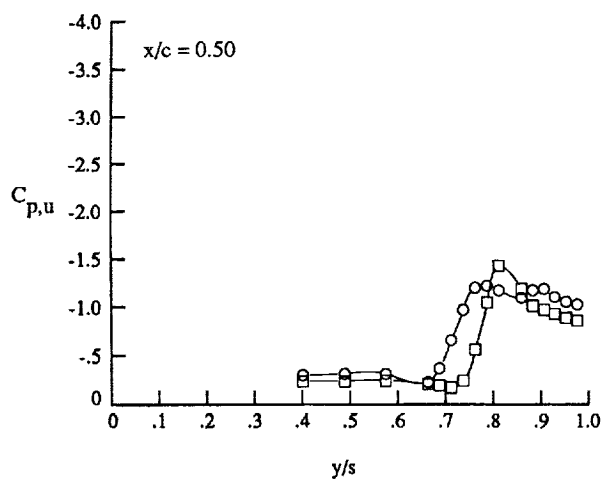
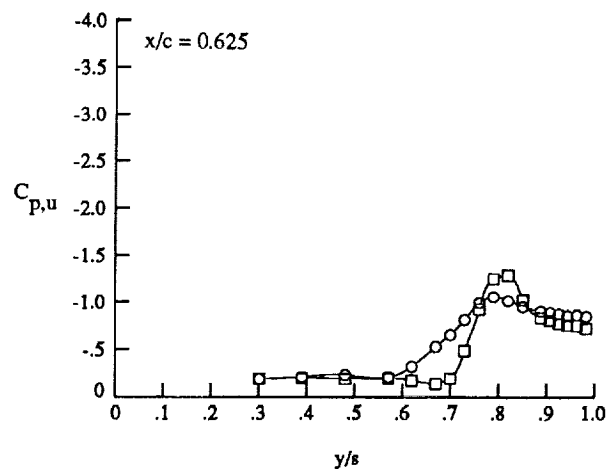
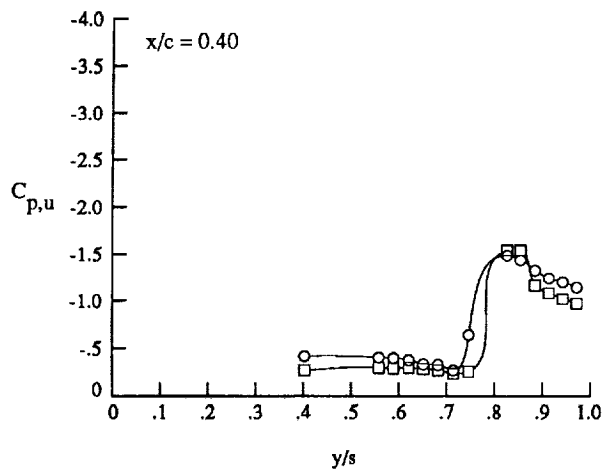
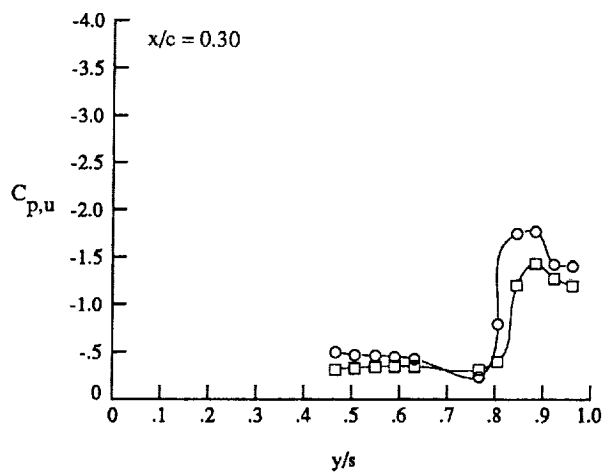
(a) Lateral-directional stability derivatives.

Figure 24. Effect of forebody strakes on lateral-directional characteristics at $M_\infty = 0.40$ with $\delta_{LE} = 0^\circ$.



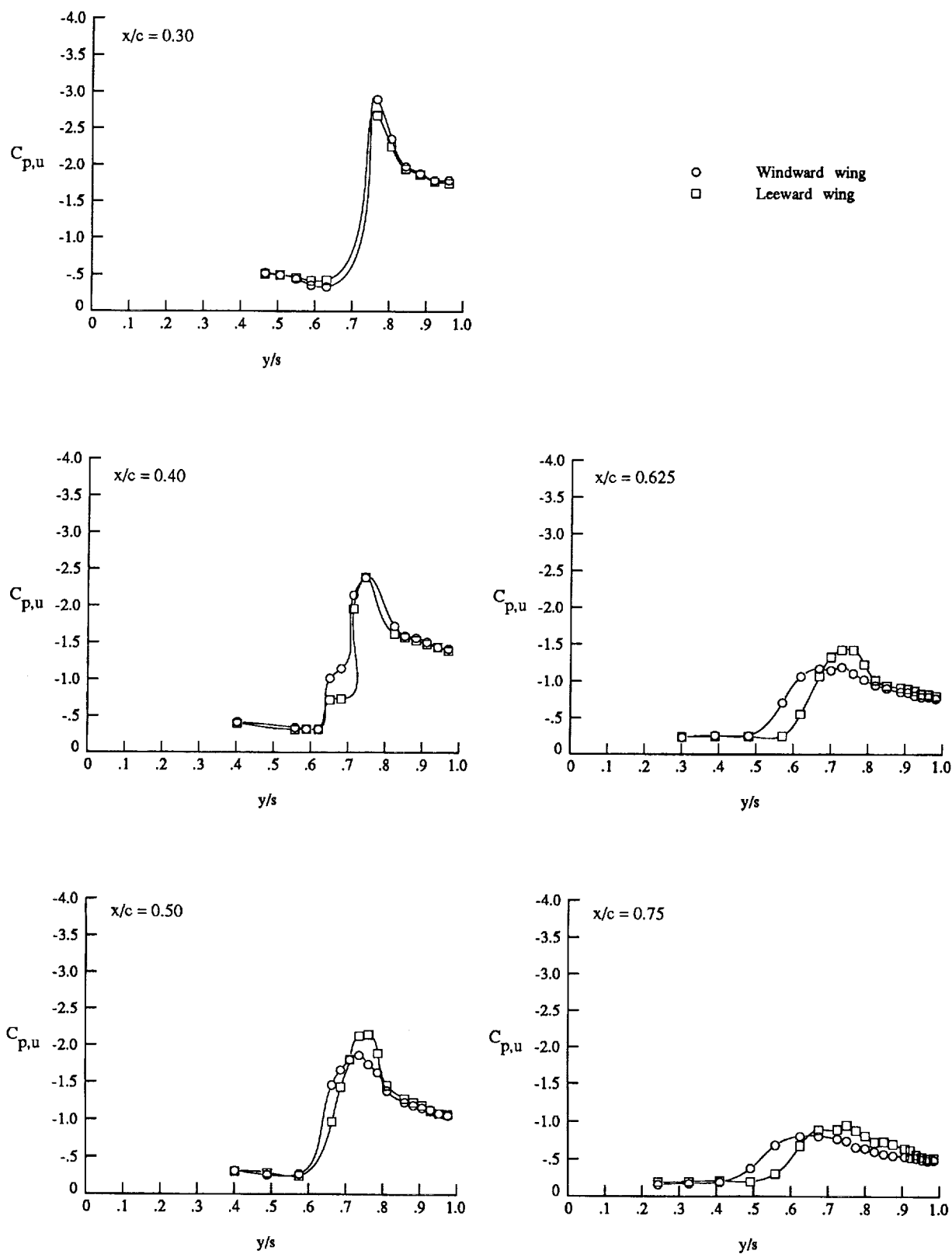
(b) Wing upper surface static pressure distributions with strakes off at $\alpha \approx 12^\circ$.

Figure 24. Continued.



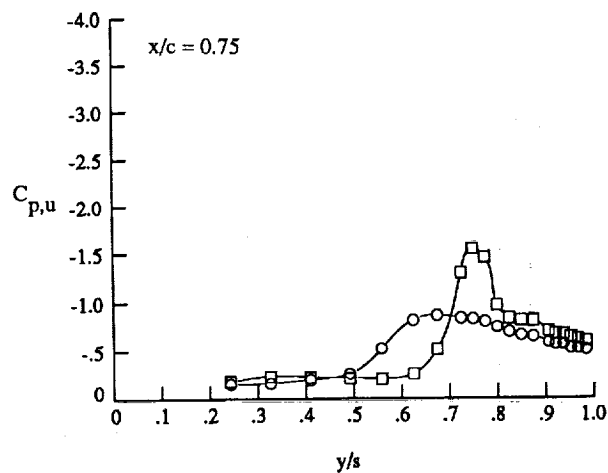
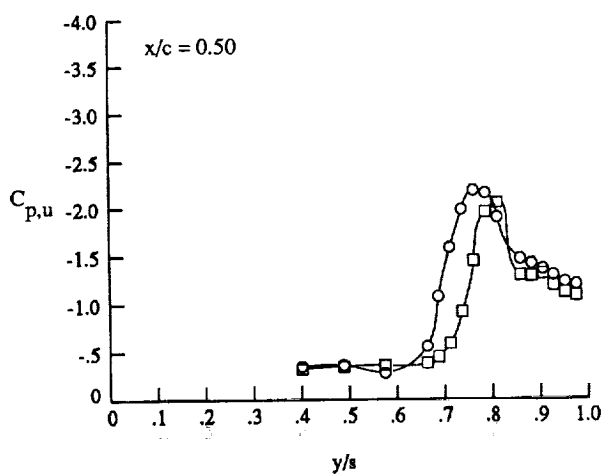
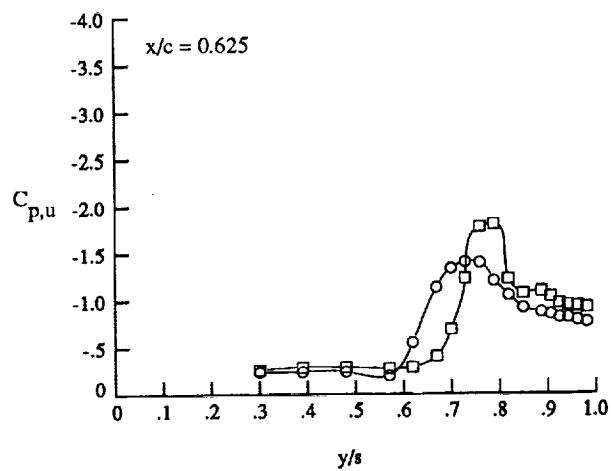
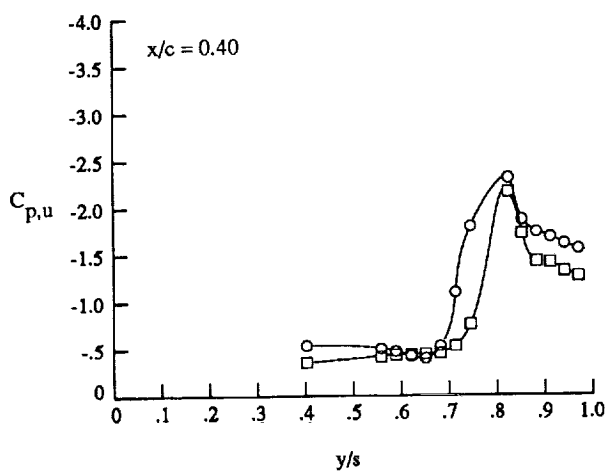
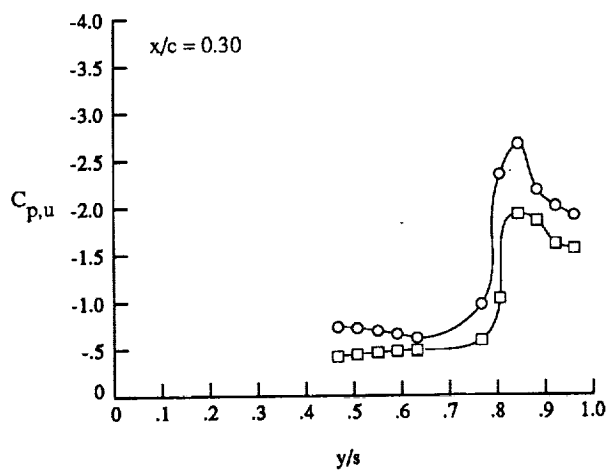
(c) Wing upper surface static pressure distributions with strakes on at $\alpha \approx 12^\circ$.

Figure 24. Continued.



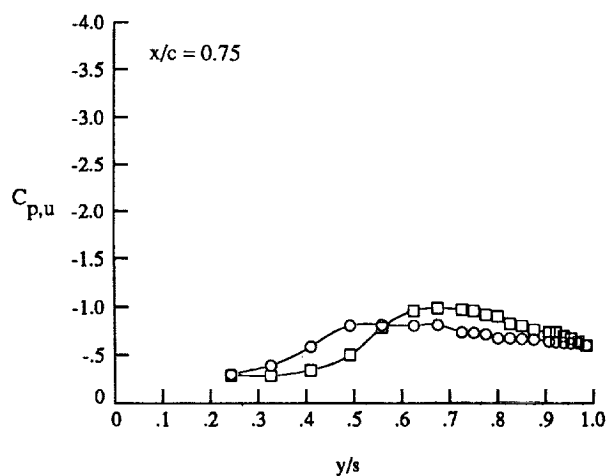
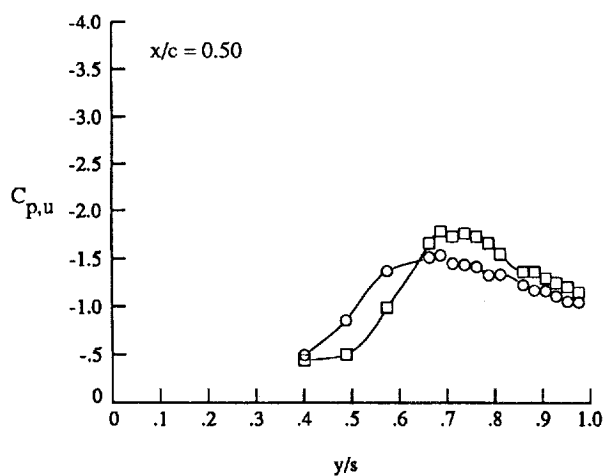
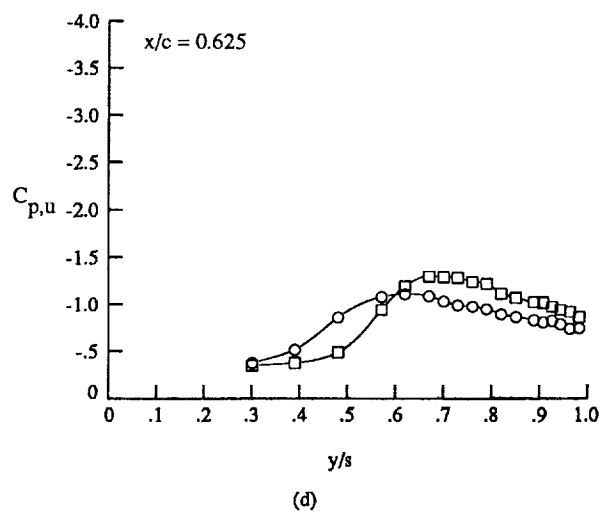
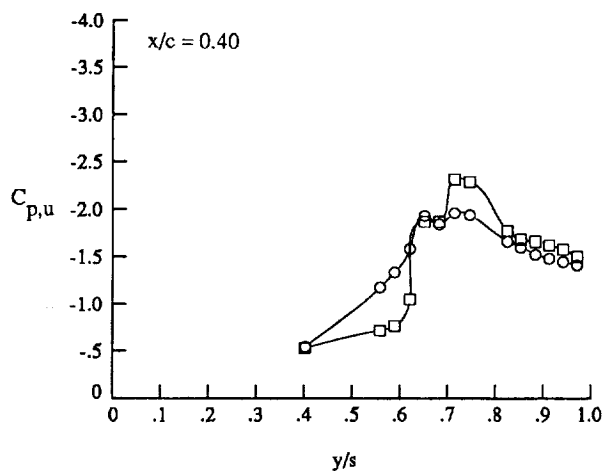
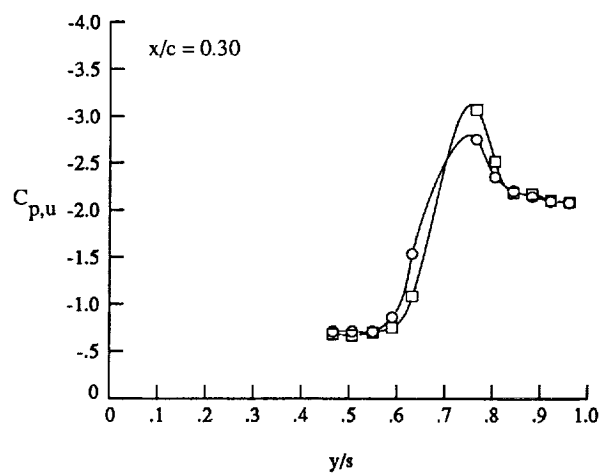
(d) Wing upper surface static pressure distributions with strakes off at $\alpha \approx 16^\circ$.

Figure 24. Continued.



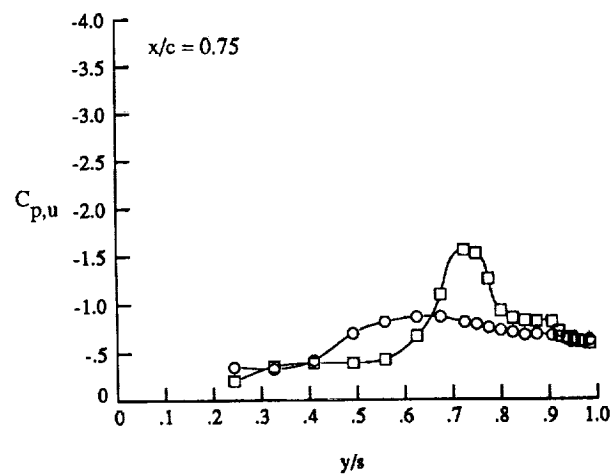
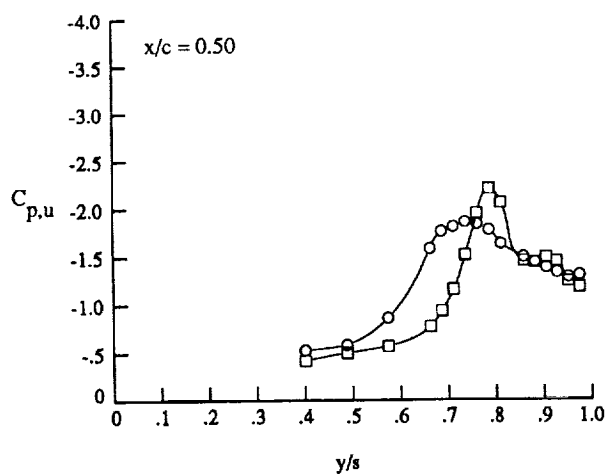
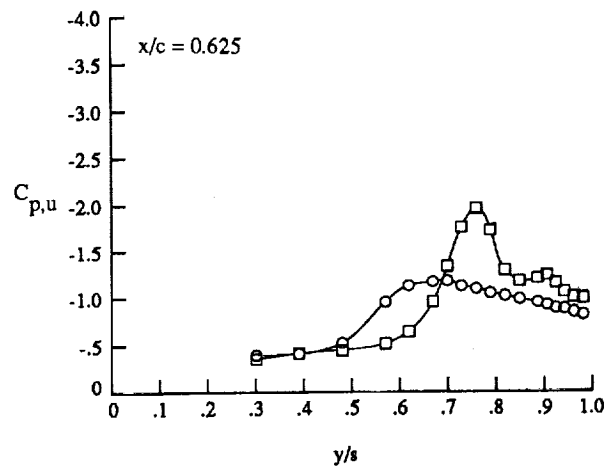
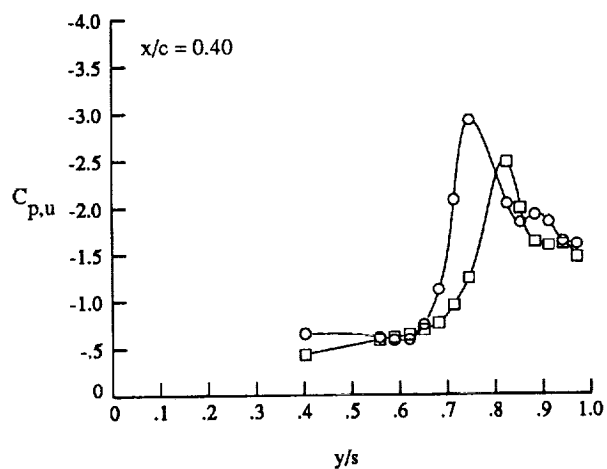
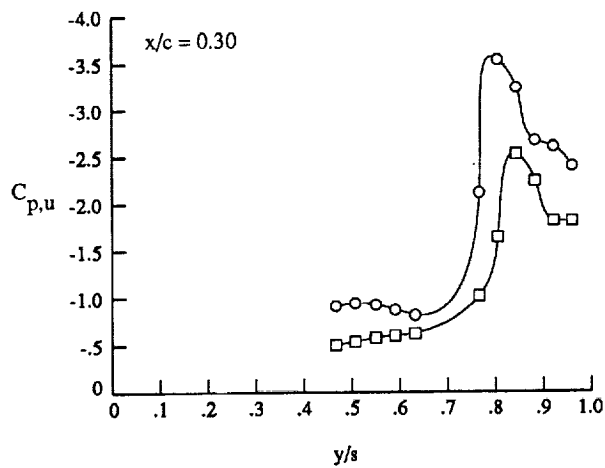
(e) Wing upper surface static pressure distributions with strakes on at $\alpha \approx 16^\circ$.

Figure 24. Continued.



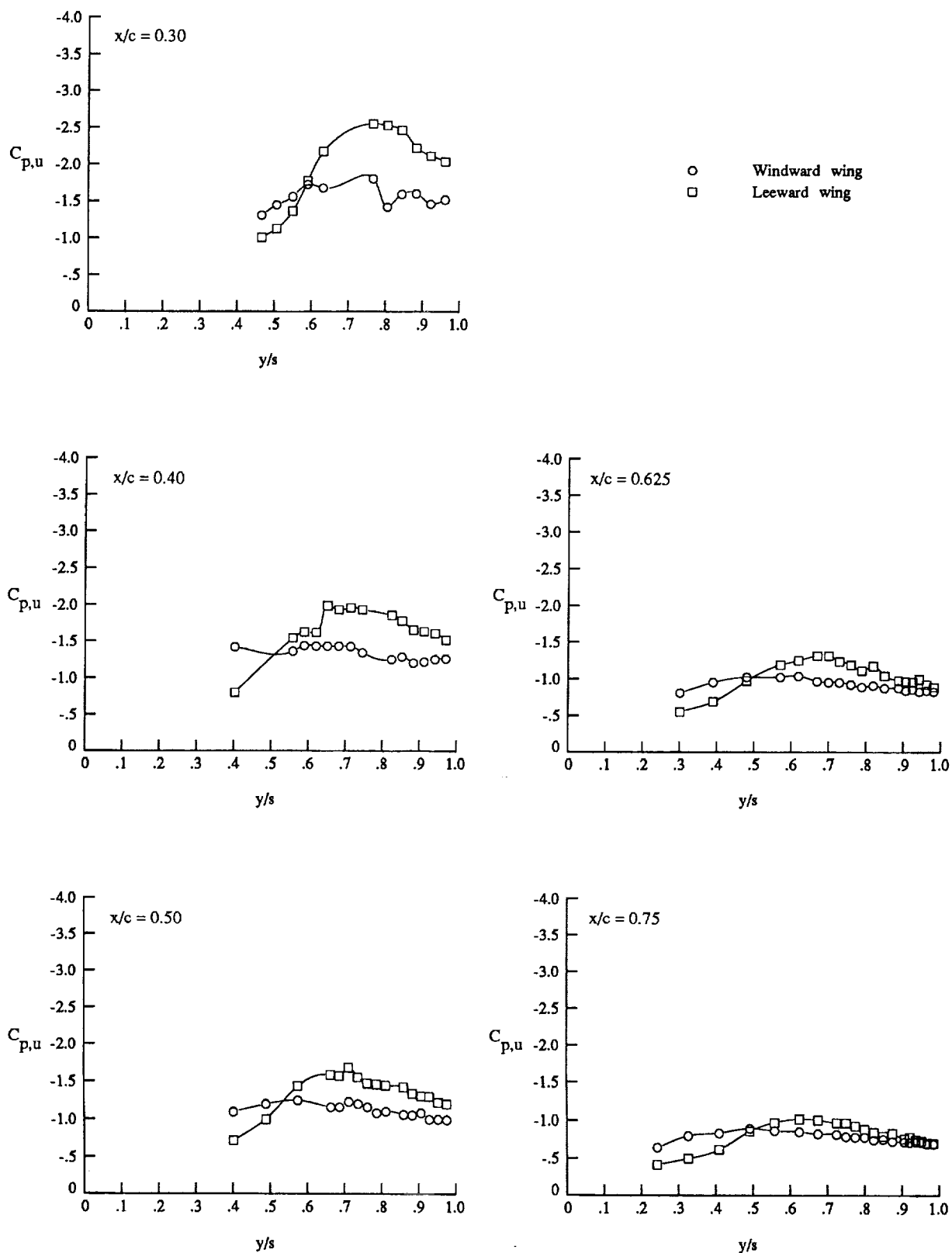
(f) Wing upper surface static pressure distributions with strakes off at $\alpha \approx 20^\circ$.

Figure 24. Continued.



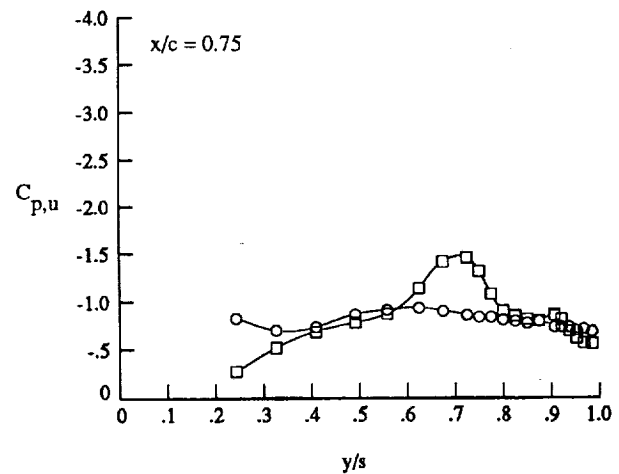
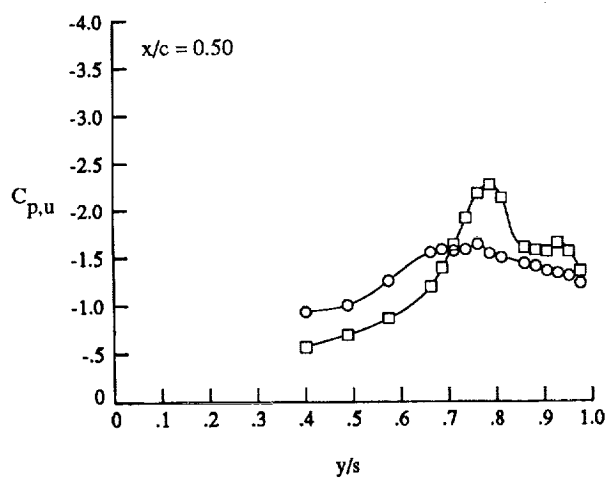
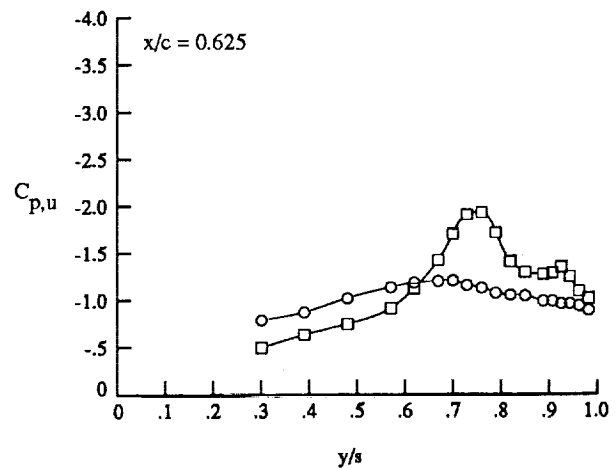
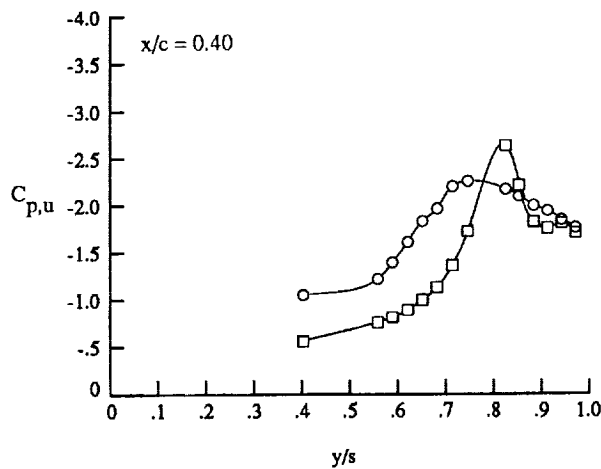
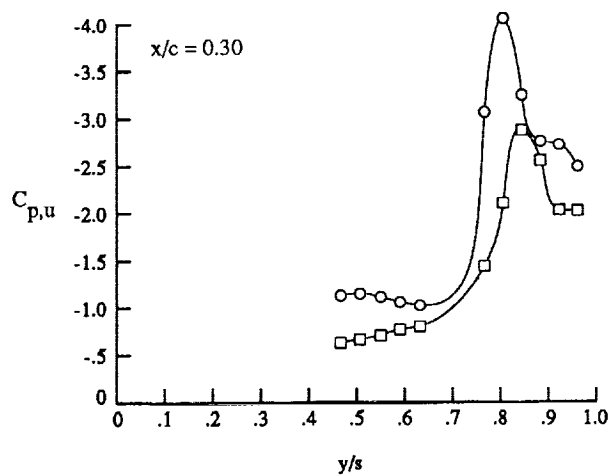
(g) Wing upper surface static pressure distributions with strakes on at $\alpha \approx 20^\circ$.

Figure 24. Continued.



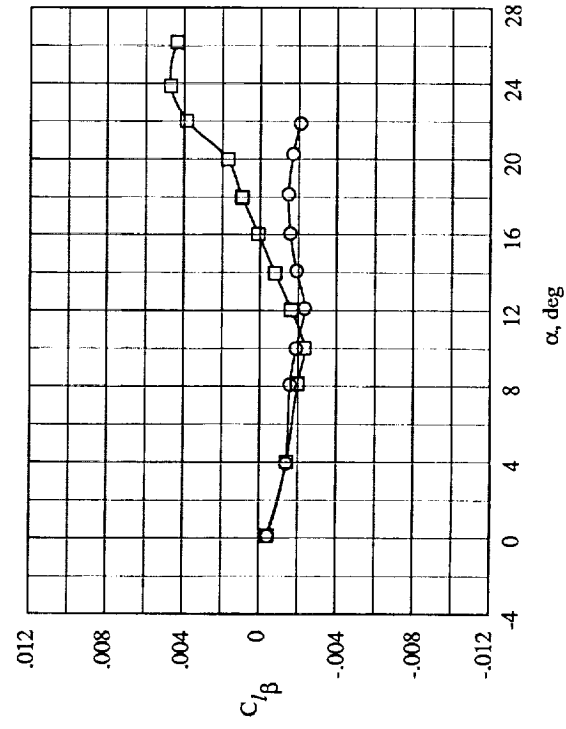
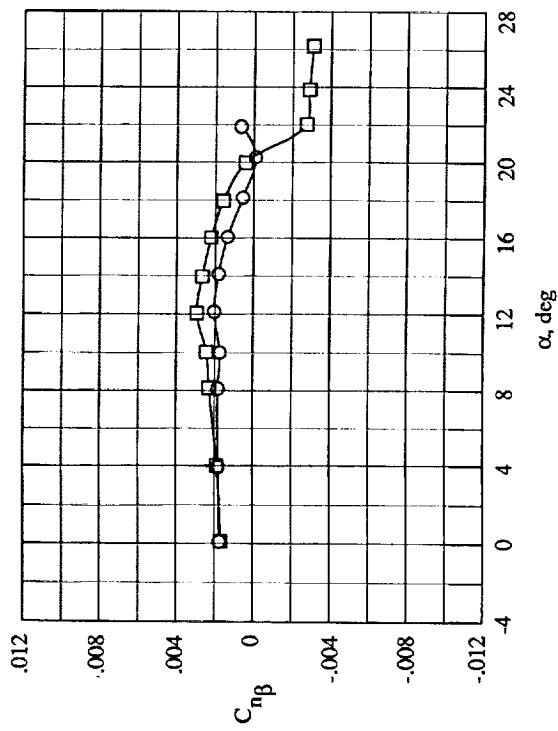
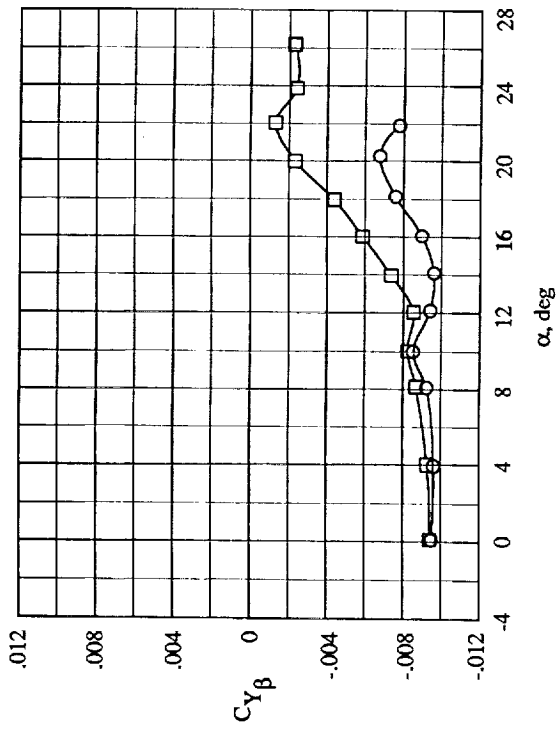
(h) Wing upper surface static pressure distributions with strakes off at $\alpha \approx 24^\circ$.

Figure 24. Continued.



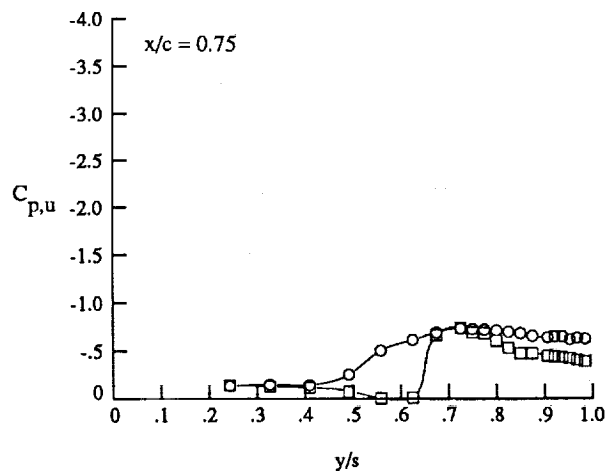
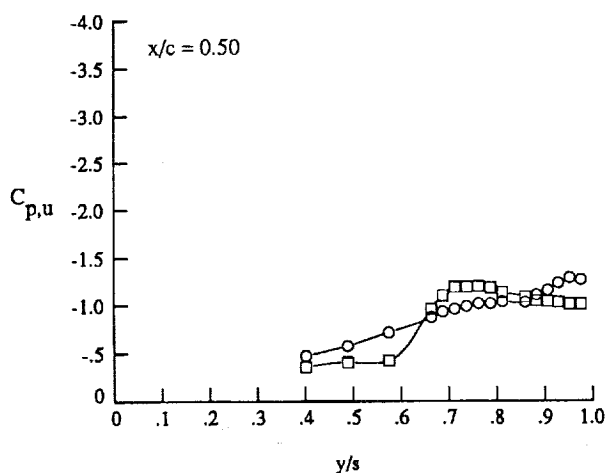
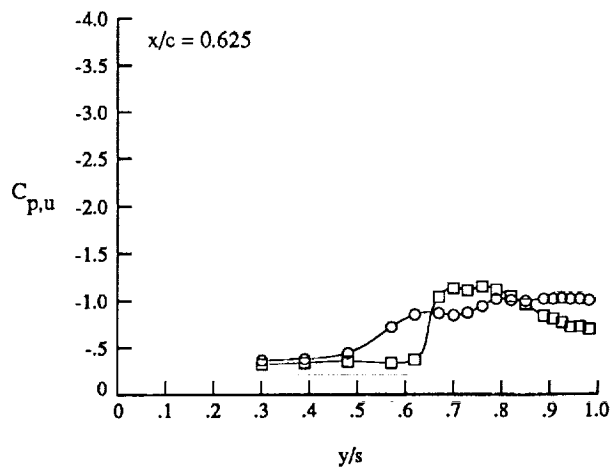
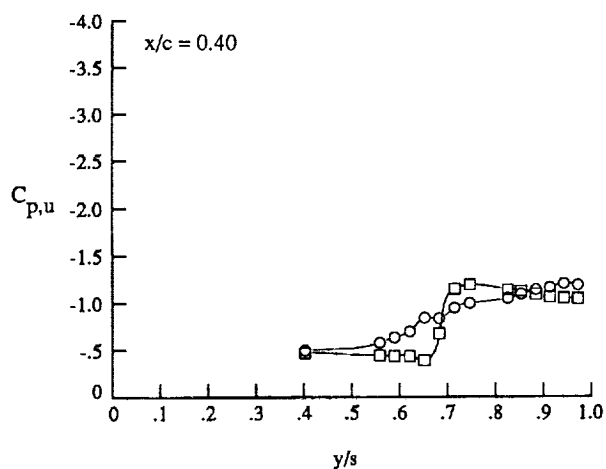
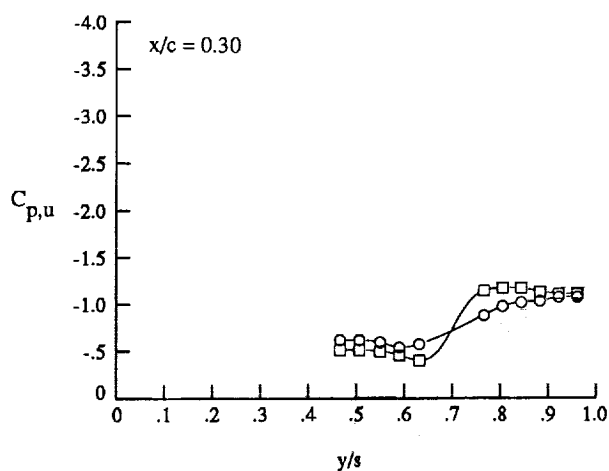
(i) Wing upper surface static pressure distributions with strakes on at $\alpha \approx 23^\circ$.

Figure 24. Concluded.



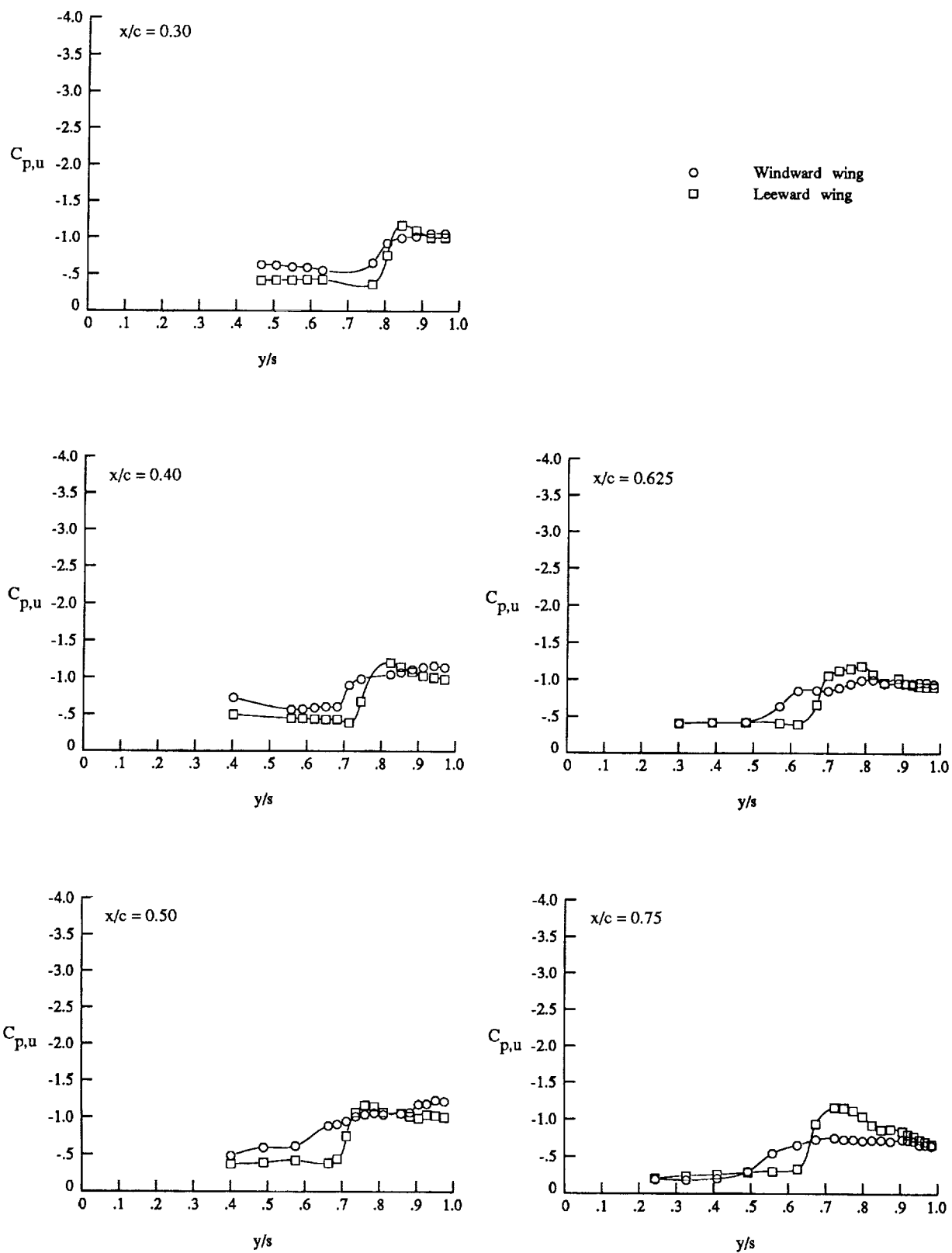
(a) Lateral-directional stability derivatives.

Figure 25. Effect of forebody strakes on lateral-directional characteristics at $M_{\infty} = 0.90$ with $\delta_{LE} = 0^\circ$.



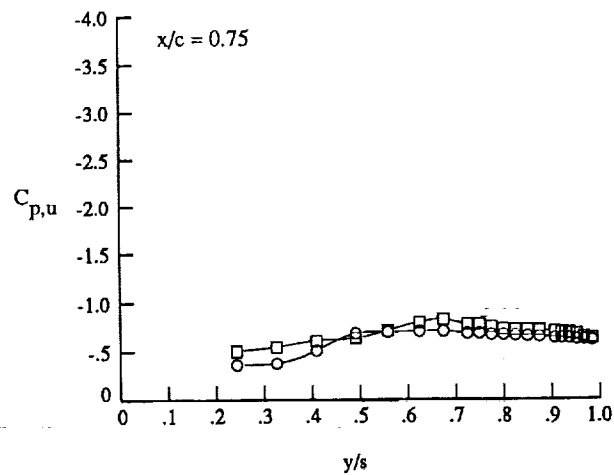
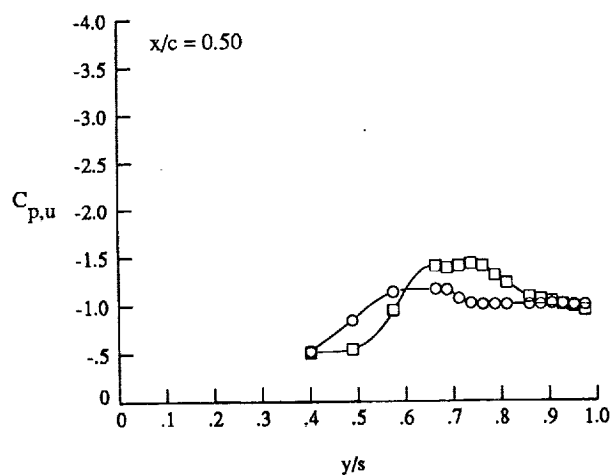
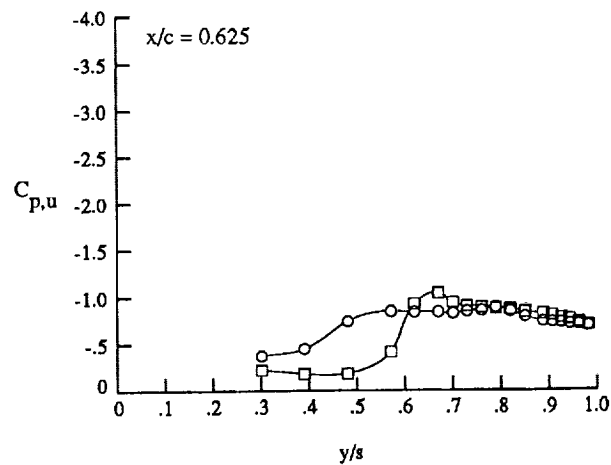
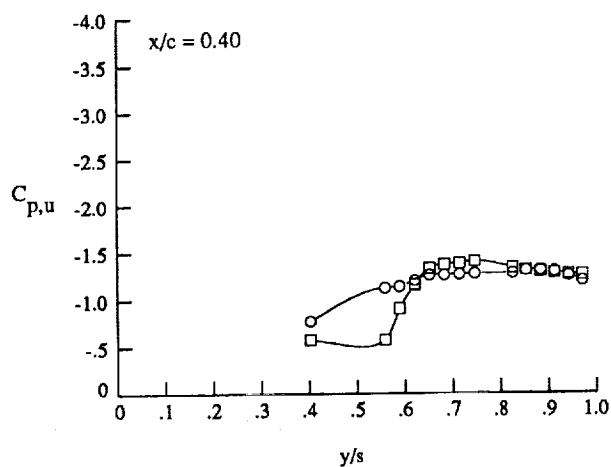
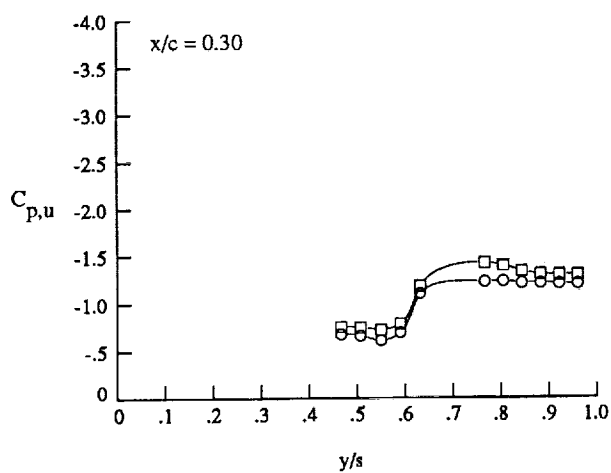
(b) Wing upper surface static pressure distributions with strakes off at $\alpha \approx 12^\circ$.

Figure 25. Continued.



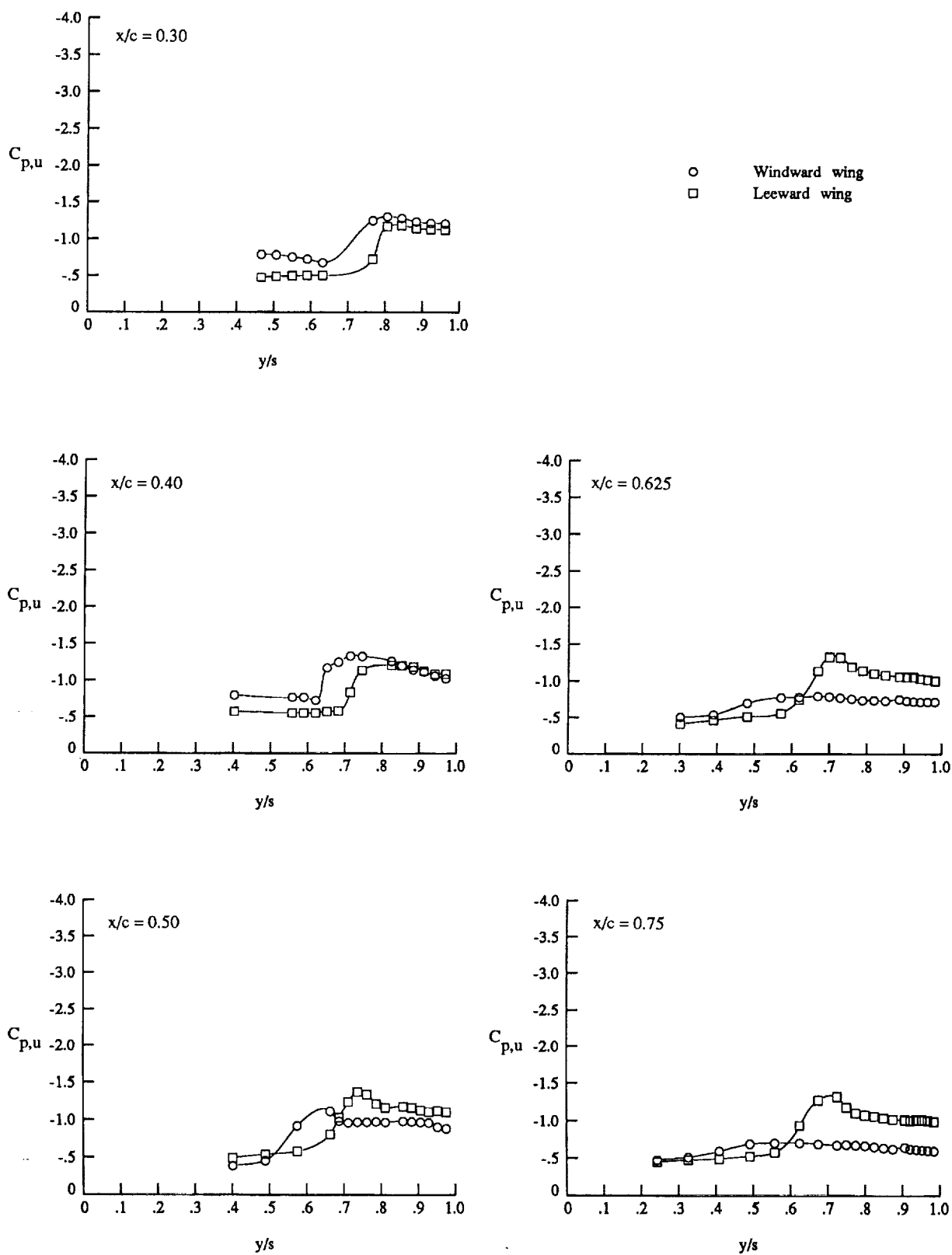
(c) Wing upper surface static pressure distributions with strakes on at $\alpha \approx 12^\circ$.

Figure 25. Continued.



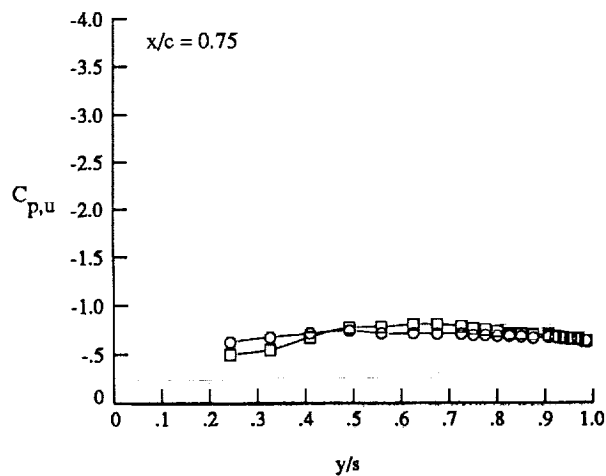
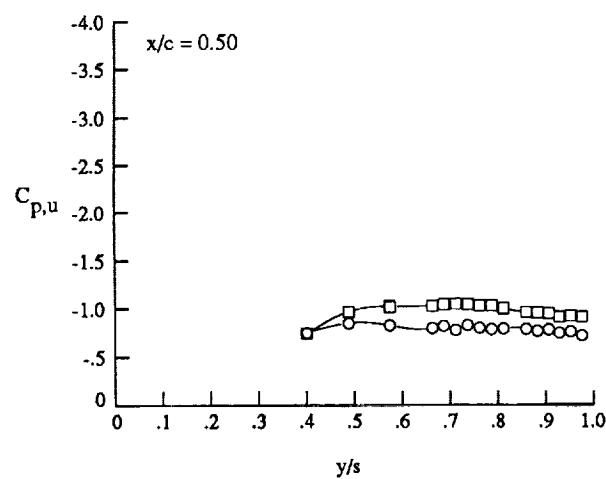
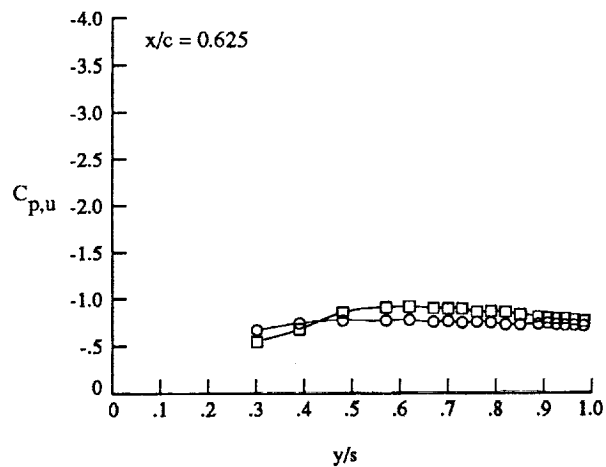
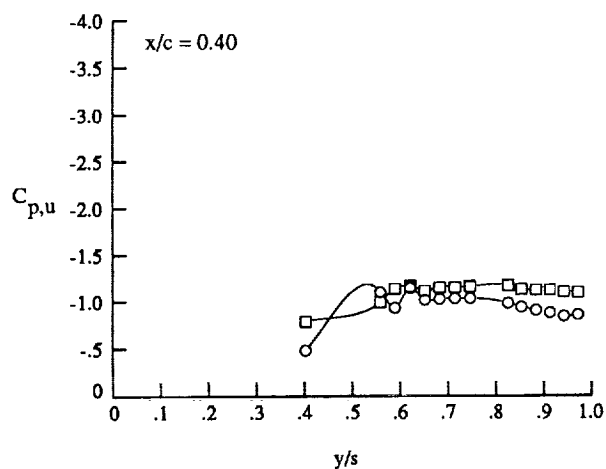
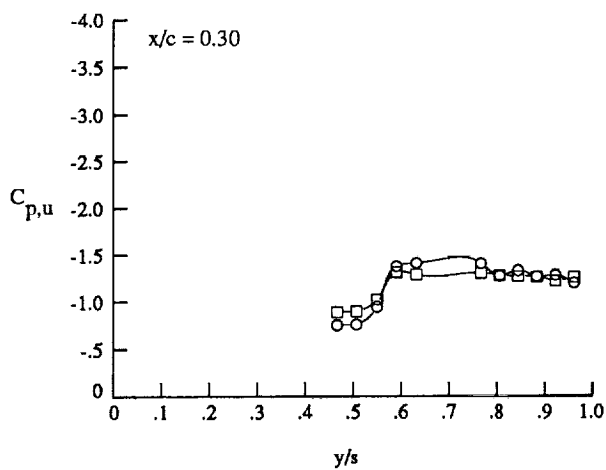
(d) Wing upper surface static pressure distributions with strakes off at $\alpha \approx 16^\circ$.

Figure 25. Continued.



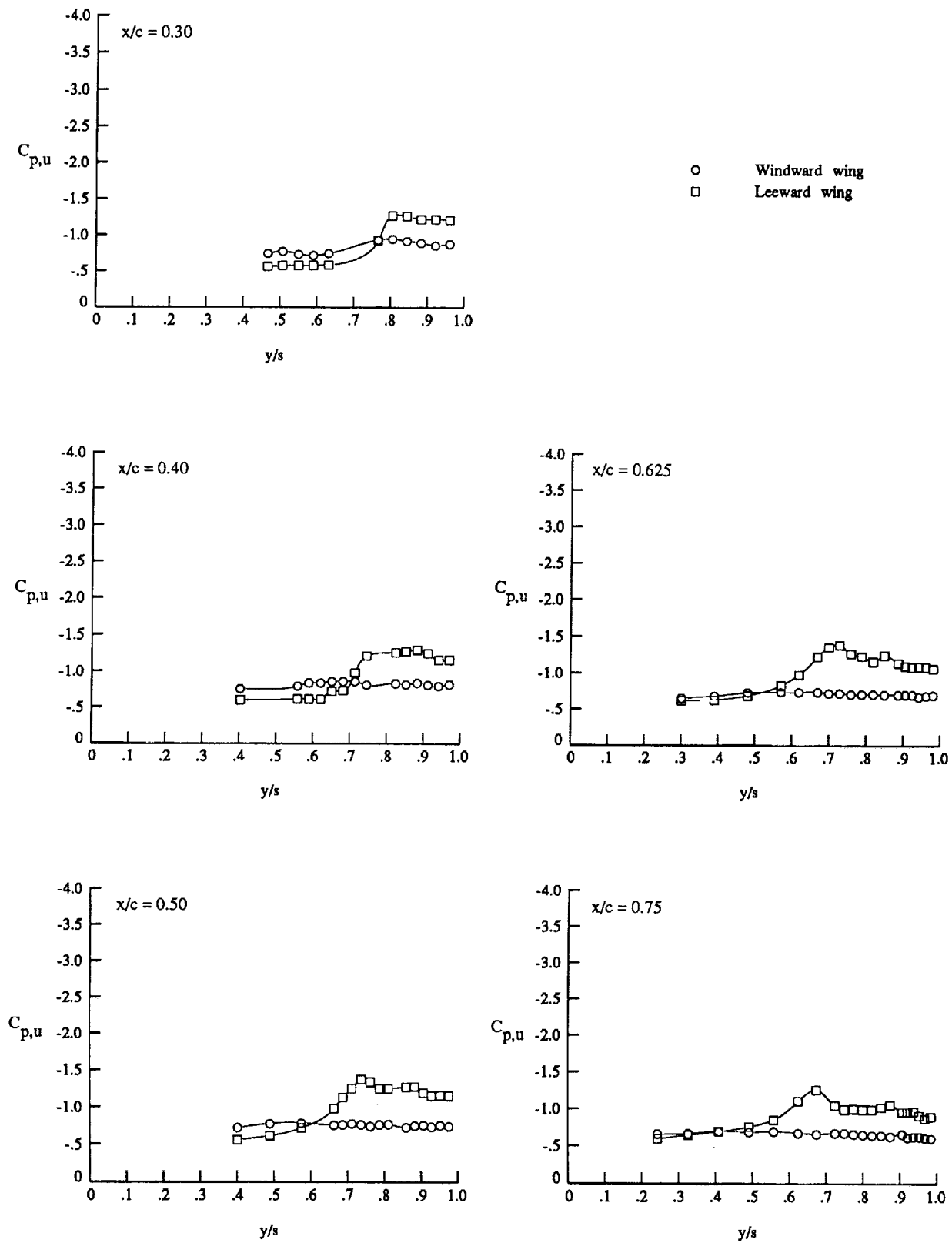
(e) Wing upper surface static pressure distributions with strakes on at $\alpha \approx 16^\circ$.

Figure 25. Continued.



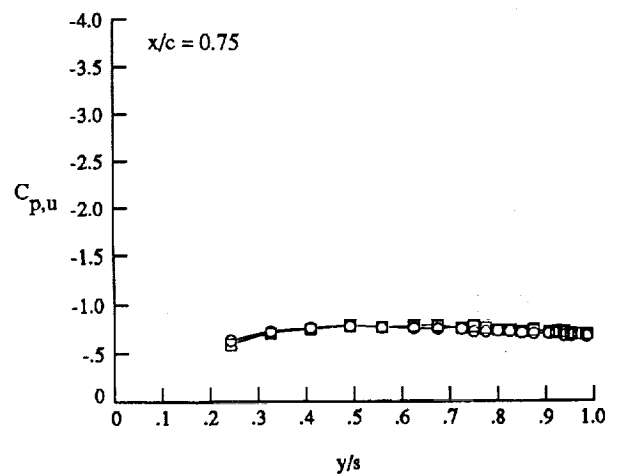
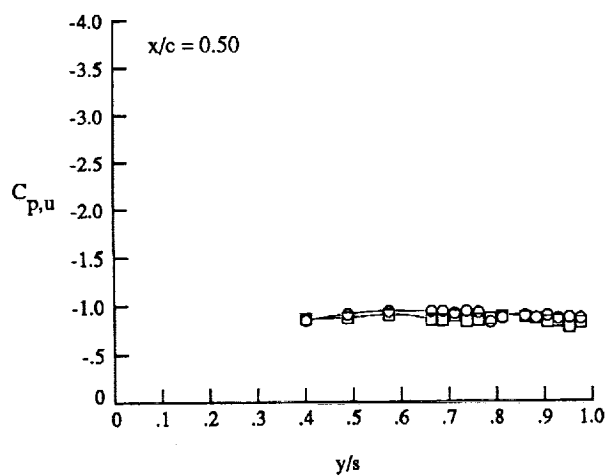
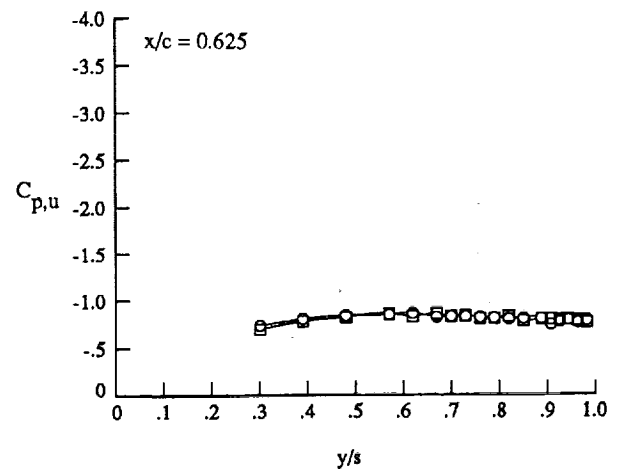
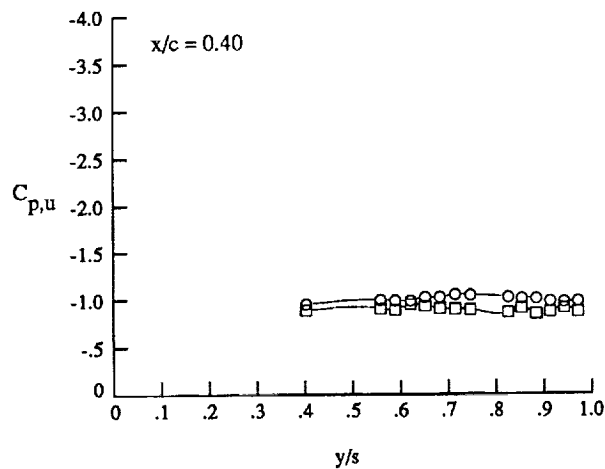
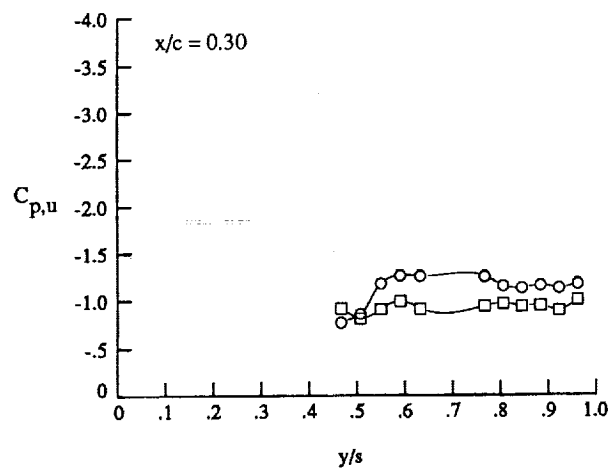
(f) Wing upper surface static pressure distributions with strakes off at $\alpha \approx 20^\circ$.

Figure 25. Continued.



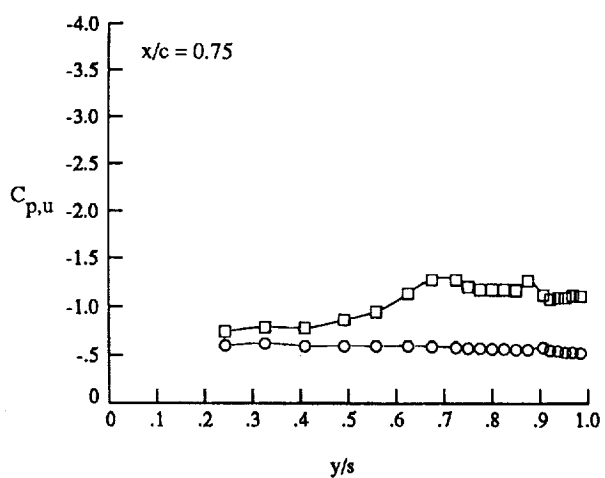
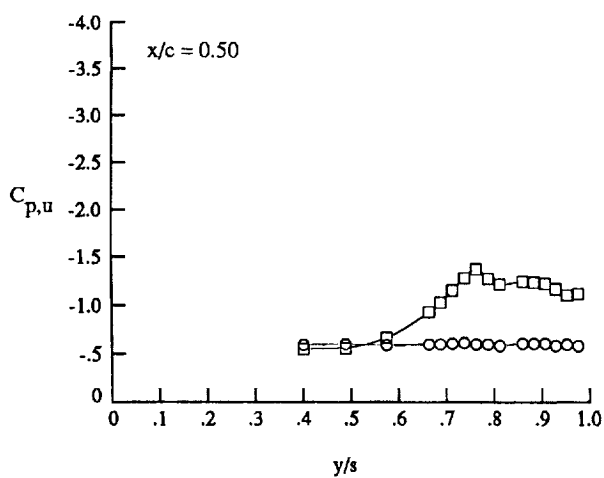
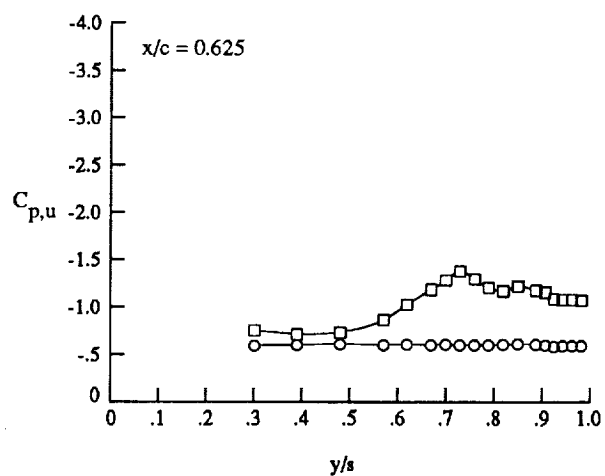
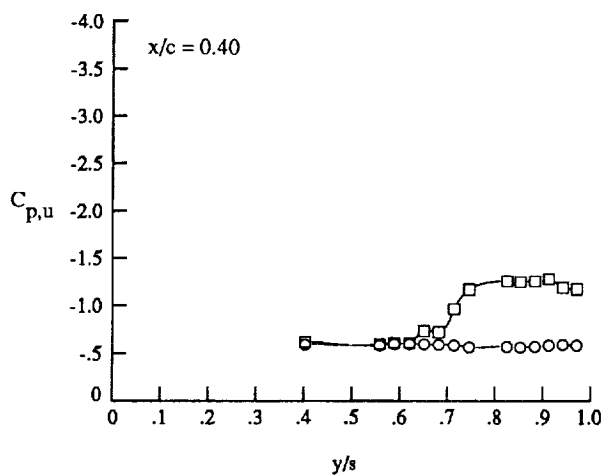
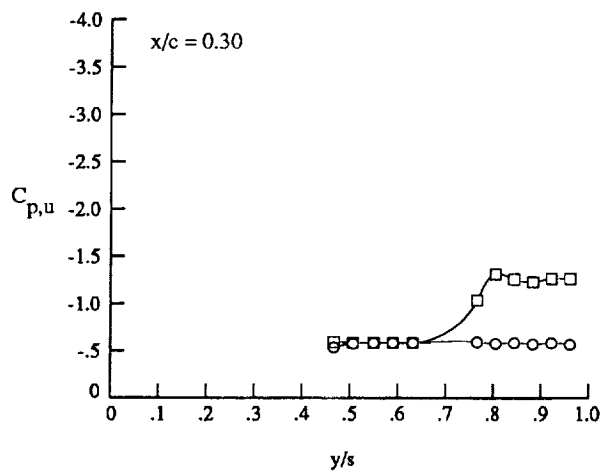
(g) Wing upper surface static pressure distributions with strakes on at $\alpha \approx 20^\circ$.

Figure 25. Continued.



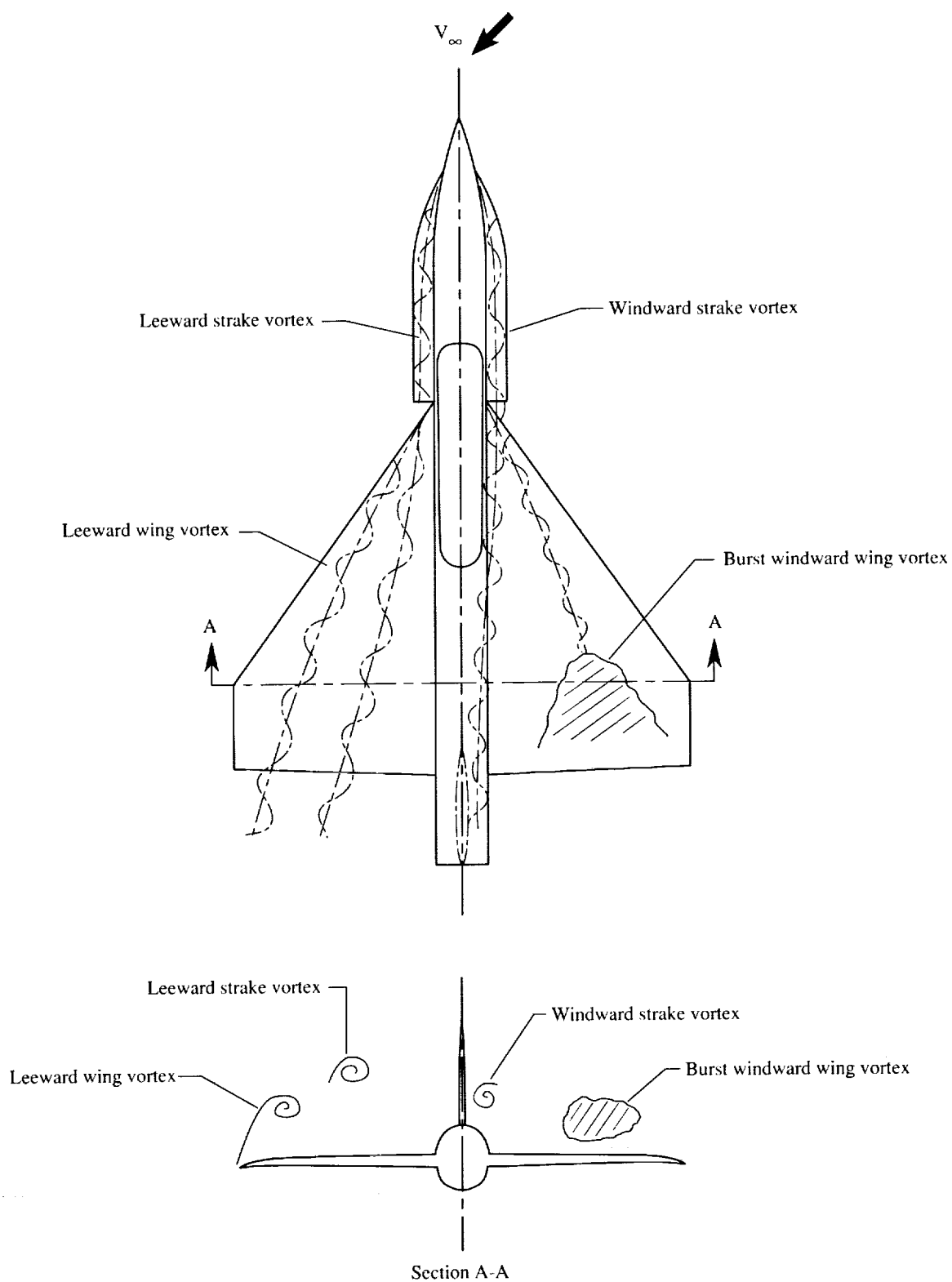
(h) Wing upper surface static pressure distributions with strakes off at $\alpha \approx 22^\circ$.

Figure 25. Continued.



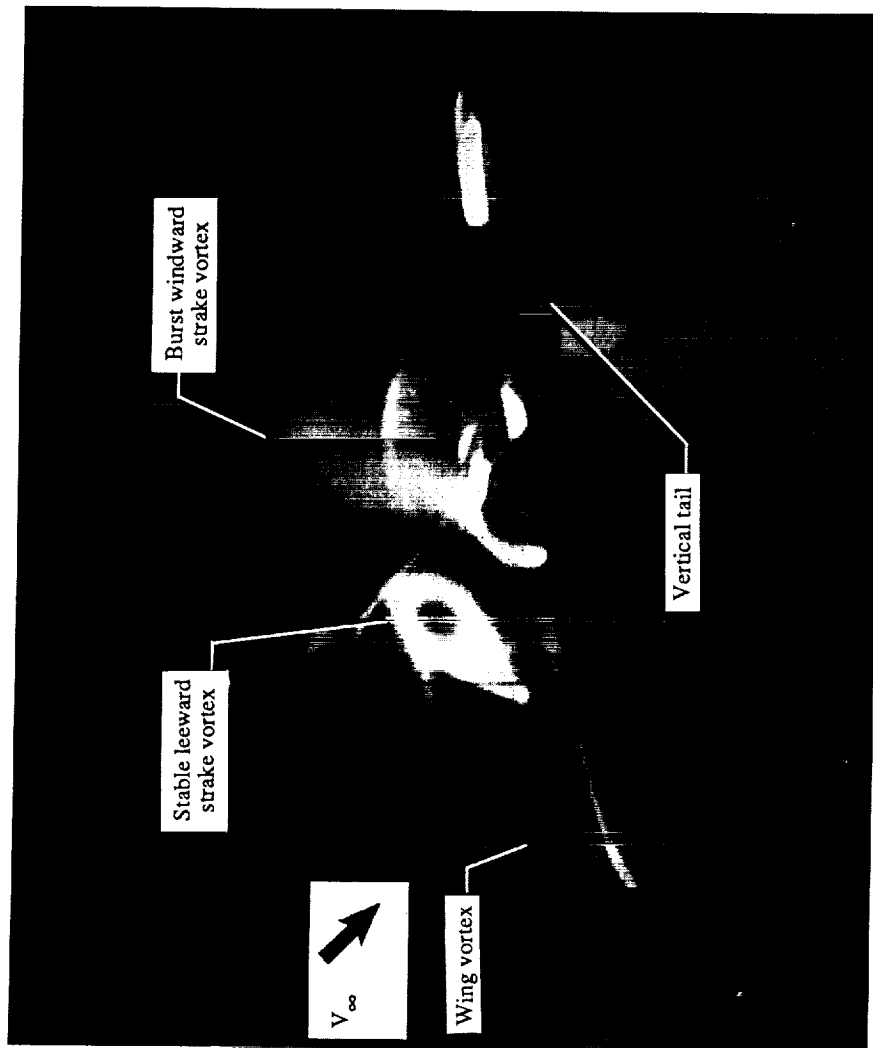
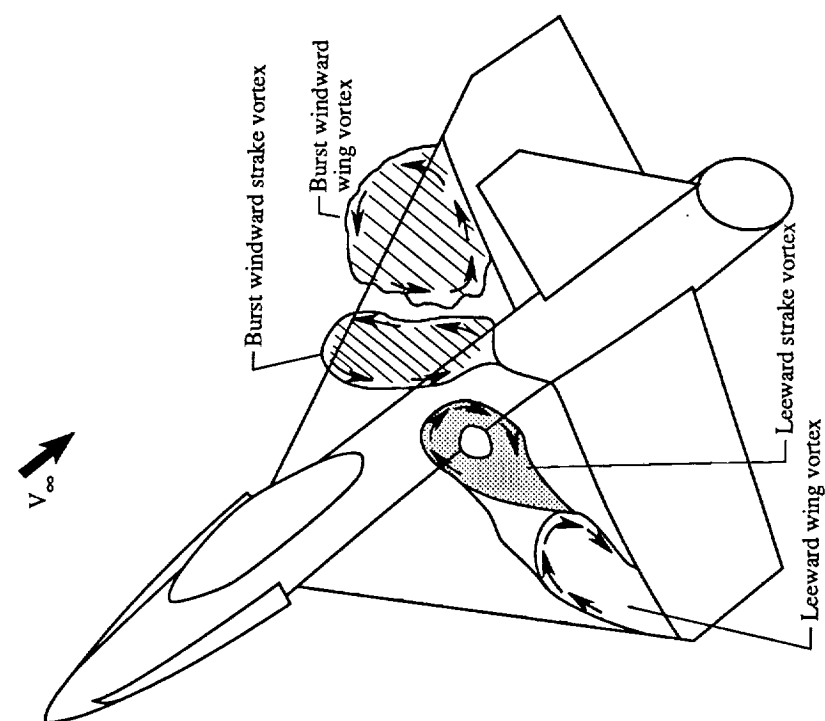
(i) Wing upper surface static pressure distributions with strakes on at $\alpha \approx 24^\circ$.

Figure 25. Concluded.



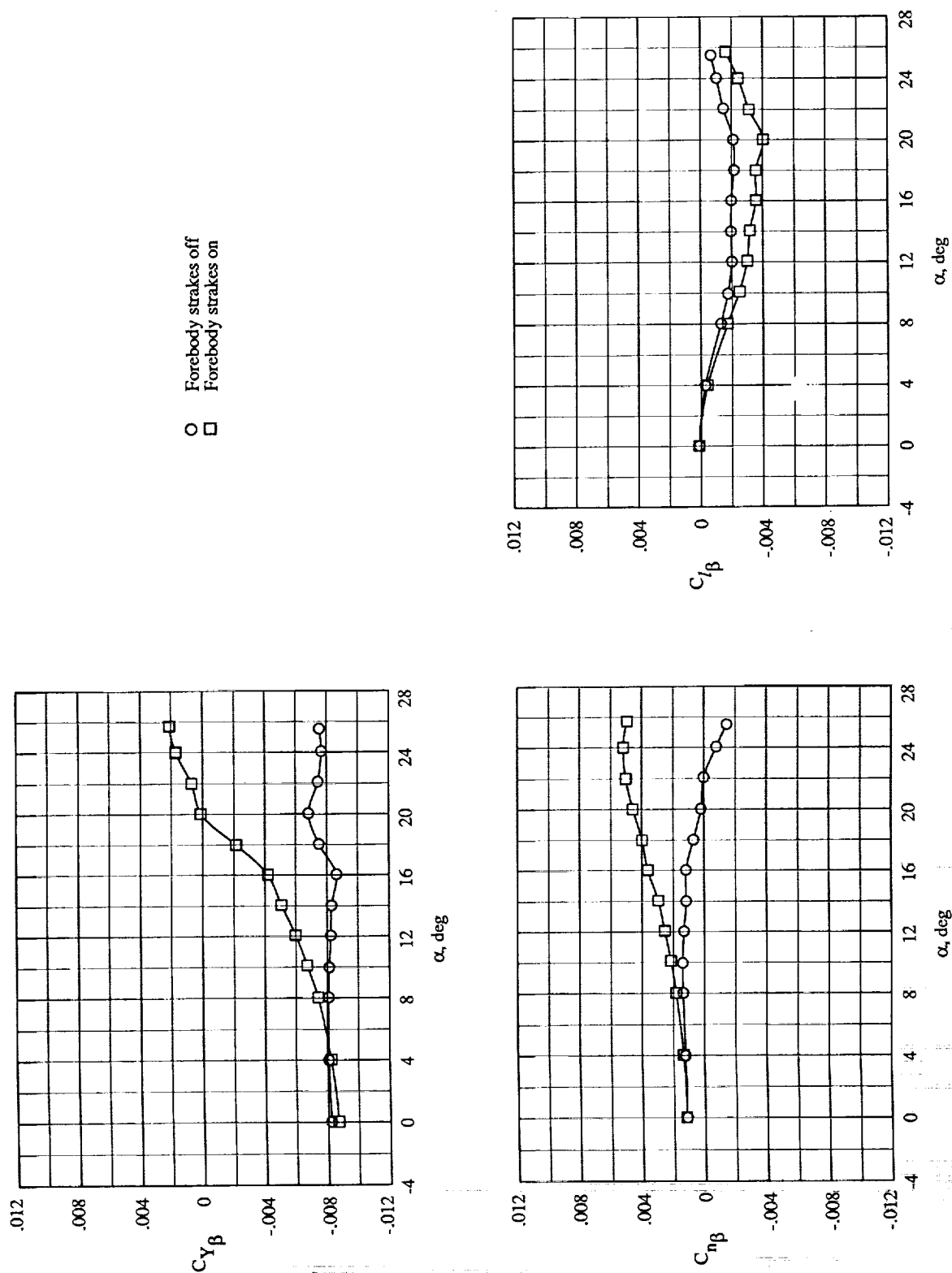
(a) Sketches based on flow-field observations at $M_\infty = 0.40$, $\alpha \approx 16^\circ$, and $\beta = +5^\circ$.

Figure 26. Off-surface flow-field characteristics in sideslip. $\delta_{LE} = 0^\circ$; strakes on.



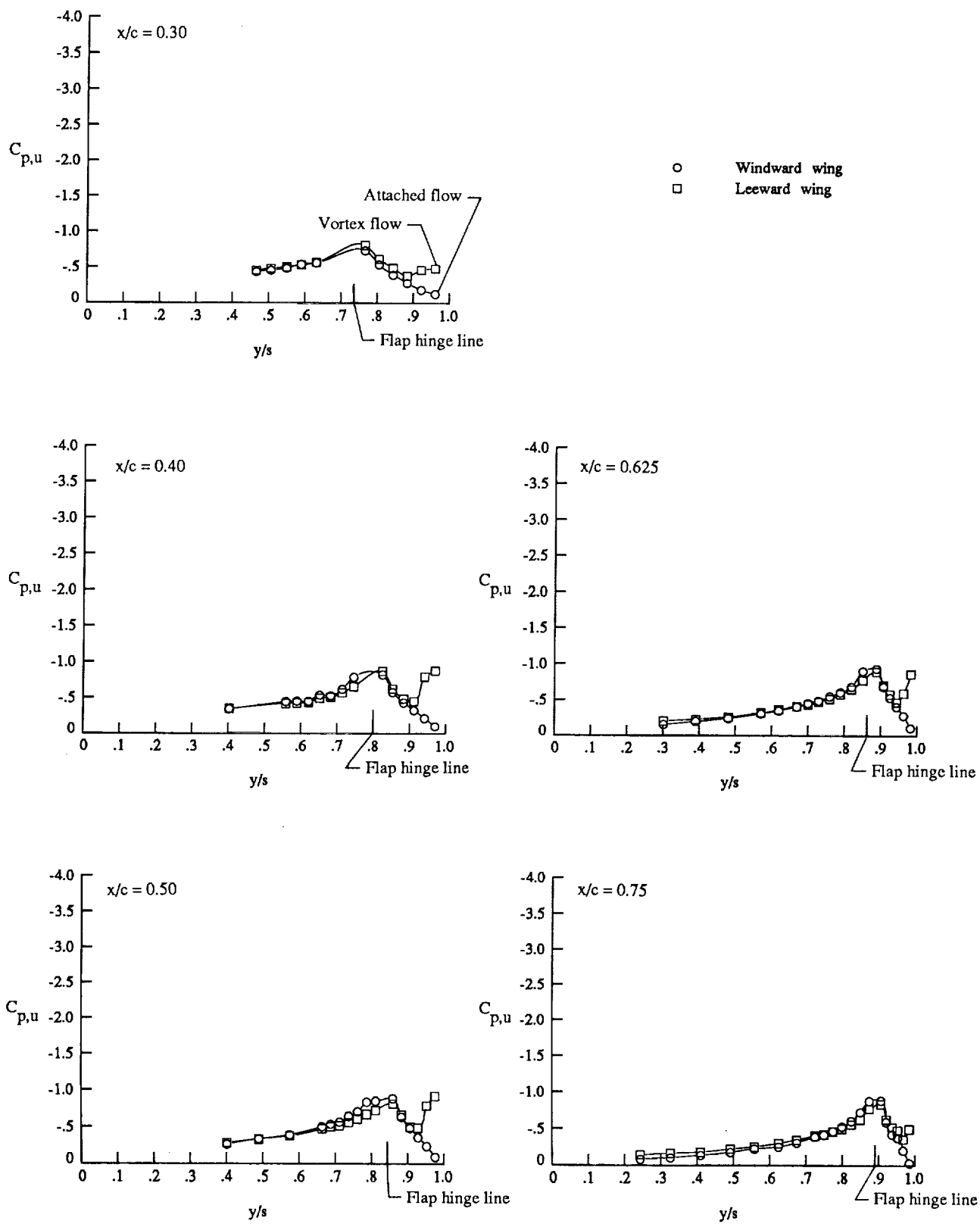
(b) Laser vapor screen result at $M_\infty = 0.90$, $\alpha \approx 22^\circ$, $\beta = +5^\circ$, and $x/c = 0.75$.

Figure 26. Concluded.



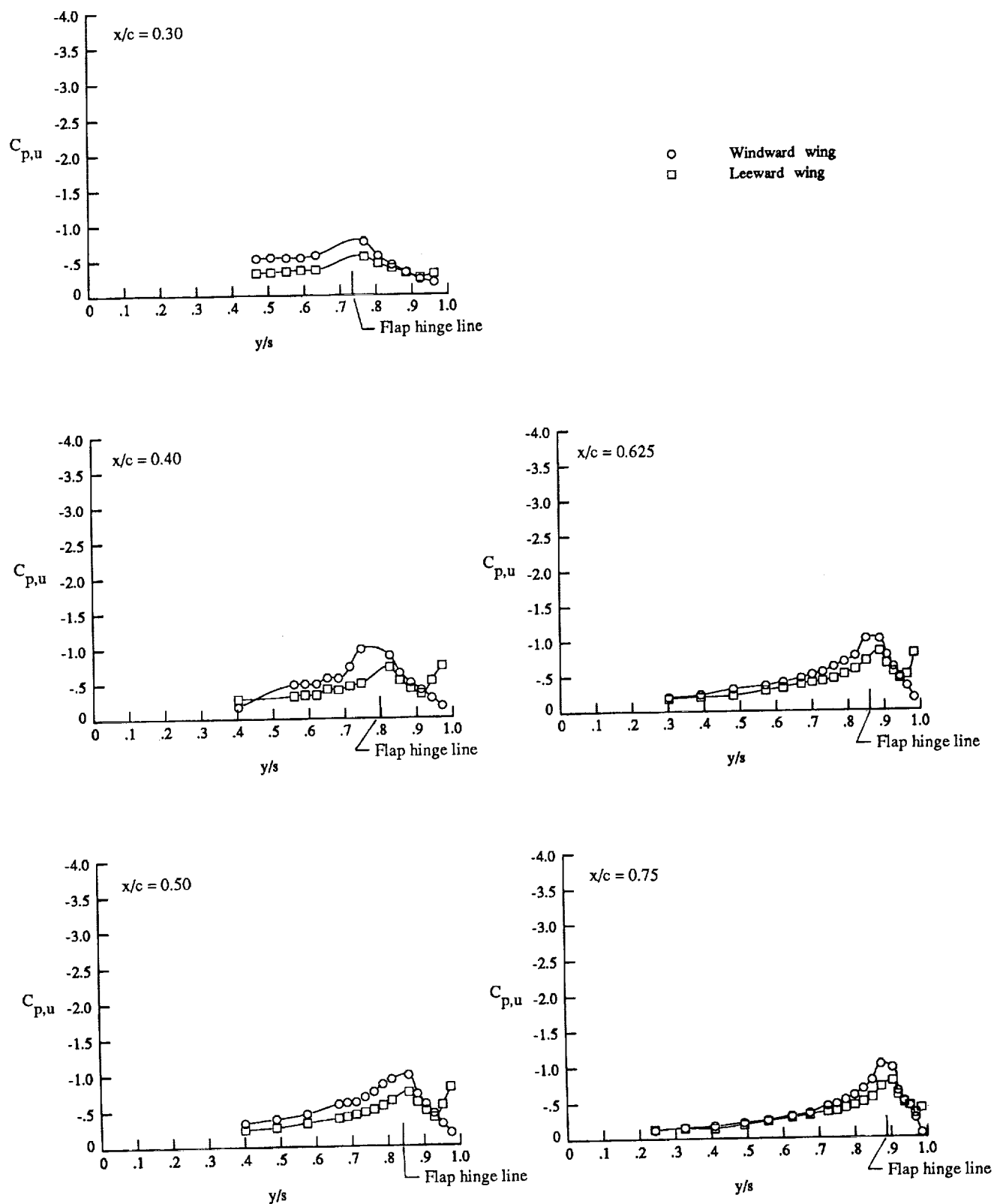
(a) Lateral-directional stability derivatives.

Figure 27. Effect of forebody strakes on lateral-directional characteristics at $M_\infty = 0.40$ with $\delta_{LE} = 30^\circ$.



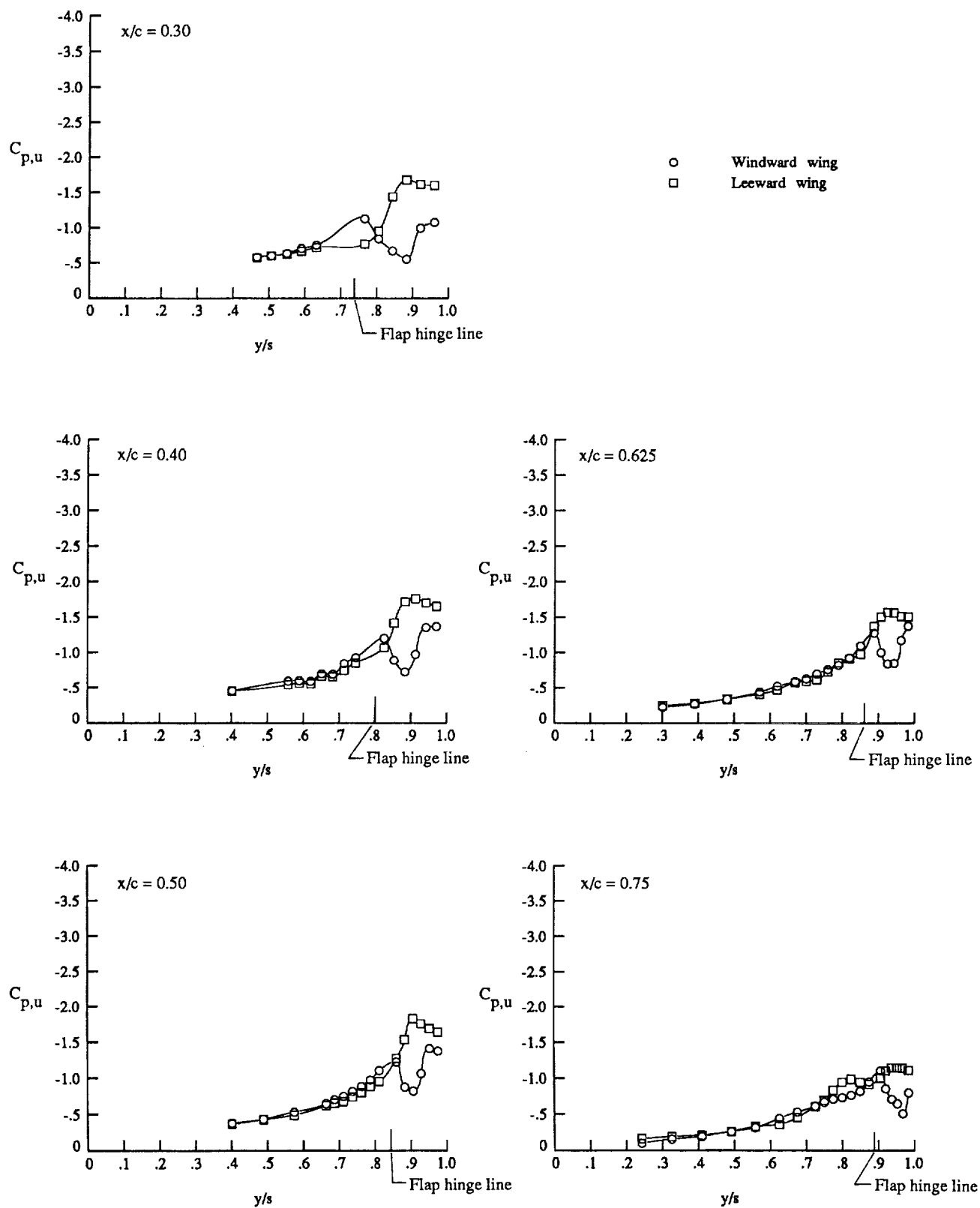
(b) Wing upper surface static pressure distributions with strakes off at $\alpha \approx 12^\circ$.

Figure 27. Continued.



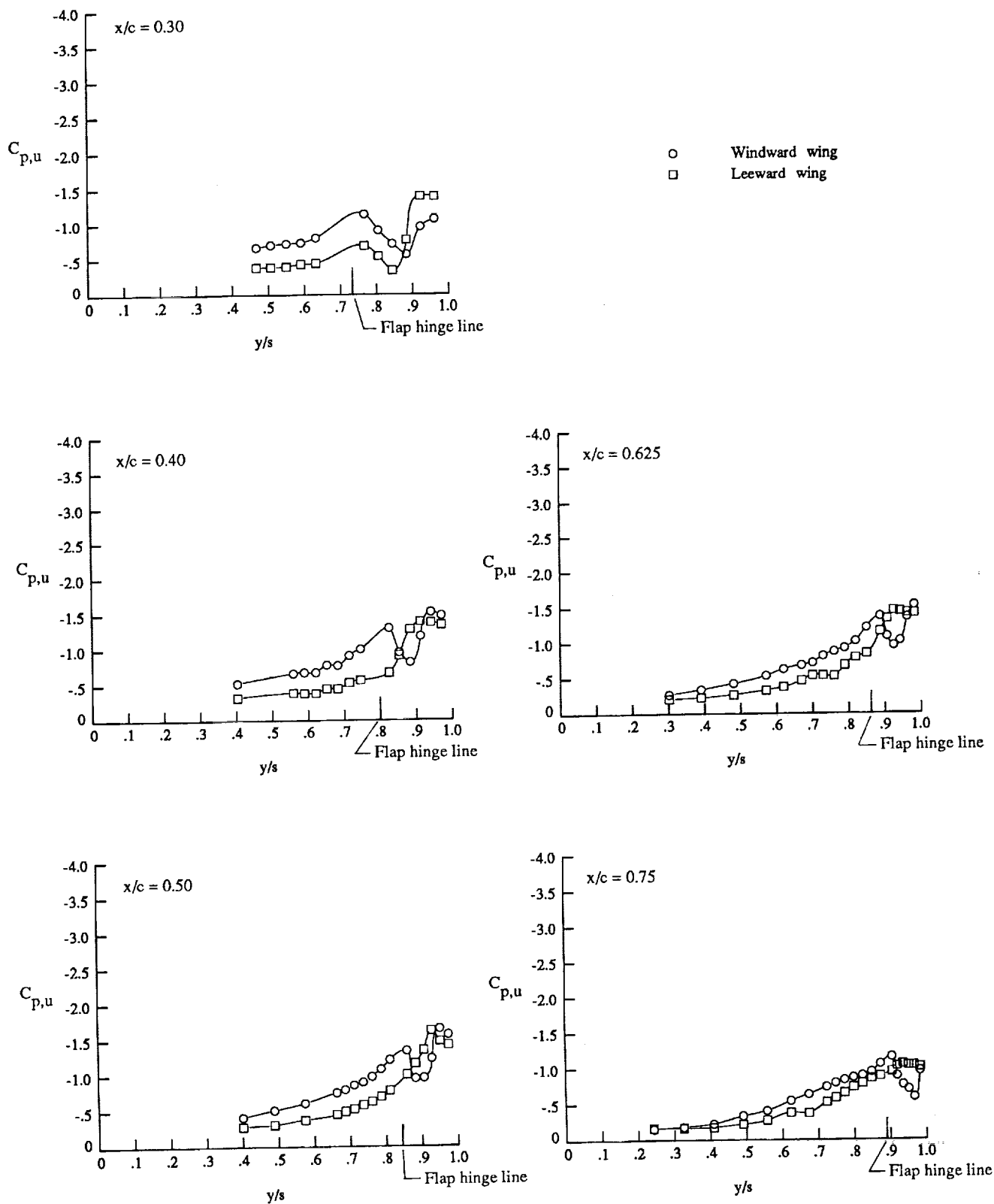
(c) Wing upper surface static pressure distributions with strakes on at $\alpha \approx 12^\circ$.

Figure 27. Continued.



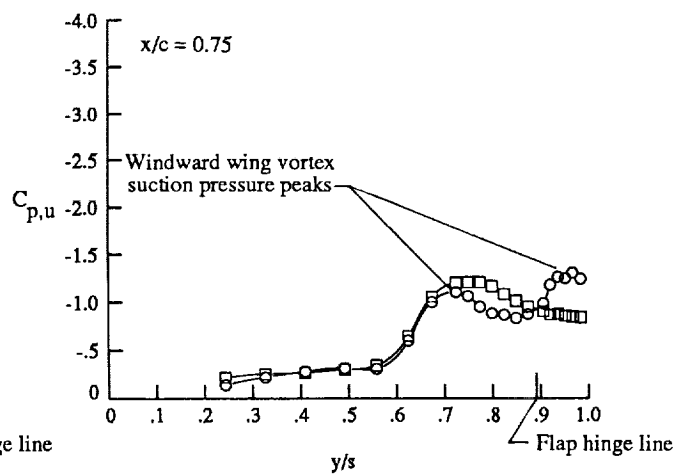
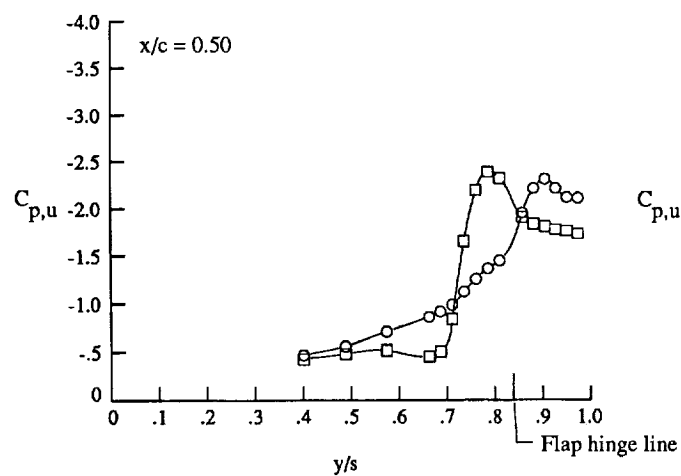
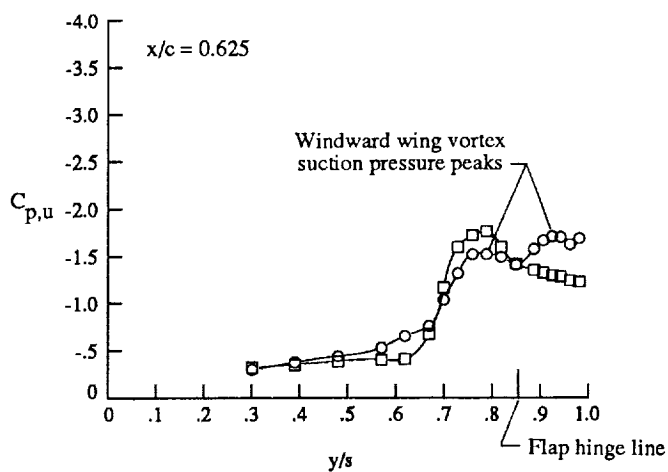
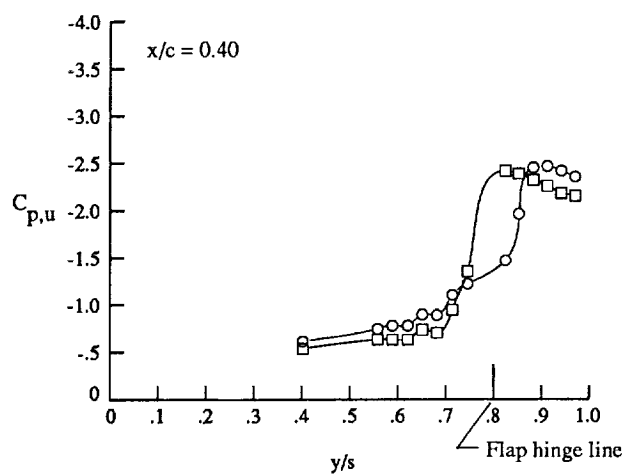
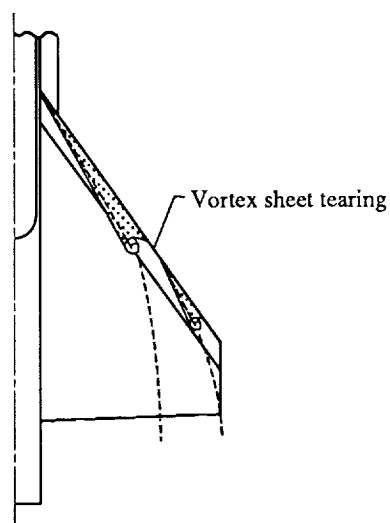
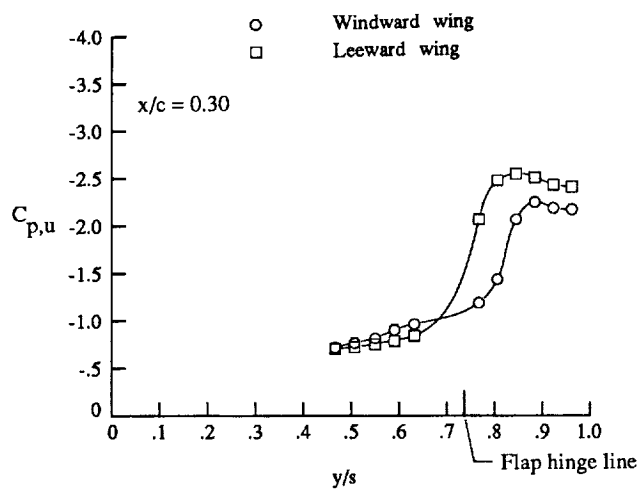
(d) Wing upper surface static pressure distributions with strakes off at $\alpha \approx 16^\circ$.

Figure 27. Continued.



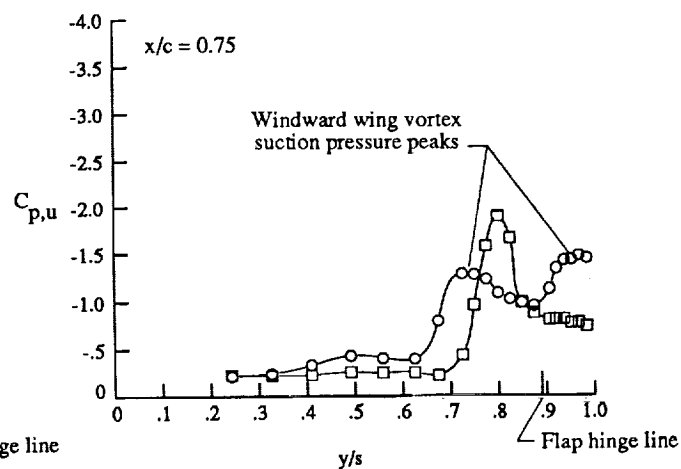
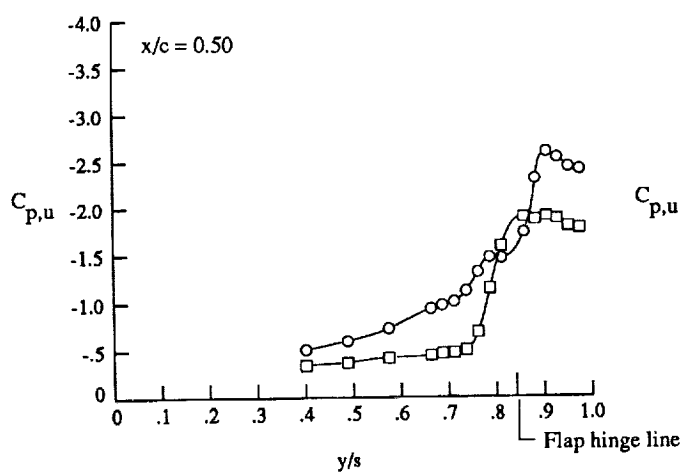
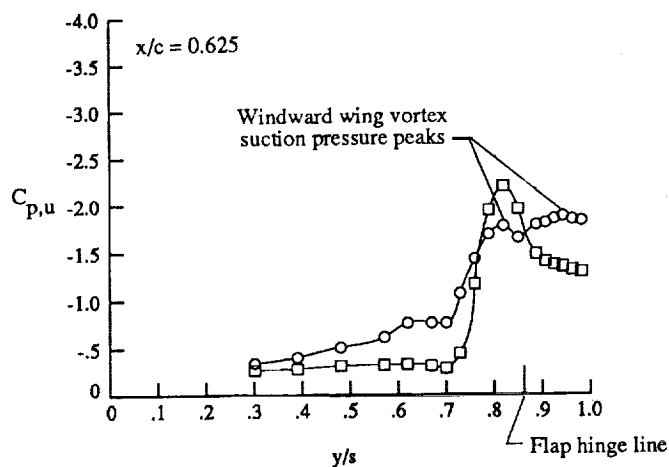
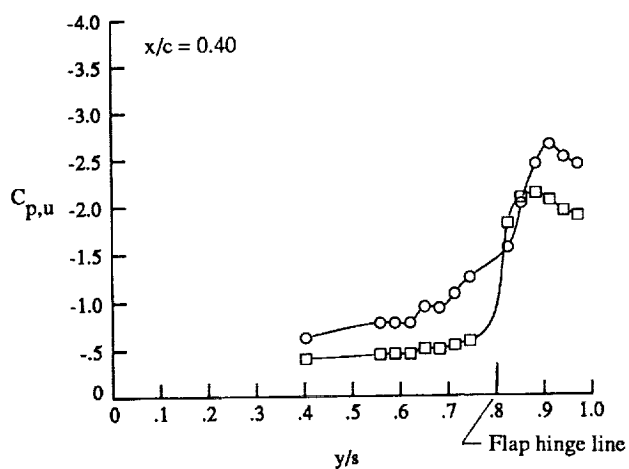
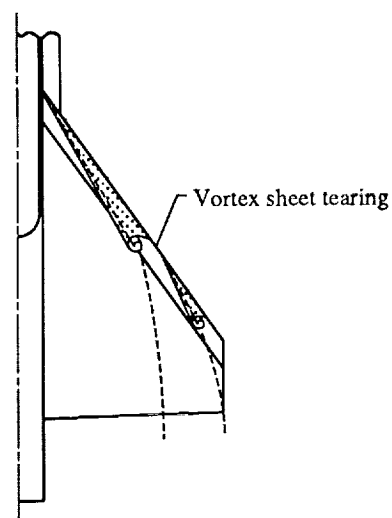
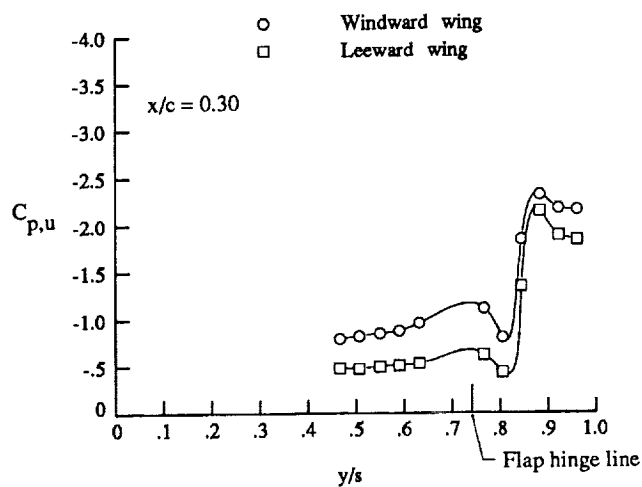
(e) Wing upper surface static pressure distributions with strakes on at $\alpha \approx 16^\circ$.

Figure 27. Continued.



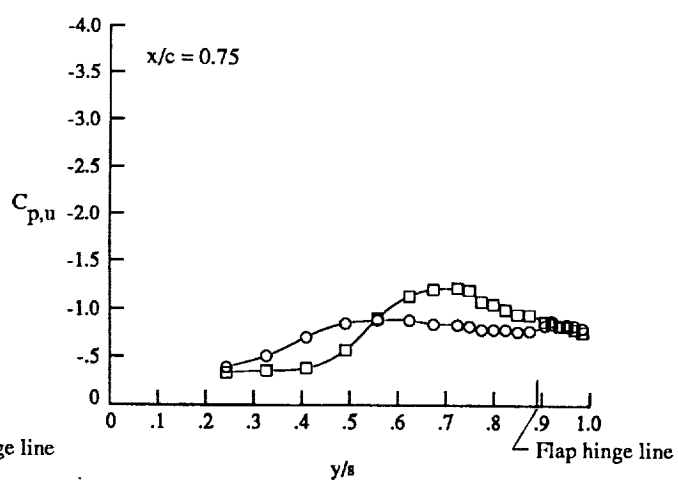
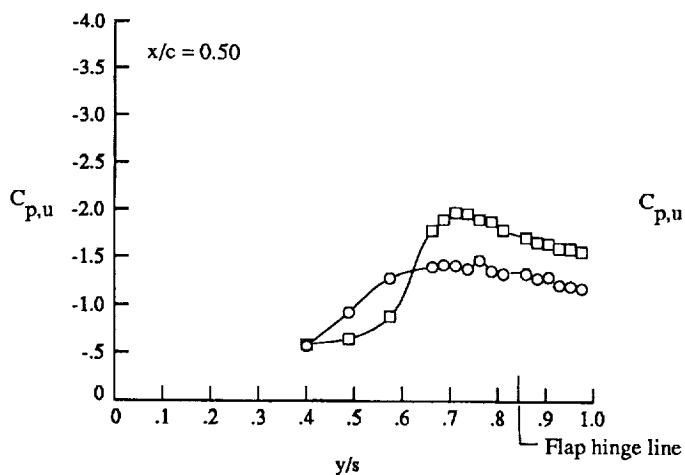
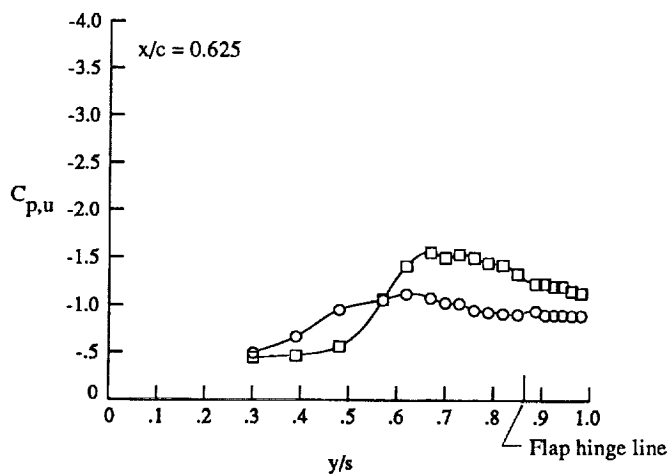
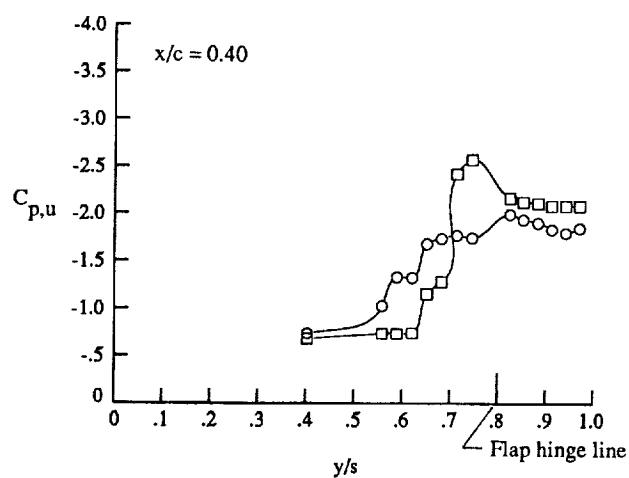
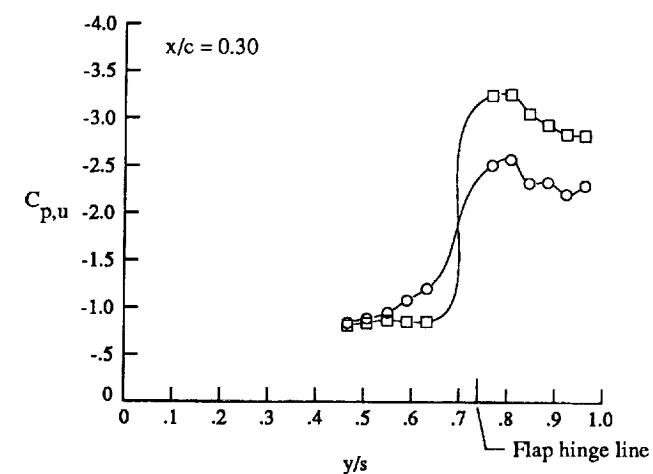
(f) Wing upper surface static pressure distributions with strakes off at $\alpha \approx 20^\circ$.

Figure 27. Continued.



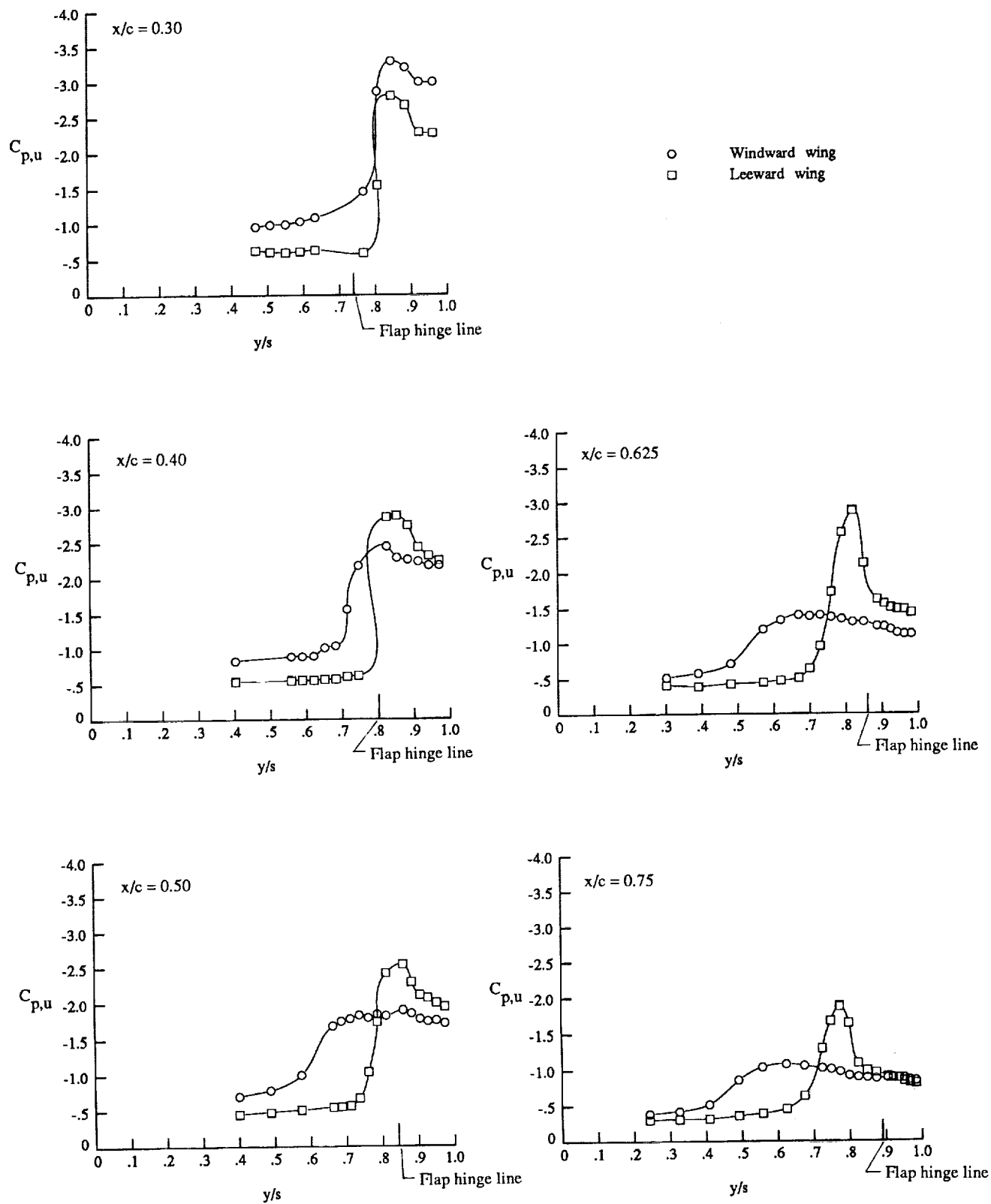
(g) Wing upper surface static pressure distributions with strakes on at $\alpha \approx 20^\circ$.

Figure 27. Continued.



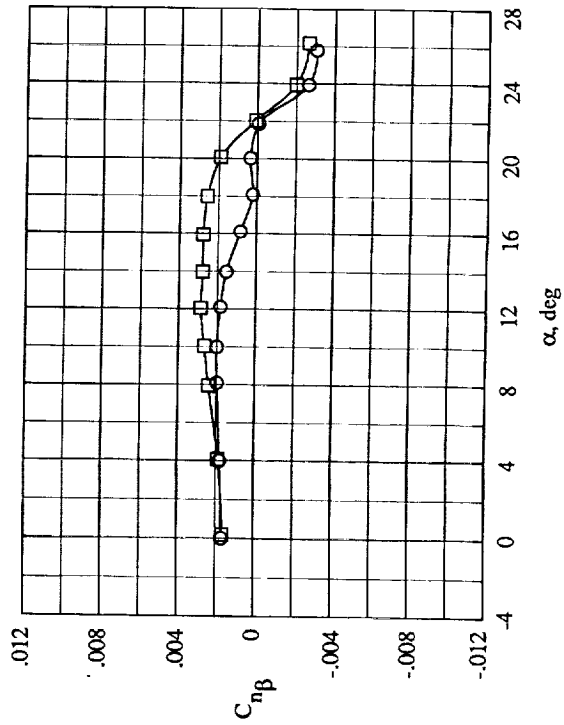
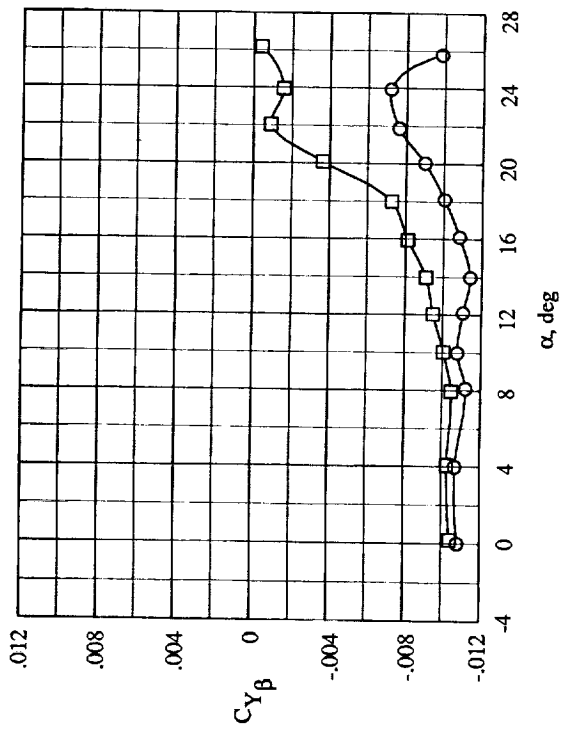
(h) Wing upper surface static pressure distributions with strakes off at $\alpha \approx 24^\circ$.

Figure 27. Continued.

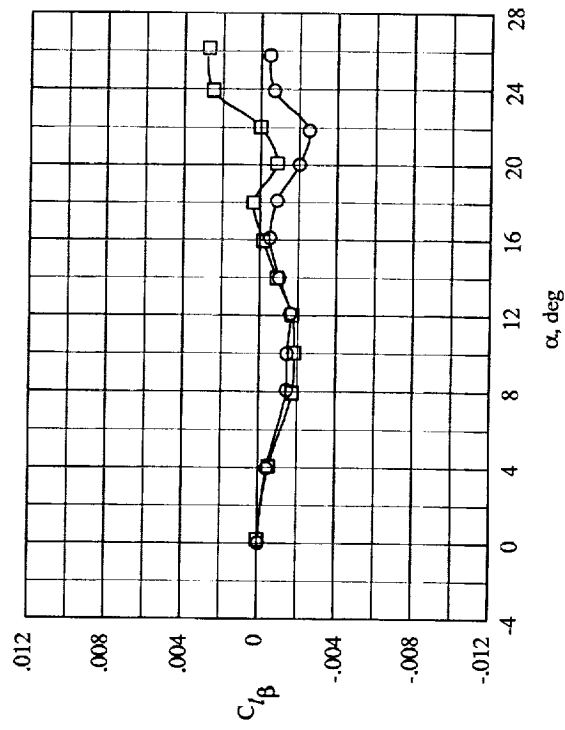


(i) Wing upper surface static pressure distributions with strakes on at $\alpha \approx 24^\circ$.

Figure 27. Concluded.

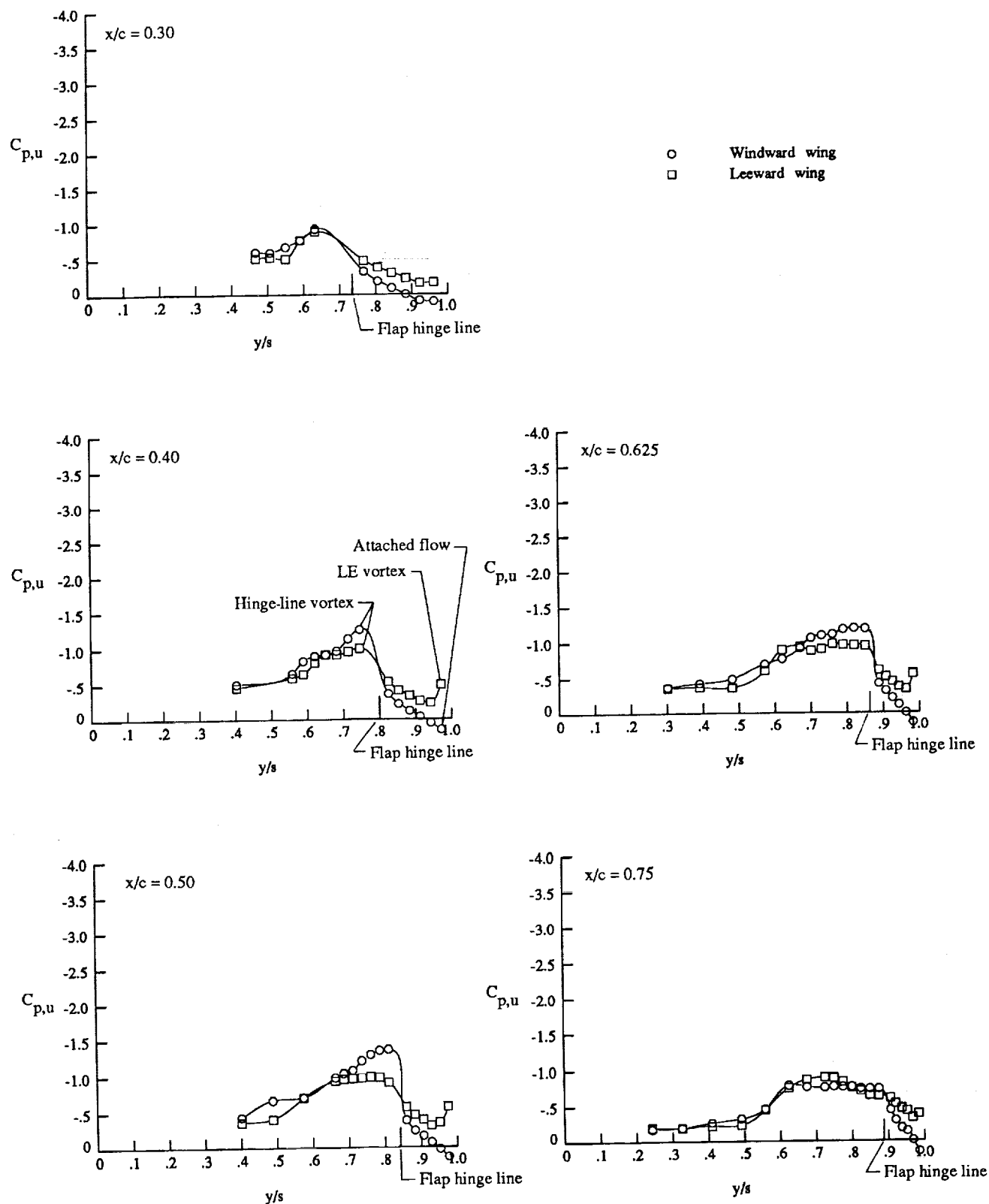


○ Forebody strakes off
 □ Forebody strakes on



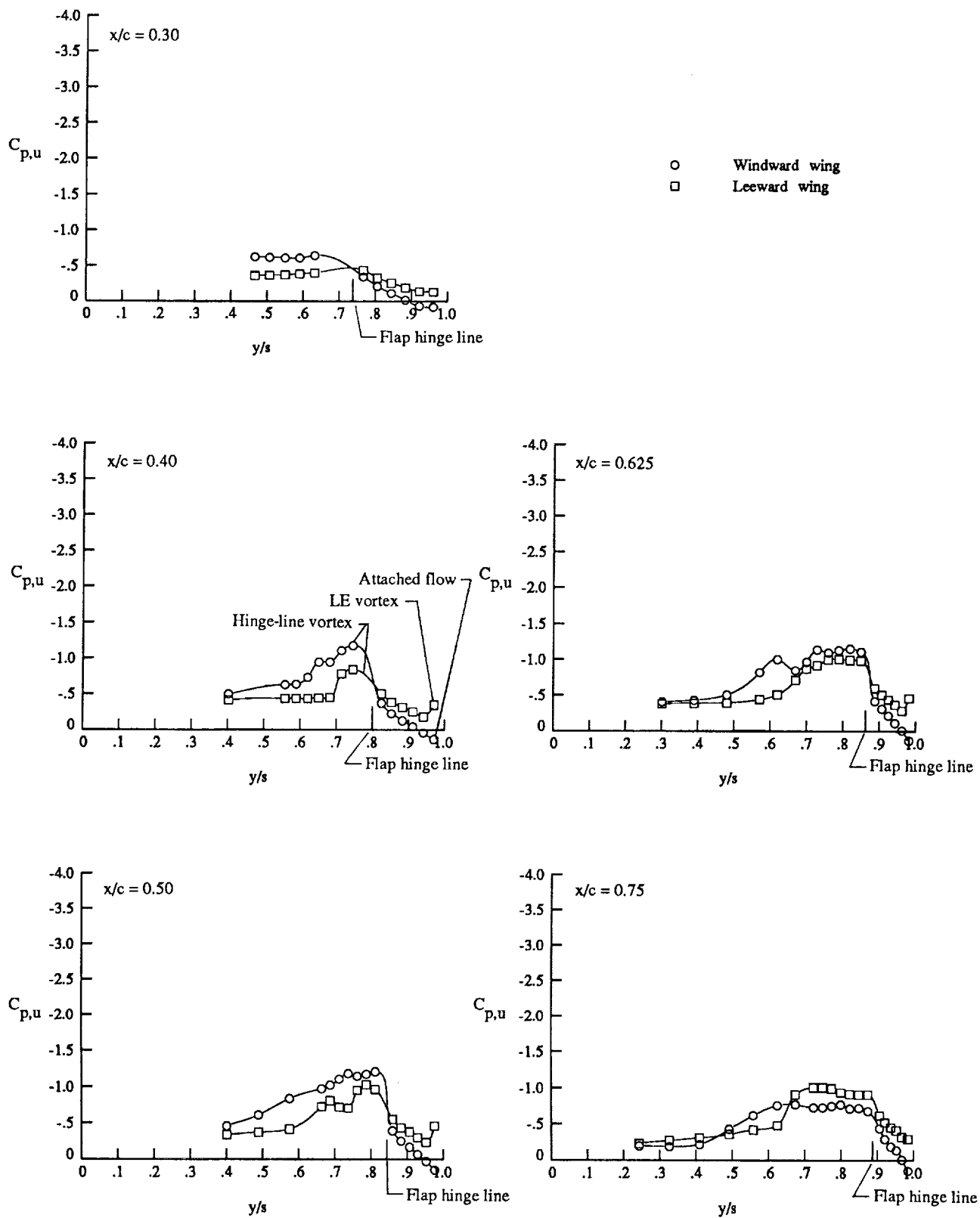
(a) Lateral-directional stability derivatives.

Figure 28. Effect of forebody strakes on lateral-directional characteristics at $M_\infty = 0.90$ with $\delta_{LE} = 30^\circ$.



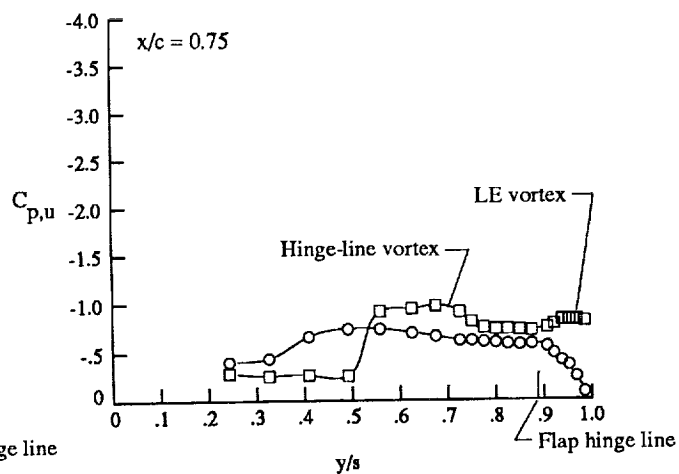
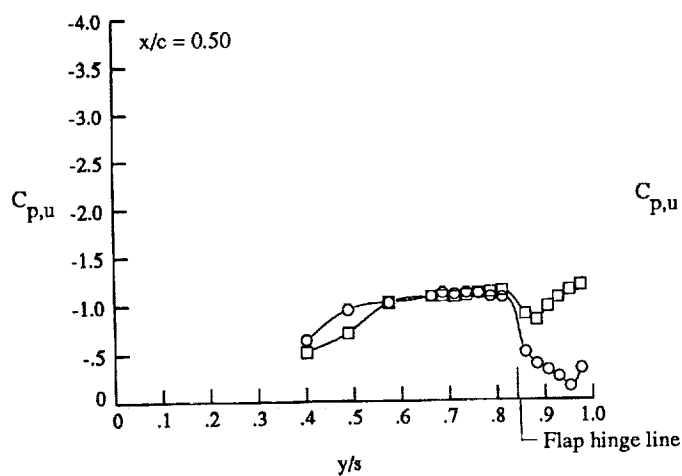
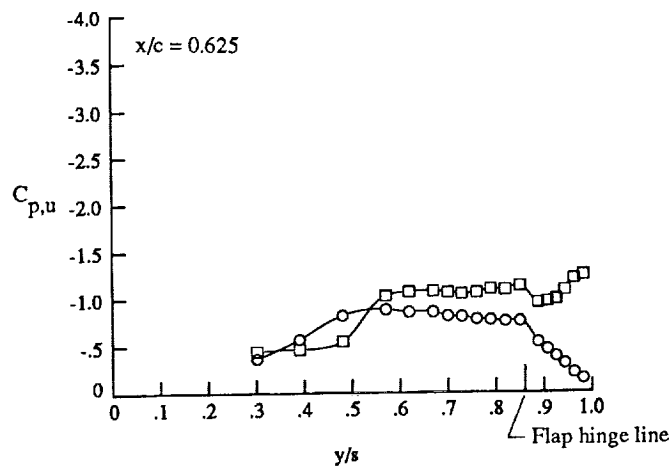
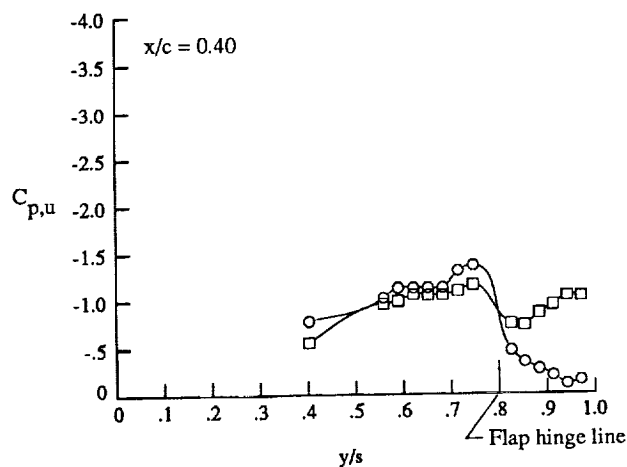
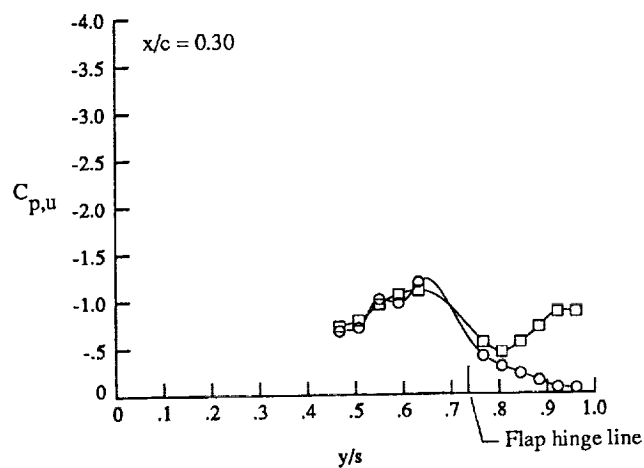
(b) Wing upper surface static pressure distributions with strakes off at $\alpha \approx 12^\circ$.

Figure 28. Continued.



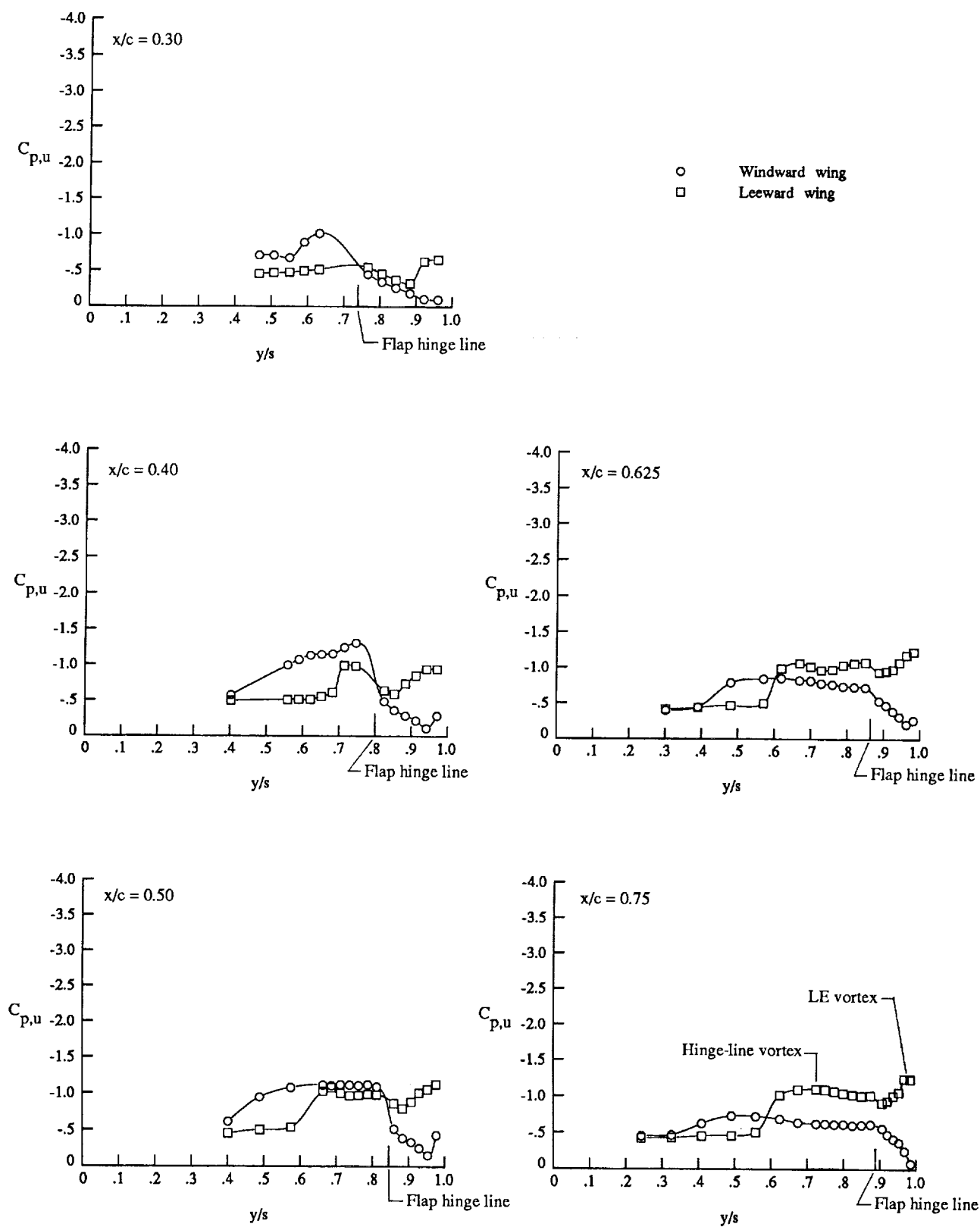
(c) Wing upper surface static pressure distributions with strakes on at $\alpha \approx 12^\circ$.

Figure 28. Continued.



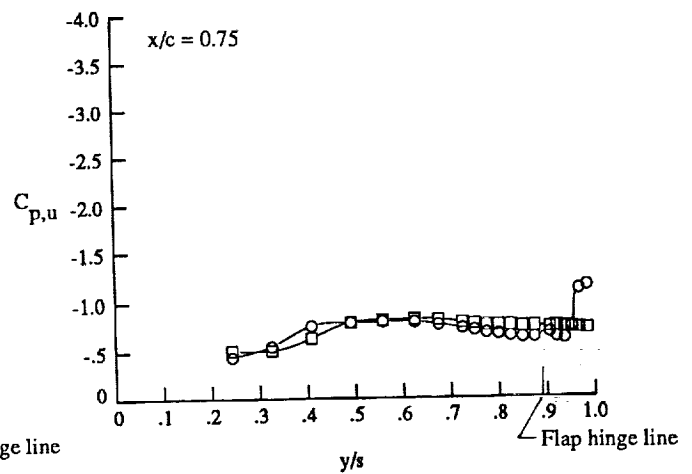
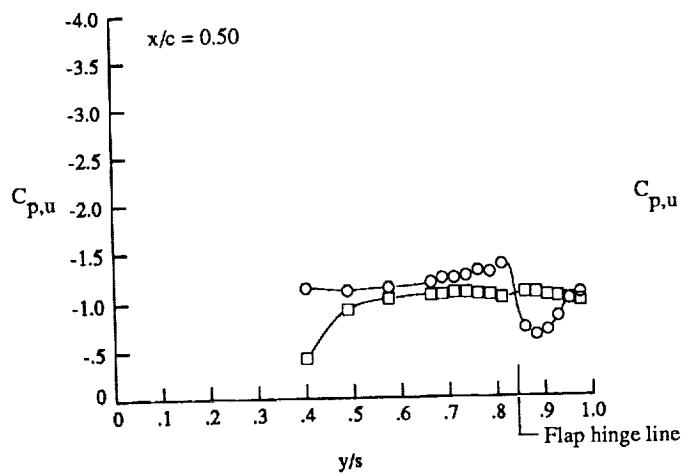
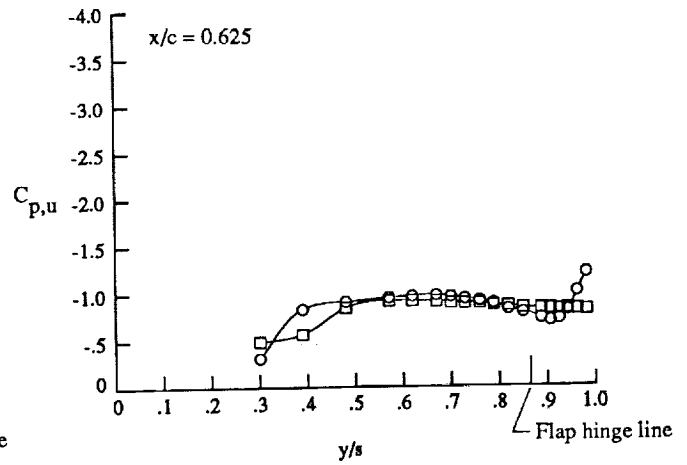
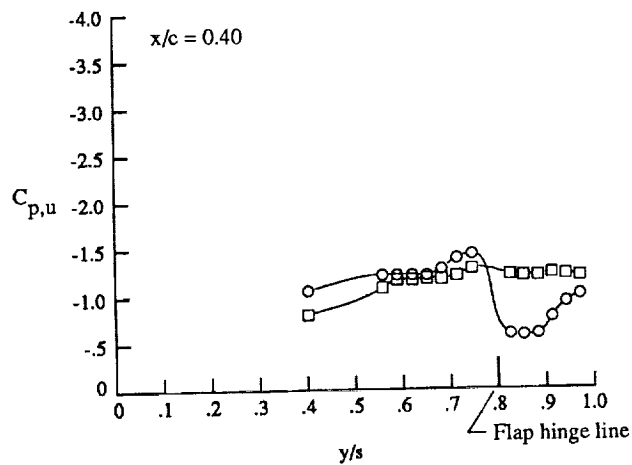
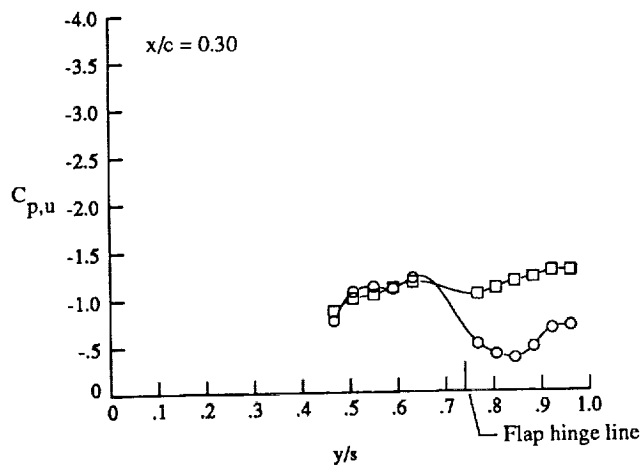
(d) Wing upper surface static pressure distributions with strakes off at $\alpha \approx 16^\circ$.

Figure 28. Continued.



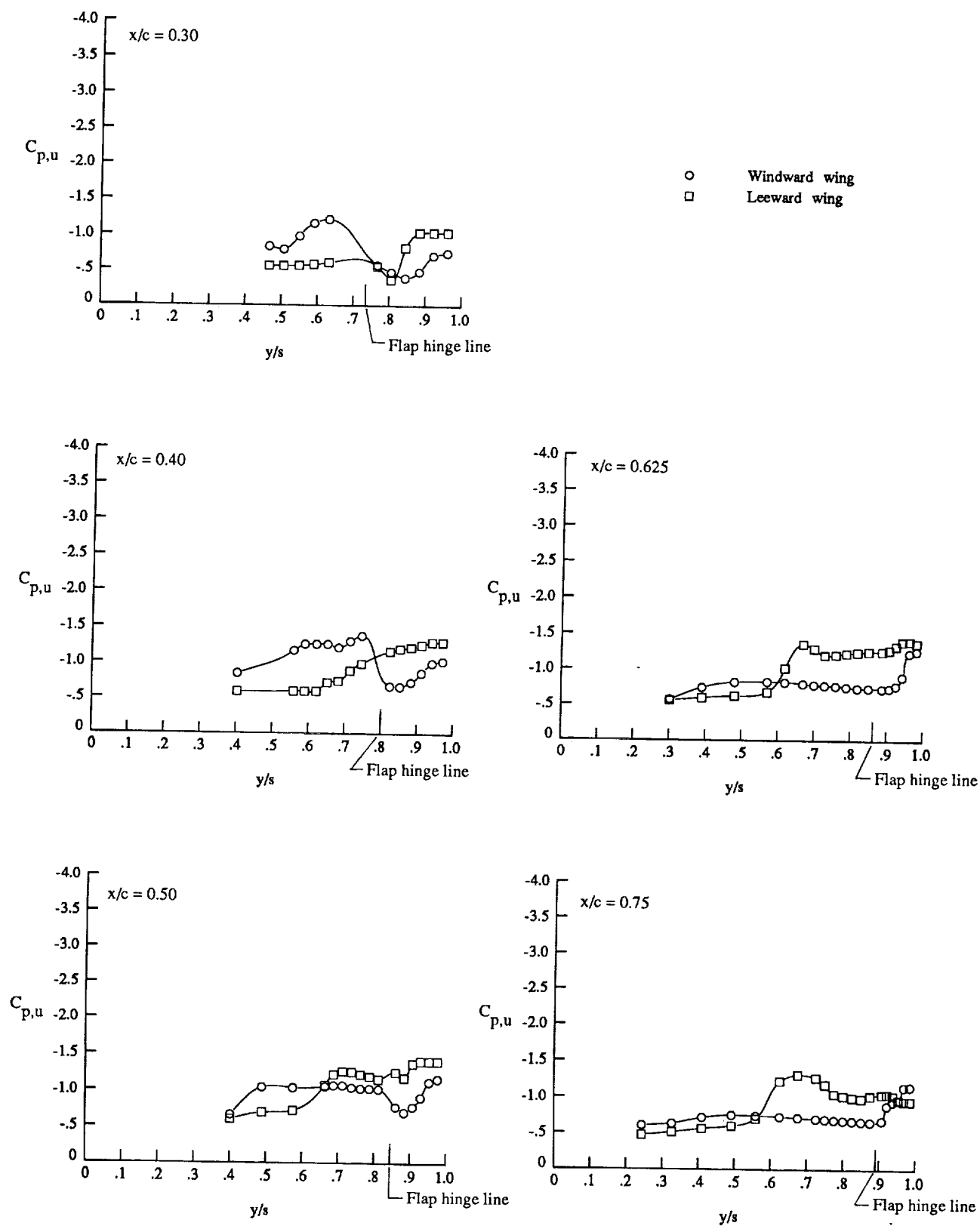
(e) Wing upper surface static pressure distributions with strakes on at $\alpha \approx 16^\circ$.

Figure 28. Continued.



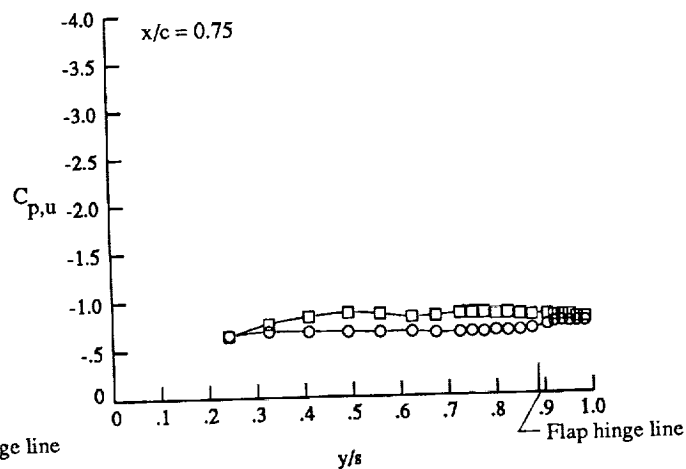
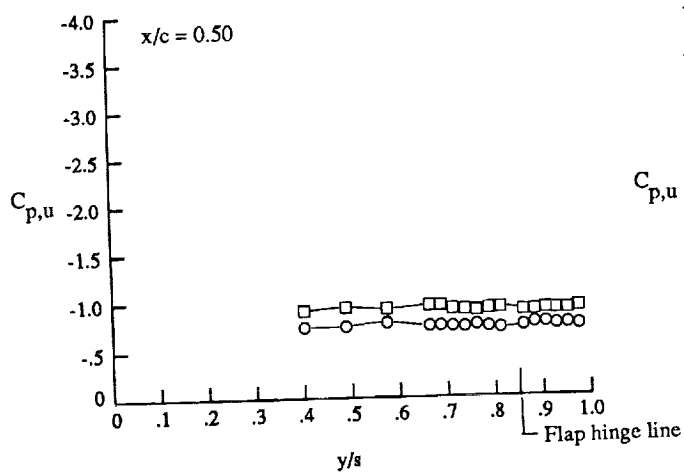
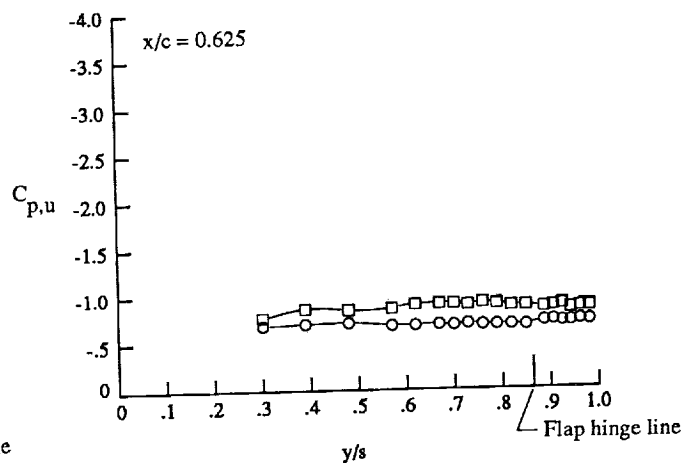
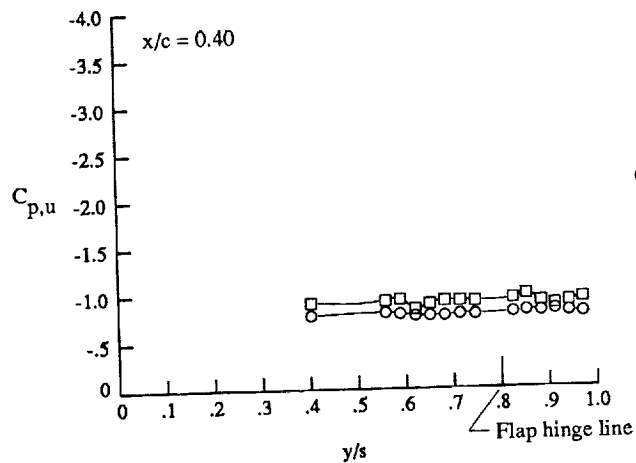
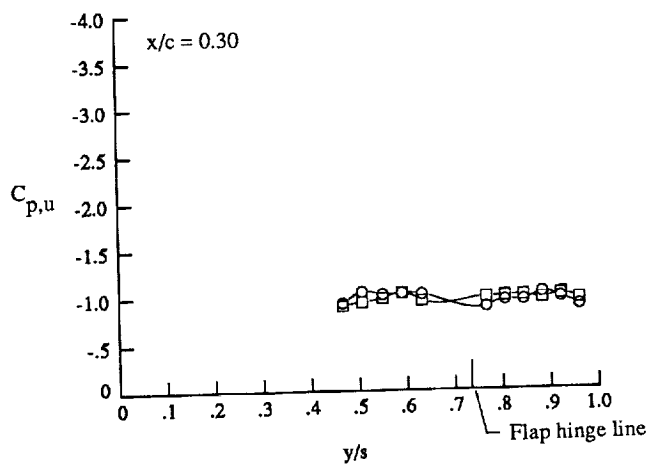
(f) Wing upper surface static pressure distributions with strakes off at $\alpha \approx 20^\circ$.

Figure 28. Continued.



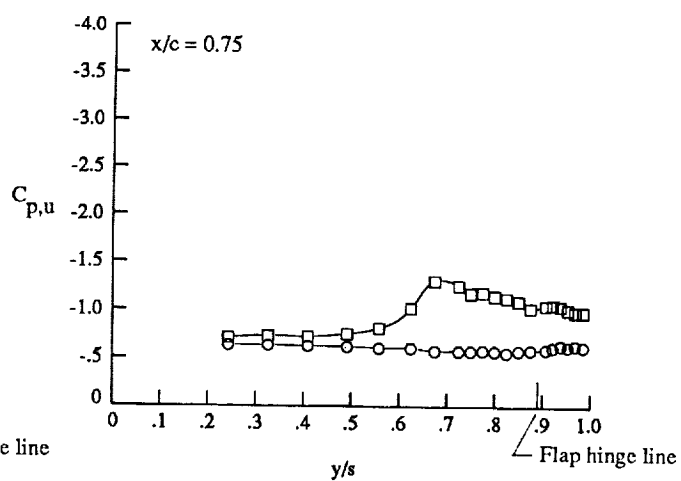
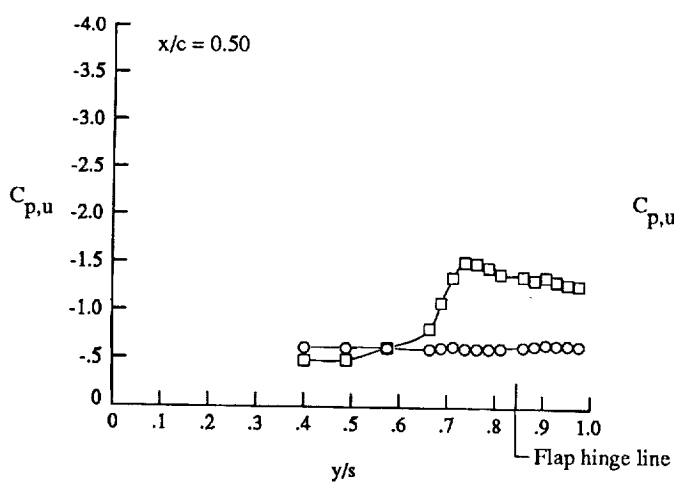
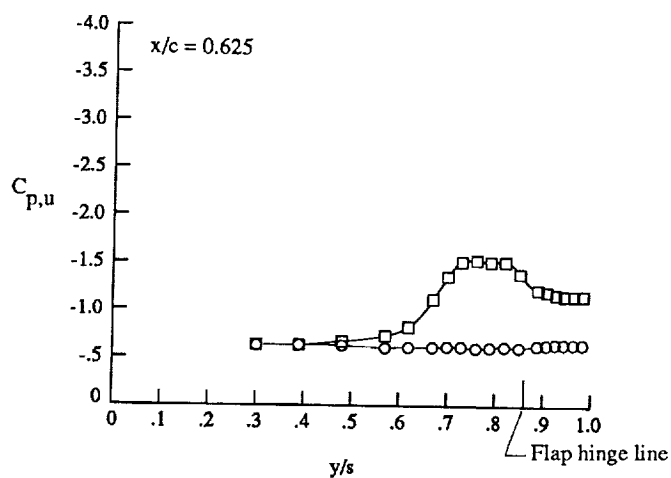
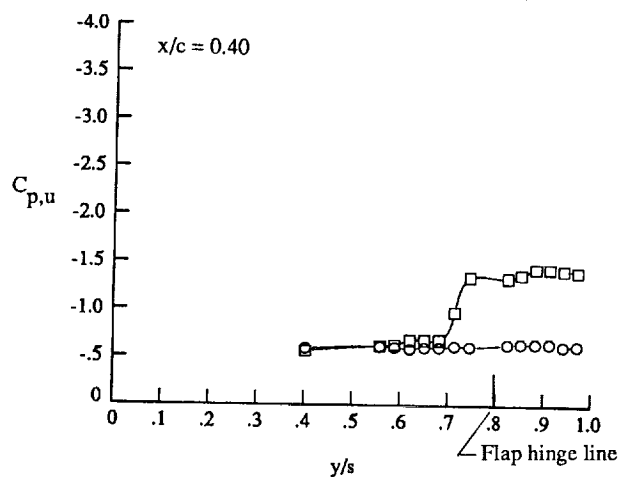
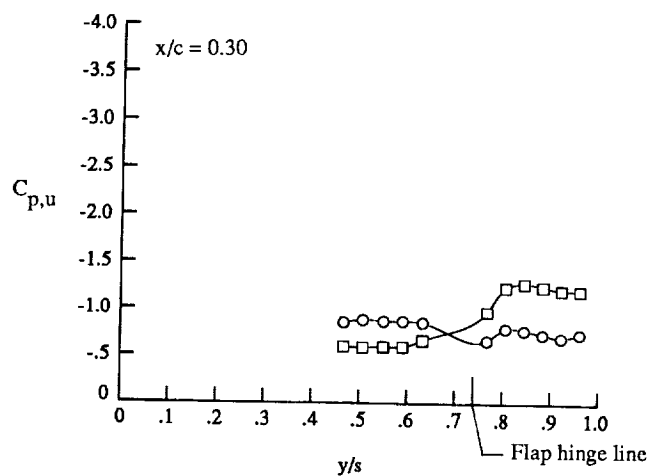
(g) Wing upper surface static pressure distributions with strakes on at $\alpha \approx 20^\circ$.

Figure 28. Continued.



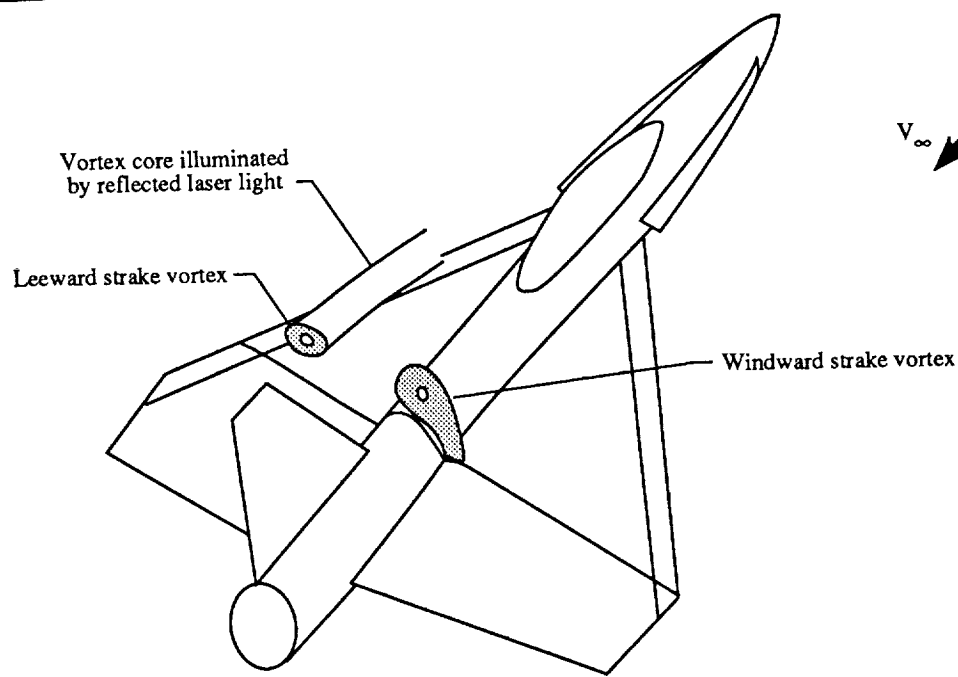
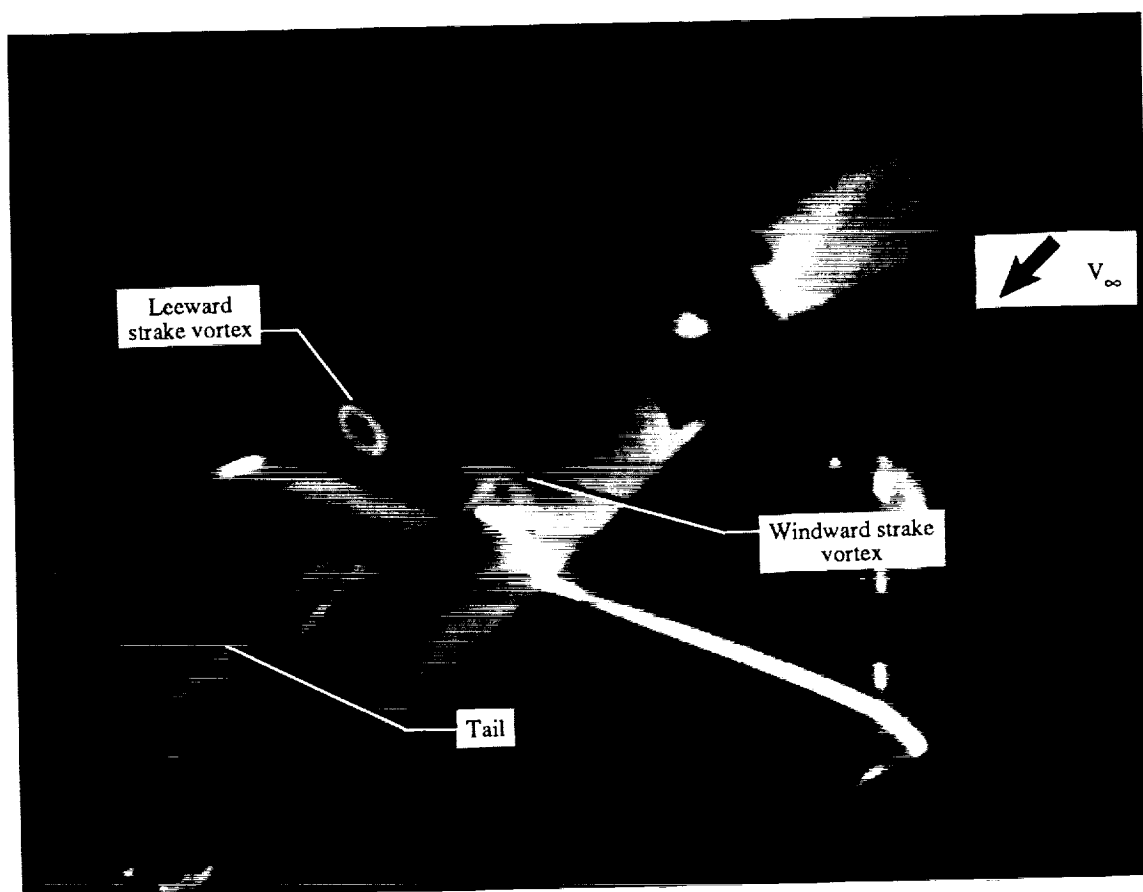
(h) Wing upper surface static pressure distributions with strakes off at $\alpha \approx 24^\circ$.

Figure 28. Continued.



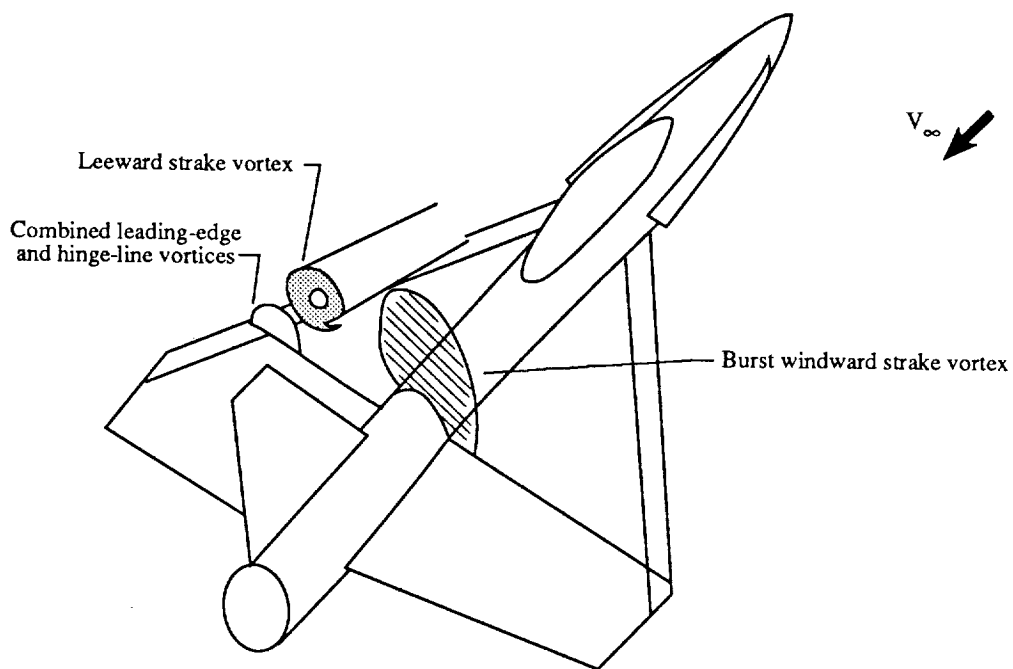
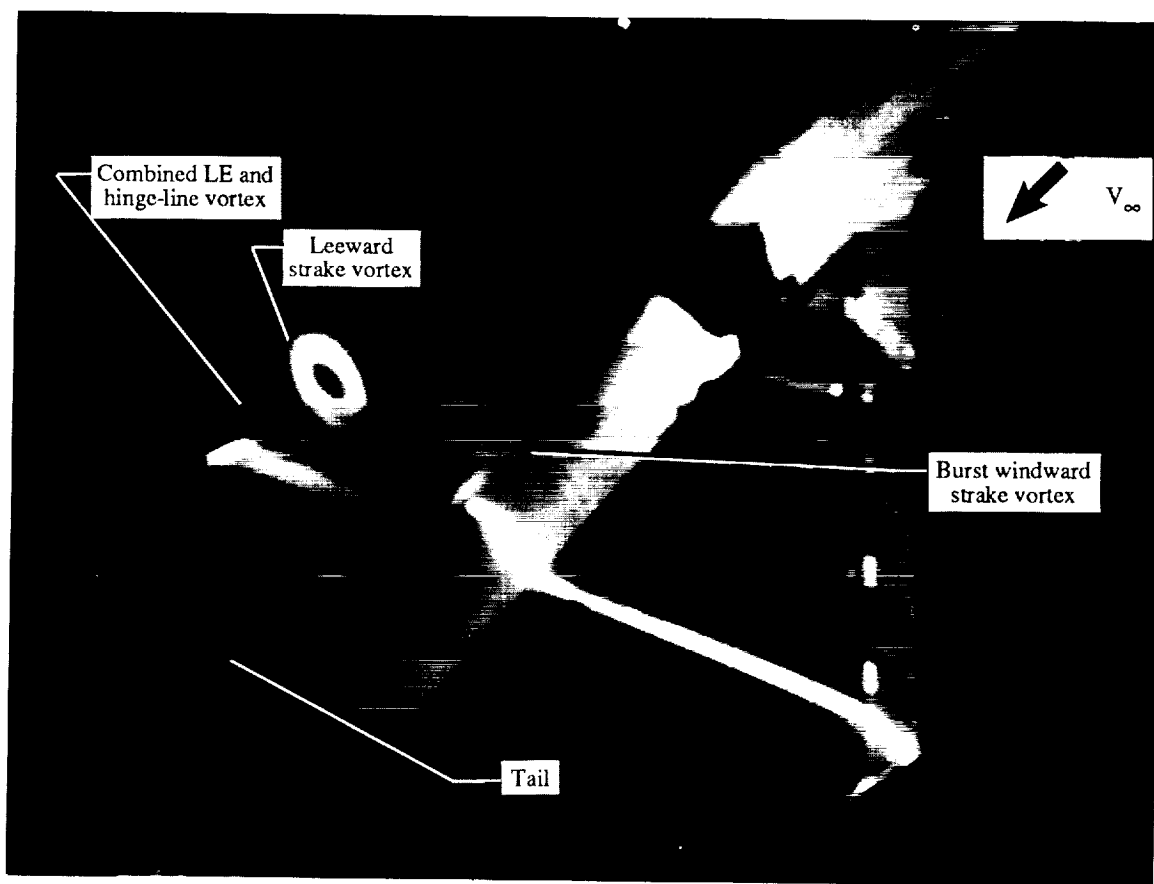
(i) Wing upper surface static pressure distributions with strakes on at $\alpha \approx 24^\circ$.

Figure 28. Concluded.



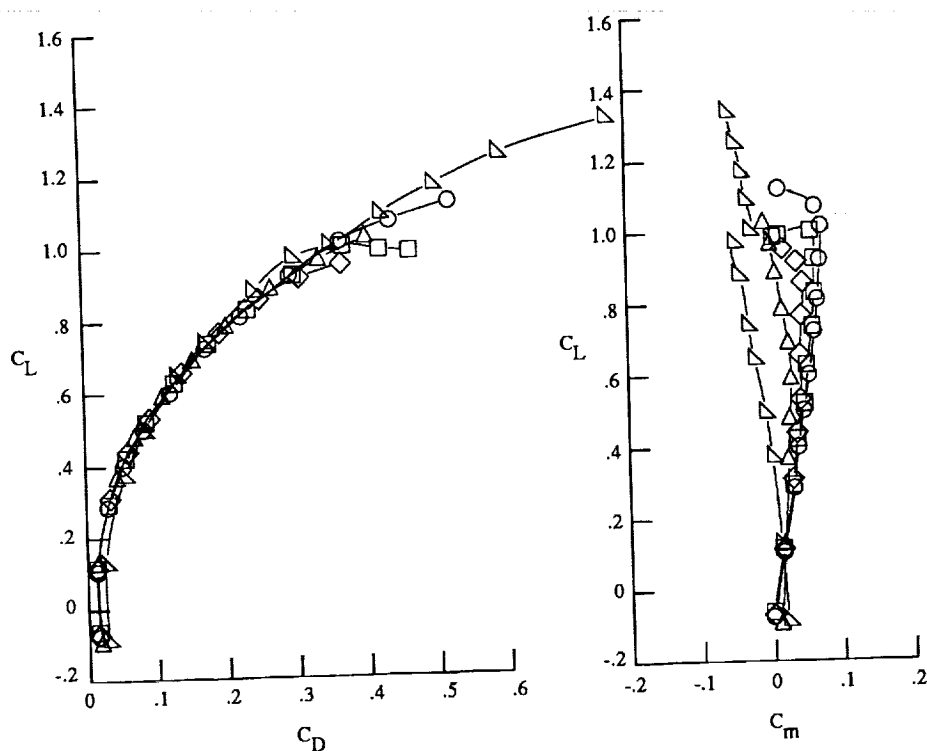
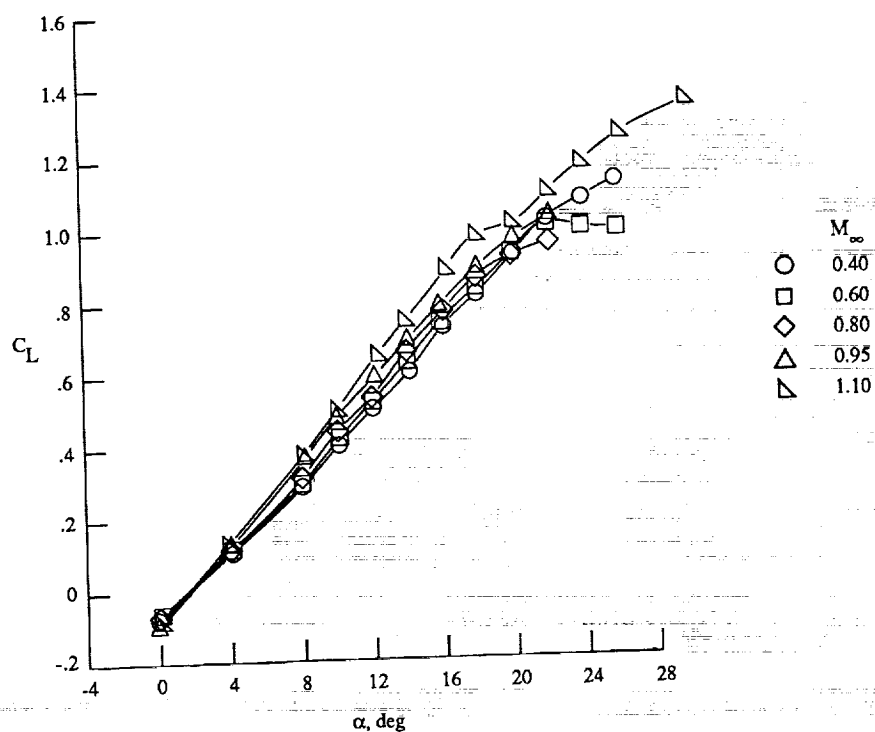
(a) $\alpha \approx 16^\circ$.

Figure 29. Laser vapor screen flow visualization (right three-quarter rear view) results at $M_\infty = 0.90$ and $\beta = +5^\circ$ with $\delta_{LE} = 30^\circ$.



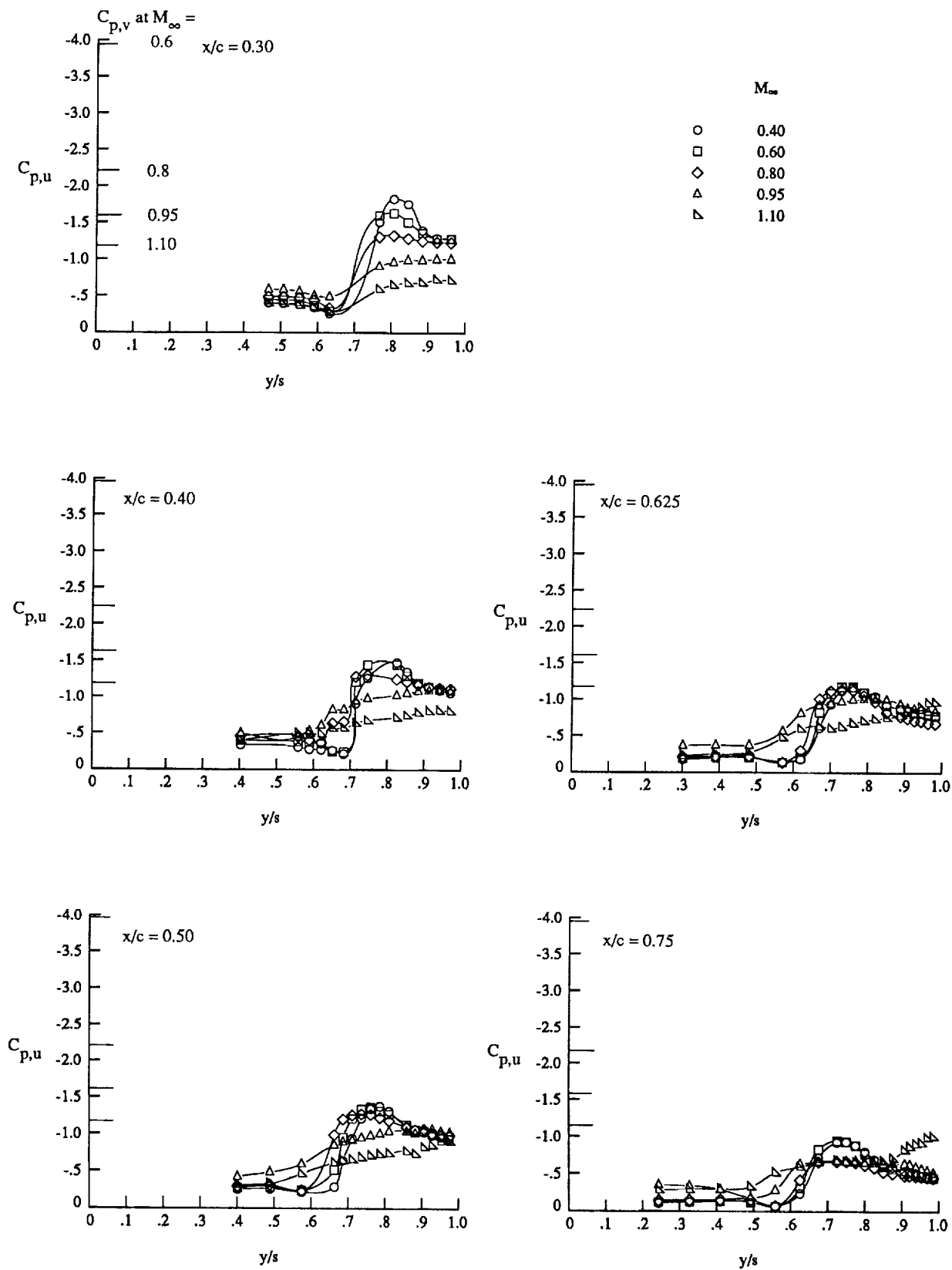
(b) $\alpha \approx 22^\circ$.

Figure 29. Concluded.



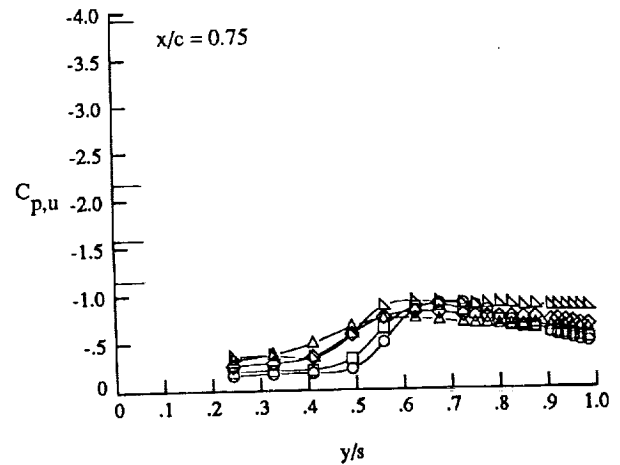
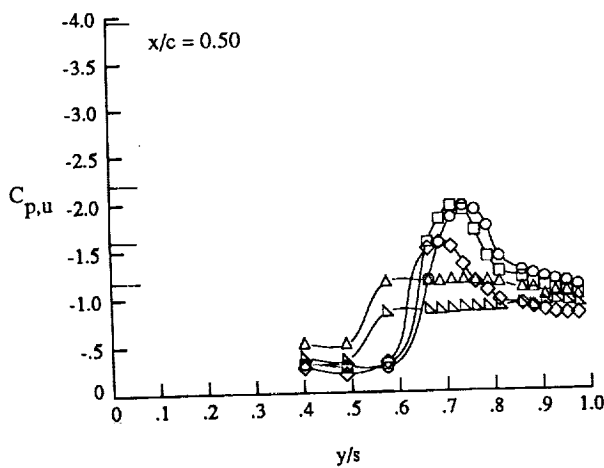
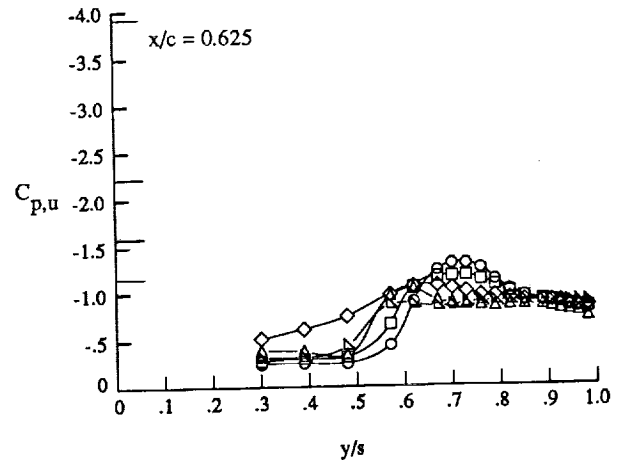
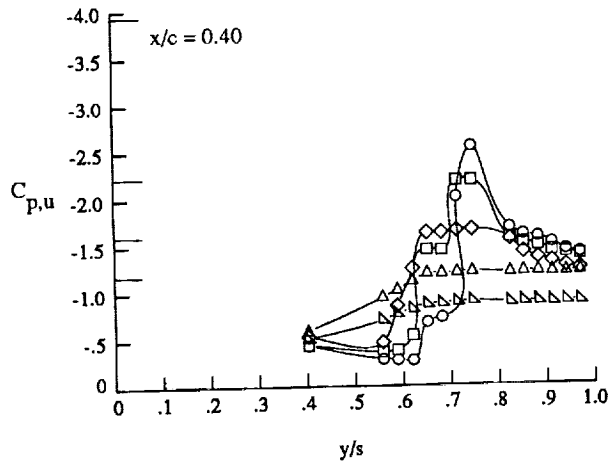
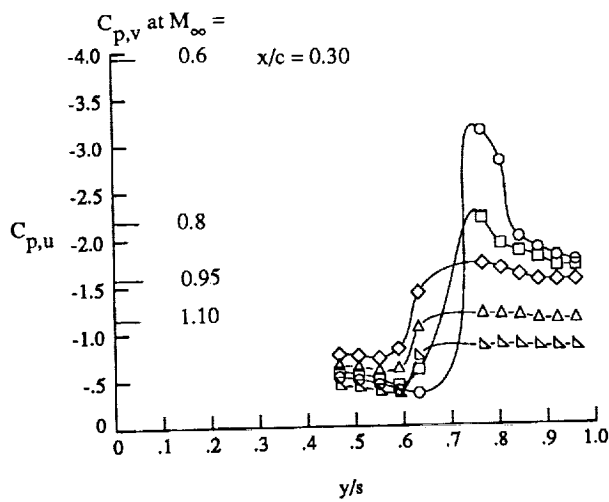
(a) Lift, drag, and pitching moment.

Figure 30. Effect of Mach number on longitudinal characteristics with strakes off and $\delta_{LE} = 0^\circ$.



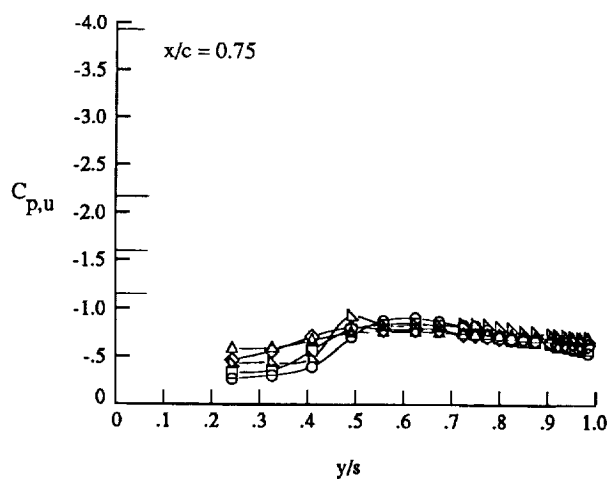
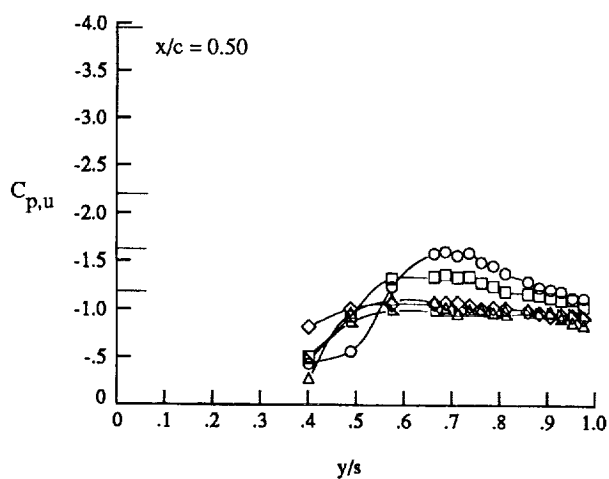
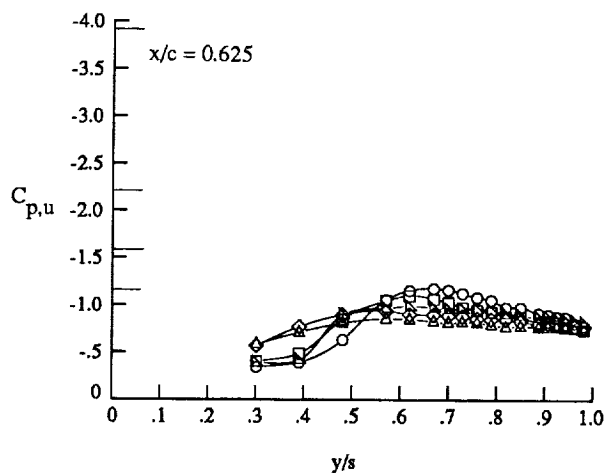
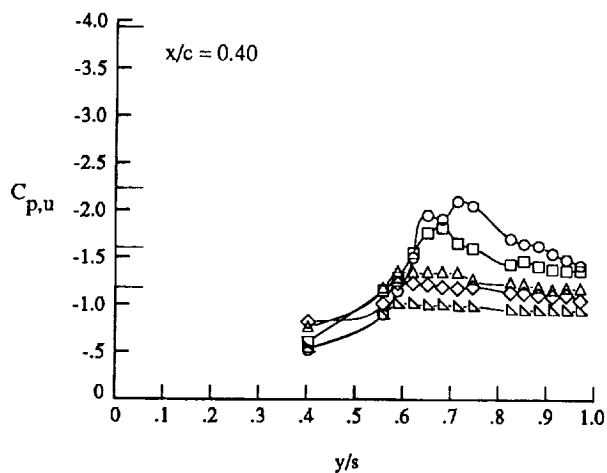
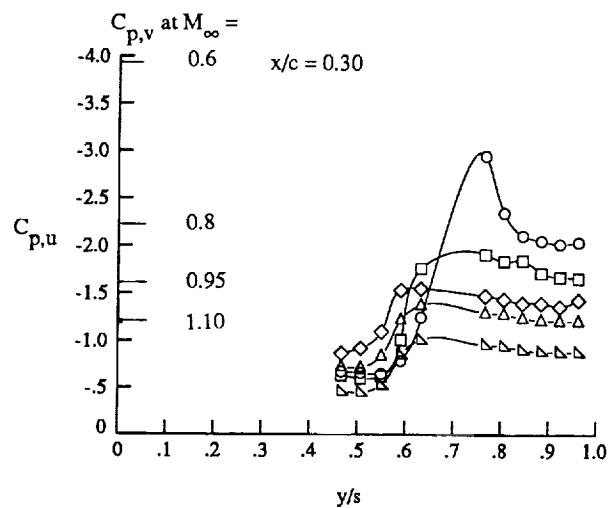
(b) Wing upper surface static pressure distributions at $\alpha \approx 12^\circ$.

Figure 30. Continued.



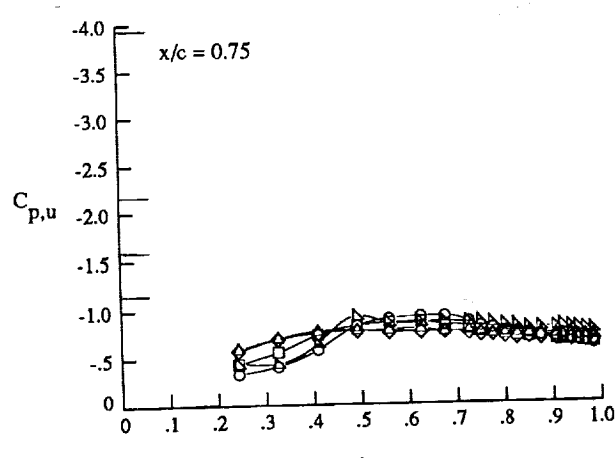
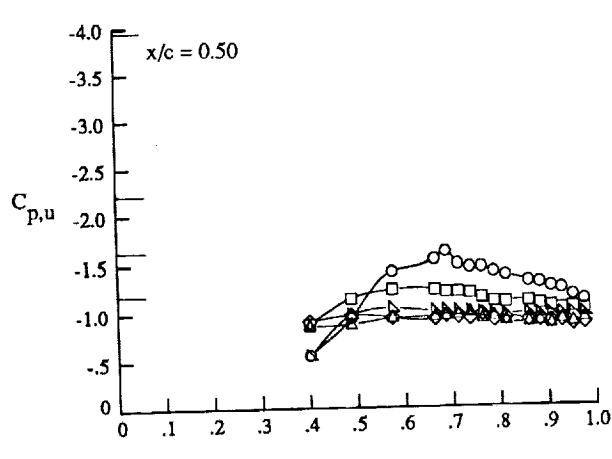
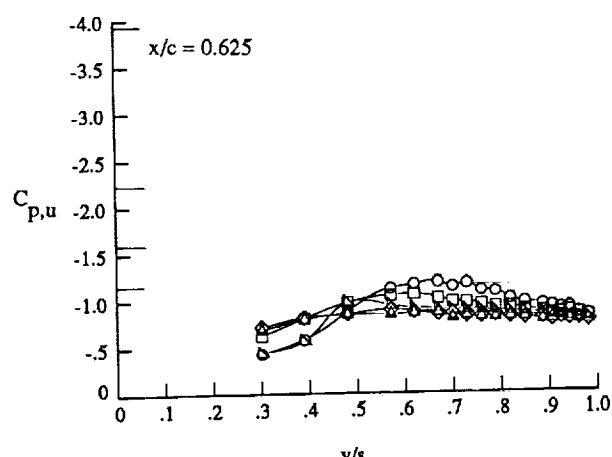
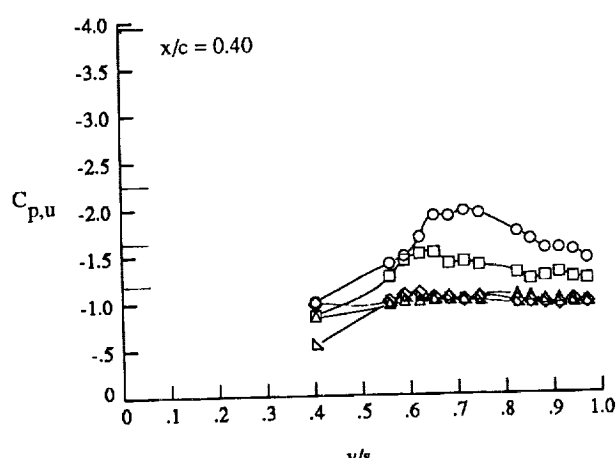
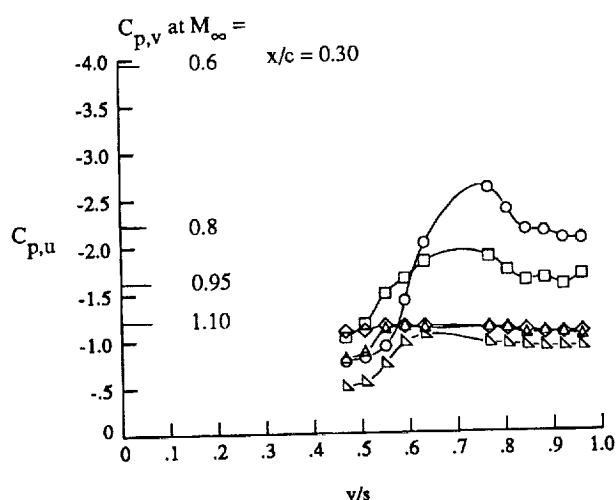
(c) Wing upper surface static pressure distributions at $\alpha \approx 16^\circ$.

Figure 30. Continued.



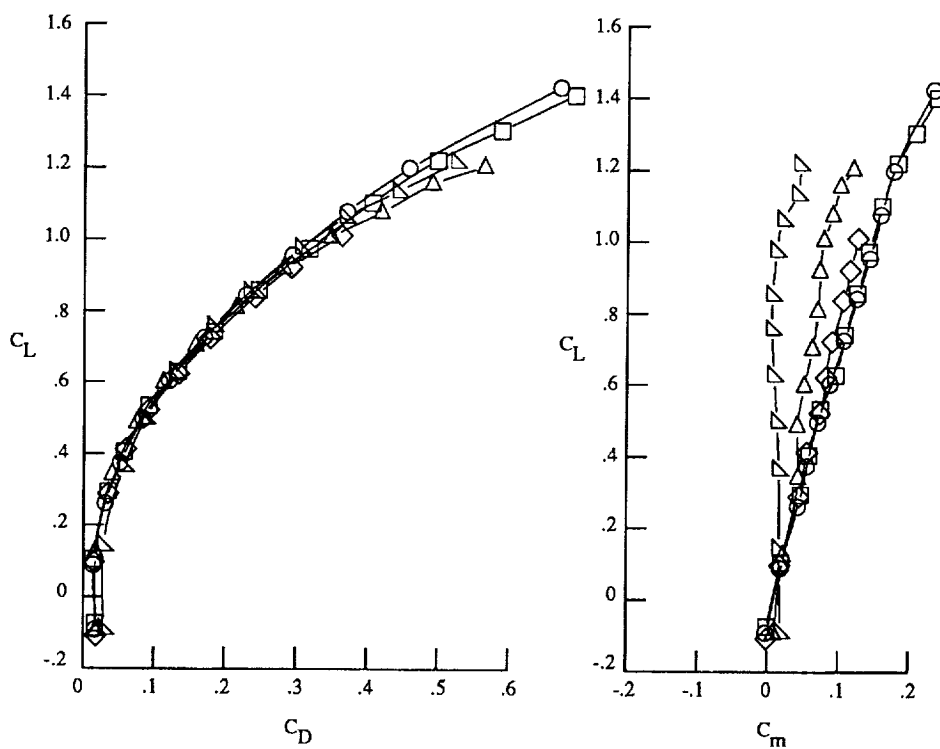
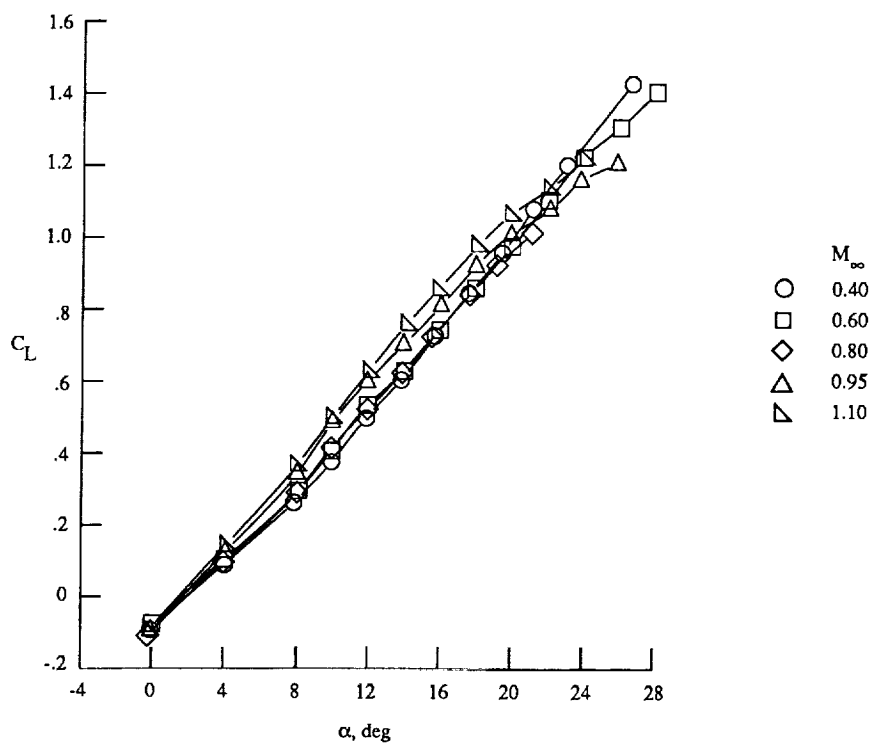
(d) Wing upper surface static pressure distributions at $\alpha \approx 20^\circ$.

Figure 30. Continued.



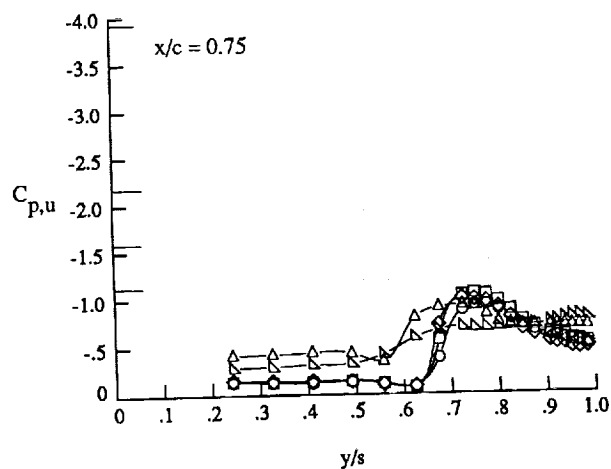
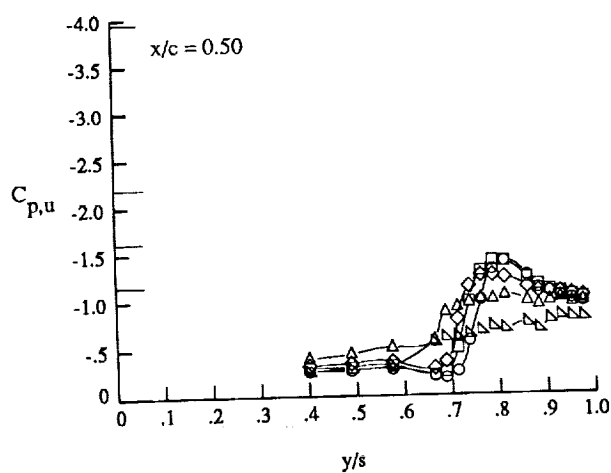
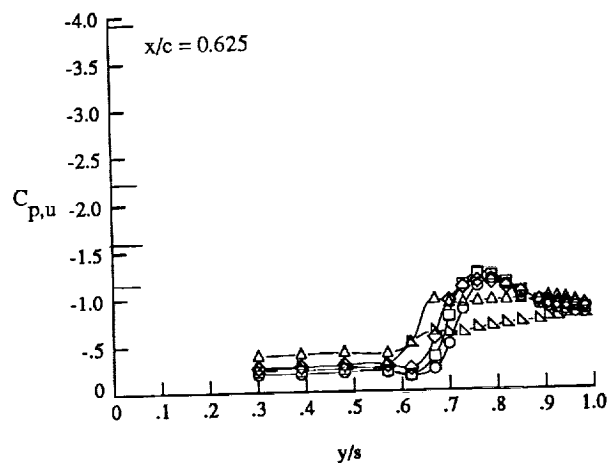
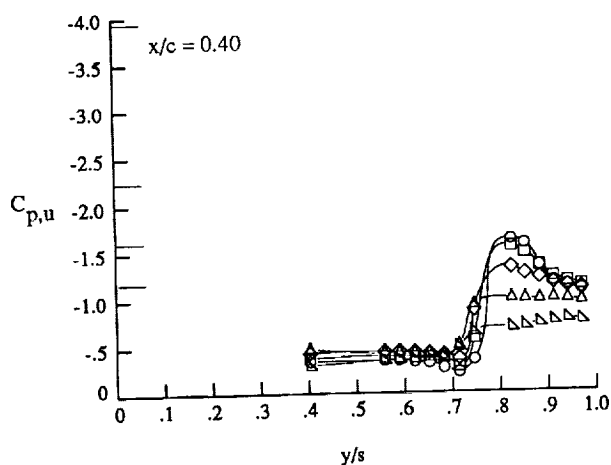
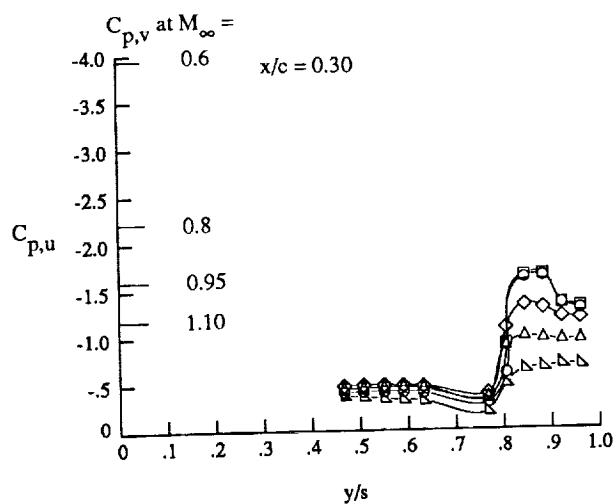
(c) Wing upper surface static pressure distributions at $\alpha \approx 22^\circ$.

Figure 30. Concluded.



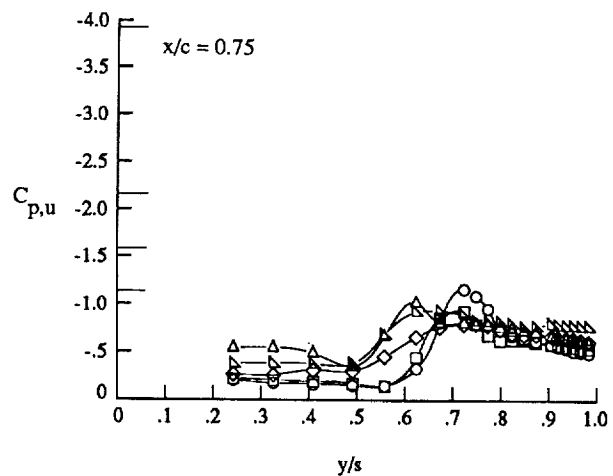
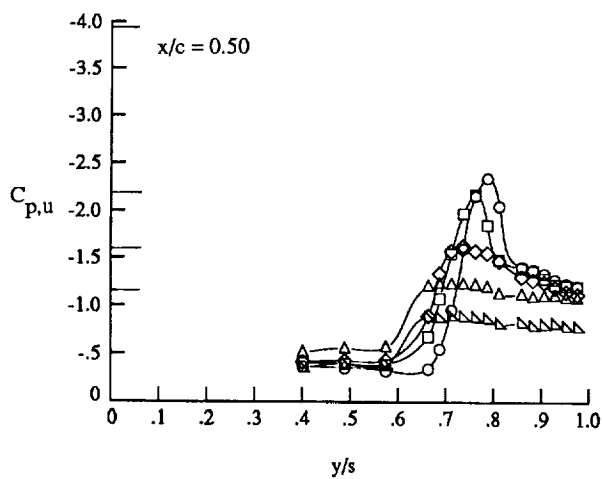
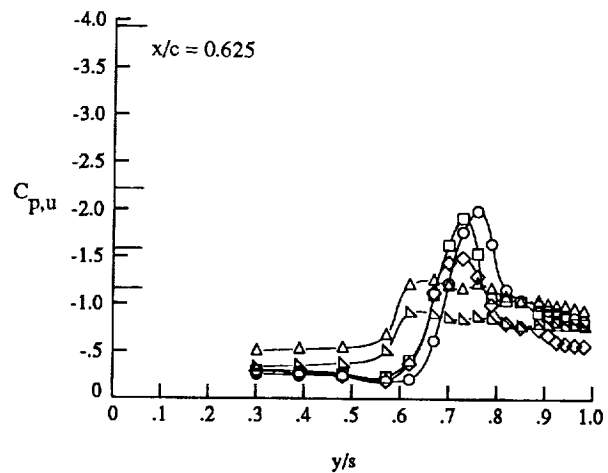
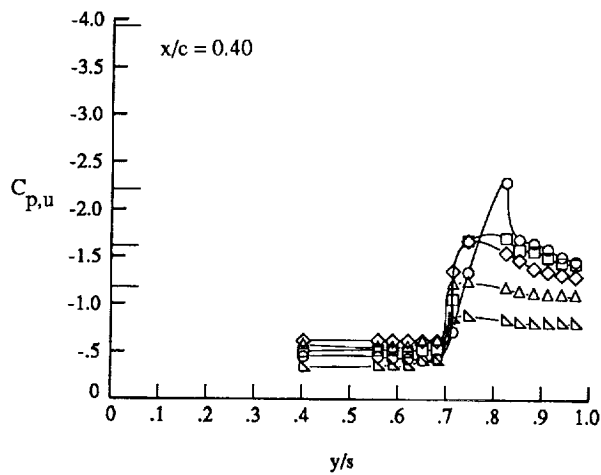
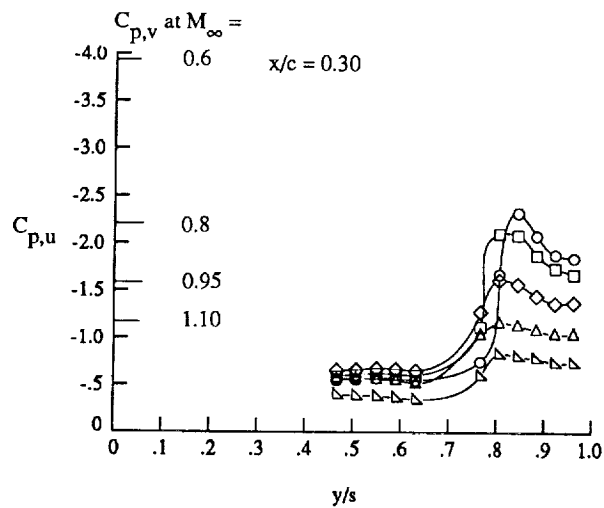
(a) Lift, drag, and pitching moment.

Figure 31. Effect of Mach number on longitudinal characteristics with strakes on and $\delta_{LE} = 0^\circ$.



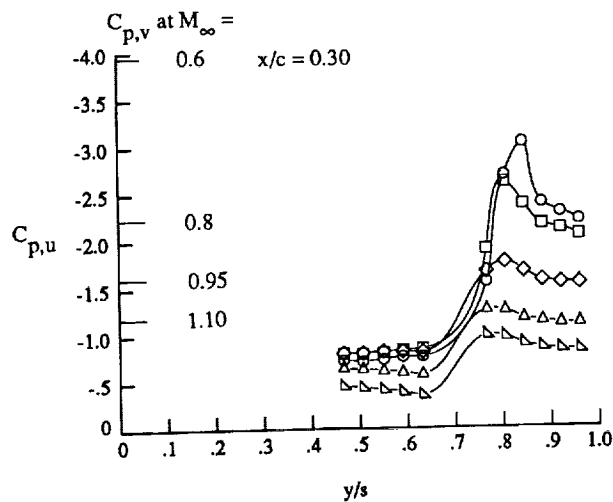
(b) Wing upper surface static pressure distributions at $\alpha \approx 12^\circ$.

Figure 31. Continued.

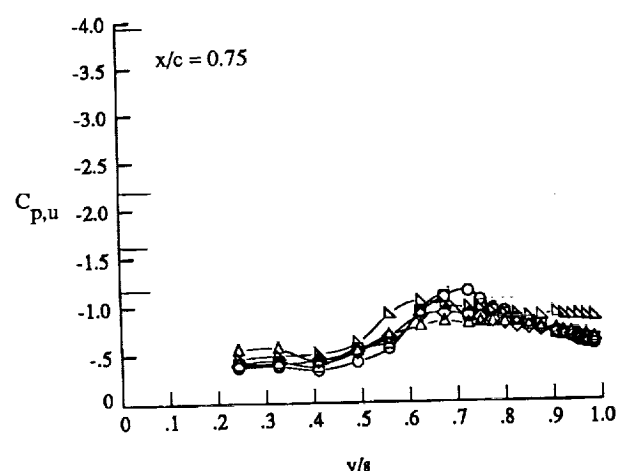
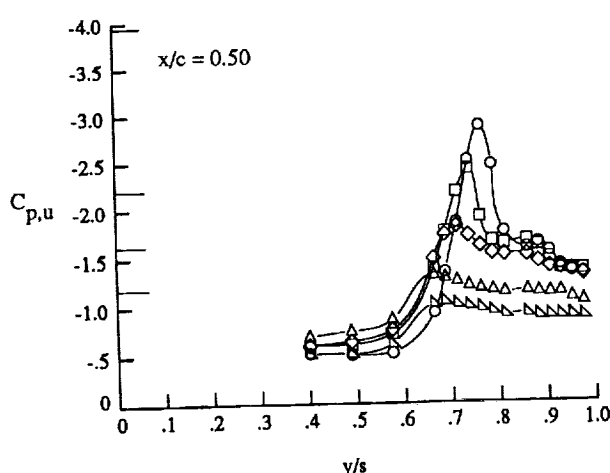
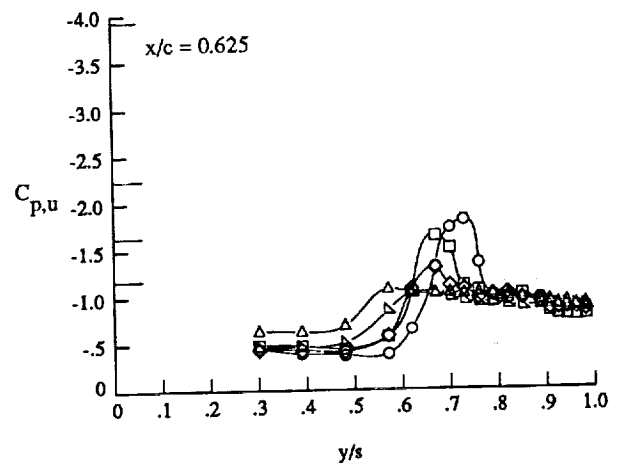
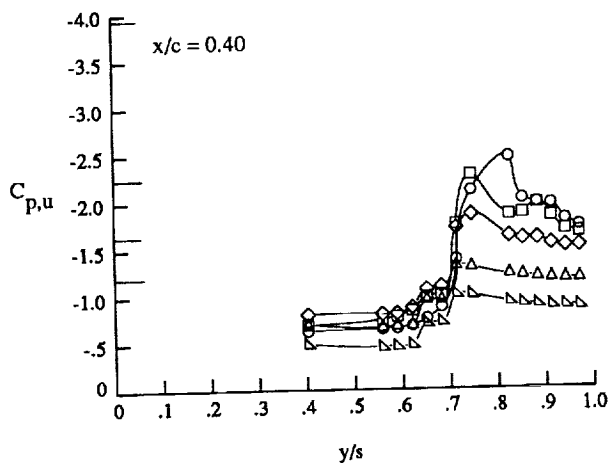


(c) Wing upper surface static pressure distributions at $\alpha \approx 16^\circ$.

Figure 31. Continued.

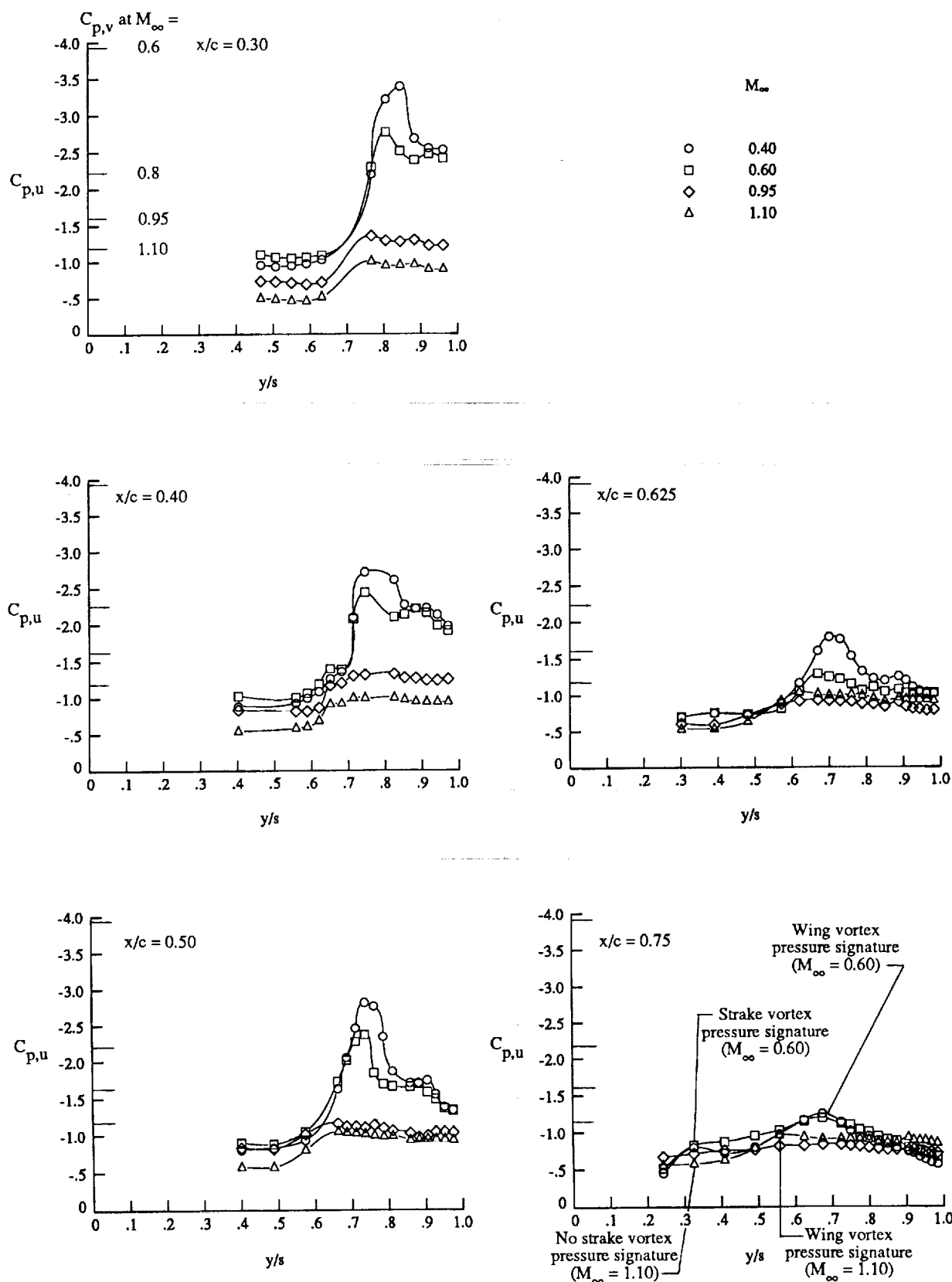


M_∞	
○	0.40
□	0.60
◇	0.80
△	0.95
▽	1.10



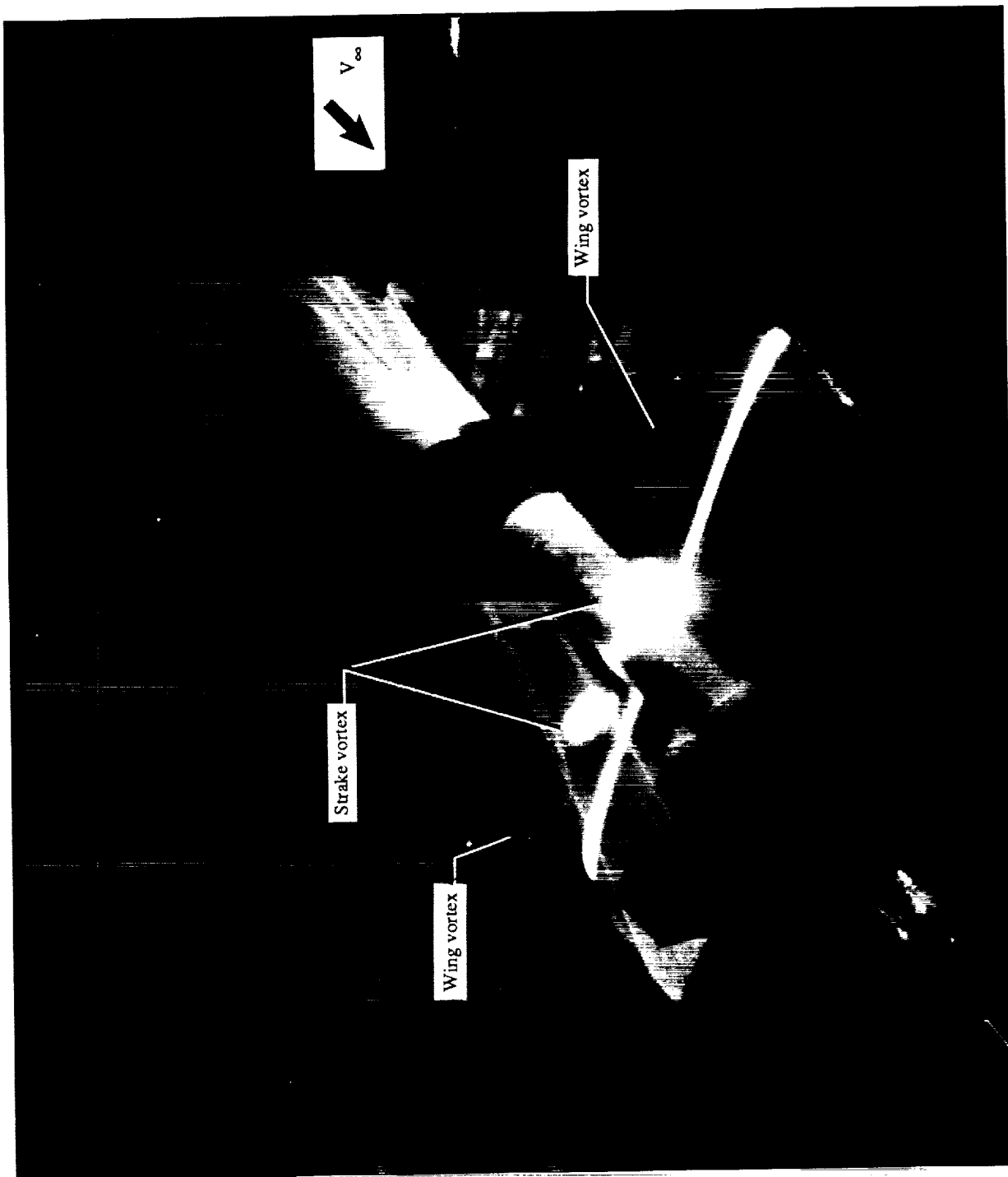
(d) Wing upper surface static pressure distributions at $\alpha \approx 20^\circ$.

Figure 31. Continued.



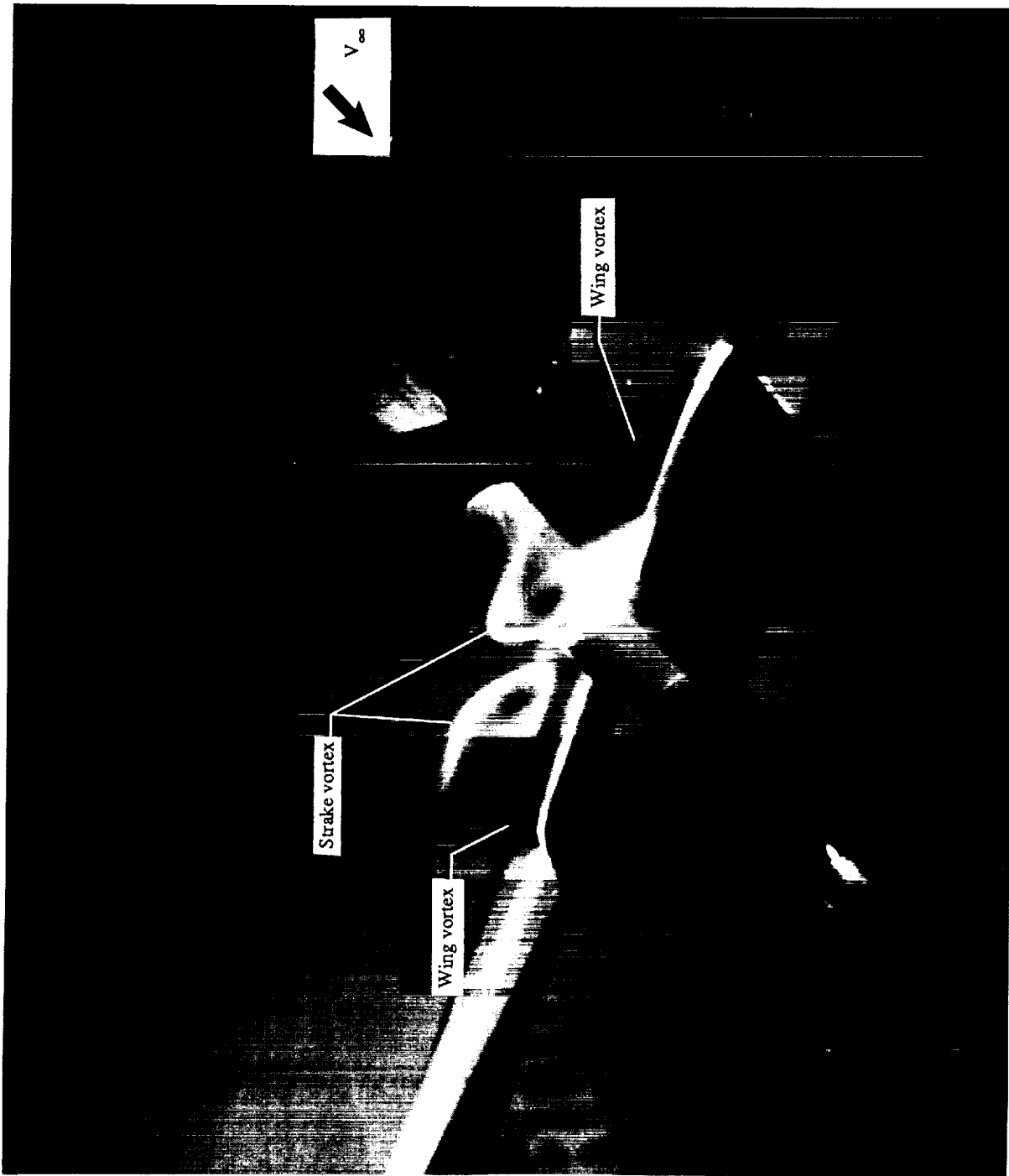
(c) Wing upper surface static pressure distributions at $\alpha \approx 24^\circ$.

Figure 31. Concluded.



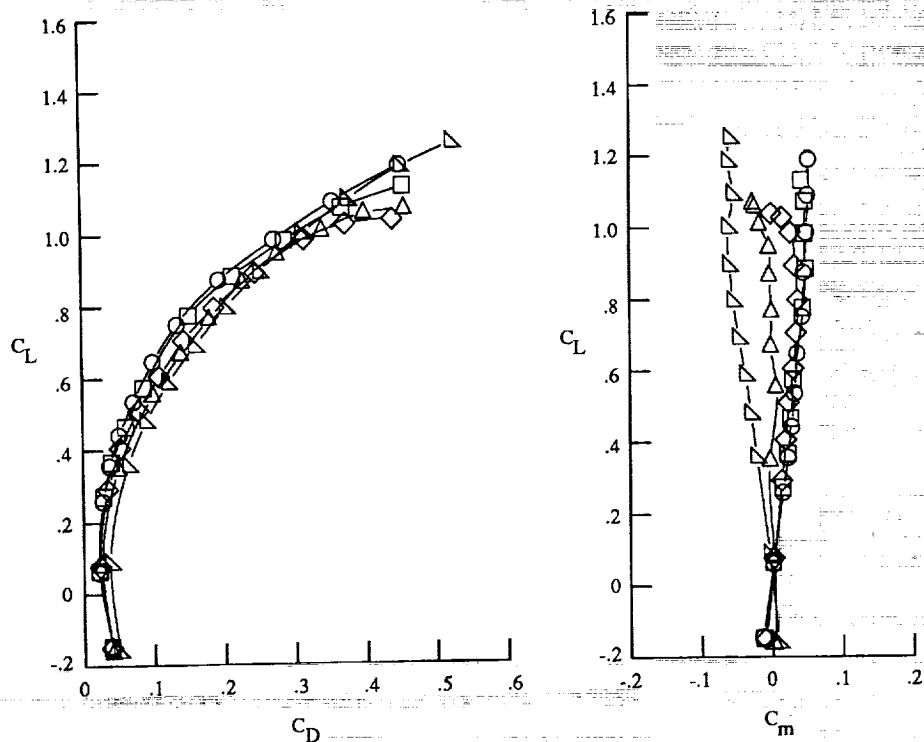
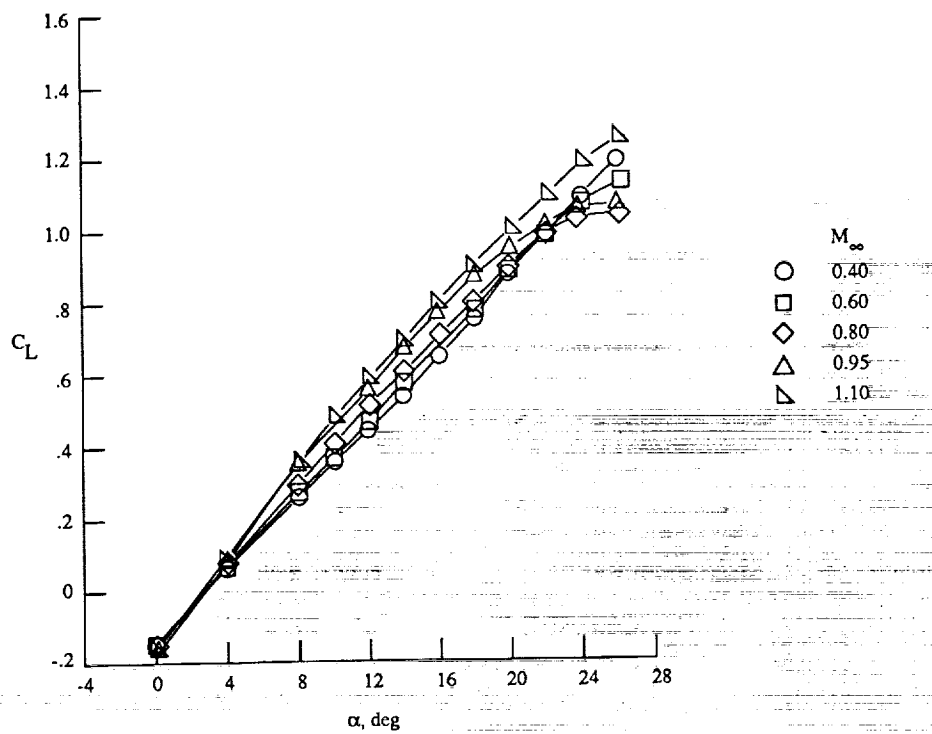
(a) $M_{\infty} = 0.60$.

Figure 32. Laser vapor screen flow visualization results. Strakes on; $\alpha \approx 20^\circ$; $\delta_{LE} = 0^\circ$; $x/c = 0.75$; right three-quarter rear view.



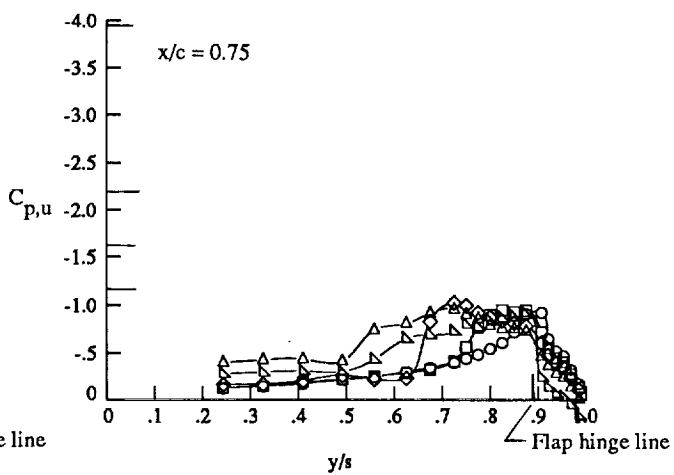
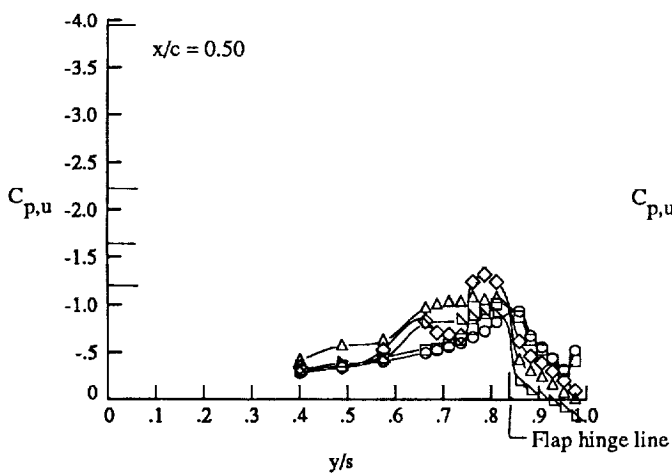
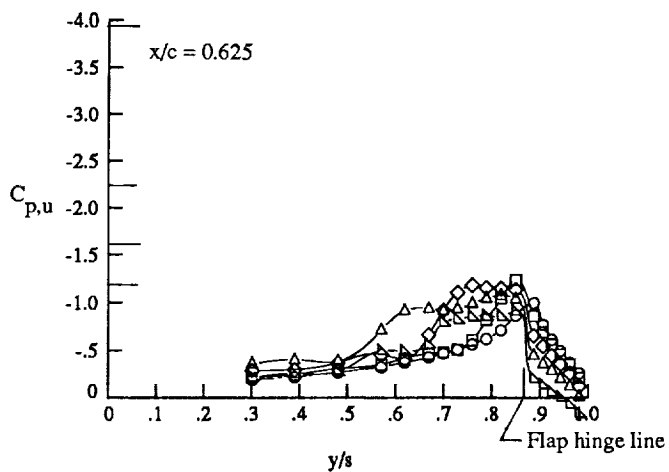
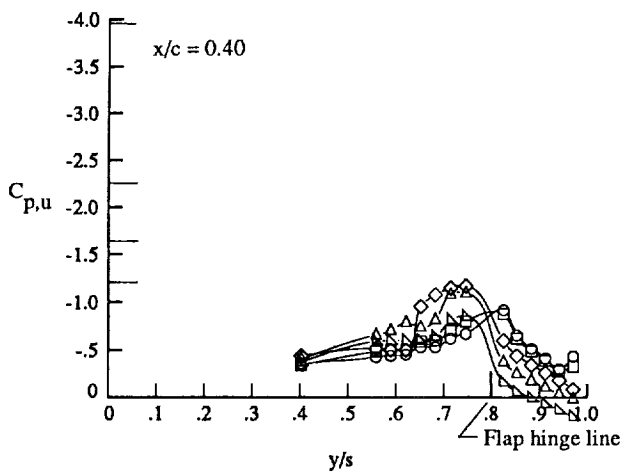
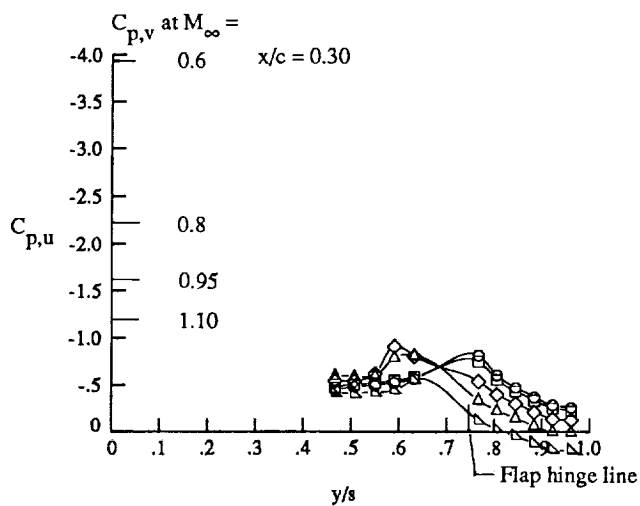
(b) $M_\infty = 1.10$.

Figure 32. Concluded.



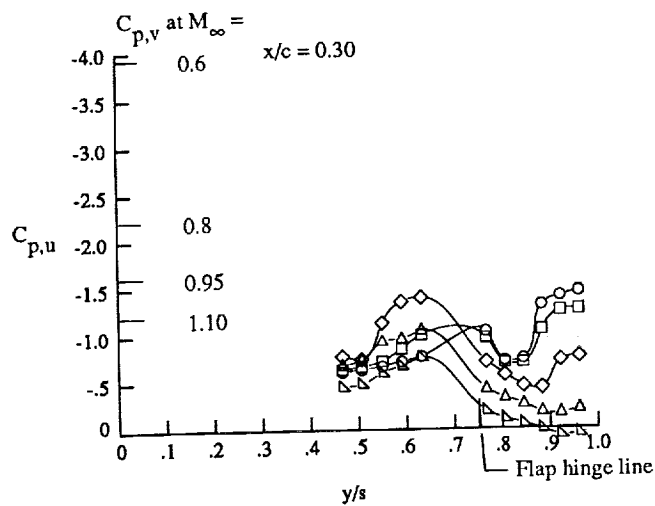
(a) Lift, drag, and pitching moment.

Figure 33. Effect of Mach number on longitudinal characteristics with strakes off and $\delta_{LE} = 30^\circ$.

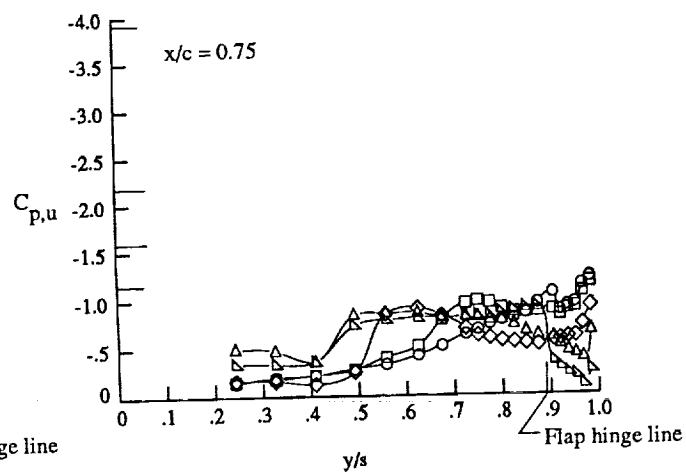
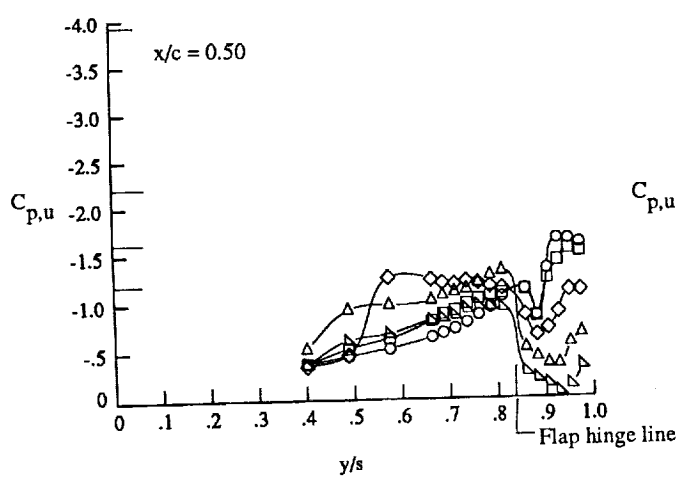
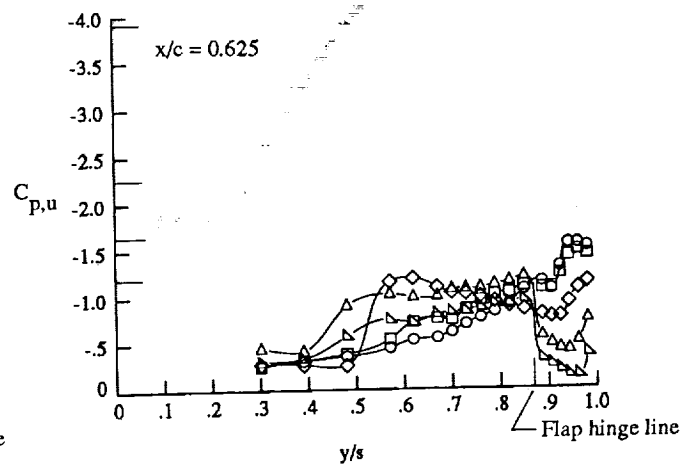
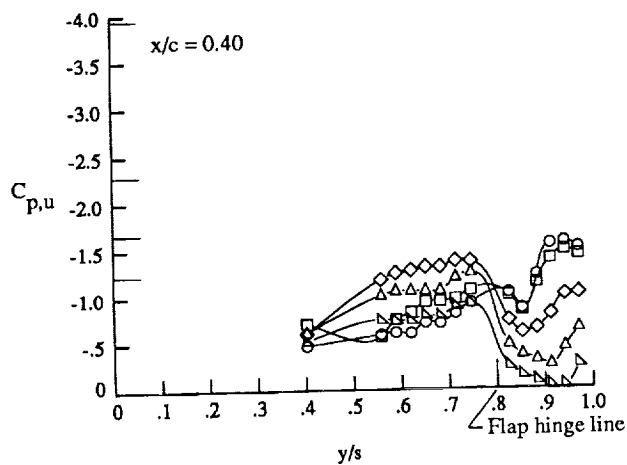


(b) Wing upper surface static pressure distributions at $\alpha \approx 12^\circ$.

Figure 33. Continued.

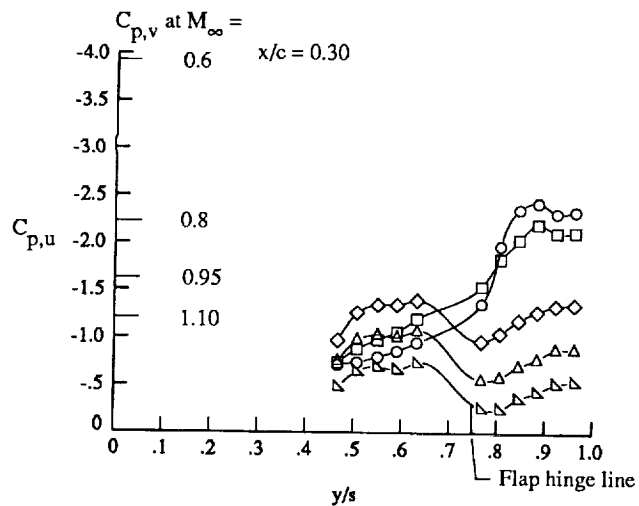


	M_∞
○	0.40
□	0.60
◇	0.80
△	0.95
▽	1.10

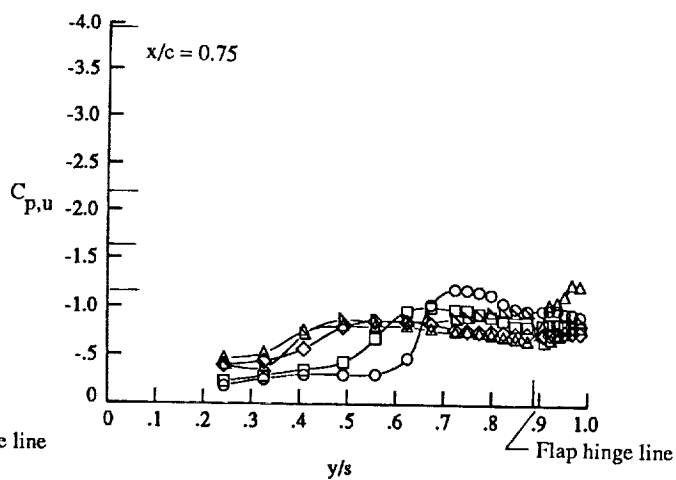
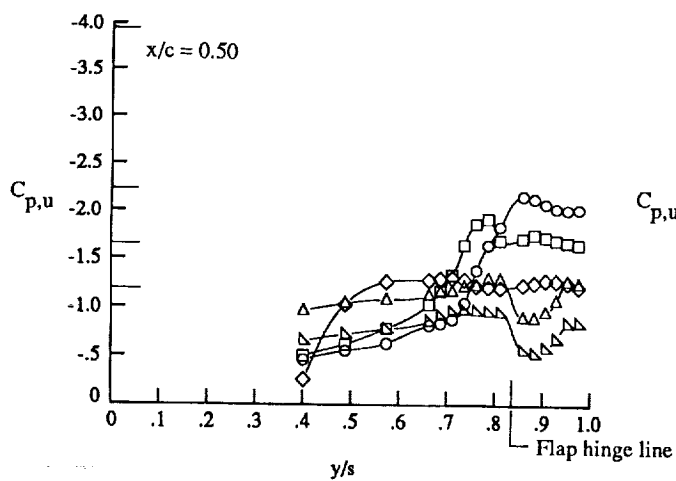
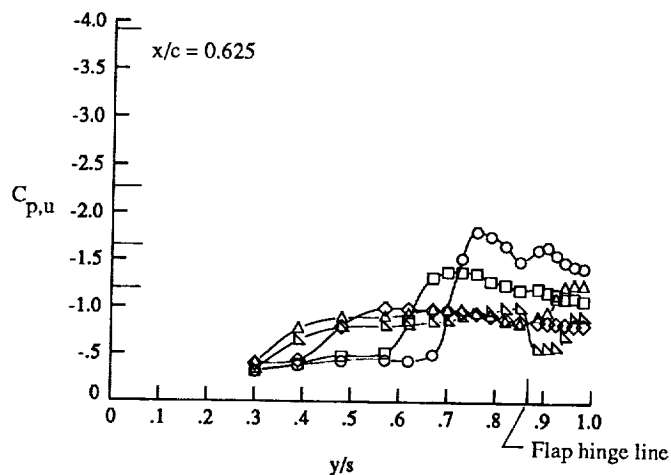
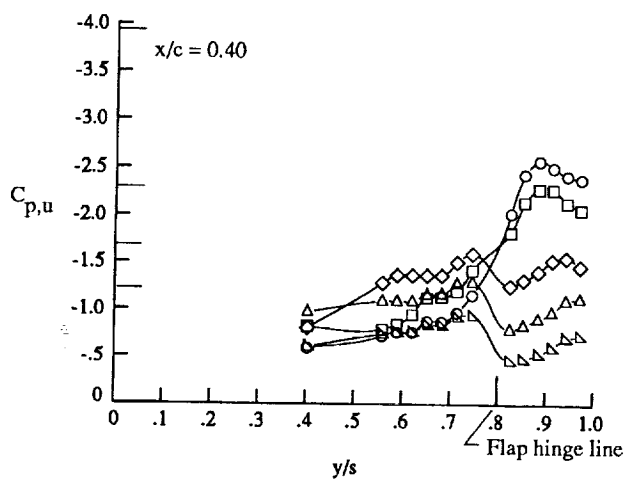


(c) Wing upper surface static pressure distributions at $\alpha \approx 16^\circ$.

Figure 33. Continued.

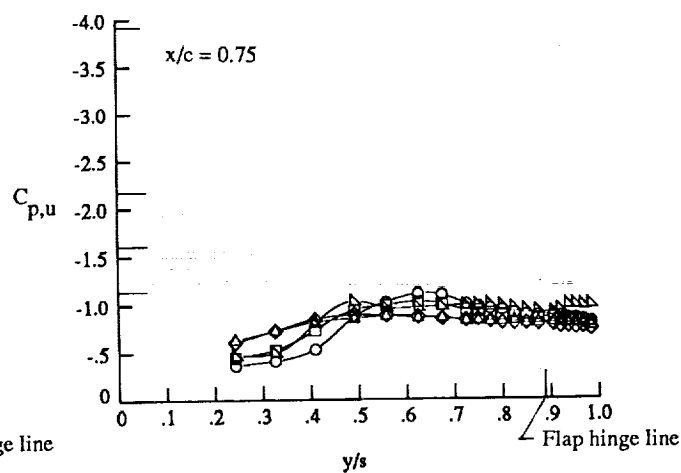
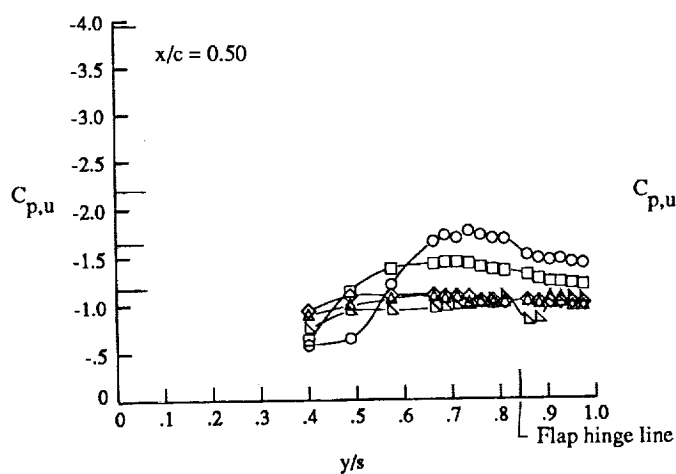
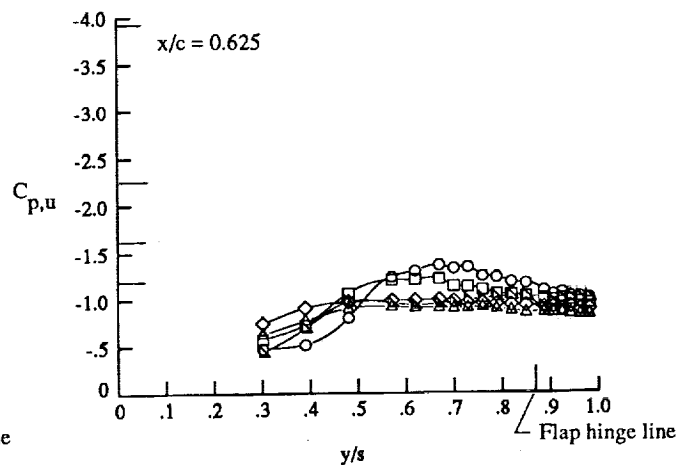
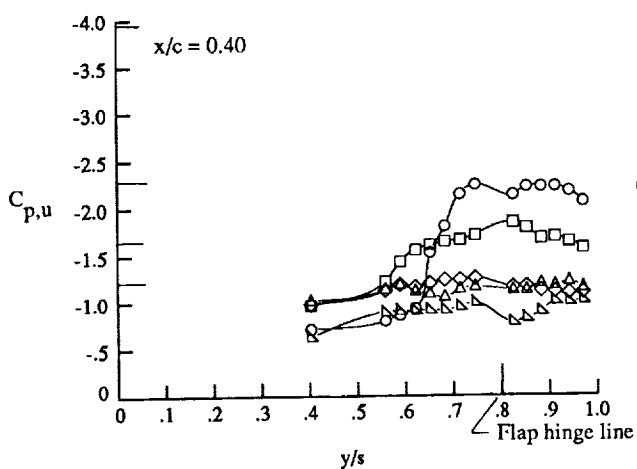
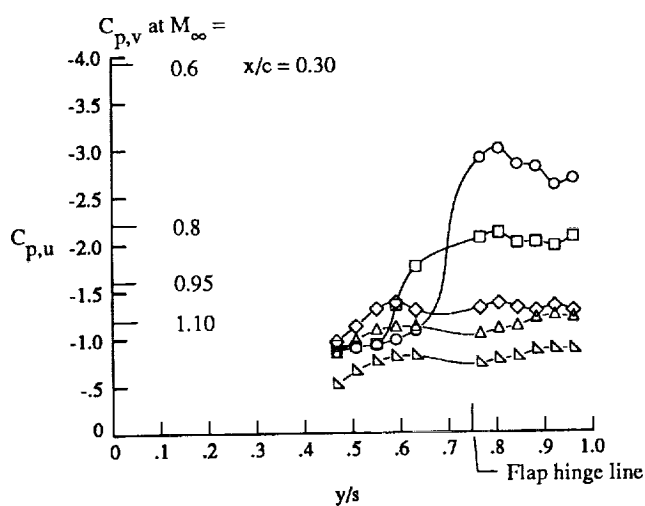


M_∞	
○	0.40
□	0.60
◇	0.80
△	0.95
▽	1.10



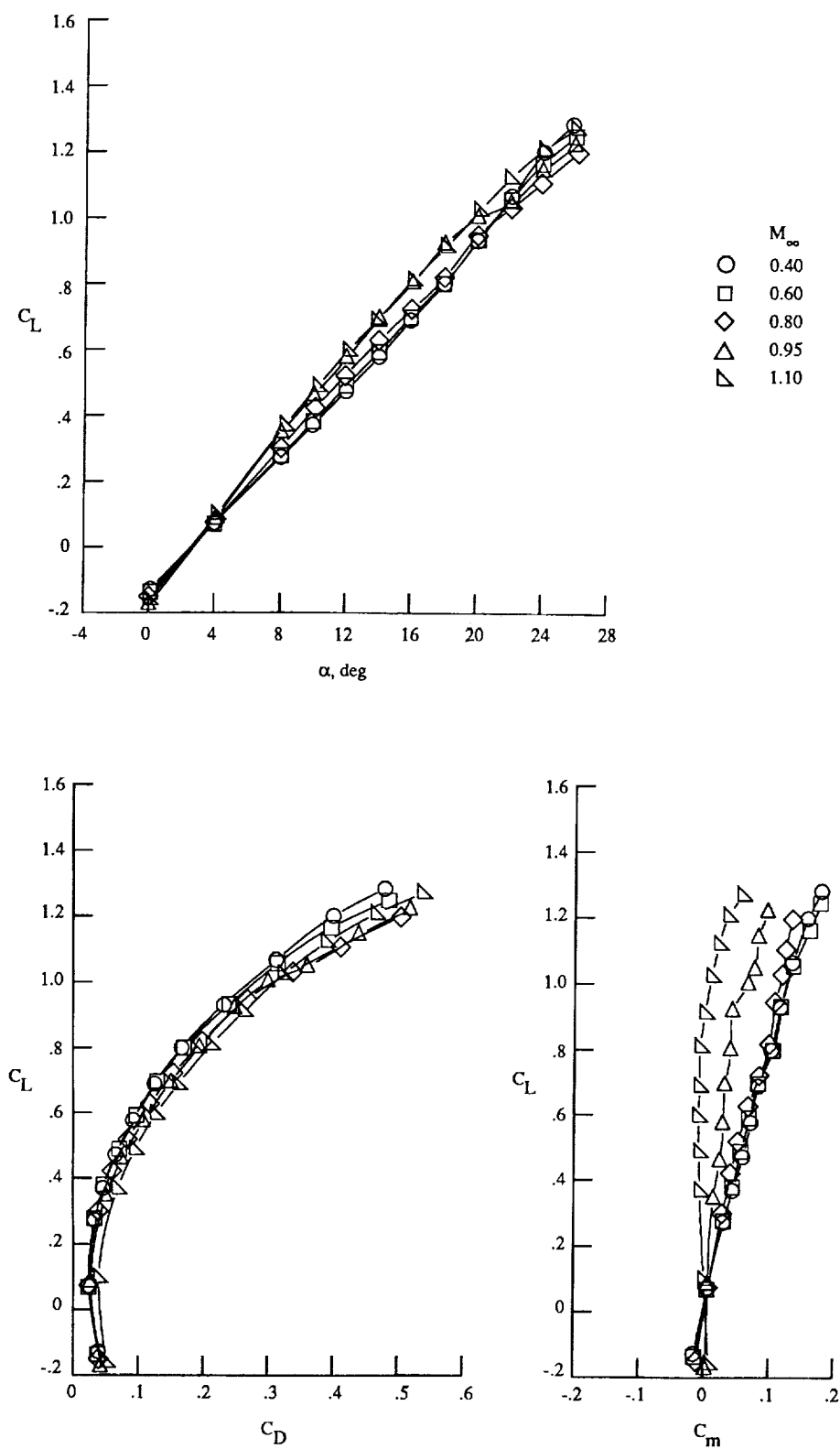
(d) Wing upper surface static pressure distributions at $\alpha \approx 20^\circ$.

Figure 33. Continued.



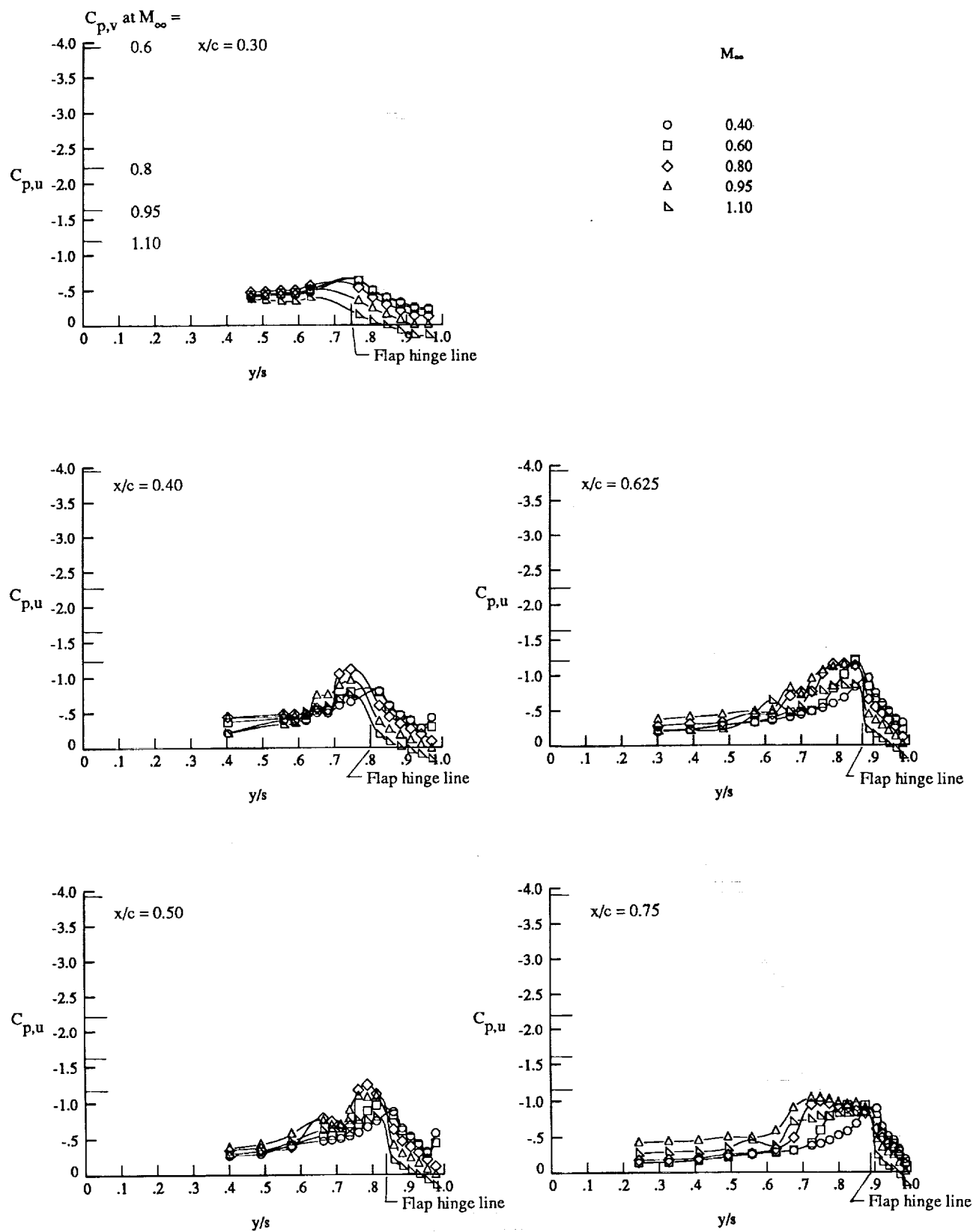
(c) Wing upper surface static pressure distributions at $\alpha \approx 24^\circ$.

Figure 33. Concluded.



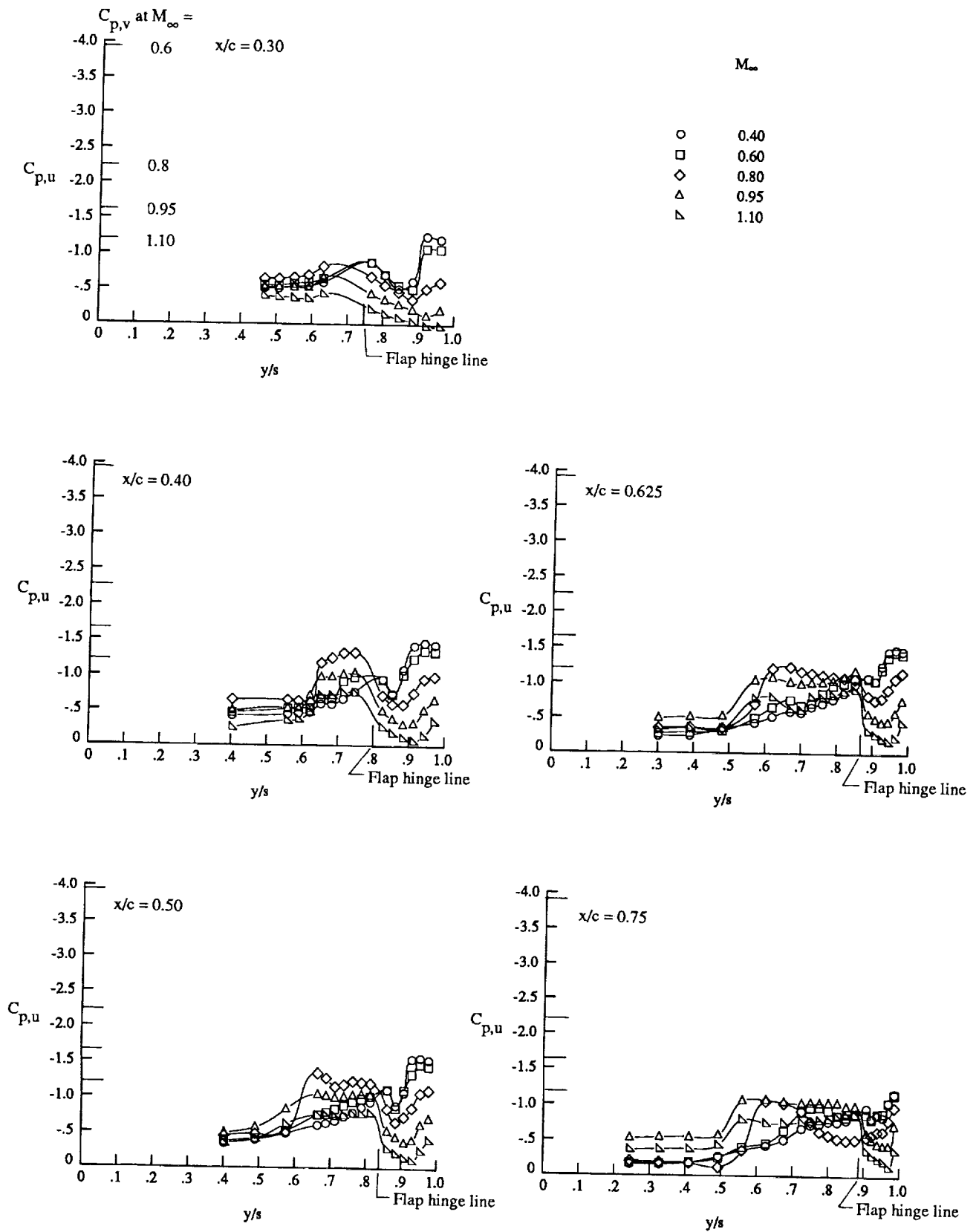
(a) Lift, drag, and pitching moment.

Figure 34. Effect of Mach number on longitudinal characteristics with strakes on and $\delta_{LE} = 30^\circ$.



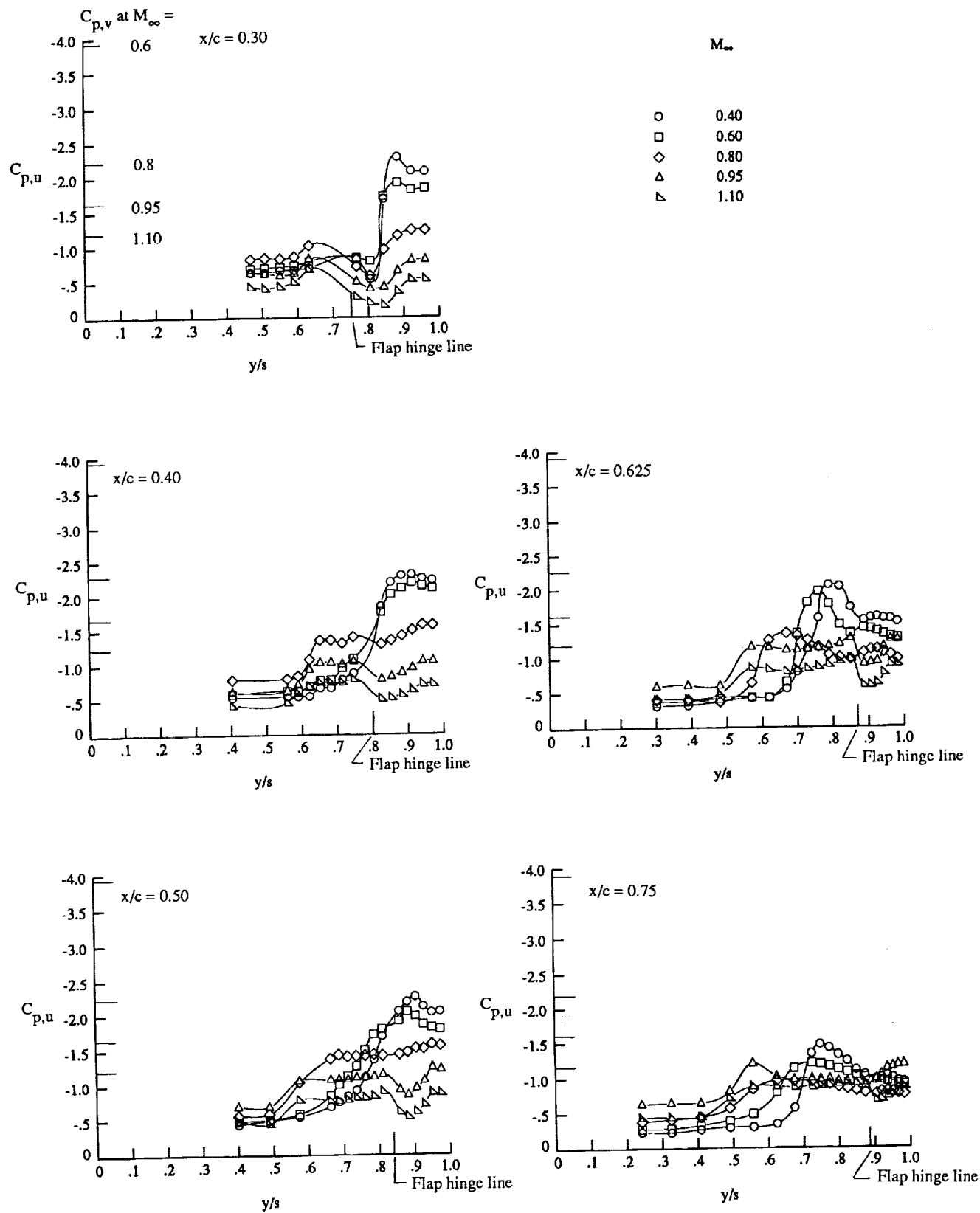
(b) Wing upper surface static pressure distributions at $\alpha \approx 12^\circ$.

Figure 34. Continued.



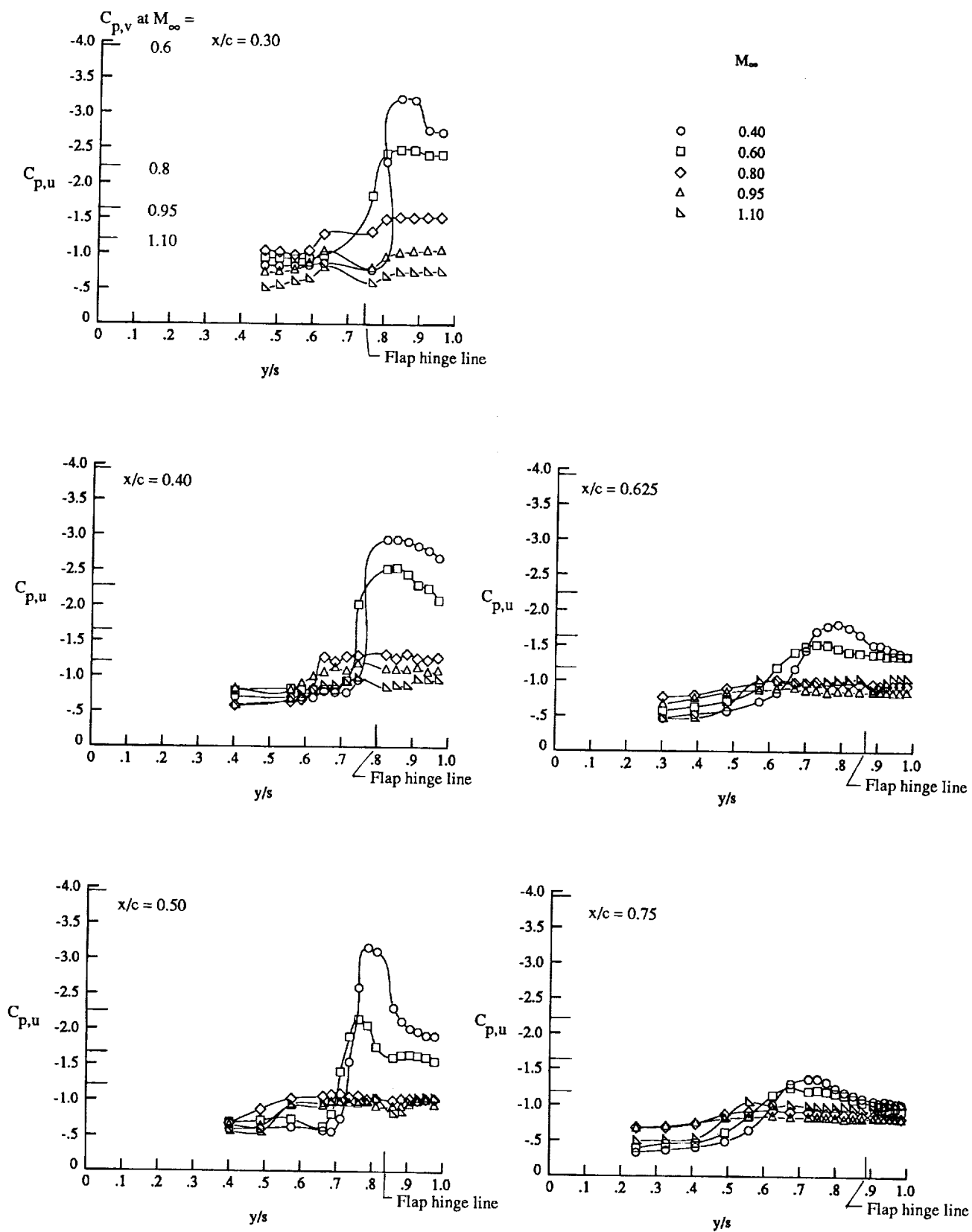
(c) Wing upper surface static pressure distributions at $\alpha \approx 16^\circ$.

Figure 34. Continued.



(d) Wing upper surface static pressure distributions at $\alpha \approx 20^\circ$.

Figure 34. Continued.



(e) Wing upper surface static pressure distributions at $\alpha \approx 24^\circ$.

Figure 34. Concluded.

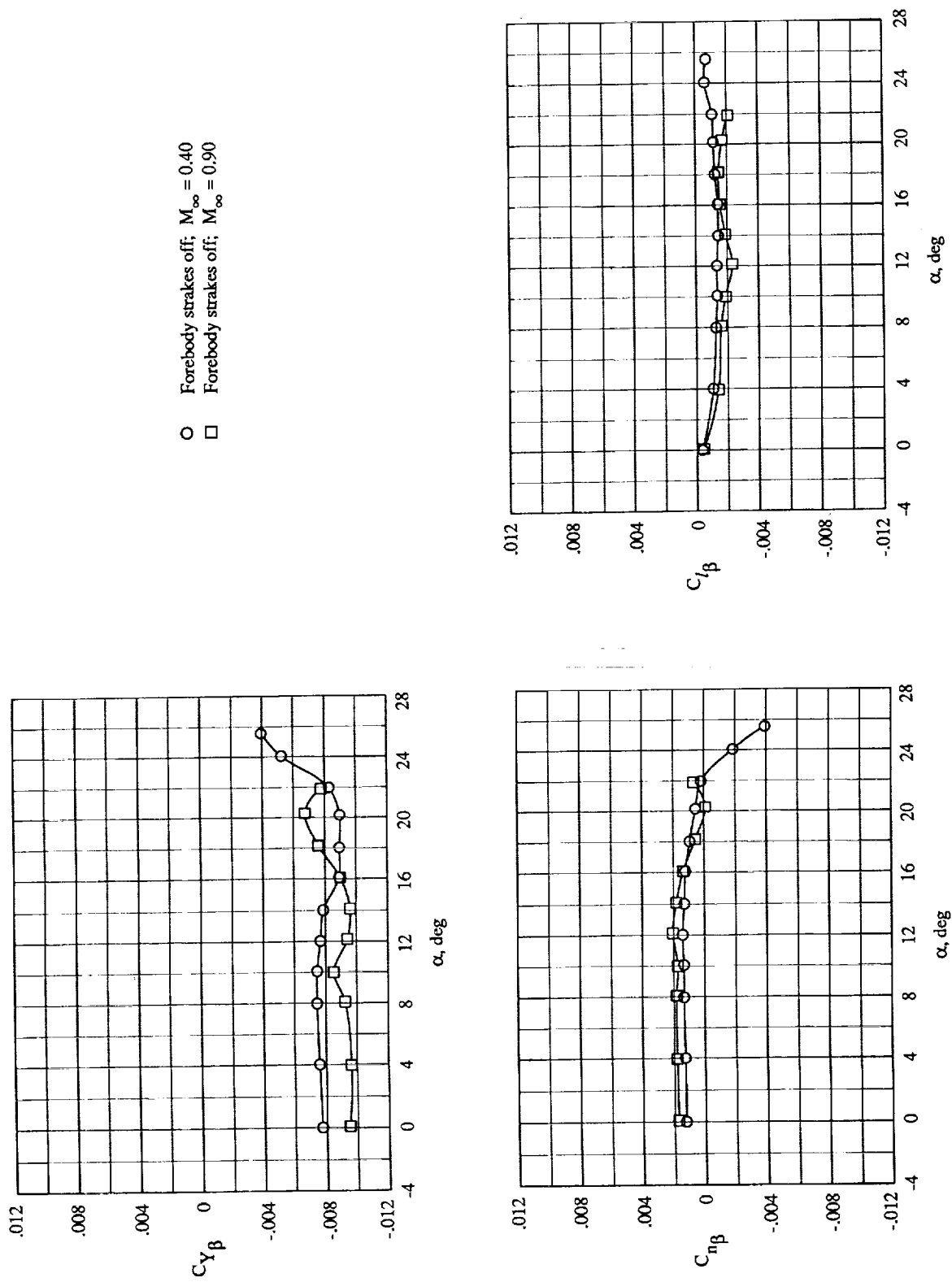


Figure 35. Effect of Mach number on lateral-directional stability derivatives with strakes off and $\delta_{LE} = 0^\circ$.

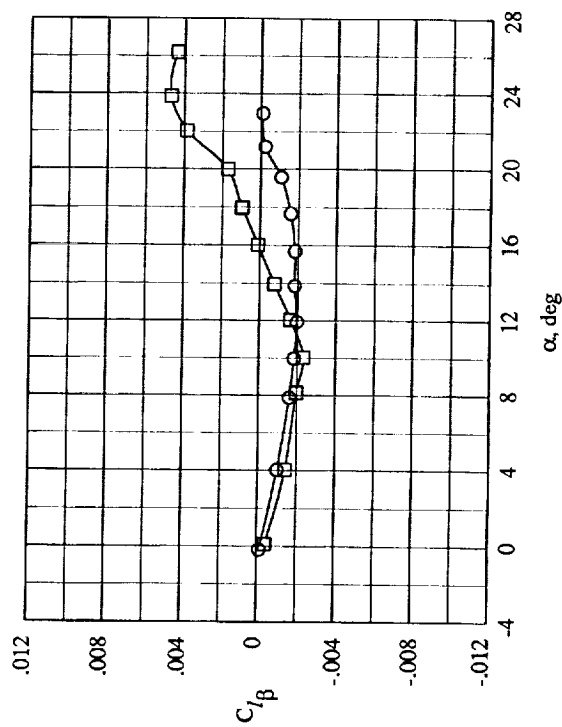
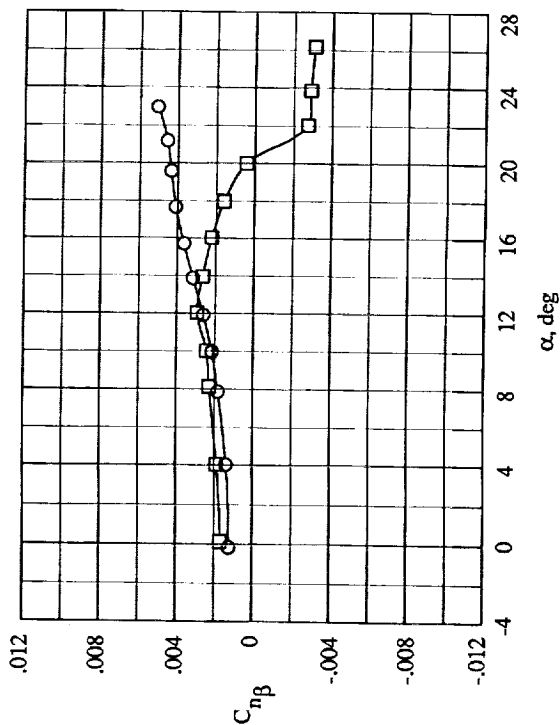
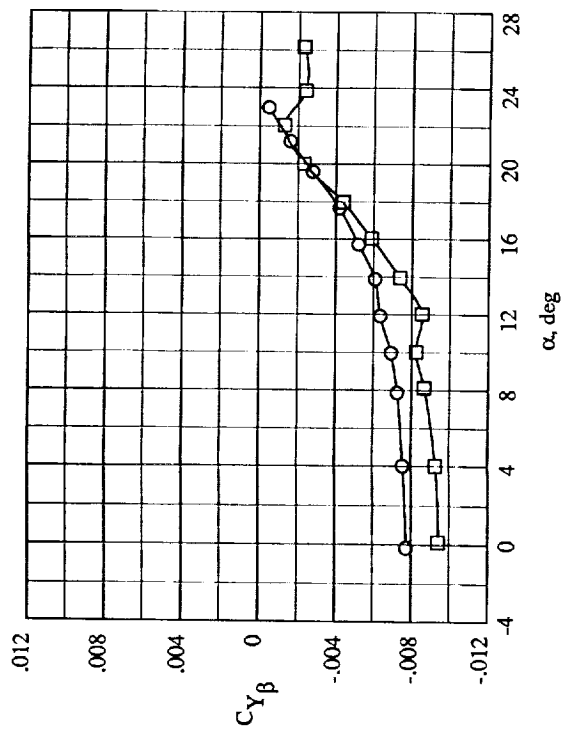


Figure 36. Effect of Mach number on lateral-directional stability derivatives with strakes on and $\delta_{LE} = 0^\circ$.

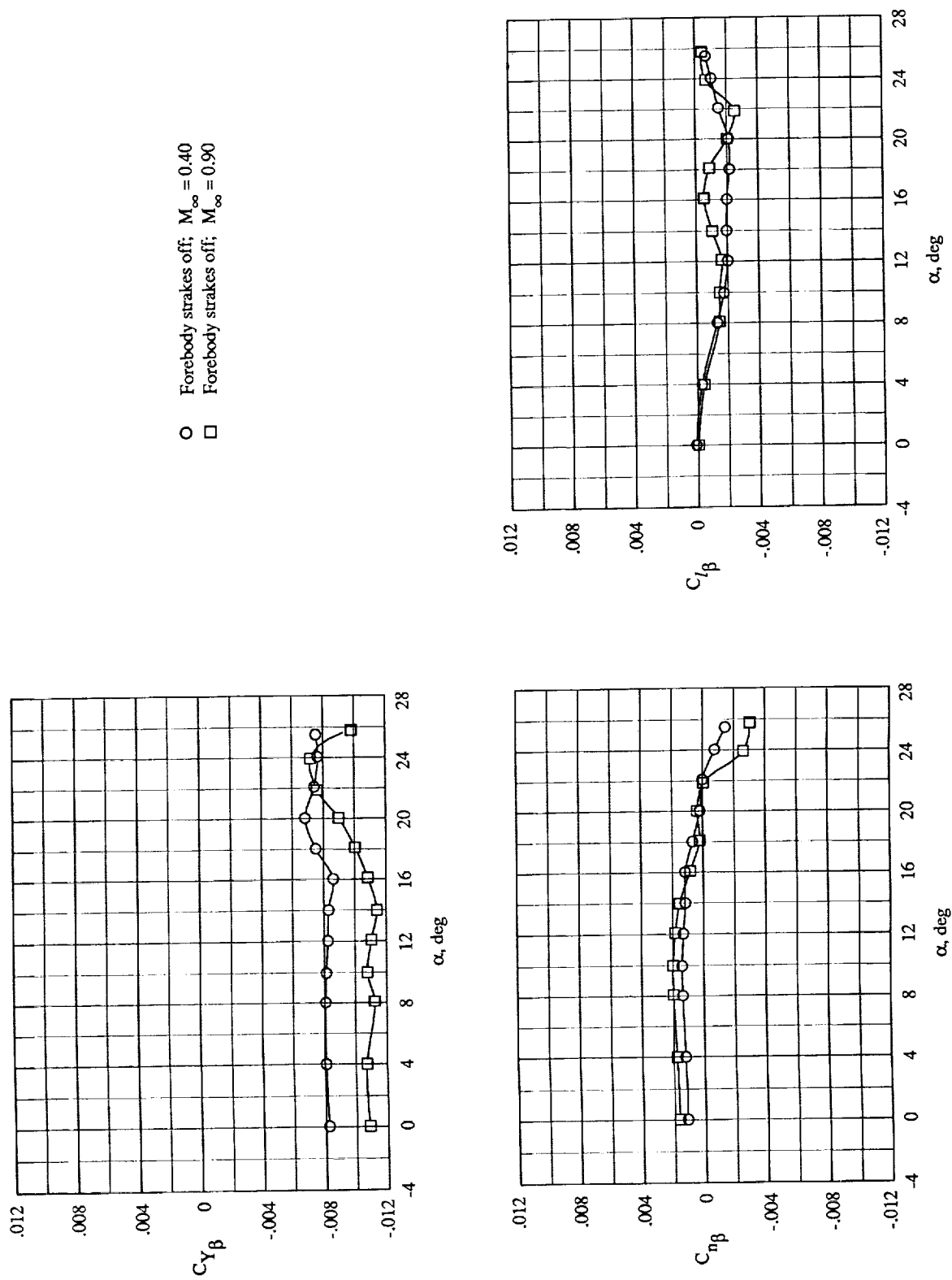
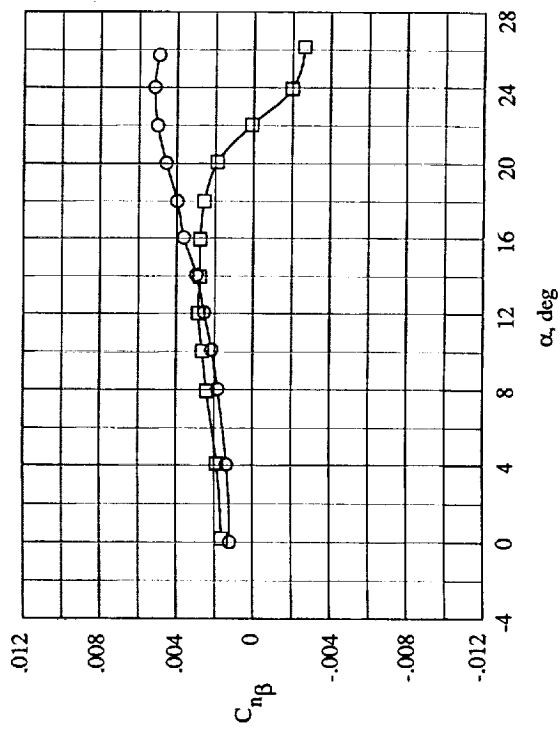
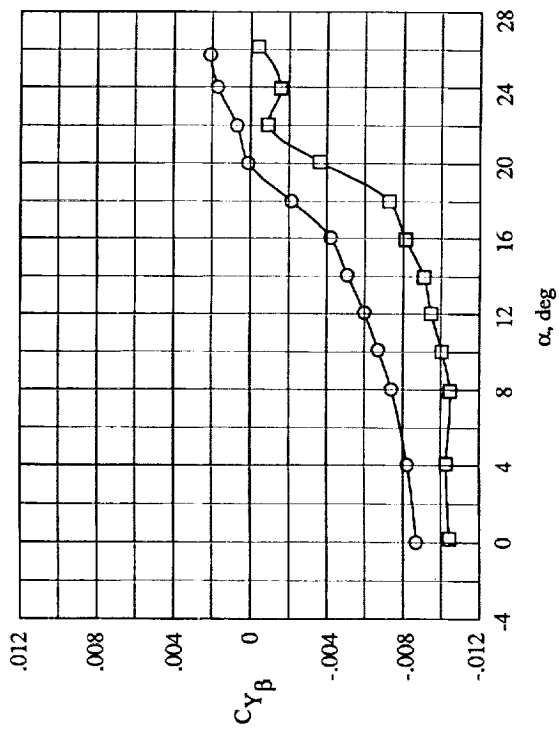


Figure 37. Effect of Mach number on lateral-directional stability derivatives with strakes off and $\delta_{LE} = 30^\circ$.



○ Forebody strakes on; $M_\infty = 0.40$
 □ Forebody strakes on; $M_\infty = 0.90$

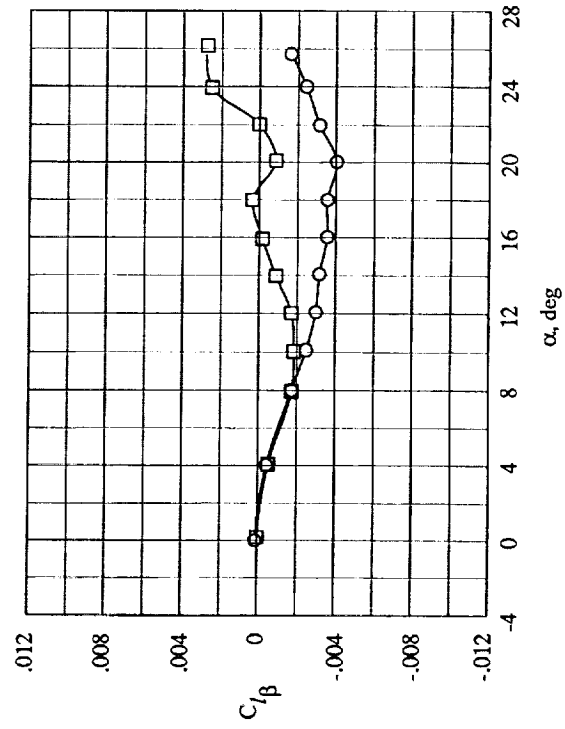


Figure 38. Effect of Mach number on lateral-directional stability derivatives with strakes on and $\delta_{LE} = 30^\circ$.

REPORT DOCUMENTATION PAGE			Form Approved OMB No. 0704-0188	
Public reporting burden for this collection of information is estimated to average 1 hour per response, including the time for reviewing instructions, searching existing data sources, gathering and maintaining the data needed, and completing and reviewing the collection of information. Send comments regarding this burden estimate or any other aspect of this collection of information, including suggestions for reducing this burden, to Washington Headquarters Services, Directorate for Information Operations and Reports, 1215 Jefferson Davis Highway, Suite 1204, Arlington, VA 22202-4302, and to the Office of Management and Budget, Paperwork Reduction Project (0704-0188), Washington, DC 20503.				
1. AGENCY USE ONLY (Leave blank)	2. REPORT DATE November 1992	3. REPORT TYPE AND DATES COVERED Technical Paper		
4. TITLE AND SUBTITLE Effects of Forebody Strakes and Mach Number on Overall Aerodynamic Characteristics of Configuration With 55° Cropped Delta Wing		5. FUNDING NUMBERS WU 505-68-30-03		
6. AUTHOR(S) Gary E. Erickson and Lawrence W. Rogers				
7. PERFORMING ORGANIZATION NAME(S) AND ADDRESS(ES) NASA Langley Research Center Hampton, VA 23681-0001		8. PERFORMING ORGANIZATION REPORT NUMBER L-17060		
9. SPONSORING/MONITORING AGENCY NAME(S) AND ADDRESS(ES) National Aeronautics and Space Administration Washington, DC 20546-0001		10. SPONSORING/MONITORING AGENCY REPORT NUMBER NASA TP-3253		
11. SUPPLEMENTARY NOTES Erickson: Langley Research Center, Hampton, VA; Rogers: Wright Laboratory-FIMM, Wright-Patterson Air Force Base, OH.				
12a. DISTRIBUTION/AVAILABILITY STATEMENT Unclassified Unlimited Subject Category 02			12b. DISTRIBUTION CODE	
13. ABSTRACT (Maximum 200 words) A wind tunnel data base was established for the effects of chine-like forebody strakes and Mach number on the longitudinal and lateral-directional characteristics of a generalized 55° cropped delta wing-fuselage-centerline vertical tail configuration. The testing was conducted in the 7- by 10-Foot Transonic Tunnel at the David Taylor Research Center at free-stream Mach numbers of 0.40 to 1.10 and Reynolds numbers based on the wing mean aerodynamic chord of 1.60×10^6 to 2.59×10^6 . The test matrix included angles of attack from 0° to a maximum of 28°, angles of sideslip of 0°, +5°, and -5°, and wing leading-edge flap deflection angles of 0° and 30°. Key flow phenomena at subsonic and transonic conditions were identified by measuring the model six-component forces and moments and wing upper surface static pressures and by conducting off-body flow visualization with a laser screen technique. These phenomena included coexisting and interacting vortex flows and shock waves, vortex breakdown, vortex flow interactions with the vertical tail, and vortices induced by flow separation from the hinge line of the deflected wing flap. The flow mechanisms were correlated with the longitudinal and lateral-directional aerodynamic data trends.				
14. SUBJECT TERMS Vortex flows; Subsonic flow; Transonic flow; Flow visualization; Vortex breakdown; Forebody strakes; Delta wings; Shock waves; Aerodynamics; Longitudinal stability; Lateral stability; Directional stability			15. NUMBER OF PAGES 170	
			16. PRICE CODE A04	
17. SECURITY CLASSIFICATION OF REPORT Unclassified	18. SECURITY CLASSIFICATION OF THIS PAGE Unclassified	19. SECURITY CLASSIFICATION OF ABSTRACT	20. LIMITATION OF ABSTRACT	